

UC Berkeley

UC Berkeley Electronic Theses and Dissertations

Title

Investigations of Organometallic Reaction Mechanisms Using Ultrafast Time-Resolved Infrared Spectroscopy

Permalink

<https://escholarship.org/uc/item/7643s5w5>

Author

Lomont, Justin

Publication Date

2014

Peer reviewed|Thesis/dissertation

Investigations of Organometallic Reaction Mechanisms Using Ultrafast Time-Resolved Infrared Spectroscopy

By

Justin Paul Lomont

A dissertation submitted in partial satisfaction of the

requirements for the degree of

Doctor of Philosophy

in

Chemistry

in the Graduate Division

of the

University of California, Berkeley

Committee in charge:

Professor Charles B. Harris, Chair

Professor Graham R. Fleming

Professor Robert W. Dibble

Fall 2014

Investigations of Organometallic Reaction Mechanisms Using Ultrafast Time-Resolved Infrared Spectroscopy

Copyright © 2014

By

Justin Paul Lomont

Abstract

Investigations of Organometallic Reaction Mechanisms Using Ultrafast Time-Resolved Infrared Spectroscopy

By

Justin Paul Lomont

Doctor of Philosophy in Chemistry

University of California, Berkeley

Professor Charles B. Harris, Chair

Ultrafast time-resolved infrared spectroscopy provides a powerful tool for studying the photochemistry of organometallic complexes. The studies described herein focus on the mechanisms of photochemically initiated organometallic reactions with a particular emphasis on two topics: the role of spin states and spin state changes in organometallic reactions, and the primary photochemical dynamics of complexes containing metal-metal bonds (e.g. transition metal dimers and clusters). Many of these studies seek to uncover trends in reactivity based on the spin states of organometallic reaction intermediates, with the goal of being able to offer some level of predictive insight into the reactivity of complexes as classified by their spin multiplicity. The reactivity of various coordinatively unsaturated reaction intermediates are studied with respect to bond activation, electron transfer, excited state photoisomerization, and other classes of reactions important to organometallic catalysis. A second focus, which shares some degree of overlap with the topic of spin state changes, is the primary photochemistry of complexes containing metal-metal bonds. Several of the studies reported herein use time-resolved infrared spectroscopy to examine the primary photochemical processes occurring upon excitation of transition metal dimers and clusters, and often spin state changes also found to play an important role. Results of computational chemistry calculations are frequently used to facilitate interpretation of the experimental results by computation of structures, relative energies, infrared spectra, and spin-orbit coupling for the complexes studied experimentally. Additional studies outside these two primary areas of focus also investigated the ring-slippage of cyclopentadienyl ligands and the CO-delivery properties of a popular CO-Releasing Molecule.

To my family

Table of Contents

Acknowledgements	v
1 Introduction	1
2 Methods	4
2.1 Picosecond Time-Resolved Infrared Spectroscopy	4
2.2 Quantum Chemical Calculations	4
3 Ultrafast Studies of Stannane Activation by Triplet Organometallic Photoproducts	6
3.1 Introduction	6
3.2 Methods	8
3.3 Results	9
3.4 Discussion	17
3.5 Conclusions	22
4 Observation of a Solvent Dependent Spin-State Equilibrium in CpCo(CO)	24
4.1 Introduction	24
4.2 Methods	25
4.3 Results and Discussion	26
4.4 Conclusions	34
5 Characterization of a Short-Lived Triplet Precursor in CpCo(CO)-Catalyzed Alkyne Cyclotrimerization	35
5.1 Introduction	35
5.2 Methods	37
5.3 Results and Discussion	37
5.4 Conclusions	43
6 Direct Observation of a Bent Carbonyl Ligand in a 19-Electron Transition Metal Complex	44
6.1 Introduction	44
6.2 Methods	45
6.3 Results and Discussion	46
6.4 Conclusions	54
7 Insights Into the In-Cage Photochemical Disproportionation of Transition Metal Dimers	55

7.1	Introduction	55
7.2	Methods	56
7.3	Results and Discussion	47
7.4	Conclusions	65
8	Reactivity of the TEMPO Radical Toward 16- and 17-Electron Organometallic Reaction Intermediates	66
8.1	Introduction	66
8.2	Methods	67
8.3	Results and Discussion	68
8.4	Conclusions	76
9	Direct Observation of a Metal-Ketene Formed by Photoexcitation of a Fischer-Carbene Using Ultrafast IR Spectroscopy	78
9.1	Introduction	78
9.2	Results and Discussion	79
9.3	Conclusions	83
10	Picosecond Time-Resolved Infrared Studies of the Photochemistry of $M_3(CO)_{12}$ ($M = Fe, Os$) Clusters in Solution	84
10.1	Introduction	84
10.2	Methods	85
10.3	Results and Discussion	86
10.4	Conclusions	97
11	Picosecond Time-Resolved Infrared and DFT Studies of the Photochemistry of $Co_4(CO)_{12}$ in Solution	99
11.1	Introduction	99
11.2	Methods	100
11.3	Experimental Results	100
11.4	DFT Results and Discussion	105
11.5	Conclusions	110
12	Exploring the Utility of Thermal-Photochemical CO-Delivery with CORM-2	112
12.1	Introduction	112
12.2	Methods	113
12.3	Results and Discussion	114
12.4	Conclusions	120
13	A TRIR/DFT Mechanistic Study of Ring-Slipped Intermediates via Photolysis	

of (η^1-CCl₃)Mn(CO)₅	121
13.1 Introduction	121
13.2 Methods	122
13.3 Results and Discussion	123
13.4 Conclusions	131
14 Primary Photochemical Dynamics of Triply-Bonded Metal Carbonyl Dimers Probed via Ultrafast Infrared Spectroscopy	133
14.1 Introduction	133
14.2 Methods	135
14.3 Results and Discussion	135
14.4 Conclusions	133
15 Should External Heavy Atom Effects be Expected in Transition Metal Complexes?	145
15.1 Introduction	145
15.2 Methods	147
15.3 Results and Discussion	149
15.4 Conclusions	155
16 Summary and Outlook	157
Bibliography	160

Acknowledgements

The first person I would like to thank is my advisor, Professor Charles B. Harris, for providing an excellent academic environment in which to pursue my doctoral studies. Charles provides his students with a high degree of freedom and opportunity to independently pursue their own research interests, simultaneously demonstrating his unyielding belief in his students' capabilities, as well as the extent to which he is willing to prioritize the education of his students over his own research or career interests. He is continually supportive of each of his students, and, though each of us have faced difficult times in our own research, I must say that, looking back, I learned an immense amount from being given the chance to approach my research with such independence.

Of course, there are many others who deserve great thanks for the help and friendship they have provided over the years. Son Nguyen has consistently been an amazing teammate to work with, and it's worth noting that he contributed to virtually all of the research described in this thesis. Jacob Schlegel provided invaluable guidance during my first years at Berkeley, and managed to do so while simultaneously being one of the most fun people to have in the group. Matt Zoerb was principally responsible for teaching Son, Adam, and I how to use the laser setup when we were first getting started and was always patient and encouraging. Of course, he was also a blast to hang out with outside the lab. Adam Hill always did an excellent job of holding the group together in various ways including sharing stories, inspiring discussion, scheduling events, and bringing several undergraduate researchers into the group.

From the "surface side" of the group, Benjamin Caplins was always full of knowledge on a wide-range of topics in chemistry, physics, computer science, and beyond. I always appreciated his willingness to share this information and to help keep everyone up to date on the latest literature. David Suich and Alex Shearer were similarly great companions to have in the group; they were both a lot of fun to hang out with while also contributing significantly to our research discussions in the group. Eric Muller and James Johns were also great friends and provided helpful guidance, particularly during my first couple of years in the Harris group.

I was also very fortunate to work with Professors Angelica Stacy and Anne Barringer, along with many students from the SESAME program and other educators in the sciences during my time at Berkeley. These interactions helped me to better understand the challenges facing science education on a variety of levels, and the discussions at the group's weekly meetings were consistently a welcome change of pace from my doctoral research.

Other great friends with whom I shared the experience of being a graduate student at Berkeley include Chandra Richards, Tiffany Pham, Lukas Valin, Chen Zhao, Karthik Balakrishnan, Dongjin Seo, and Katie Martins (I'm sure I've left some people out). All of these friends helped to make life as a graduate student much more fun than it could possibly have been without them.

Finally moving on to friends and colleagues outside of Berkeley, I also had the chance to spend the summer of 2013 working in the group of Professor Jianping Wang at the Institute of Chemistry, Chinese Academy of Sciences in Beijing, and I thank his entire group for their warm hospitality and friendship. My undergraduate research advisor and long-time mentor, Brian Coppola, deserves significant praise for his continued guidance. Also a big thank you to Ian Stewart, with whom I shared the various challenges of writing our first book together during my time at Berkeley. Professor Michael George of Nottingham has been a continued supporter,

advisor, and collaborator in research, whose group's research often follows parallel and intertwined research directions with ours in the Harris group; I've always enjoyed our conversations and his genuine, deep interest in the field.

There are many friends from my personal life who probably deserve some of the greatest thanks of all for making life fun and keeping me sane over the past several years. I cannot express how much I have appreciated the friendship of Ian Wall, Steven Hughes, Keary Engle, Victoria Shen, Melody Campbell, HaeLee Choi, and many other friends for their continued support and encouragement over the years.

Of course, the last people who remain to be thanked are my family, to whom I owe so much.

1 Introduction

Organometallic Chemistry is a field at the intersection of organic and inorganic chemistry, with applications to a wide range of chemical processes. These include, perhaps most notably, catalysis of synthetically useful chemical reactions, though organometallic complexes also play key roles in numerous other processes including biochemical pathways and metallurgy, and have also found applications as dietary supplements and as CO- and NO-releasing molecules used to control physiological functions. The majority of research investigations into the behavior of organometallic complexes have traditionally been carried out using approaches more native to synthetic chemistry, though in recent years time-resolved spectroscopic techniques have become increasingly popular for studying the structure and reactivity of these species. The studies described in this thesis use ultrafast time-resolved infrared (TRIR) spectroscopy to study the reactivity of a variety of prototypical organometallic complexes with the goal of identifying unifying underlying principles that can be applied to a broad range of organometallic reactions.

The experimental technique used to investigate each of these topics is picosecond time-resolved infrared spectroscopy. Certainly not all chemical reactions can be studied on the picosecond timescale, but this experimental approach is typically quite well-suited for studying reactions with relatively small free energy barriers, changes in spin state, solvent coordination, excited state lifetimes, geminate recombination processes, and rearrangements of solvent molecules, as these dynamics very often take place in the picosecond regime. Indeed, many of these topics are the focus of study in this thesis. Moreover, many organometallic complexes contain reporter ligands, such as CO, NO, or CN groups, with strong absorptions in the mid-infrared region, thus rendering such complexes readily amenable to study by TRIR spectroscopy. In many cases, quantum chemical calculations are also used to facilitate, and expand upon, our interpretation of the experimental results.

In Inorganic Chemistry it is often the case that isoconfigurational transition metal ions (i.e. those with the same d^n electron configuration) exhibit similar properties; thus d^6 Co(III) will behave more similarly to d^6 Fe(II) than to d^7 Co(II). Analogously, it is also often the case that the total electron count of an organometallic complex is a strong predictor of its shared trends in reactivity with other organometallic complexes. 18-electron species are typically stable and unreactive, while their coordinatively unsaturated 17-electron counterparts tend to participate in reaction mechanisms involving other radical species/intermediates, and 16-electron complexes typically react more readily with 2-electron donor ligands. Such trends can further be elucidated by careful inspection of the more detailed electronic structure of organometallic complexes. One such parameter that has been the focus of intense study in this thesis is the spin state of an organometallic complex, which may often rightfully be thought of as a sort of proxy for discussing radical or diradical electronic character in the reactive frontier orbitals of a complex.

Photoproducts of three spin states, singlet, doublet, and triplet ($S = 0, \frac{1}{2},$ and 1 , respectively) have been studied in this thesis. Beginning from a stable 18-electron organometallic complex, photochemical dissociation of a 2-electron ligand results in the formation of a coordinatively unsaturated 16-electron photoproduct. Such photoproducts most commonly have a singlet ground state, though some species, such as $\text{Fe}(\text{CO})_4$ and $\text{CpCo}(\text{CO})$ are known to be stable in a triplet ground spin state under certain conditions (for the two examples listed, this is true in non-coordinating solvents and in the gas phase). While triplet complexes are typically expected to be less reactive than their singlet counterparts, our group and others have found evidence that this is

not always the case, and indeed that many examples exist in which the course of a chemical reaction can be accelerated by following a pathway that involves spin crossover processes during the course of the reaction. Chapters 3 through 5 of this thesis explore the reactivity of triplet reaction intermediates on the ultrafast timescale and explore spin crossover processes in several prototypical organometallic photoproducts.

Chapters 6 and 7 of the thesis move on to study odd-electron photoproducts. While these species are typically unreactive toward most weak 2-electron donor ligands/solvents, many phosphines and phosphites have been shown to be strongly coordinating enough to add to 17-electron complexes to yield 19-electron adducts. These electron-rich adducts may then undergo subsequent disproportionation (electron transfer) reactions, which, under appropriate conditions, can be observed on the picosecond timescale. Interestingly, one such 19-electron adduct was observed to redistribute some of its excess electron density onto a CO ligand, causing the ligand to adopt a bent geometry, and effectively resulting in a complex with 18-electrons localized at the metal center; this is described in Chapter 6. The reactivity of several odd-electron complexes toward in-solvent-cage disproportionation was explored and compared in Chapter 7.

Having delved into the reactivity of both even- and odd-electron reaction intermediates, we turn next to an investigation of the reactivity of a very popular organic radical, TEMPO, as a ligand toward both classes of coordinatively unsaturated organometallic complexes. The TEMPO radical has found applications in a truly expansive array of chemical applications, including alcohol oxidation reactions, the Pauson-Khand reaction, free-radical polymerizations, nanoparticle synthesis, and serving as an EPR probe in biological systems. While in the past there have not been any predictive models developed for how TEMPO will coordinate as a ligand to a metal center (many coordination modes are possible), we find that TEMPO appears to consistently coordinate as an anionic ligand to low-valent 16- and 17-electron organometallic species. This work is described in Chapter 8.

Chapter 9 shifts focus to investigate an example how spin state changes can affect excited state photochemistry, looking at the mechanism of formation of a key metal-ketene intermediate that has long been postulated to form in reactions involving chromium and molybdenum Fischer carbene complexes. For the first time, we have directly characterized the structure and spin state of the metal-ketenes that form upon visible excitation of a prototypical Fischer carbene, $\text{Cr}(\text{CO})_5[\text{C}(\text{CH}_3)\text{OCH}_3]$ via photocarbonylation from the carbene precursor. We also look at the photochemistry of the tungsten congener of this complex, which we find does not form any metal-ketene intermediates, explaining its lack of reactivity in synthetic applications.

In Chapters 10 and 11 we explore the photochemistry of trimetallic and tetrametallic metal carbonyl clusters. In addition to their catalytic applications, these clusters have been used as synthetic precursors to other organometallic complexes. Considering the numerous metal-ligand and metal-metal bonds present, it is not easy to predict the photochemical reactivity of these complexes, and thus picosecond infrared spectroscopy is a very useful tool for examining the primary photochemical processes in these clusters.

The focus of Chapter 12 is on an application of metal carbonyl complexes that is distinct that discussed in the other chapters in this thesis: delivery of CO as a form of medical treatment via CO-Releasing Molecules (CO-RMs). The CO-release properties of one of the most popular CO-RMs to date, $\text{Ru}_2\text{Cl}_4(\text{CO})_6$ (CORM-2) is explored in biologically relevant solvent environments. In DMSO, the solubilizing agent commonly used in preclinical trials, it is found that CORM-2 is actually unstable, reacting to form a mixture of products on the time scale of hours to days after dissolution. The reactivity of the DMSO-ligated products, as well as that of the parent CORM-2

molecule, is also examined in mouse serum, finding that while the parent complex does release CO spontaneously in mouse serum, the DMSO-ligated monomeric products do not. This suggests that a significant fraction of the drug delivered in the 150+ studies on this complex to date is likely inactive with regard to CO-delivery. Photochemical CO-release with this complex is explored in both solvent environments, and it is concluded that a combined thermal-photochemical approach to CO release with this popular CO-RM can likely significantly improve its efficacy as a drug molecule. Though a combined thermal-photochemical approach has not been taken with any CO-RM to date, such an approach will likely be useful with a significant number of existing and future (yet to be developed) CO-RMs.

Chapter 13 explores the slippage of cyclopentadienyl rings, which are among the most widely utilized ligands in organometallic chemistry. This study builds on earlier work in the Harris group, making use of an η^1 parent complex to observe the ring-slipped intermediates formed upon dissociation of a CO ligand. Interestingly, we find evidence that the slipped ring behaves similarly to a compressed spring, whose energy facilitates ejection of an additional CO ligand as it relaxes to form an η^5 dicarbonyl loss product.

Chapter 14 describes explorations into the photochemistry of a pair of $[\text{Cp}^*\text{M}(\text{CO})_2]_2$ ($\text{M} = \text{Cr}, \text{Mo}$) dimers, which differ from the metal-metal bonded complexes discussed in the preceding chapters of this thesis in that this pair of complexes is characterized by a metal-metal triple bond. The carbonyl ligands in the parent complexes also adopt fairly unusual semi-bridging geometries. The photochemistry of these triply metal-metal bonded dimers differs from that of the singly bonded dimers studied to date in that the stronger metal-metal bond prevents homolysis via a single photon process, and thus the photochemistry of these complexes on diffusion limited and longer time scales will be determined by ligand dissociation processes. For the chromium complex, population of an excited state triplet intermediate with a lifetime of ca. 380 ps is observed to be the primary photochemical pathway.

Finally, Chapter 15 describes a purely computational study into the presence (or lack thereof) of an external heavy atom effect in organometallic reactions. Though external heavy atom effects have long been known to be important in the photophysics and reactivity of organic molecules, such effects remain almost entirely unexplored for organometallic complexes. DFT and CASSCF calculations are used to explore the changes in spin-orbit coupling that take place along a bimolecular reaction coordinate for reactions of the prototypical reaction intermediate $\text{Fe}(\text{CO})_4$. Interestingly, these calculations show no evidence for an external heavy atom effect, and the reasons for the results of these calculations are explored.

The final chapter, Chapter 16, describes the overall conclusions reached in the studies described in the preceding chapters and touches on potential future directions for research in the areas discussed in this thesis.

2 Methods

The following chapter is reproduced (adapted) in part with permission from (Lomont, J. P.; Nguyen, S. C.; Schlegel, J. P.; Zoerb, M. C.; Hill, A. D.; Harris C. B. *J. Am. Chem. Soc.* 2012, *134*, 3120-3126.). Copyright (2012) American Chemical Society.

2.1 Picosecond Time-Resolved Infrared Spectroscopy

The basic details of the experimental apparatus used to collect picosecond time-resolved infrared spectra are outlined below. This setup has recently been described in substantial detail in the theses of multiple other students working on the same instrument in the Harris group laboratory,¹⁻³ and thus will not be detailed in full here.

The experimental setup consists of a Ti:sapphire regenerative amplifier (SpectraPhysics, Spitfire) seeded by a Ti:sapphire oscillator (SpectraPhysics, Tsunami) to produce a 1 kHz train of 100 fs pulses centered at 800 nm with an average pulse power of 1.1 mJ. The output of this commercial system is split, and 30% of the output is used to generate 400 and 267 nm pump pulses (80 and 6 μJ per pulse at sample, respectively) via second and third harmonic generation. The other 70% is used to pump a home-built two-pass BBO-based optical parametric amplifier (OPA),⁴ the output of which is mixed in a AgGaS₂ crystal to produce mid-IR probe pulses tunable from 3.0 to 6.0 μm with a 200 cm^{-1} spectral width and a ca. 100 fs pulse duration. The 400 and 267 nm pulses pass through a 25 cm silica rod, which stretches the pulses in time to 1 ps, and gives a cross correlation of the mid-IR and 400 or 267 nm pulses of 1.1 ps at the sample. The stretched 400 and 267 nm pulses are necessary to achieve high pump powers without generating products resulting from multi-photon excitation. The stretched pulses also reduce artifacts resulting from nonlinear optical effects in the sample cell windows.

The polarization of the pump beam is held at the magic angle (54.7°) with respect to the mid-IR probe beam to eliminate effects from rotational diffusion. A computer controlled translation stage (Newport) allows for variable time delays up to ca. 1.5 ns between pump and probe pulses. The sample is flowed using a mechanical pump through a stainless steel cell (Harrick Scientific) fitted with 2 mm thick CaF₂ windows separated by spacers ranging from 100 to 2000 μm . The pump and probe beams are spatially overlapped at the sample and focused so that the beam diameters are ca. 200 and 100 μm respectively. The sample cell is moved by computer controlled translational stages (Standa) during the course of data collection so that absorptions are not altered by any accumulation of photoproduct on the sample windows. Reference and signal mid-IR beams are sent along a parallel path through a computer controlled spectrograph with entrance slits set at 70 μm (Acton Research Corporation, SpectraPro-150) and detected by a 2 \times 32 element MCT-array IR detector (InfraRed Associates, Inc.) and a high-speed signal acquisition system and data-acquisition software (Infrared Systems Development Corp.) with a resolution of ca. 2.5 cm^{-1} . Collected signals are typically averaged over ca. 2 \times 10⁴ laser shots to correct for shot-to-shot fluctuations. Differences in optical density as small as 5 \times 10⁻⁵ are observable after 1 s of data collection.

2.2 Quantum Chemical Calculations

Two classes of quantum chemical calculations were used in the studies described in this thesis: density functional theory (DFT) calculations, and complete active space self-consistent field (CASSCF) calculations.

DFT calculations were used to investigate the structures, energies, and frequencies of the organometallic complexes observed in the experimental studies described in the studies outlined in this thesis. The efficient scaling of DFT methods with the number of electrons in the system ($\sim N^3$, where N is the number of electrons), combined with the relatively high level of accuracy of these methods for studying organometallic systems, means that DFT methods often offer the best available combination of accuracy and efficiency for studying organometallic complexes, especially when there are a large number of calculations to be done. Indeed, the literature contains a tremendous number of DFT approaches to studying organometallic systems, and a variety of computational packages exist with DFT methods built in that can be used easily even by researchers who are relatively inexperienced with computational methods.

CASSCF methods were used in cases where the spin-orbit coupling (SOC) between different spin states was of interest. For the purposes of the studies in this thesis, this almost exclusively involved singlet and triplet states. CASSCF methods are among the most “hands-on” electronic structure calculations, as the user must select a set of active space orbitals, and a number of valence electrons, within which all possible excitations will be considered in the wave function. These may commonly range between active spaces as small as say 2 electrons in 4 orbitals, but may become as large as say 16 electrons in 16 orbitals. For organometallic complexes, one typically would like to at least include all of the valence orbitals (both bonding and anti-bonding) with substantial d-orbital character, typically resulting in at least 10 orbitals in the active space. This leads to a very long (in terms of computational hours) calculation of the wave function itself, meaning that more involved calculations, such as those to scan the potential energy surface, or even those to simply optimize geometries at the CASSCF level, would usually take too long to make such an approach practical. However, there is another reason yet that such calculations may be impractical, and this involves how the active space orbitals may change as changes are made to the geometry of the nuclei. If the active space orbitals change significantly in character as the geometry of the nuclei is modified (say during a geometry optimization calculation), the ordering or nature of the active space orbitals may change, such that the user would need to re-select the set of active space orbitals. Thus, to do such a calculation carefully, the user would need to periodically re-inspect the active space orbitals to make sure that they are still the desired choice. Thus, in practice, it is fairly common to obtain nuclear positions from a lower level calculation (such as a DFT-level geometry optimization), and then use these to calculate properties at the CASSCF level. Considering all of these difficulties, one must ask, why use CASSCF to calculate SOC? The answer lies in the fact that the singlet and triplet states in which we are interested involve differences in electronic configurations in closely spaced d-orbital energy levels, and thus the wave functions in which we are interested tend to involve significant multi-reference character. It is worth noting that time-dependent DFT methods capable of performing SOC calculations have also been developed, though these have been less thoroughly tested (to date) and, due to the fact that DFT orbitals may be unreliable in general, it seems only natural to question whether one can reliably interpret individual orbital contributions to SOC in such calculations.

3 Ultrafast Studies of Stannane Activation by Triplet Organometallic Photoproducts

The following chapter is reproduced (adapted) in part with permission from (Lomont, J. P.; Nguyen, S. C.; Harris C. B. *Organometallics* 2012, *31*, 3947-3957.). Copyright (2012) American Chemical Society.

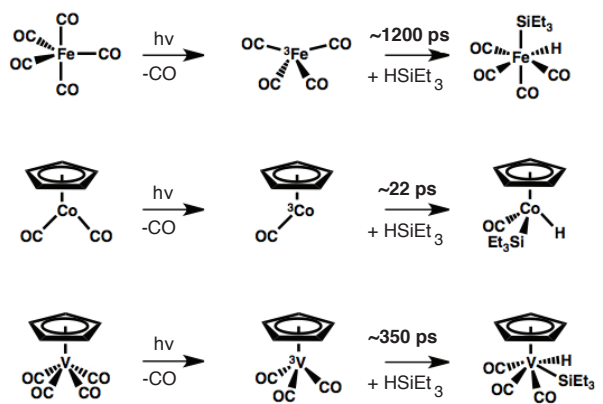
3.1 Introduction

The activation of chemical bonds by coordinatively unsaturated organometallic complexes is a broad topic of intense research.⁵⁻⁹ The role of spin state changes in these reactions have, in many cases, been used to rationalize a lack of reactivity due to spin-blocking as triplet metal centers coordinate to form singlet bond activated products.¹⁰⁻¹⁴ Previous studies using ultrafast time-resolved infrared (TRIR) spectroscopy to monitor silane activation by singlet and triplet photoproducts in neat HSiEt₃ solution led to a counterintuitive result, demonstrating that triplets are actually able to activate Si-H bonds faster than their singlet counterparts (Figure 3.1).¹⁵⁻¹⁹ In the present work, we explore the role of spin state changes in the activation of Sn-H bonds in neat HSnBu₃, which represents the most widely used organotin reagent.²⁰ Activation of Sn-H bonds allows for hydrostannylation of alkenes and alkynes, affording synthetically versatile intermediates; thus it is of interest to better understand the detailed factors governing catalytic Sn-H bond cleavage.^{20,21}

Previous studies have shown that ground state singlet 16-electron photoproducts can coordinate to alkyl groups as token ligands with favorable binding energies on the order of 10 kcal/mol.²² Triplet metal centers interact much more weakly with solvent molecules, and spin crossover to a singlet state is typically required for coordination of a solvent molecule to the metal center.^{18,23-30} The rate of spin state changes depends sensitively on the solvent, however, and coordinating functional groups can facilitate formation of solvated singlet species.^{18,25}

Figure 3.1 summarizes the differences in reactivity observed for the activation of Si-H bonds by singlet and triplet photoproducts. The increased rates of reactivity for triplet 16-electron photoproducts were rationalized as follows: triplets interact weakly at best with alkyl groups, allowing them to diffuse through the solvent rapidly, relative to their singlet counterparts. Upon encountering a more coordinating Si-H bond, triplets readily undergo spin crossover, allowing bond activation to take place. This combination of factors causes triplet photoproducts to activate Si-H bonds more readily than similar singlet species, despite the fact that one might expect the triplet-catalyzed reactions to be spin-blocked.¹⁸ Thus far, this paradigm in reactivity has only been demonstrated for the activation of Si-H bonds in neat HSiEt₃ solution. Here we explore how this description extends to another bond activation reaction by carrying out TRIR experiments in neat HSnBu₃ using Fe(CO)₅, CpCo(CO)₂, and CpV(CO)₄ catalysts (the CpRh(CO)₂ species is not involved in the present study).

Triplet Reactivity in Silane Activation



Singlet Reactivity in Silane Activation

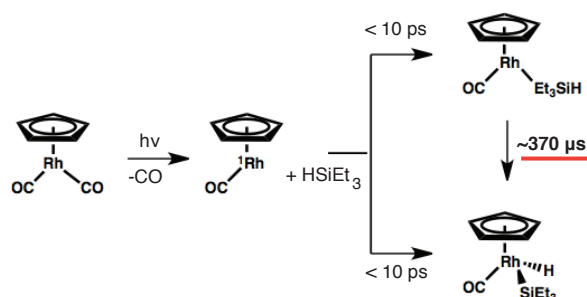


Figure 3.1. Summary of previous results on silane activation by triplet and singlet 16-electron photoproducts in neat HSiEt_3 solution.

The time-resolved photochemistry of $\text{Fe}(\text{CO})_5$,^{18,25,29–31} $\text{CpCo}(\text{CO})_2$,^{18,23,24,32} and $\text{CpV}(\text{CO})_4$ ^{17,33,34} has been studied previously. In alkane solution each undergoes CO-loss to yield a ground state triplet photoproduct. In alkanes, $^3\text{Fe}(\text{CO})_4$ has a lifetime of tens of nanoseconds before spin crossover and alkyl solvation of the singlet species occur,³⁰ while in alcohol solvents spin crossover and solvent coordination happen on the picosecond timescale.²⁵ In alkanes, $^3\text{CpCo}(\text{CO})$ is stable as an unsolvated triplet and decays only after reacting with a parent molecule to form $\text{Cp}_2\text{Co}_2(\text{CO})_3$.²⁴ Recent studies by our group have demonstrated that $^3\text{CpCo}(\text{CO})$ can also form complexes with some coordinating solvent molecules without undergoing a change of spin state.³⁵ Among this set of complexes, $\text{CpV}(\text{CO})_4$ is unique in that it undergoes CO-loss in alkane solution to initially form a mixture of unsolvated $^3\text{CpV}(\text{CO})_3$ and alkyl-solvated $^1\text{CpV}(\text{CO})_3$ in comparable quantities.¹⁸

In this paper we investigate activation of Sn–H bonds by triplet 16-electron photoproducts, hoping to gain insight into whether previous observations with regard to Si–H bond activation by triplet species¹⁸ will generalize to other bond activation processes. TRIR experiments are used to monitor Sn–H bond activation on the ultrafast timescale via changes in the CO-stretching region of the spectrum. We also use electronic structure theory calculations to investigate changes in spin–orbit coupling (SOC) between singlet and triplet states with the approach of both silane and stannane complexes to the metal centers. At the outset of this study, we expected that an external heavy–atom effect, similar to that reported by Kasha in fluorescence experiments on organic molecules roughly 60 years ago,³⁶ might be important. Interestingly, we find no evidence for an external heavy atom effect in the present study.

3.2 Methods

3.2.1 Sample Preparation

Fe(CO)₅ was purchased from Sigma-Aldrich Co., CpCo(CO)₂, and CpV(CO)₄ were purchased from Strem Chemicals Inc., and tributylstannane was purchased from Alfa Aesar. All samples and solvents were used without further purification. Dilute solutions of all samples were stable in air at ambient temperatures (verified via FTIR), except for CpV(CO)₄, which was handled under an inert atmosphere. Samples used to collect TRIR spectra were prepared at concentrations of ca. 5 mM.

3.2.2 Data Analysis

Kinetic data in this work result from spectra measured at delay times between 0 and 1100 ps between the visible pump and mid-IR probe pulses. Kinetic traces for each spectral feature were obtained by integrating a narrow spectral region (ca. 3 cm⁻¹ wide) surrounding the reported center frequency. The kinetic data were then fit to exponential curves using Origin Pro 8 software. To obtain fits with exponential rise and decays, a separate, home-written, fitting program was used, as the Origin software does not contain this function. Experimental errors are reported as 95% confidence intervals.

3.2.3 Quantum Chemical Modeling

Geometry optimizations were carried out using three different density functionals (BP86,^{37,38} B3LYP,^{37,39} PW91⁴⁰⁻⁴²) in the Gaussian09 package.⁴³ The lanl2dz basis set was used for Sn,^{44,45} while aug-cc-pDVZ basis set⁴⁶⁻⁴⁸ was used on all other atoms. All geometry optimizations were followed with a frequency analysis for use in interpreting the TRIR results, and also to verify that the calculated geometries were genuine local minima. Our choice of basis set was checked against calculations with a larger basis set, using the Los Alamos ECP for Sn with the aug-cc-pTVZ-PP basis on Sn and the aug-cc-pTVZ basis on all other atoms. The calculations reported in Table 3.2 were performed with both basis sets. The fact that the calculations gave very similar results suggests that the smaller (double-zeta) basis should be appropriate to use in performing partial geometry optimization scans to locate an approximate minimum energy crossing point (MECP). The ground spin state of each of the transition metal photoproducts in this study have been considered previously.^{17,18,26,49-54} For computational efficiency, the *n*-butyl groups of tributylstannane were replaced with methyl groups in all calculations. To investigate the reactivity of triplet and singlet CpV(CO)₃, Fe(CO)₄, and CpCo(CO), potential energy curves to describe the approach of HSnMe₃ to the metal center were calculated by fixing the metal-Sn separation at various distances and optimizing the remaining geometric parameters. This type of analysis builds an approximate potential energy surface for the bond-activation reaction as a function of the metal-Sn distance,⁵⁵ although the actual reaction coordinate is more complex due to the high dimensionality of the energy surfaces. As described in the results section, similar calculations were carried out with HSiMe₃ for comparison. Minimum energy crossing point (MECP) metal-Sn and metal-Si distances were located by linear interpolation of distances on

either side of the crossing, and a final geometry optimization was performed with this distance constrained to obtain the MECP geometry.

To investigate the strength of spin-orbit coupling (SOC) between the singlet and triplet spin states, complete active space multiconfigurational self-consistent field (casscf) calculations were carried out in the GAMESS-US package⁵⁶ using Ahlrich's pDVZ basis set⁵⁷ with one additional d function on C and O atoms, and an additional f function on Co, V, and Fe. The aug-cc-pVDZ-PP⁵⁸ basis was used for Sn. For dissociation limit SOC calculations, B3LYP geometries were used in each case. For the MECP SOC calculations, the DFT optimized geometries at the approximate MECP were used. The active space of the casscf calculations for each species used 8 electrons in 10 d-type orbitals, constituting an (8,10) active space. The choice to include unoccupied d-type orbitals containing an extra node was made to account for the double-shell effect.⁵⁹ Calculations were performed as follows: restricted or restricted open shell Hartree-Fock calculations were performed for singlet and triplet states, respectively, to generate the initial wavefunctions. After inspecting the active space orbitals, the casscf wavefunction was generated for the triplet state. The core orbitals from the triplet casscf wavefunction are then frozen in the subsequent calculation of the singlet casscf wavefunction, as this is necessary for the corresponding orbital transformation necessary to calculate the SOC matrix elements.⁶⁰ Finally, SOC between singlet and triplet states was calculated using the full Breit-Pauli spin-orbit Hamiltonian.⁶¹⁻⁶³ This method of calculating SOC is favorable, as it allows for different molecular orbitals to describe the ground and excited states.

3.3 Results

TRIR spectra in the CO-stretching region are presented as difference absorbance spectra. Positive absorptions correspond to newly formed species, while negative bands (bleaches) correspond to the depletion of parent molecules. All TRIR spectra in this study were collected using 400 nm excitation to avoid absorptions present at shorter wavelengths in the UV-Vis spectrum of the tributylstannane solvent.

3.3.1 Photolysis of Fe(CO)₅ in HSnBu₃ Solution

TRIR spectra of Fe(CO)₅ in neat tributylstannane solution were collected following 400 nm photolysis and are shown in Figure 3.2. New absorptions initially appear at 1965 and 1987 cm⁻¹, corresponding to unsolvated ³Fe(CO)₄.²⁵ These decay with the concomitant rise of absorptions at 2013 and 2081 cm⁻¹, which DFT calculations (*vide infra*) and comparison to previous studies¹⁸ allow us to assign to the Sn-H bond activated product. The absorption at 1947 cm⁻¹ corresponds to alkyl-solvated ¹Fe(CO)₄ and has contributions from hot bands at earlier times.³⁰ Due to the stronger neighboring absorptions of ³Fe(CO)₄, the kinetics of the 1947 cm⁻¹ absorption are difficult to accurately obtain, but we do not see significant decay of this species, suggesting the alkyl-solvated singlet does not rearrange to form a bond activated product on the picosecond timescale.

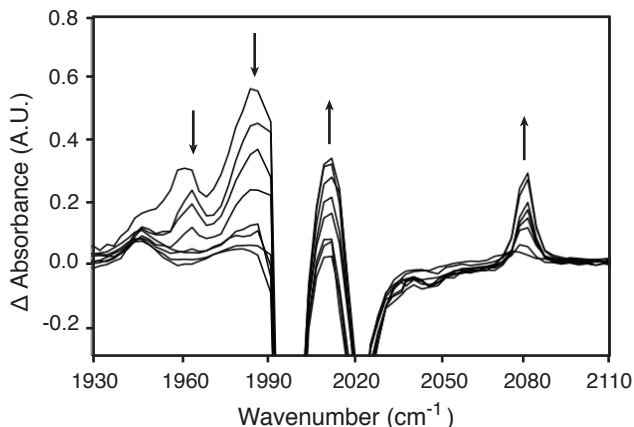


Figure 3.2. TRIR spectra of $\text{Fe}(\text{CO})_5$ in neat tributylstannane at 20, 50, 100, 150, 300, 500, 700, and 1000 ps following 400 nm photolysis. Rising absorptions at 2013 and 2081 cm^{-1} indicate formation of the Sn–H bond activated product, while decaying absorptions at 1965 and 1987 cm^{-1} show depletion of $^3\text{Fe}(\text{CO})_4$. Parent bleaches at 2000 and 2024 cm^{-1} make it difficult to access some regions of the product spectrum. (A.U. = Arbitrary Units)

The kinetic traces of the absorptions at 1987 and 2081 cm^{-1} are plotted in Figure 3.3. For the absorption at 1987 cm^{-1} , we observe a fast rise time of 6 ± 2 ps followed by a 125 ± 22 ps decay. The absorption at 2081 cm^{-1} shows a monoexponential rise time of 114 ± 16 ps, and we assign this time constant to the formation of the bond activated product, as it is the only absorption not obscured by parent bleaches, hot bands, or overlapping peaks of other species.

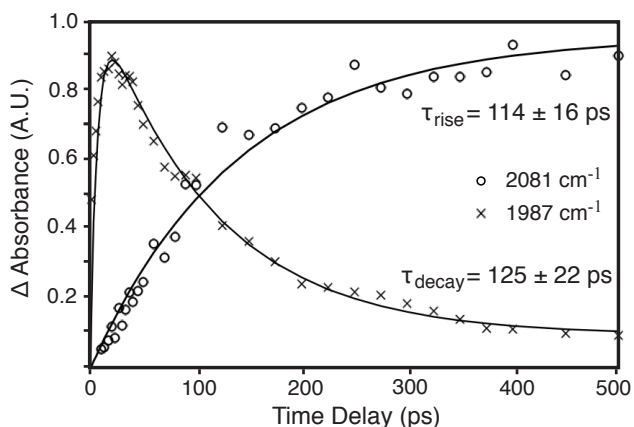


Figure 3.3. Ultrafast kinetics of $\text{Fe}(\text{CO})_5$ photoproducts in neat tributylstannane following 400 nm photolysis. The rise time of 114 ± 16 ps corresponds to formation of the Sn–H bond activated product. (A.U. = Arbitrary Units)

3.3.2 Photolysis of $\text{CpCo}(\text{CO})_2$ in HSnBu_3 Solution

TRIR spectra of $\text{CpCo}(\text{CO})_2$ in neat tributylstannane are shown in Figure 3.4. The most prominent feature in these spectra is a broad absorption due to an electronically excited state of

the parent molecule, which decays in ca. 30 ps. We have previously observed evidence for this absorption following 400 nm excitation in other solvents, and this was assigned to an excited state of the parent molecule based on the significant degree of concomitant bleach recovery accompanying its relaxation.³⁵

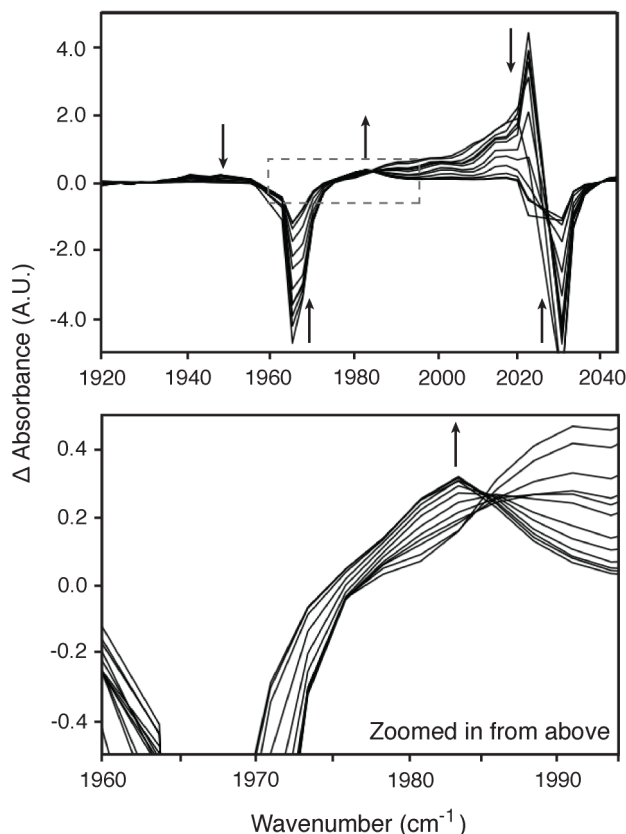


Figure 3.4. TRIR spectra for $\text{CpCo}(\text{CO})_2$ in neat tributylstannane at 2, 5, 10, 13, 17, 20, 30, 40, 60, 90, 130, and 150 ps following 400 nm photolysis. The primary photochemical pathway using 400 nm excitation is a non-dissociative electronic excitation of $\text{CpCo}(\text{CO})_2$, which results in strong, broad absorptions whose decay coincides with parent bleach recovery. The CO loss photoproduct rapidly activates the Sn–H bond, as monitored by its absorption centered at 1984 cm^{-1} , shown in the lower panel. (A.U. = Arbitrary Units)

The kinetic trace of the absorption at 1984 cm^{-1} is plotted in Figure 3.5. Based on analogy to a previous study on silane activation,¹⁸ this absorption corresponds to the $\text{CpCo}(\text{CO})$ Sn–H bond activated product. Considering the significant overlap with the absorptions of electronically excited $\text{CpCo}(\text{CO})_2$ and vibrational cooling of the nascent photoproduct on a similar timescale, we feel the time constant of $28 \pm 4\text{ ps}$ for the rise of this absorption is best viewed as a rough upper limit to the timescale for Sn–H activation.

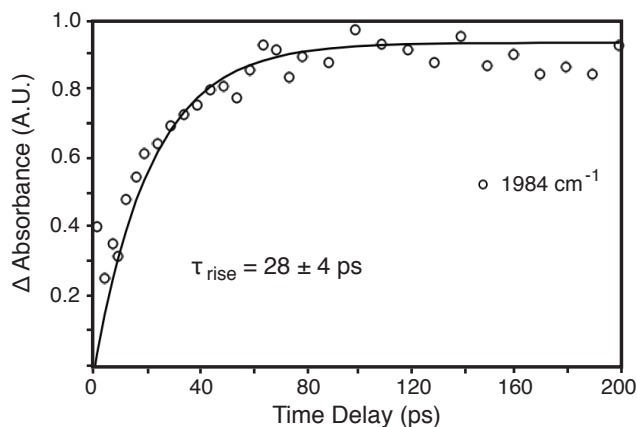


Figure 3.5. Ultrafast kinetics of $\text{CpCo}(\text{CO})_2$ photoproducts in neat tributylstannane following 400 nm photolysis. (A.U. = Arbitrary Units)

3.3.3 Photolysis of $\text{CpV}(\text{CO})_4$ in HSnBu_3 Solution

Figure 3.6 shows TRIR spectra of $\text{CpV}(\text{CO})_4$ in neat tributylstannane. Absorptions at 2017 and 1988 cm^{-1} rise at early times, and decay with the concurrent rise of a peak at 1998 cm^{-1} . Based on analogy to previous studies¹⁷ and DFT calculated frequencies, we assign the absorption at 2017 cm^{-1} to unsolvated $^3\text{CpV}(\text{CO})_3$, the absorption at 1988 cm^{-1} to alkyl-solvated $^1\text{CpV}(\text{CO})_3$, and the absorption at 1998 cm^{-1} to the bond activated product, $^1\text{CpV}(\text{CO})_3(\text{HSnBu}_3)$. Kinetic traces for these species are shown in Figure 3.7. Another absorption present at 1888 cm^{-1} (not shown) demonstrates kinetics that correlate well to the 1988 cm^{-1} absorption of alkyl-solvated $^1\text{CpV}(\text{CO})_3$. Due to the fact that the tributylstannane solvent has a Sn–H absorption centered at 1809 cm^{-1} , we focus on the absorptions shown in Figure 3.6 to monitor product formation and decay.

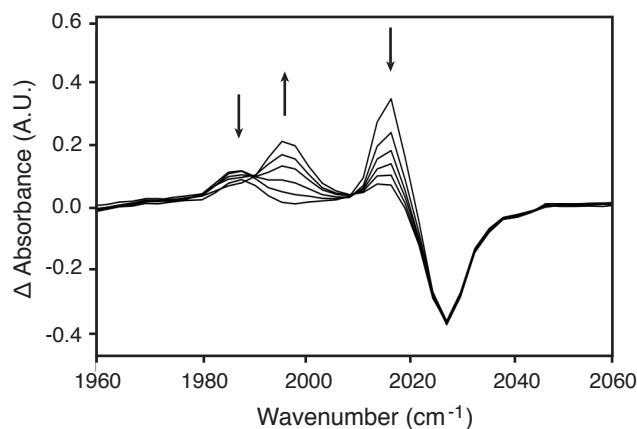


Figure 3.6. Transient difference spectra for $\text{CpV}(\text{CO})_4$ in neat tributylstannane at 50, 150, 300, 500, 700, and 1000 ps following 400 nm photolysis. (A.U. = Arbitrary Units)

The peak corresponding to alkyl-solvated $^1\text{CpV}(\text{CO})_3$ displays a rise time constant of 69 ± 16 ps and decays with a time constant of ca. 3500 ps, which is quite long relative to the experimentally accessible time delays, resulting in large uncertainties. We simply conclude the decay of this species to be slow relative to other timescales in the present study. A kinetic trace of the parent bleach at 2028 cm^{-1} shows that the singlet does not decay to reform the parent species, and for this reason we correlate its decay to rearrangement to form the Sn–H activated product. The 2017 cm^{-1} absorption, corresponding to $^3\text{CpV}(\text{CO})_3$, rises with a time constant of 4 ± 2 ps and decays biexponentially with time constants of 69 ± 10 and 770 ± 255 ps.

The fast decay component of the triplet correlates to the rise time of the alkyl-solvated singlet, which is consistent with the previous observation of a fast decay of the triplet to form a quantity of the alkyl-solvated singlet in *n*-heptane solvent.¹⁷ It seems likely that the interconversion of $^3\text{CpV}(\text{CO})_3$ to $^1\text{CpV}(\text{CO})_3$ at early times is coupled to vibrational cooling of the nascent photoproduct. The absorption at 1998 cm^{-1} , corresponding to the bond activated product, is fit to an exponential rise with a time constant of 860 ± 108 ps.

Table 3.1. Observed vibrational frequencies, DFT frequencies, and literature references

Complex	Observed Frequencies in neat HSnBu ₃	Calculated Frequencies ^a	Reference
Fe(CO) ₅	2000, 2022	1974, 1993	2000, 2023 (heptane)
³ Fe(CO) ₄	1965, 1987	1956, 1957, 1965	1965, 1987 (heptane)
¹ Fe(CO) ₄ (HSnBu ₃)	2013, ^b 2081	1962, 1980, 1984, 2041	2006, 2017, 2091 (HSiEt ₃)
CpCo(CO) ₂	1966, 2028	1947, 1997	1971, 2031 (heptane)
³ CpCo(CO)	not observed	1958	1990 (heptane)
¹ CpCo(CO)(HSnBu ₃)	1984	1949	1995 (HSiEt ₃)
CpV(CO) ₄	1928, 2028	1912, 1992	1931, 2030 (heptane)
³ CpV(CO) ₃	2017	1889, 1899, 1970	2020 (heptane)
¹ CpV(CO) ₃ (alkyl)	1886, 1988	1871, 1876, 1949	1895, 1990 (heptane)
¹ CpV(CO) ₃ (HSnBu ₃)	1998 ^c	1872, 1886, 1942	1876, 1972 (HSiEt ₃)

(a) DFT frequencies in this table were calculated using the BP86 functional. (b) The center frequency of this absorption appears at 2013 cm^{-1} but is difficult to characterize due to overlap with parent bleaches. (c) Another absorption appears to be present at ca. 1865 cm^{-1} but could not be observed clearly due to the absorption of the Sn–H stretch of the solvent.

Table 3.1 summarizes the experimental and calculated CO-stretching vibrational frequencies for each species observed, along with relevant literature values for comparison.

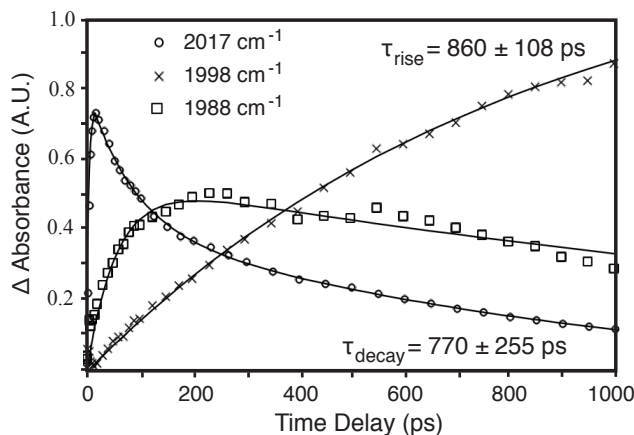


Figure 3.7. Ultrafast kinetics of $\text{CpV}(\text{CO})_4$ photoproducts in neat tributylstannane following 400 nm photolysis. The trace at 1988 cm^{-1} corresponds to alkyl solvated $^1\text{CpV}(\text{CO})_3$, the trace at 1998 cm^{-1} to the Sn–H bond activated product, and the trace at 2017 cm^{-1} to $^3\text{CpV}(\text{CO})_3$. (A.U. = Arbitrary Units)

Kinetic traces of the parent bleaches were also performed for each species studied. For $\text{Fe}(\text{CO})_5$, ca. 30% of the parent bleach at 2024 cm^{-1} recovers with a time constant of $71 \pm 40\text{ ps}$. For $\text{CpV}(\text{CO})_4$, ca. 20% of the parent bleach at 2028 cm^{-1} recovers with a time constant of $23 \pm 4\text{ ps}$. Both of these recoveries are attributed to primary geminate recombination, with no evidence for further recovery on the timescale studied. The bleach trace for $\text{CpCo}(\text{CO})$ performed at 1967 cm^{-1} recovers significantly more (ca. 75%) on the timescale studied, and this is to be expected, as 400 nm excitation populates an electronic excitation as well as a dissociative CO-loss pathway. The time constant for this recovery is $32 \pm 3\text{ ps}$.

3.3.4 DFT and ab Initio Calculation Results

Density functional theory (DFT) and ab Initio calculations have been carried out to gain a more detailed understanding of the factors that govern activation of Sn–H bonds by the complexes studied experimentally.

Calculated Structures and Energies

Geometry optimizations were carried out with each photoproduct interacting with the Sn–H site in HSnMe_3 . The *n*-butyl groups of the tributylstannane molecule were replaced with methyl groups for computational efficiency. These calculations indicated that only the singlet state of each photoproduct is capable of activating the Sn–H bond, consistent with the previous understanding of triplet organometallic reactivity. The relative spin state energies for each photoproduct, and the binding energy of the singlet Sn–H activated species, are listed in Table 3.2. Of the three functionals tested, the B3LYP hybrid functional appears to give the most accurate results for the energies of $\text{Fe}(\text{CO})_4$ and $\text{CpV}(\text{CO})_3$, while the BP86 and PW91 functionals more accurately characterize the energies of $\text{CpCo}(\text{CO})$. For this reason, we will use the BP86 functional to characterize the reactions involving $\text{CpCo}(\text{CO})$ and the B3LYP functional for $\text{Fe}(\text{CO})_4$ and $\text{CpV}(\text{CO})_3$ in the next section. While it would be desirable to find a single

functional that accurately characterizes the spin state energy differences of all three 16-electron species, none of the functionals tested fit this criterion.

The calculated BP86 geometries of the bond activated products are shown in Figure 3.8 (the geometries obtained with each functional were similar). We selected three parameters to characterize the bond activated structures: the M–H, M–Sn, and Sn–H bond lengths, where the H atom in question is that from the Sn–H bond. The Fe(CO)₄ and CpCo(CO) structures show significant elongation of the Sn–H bond, relative to the Sn–H distance of 1.73 Å calculated for the free HSnMe₃ species, indicating that the Sn–H interaction has been significantly weakened. The CpV(CO)₃ bond activated complex shows lengthening of this bond to a lesser extent, consistent with the lower calculated binding energy for this species. The H atom approaches the metal center more closely in the iron and cobalt complexes, relative to the vanadium complex, and the M–Sn distance is also longest for the vanadium complex. These details point to the fact that CpV(CO)₃ interacts with the Sn–H bond to a lesser extent than the iron and cobalt species, which is also evident from the binding energies calculated in Table 3.2.

The metal hydride bonds formed in these reactions were not observed experimentally, which is not surprising considering they are expected to have significantly weaker oscillator strengths than the CO-stretching modes. Our experiments do not provide evidence for the extent of coupling between the M-H stretch and the CO-stretching modes, but, considering the general interest in metal-hydride bonds, we will relate just a couple of DFT results on this topic; for each bond activated species, DFT frequency calculations predict one isolated M-H stretching mode that is only very weakly coupled to the CO-stretching modes. The M-H stretch is also predicted to be couple to at least some of the CO-stretching modes in each species. However, with only the limited results obtained for these three species, it remains difficult to draw any general conclusions regarding the extent of coupling between M-H and CO modes.

Table 3.2. DFT calculated energy differences for the singlet and triplet states and calculated binding energies of HSnMe₃ to each singlet photoproduct, measured relative to the singlet dissociation limit

Photoproduct	$\Delta E_{\text{Triplet-Singlet}}$ (kcal/mol)	$\Delta E_{\text{binding Sn-H activated product}}$ (kcal/mol)
Fe(CO) ₄		
BP86	0.3	-42.0
PW91	0.0	-46.2
B3LYP	-8.6	-34.1
CpCo(CO)		
BP86	-13.0	-52.8
PW91	-12.9	-56.4
B3LYP	-25.6	-41.9
CpV(CO) ₃		
BP86	0.2	-24.5
PW91	0.8	-29.1
B3LYP	-4.9	-16.3

Locating Minimum Energy Crossing Points

In the context of nonadiabatic transition state theory, the nuclear configuration at which a change of electronic state takes place is found by locating the minimum energy crossing point (MECP) between the two relevant electronic surfaces. In the present reactions, we can characterize the enthalpic barrier to the reaction at the MECP geometry, keeping in mind the

additional requirement that a change in electronic configuration needs to take place in the vicinity of the crossing. Spin-orbit coupling (SOC) between singlet and triplet states is a defining factor in determining the probability of the change of spin state, and it is at the MECP geometry that we wish to calculate the magnitude of SOC.

In cases where the essential features of the reaction coordinate are captured by a single geometric parameter, one method for locating an approximate MECP involves performing partial geometry optimizations on both potential energy surfaces at many constrained values of the parameter used to characterize the reaction coordinate.⁵⁵ In this case, we have used the M–Sn (M = Fe, Co, or V) distance as our reaction coordinate. Figure 3.9 shows the results of these calculations, where the B3LYP functional was used for Fe(CO)₄ and CpV(CO)₃, and the BP86 functional was used for CpCo(CO). In addition to the enthalpic barriers, we are interested in whether the approach of the Sn atom affects SOC at the metal center. It's high atomic number ($Z=50$), and the fact that SOC in atoms typically scales with Z^4 , suggest that this could be the case. In the 1950's, Kasha reported the first observation of an external heavy atom effect (i.e. where the heavy atom is not chemically bonded to the species undergoing a change of spin state) in fluorescence quenching experiments,³⁶ and external heavy atom effects have since been implicated in a wide number of other situations.^{64–70}

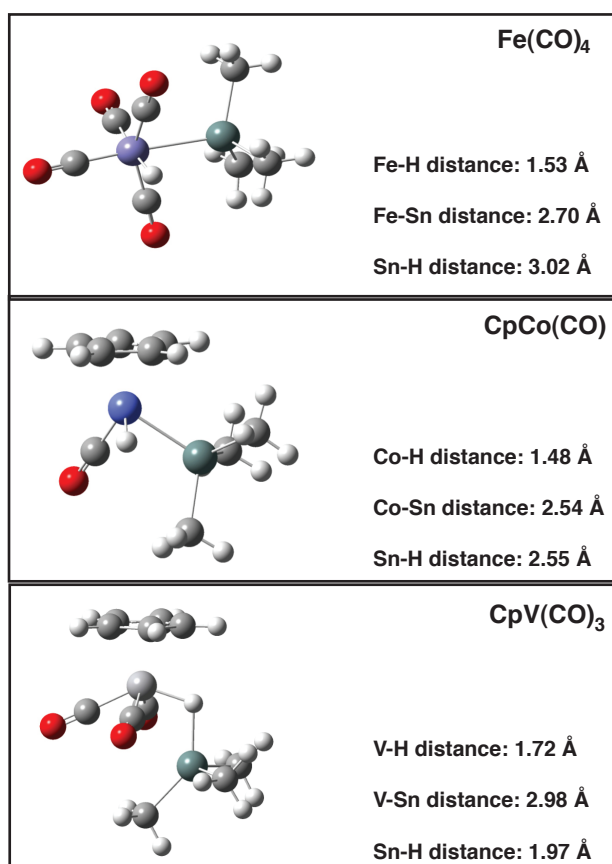


Figure 3.8. Geometries of the Sn–H bond activated products obtained using the BP86 functional. Distances between the metal center, Sn atom, and H atom involved in bond activation are indicated for each structure. For comparison, the Sn-H distance calculated for HSnMe₃ is 1.73 Å.

We carried out casscf calculations to characterize SOC between the singlet and triplet states. SOC values are reported as the r.m.s. value between the three triplet substates and the nearest singlet state. In an earlier study on silane activation, SOC was calculated only for the isolated 16-electron organometallic fragments, and the effect of the approaching silane on SOC was not considered. This was not an unreasonable approximation, as only qualitative trends between the three complexes were being made. Here we calculated SOC for both the free transition metal species, as well as at the MECP geometries. The free energy barriers for Sn–H activation, time constants for bond activation, and calculated r.m.s. SOC values, both at the MECP for Sn–H activation and at the dissociation limit, are shown in Table 3.3.

Table 3.3. Calculated energetic barriers to reach the MECP for each photoproduct, along with r.m.s. SOC at the dissociation limit, and the observed time constants for Sn-H activation

Complex	ΔE_{MECP} (kcal/mol)	$\text{SOC}_{\text{dissociation}}$ (cm^{-1})	$\tau_{\text{Sn-H activation}}$ (ps)
$\text{Fe}(\text{CO})_4$	-0.4	38.4	114
$\text{CpCo}(\text{CO})$	-6.0	206.2	22
$\text{CpV}(\text{CO})_3$	0.8	64.8	770

For comparison to previous studies on silane activation by these three photoproducts, we used the same method to locate MECPs for the reactions of each species with HSiMe_3 , and we then calculated SOC at each of the MECPs associated with Si–H activation. Table 3.4 compares the M–Si and M–Sn distances at each MECP as well as the magnitude of SOC at the MECP geometry.

3.4 Discussion

The results of this study establish that $\text{Fe}(\text{CO})_4$, $\text{CpCo}(\text{CO})$, and $\text{CpV}(\text{CO})_3$ are capable of activating Sn–H bonds on the picosecond timescale. $\text{Fe}(\text{CO})_4$ and $\text{CpCo}(\text{CO})$ appear to catalyze Sn–H activation exclusively through an unsolvated triplet intermediate, while $\text{CpV}(\text{CO})_3$ forms the Sn–H activated product through either an unsolvated triplet or alkyl-solvated singlet photoproduct. The results are consistent with the previously proposed mechanism for bond activation by triplet photoproducts developed in studies on silane bond activation.

3.4.1 Mechanism of Stannane Activation by Triplet Photoproducts

Following 400 nm photolysis of $\text{Fe}(\text{CO})_5$ in tributylstannane solution, the initially formed photoproduct is $^3\text{Fe}(\text{CO})_4$, observed via characteristic absorptions at 1965 and 1987 cm^{-1} . The decay kinetics of this species correlate to the 114 ps rise ($k_{\text{bimol}} = 1.4 \times 10^9 \text{ M}^{-1}\text{s}^{-1}$) of the Sn–H activated product. While some quantity of alkyl-solvated $^1\text{Fe}(\text{CO})_4$ is also observed, it does not appear to rearrange to form the bond activated complex on the timescale studied.

The photochemistry of $\text{CpCo}(\text{CO})_2$ has previously been studied on picosecond through microsecond timescales, and no alkyl-solvated singlet species has been observed, suggesting that the unsolvated triplet is more thermodynamically stable than any alkyl solvated intermediates.^{18,23,24,32} In tributylstannane, we observe formation of the bond activated product via the absorption at 1984 cm^{-1} with a rise time of 28 ps ($k_{\text{bimol}} = 9.4 \times 10^9 \text{ M}^{-1}\text{s}^{-1}$). The rapid rate of Sn–H activation is similar to that observed for silane activation in HSiEt_3 by $\text{CpCo}(\text{CO})$.¹⁸

$\text{CpV}(\text{CO})_4$ provides an interesting comparison to the other two species, as it is known to form both an unsolvated triplet and an alkyl solvated singlet during the first several tens of picoseconds following photolysis.¹⁷ The singlet presumably forms via the vibrationally excited triplet, as triplet to alkyl solvated singlet is not observed at longer delay times.¹⁷ We observe kinetics that correlate the decay of $^3\text{CpV}(\text{CO})_3$ to the growth of the Sn–H activated product, with Sn–H activation via the alkyl-solvated singlet intermediate occurring on a longer timescale. As mentioned in the results section, we conclude that the alkyl solvated singlet rearranges to form the Sn–H activated product, as opposed to reforming the parent complex, since no decay of the bleach at 2028 cm^{-1} is observed on the timescale studied. Figure 3.10 summarizes the observed reactivity of $\text{CpV}(\text{CO})_3$. The faster rate of activation by $^3\text{CpV}(\text{CO})_3$, despite the requirement for spin crossover, is consistent with previous results for silane activation,⁵ while the slower rate of interconversion observed for the singlet is more akin to the behavior of the singlet 16-electron photoproduct $\text{CpRh}(\text{CO})$, described in Figure 3.1 (though the vanadium species does rearrange significantly faster).

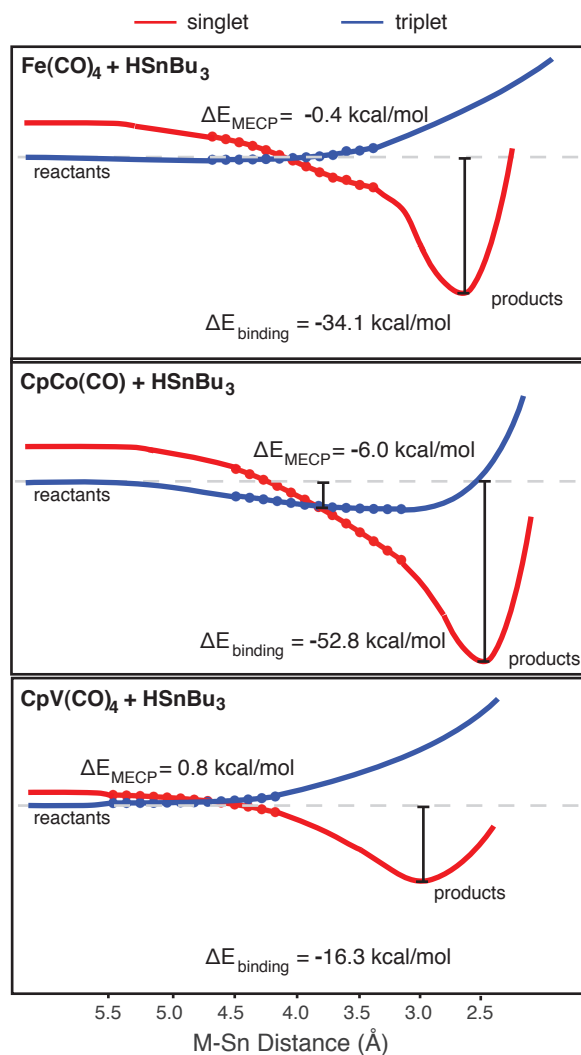


Figure 3.9. Reaction coordinate diagrams for the reactions of HSnBu_3 with $\text{Fe}(\text{CO})_4$, $\text{CpCo}(\text{CO})$, and $\text{CpV}(\text{CO})_3$. The data points (circles) were generated by performing DFT partial geometry

optimizations with only the M–Sn distance constrained at each step (HSnMe₃ was used in the calculations). Circles represent data points from DFT calculations to locate an approximate MECP, while lines are intended only as visual aids. Binding energies are those listed in Table 3.2. As described in the text, the B3LYP functional was used for reactions of Fe(CO)₄ and CpV(CO)₃, while the BP86 functional was used with CpCo(CO).

Table 3.4. SOC values calculated at the dissociation limit, along with those calculate at the MECP geometries located for activation of Si–H and Sn–H bonds in Me₃SiH and Me₃SnH. The metal–Si and metal–Sn distances are also indicated

Complex	SOC _{dissociation} (cm ⁻¹)	M–Si MECP distance (Å)	SOC _{Si–H MECP} (cm ⁻¹)	M–Sn MECP distance (Å)	SOC _{Sn–H MECP} (cm ⁻¹)
Fe(CO) ₄	38.4	3.75	63.5	4.04	64.8
CpCo(CO)	206.2	3.51	223.2	3.72	214.1
CpV(CO) ₃	64.8	4.43	45.0	4.66	29.5

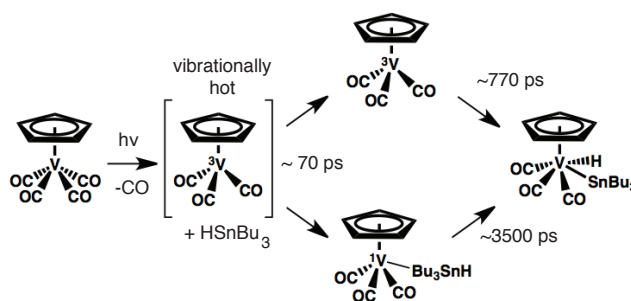


Figure 3.10. Observed reactivity of CpV(CO)₃ species toward Sn–H activation in HSnBu₃.

The rapid rates of Sn–H bond-activation observed for the three photoproducts are similar to those observed for silane activation (see Table 3.5), and suggest that the previous mechanistic description for the activation of Si–H bonds by triplet photoproducts also characterizes the activation of Sn–H bonds by these species. The triplet photoproducts diffuse freely through the alkyl groups of the solvent with minimal interactions, and, upon encountering the more coordinating Sn–H bond, undergo a concerted spin crossover and bond activation reaction. Were the triplet photoproducts to coordinate to alkyl groups, previous kinetic studies into rearrangement of alkyl coordination products⁷¹ suggest the stannane reactions should be significantly slowed due to the longer alkyl chains of tributyl stannane, relative to triethyl silane. The rate coefficients in Table 3.5 show that this is clearly not the case. The fact that singlet CpV(CO)₃ rearranged on a much slower timescale in the present study involving longer alkyl chains (3500 ps) than in triethylsilane (470 ps)¹⁷ strongly suggests that coordination to alkyl groups also slows rearrangement in the present case.

Table 3.5. Bimolecular rate constants for Si–H and Sn–H activation by 16-electron photoproducts in triethylsilane and tributylstannane, respectively

Complex	$k_{\text{Silane Activation}}$ ($\text{M}^{-1}\text{s}^{-1}$)	$k_{\text{Stannane Activation}}$ ($\text{M}^{-1}\text{s}^{-1}$)
Fe(CO) ₄	1.3×10^8	2.3×10^9
CpCo(CO)	7.3×10^9	9.4×10^9
CpV(CO) ₃	4.5×10^8	3.4×10^8

3.4.2 Trends in Reactivity

The relative rates of reactivity of the three triplet photoproducts toward Sn–H bond activation can be rationalized on the basis of the DFT calculated energy surfaces and SOC between singlet and triplet states. CpCo(CO) has a favorable interaction energy toward approach of the HSnMe₃ moiety on the triplet surface, resulting in an MECP that lies 6.0 kcal/mol *below* the dissociation limit. This attractive interaction, combined with the relatively large SOC constant (206.2 cm⁻¹ at the dissociation limit) explains the rapid rate of Sn–H bond activation by this species. Fe(CO)₄ gives the next fastest reaction rate, and this species is also calculated to have an attractive interaction with HSnMe₃ on the triplet surface, resulting in an MECP that lies 0.4 kcal/mol below the dissociation limit. The lower SOC constant (38.4 cm⁻¹ at the dissociation limit), relative to CpCo(CO), combined with the weaker interaction with the Sn–H group on the triplet surface, is consistent with the slower reaction rate. The slowest rate of Sn–H activation by a triplet catalyst in this study is that of CpV(CO)₃, which is the only species that displays a positive classical energy barrier to reach the MECP, albeit a small one of only 0.8 kcal/mol. As mentioned in the results section, calculations also predict this catalyst to have a weaker interaction with the Sn–H bond in the final product. The less favorable interactions with the Sn–H group, relative to the other photoproducts studied, likely explain the slower rate of bond activation by ³CpV(CO)₃. The weaker interactions in the CpV(CO)₃ bond activated adduct may also imply that subsequent reactivity, such as addition of the stannane across an unsaturated carbon–carbon bond, may be less facile using this catalyst.

3.4.3 Comparison to Silane Activation

Each of the three triplet photoproducts studied have previously been shown to activate Si–H bonds in neat HSiEt₃ solvent on the ultrafast timescale, so it is of interest to compare the reactivity toward these two congeners.

CpCo(CO) reacts very rapidly to activate both Si–H and Sn–H bonds, with observed time constants of 22 ps in HSiEt₃ and 28 ps in HSnBu₃. These time constants occur on a similar timescale to that of vibrational cooling, so we feel the most reasonable conclusion is that both reactions happen on this timescale or faster. The DFT calculations suggest that both Si–H and Sn–H bonds are activated by this catalyst with significantly favorable binding energies.¹⁸ The observed rate constant for bond activation by Fe(CO)₄ in tributylstannane is $2.3 \times 10^9 \text{ M}^{-1}\text{s}^{-1}$, while that in triethylsilane from a previous study was $1.3 \times 10^8 \text{ M}^{-1}\text{s}^{-1}$. As these processes are occurring near the diffusion-limited regime, we also point out that the viscosities of the solvents differ (0.39 cP for triethylsilane⁷² vs. 1.5 cP for tributyl stannane, obtained from the MSDS). The rate constant is expected to scale with the inverse of the solvent viscosity for a diffusion limited process,⁷³ we may expect the rate constant in tributylstannane to be slower by a factor of ca. 3.8

due to slower diffusion. Looking at our DFT calculations, the fact that the rate constant for Sn–H activation is higher is best explained by the lack of a classical energy barrier to the Sn–H reaction, while an enthalpic barrier does exist for the Si–H reaction.¹⁸ The changes in SOC between the two MECP structures are negligible (63.5 cm⁻¹ for the Si–H reaction and 64.8 cm⁻¹ for the Sn–H reaction). We will consider the SOC calculations in more detail shortly.

Following photolysis of CpV(CO)₄, there are two photoproduct species involved in bond activation: unsolvated ³CpV(CO)₃, and alkyl solvated ¹CpV(CO)₃. Of these, the triplet species appears to be primarily responsible for activating the Sn–H bond on the timescale studied, while both species appeared to play a role in Si–H bond activation in triethylsilane.¹⁷ The rate of bond activation by the alkyl-solvated singlet species is significantly slower in tributylstannane than in triethylsilane, which can be attributed to the higher concentration of alkyl sites to which the singlet can coordinate. The reactivity of singlet photoproducts has previously been demonstrated to *not* follow diffusion-limited kinetics on the picosecond timescale, and the time for rearrangement of a singlet photoproduct to reach a more coordinating site can increase rapidly with the number of alkyl groups present.⁷¹

The rate constant for stannane activation in tributylstannane by ³CpV(CO)₃ is 3.5x10⁸ M⁻¹s⁻¹, while that for silane activation in HSiEt₃ by the same species is 4.5x10⁸ M⁻¹s⁻¹. Our calculation of the MECP for Sn–H activation places the barrier at 0.8 kcal/mol above the dissociation limit, while that for Si–H activation is 1.3 kcal/mol above the dissociation limit. The SOC values are again relatively similar, with a value of 29.5 cm⁻¹ at the Sn–H MECP and 45.0 cm⁻¹ at the Si–H MECP. Taking into account the fact that Sn–H activation is expected to be slowed by the larger viscosity, these numbers appear to be reasonably consistent with the difference in rates of bond activation.

Overall, the Si–H activation reaction showed more repulsive interactions with approach of the various triplet catalysts than did the Sn–H case. This could be because the Sn–H bond is intrinsically weaker, with a bond enthalpy of ca. 70 kcal/mol⁷⁴ compared to that of ca. 90 kcal/mol for an Si–H bond.⁷⁵ It may also be the greater polarizability of Sn relative to Si, or simply more favorable overlap with the metal centered triplet orbitals that allows it to avoid the repulsive interactions that characterize the interactions of triplet 16-electron photoproducts with many other ligands.

3.4.4 Looking for an External Heavy Atom Effect on SOC

One final point of interest is whether a heavy atom effect is important in the Sn–H bond activation reaction. Table 3.2 contains the values of SOC at both the dissociation limit and at the MECPs located for activation of HSnMe₃ and HSiMe₃ by each photoproduct. If an external heavy atom effect does affect the rate of bond activation, non-adiabatic transition state theory suggests that it would have to change SOC at the MECP geometry.^{76–78} For Fe(CO)₄, both species result in an increase in SOC from 38.4 cm⁻¹ at the dissociation limit to 64.8 (63.5) cm⁻¹ at the stannane (silane) MECP. The dissociation limit SOC for Fe(CO)₄ was also recently calculated by Harvey and Aschi⁷⁹ to be 29 cm⁻¹, which is in good agreement with the present result. Harvey and Aschi also calculated SOC for Fe(CO)₄ at the MECP for CO addition and found a value of 66 cm⁻¹, which is also remarkably close to the MECP values we found for stannane and silane addition. For CpV(CO)₃, both MECPs show a decrease in SOC relative to the dissociation limit, with the decrease actually being larger for the approach of the stannane

complex. For CpCo(CO), we observe similar calculated values at the dissociation limit and both MECPs.

In each case, we observe some changes in SOC at the MECP geometry associated with stannane and silane activation, however the changes are generally similar for the approach of the Sn–H or Si–H bonds, despite the differences in atomic number of Sn vs. Si (50 vs. 14). Importantly, there is no evidence for a heavy atom effect.

We note that all trends in reactivity are in reasonable agreement with the results of the calculations; the classical barriers and qualitative SOC trends from the dissociation limit values appear consistent with trends in the experimental rates. At the very least, this does not cast any obvious doubt on the accuracy of the calculations. If an external heavy atom effect were to play a role, it seems that one of two scenarios would need to occur near the MECP: either the valence orbitals of the species undergoing a change of spin state would need to delocalize onto the incoming heavy atom (in both the singlet and triplet wave functions), or the heavy atom would need to approach closely enough to the metal center for the electrons its valence orbitals to have significant electrostatic interactions with the heavy atom (in the context of the SOC operator). Inspection of the active space orbitals in the present calculations shows that the first scenario is not the case. The second scenario is based on the fact that the often-quoted Z^4 dependence of the heavy atom effect has its origin in the expectation value of the $1/r^3$ term of the operator, which contributes a factor of Z^3 to the value. Since the diradical electron density remains in the Fe, Co, or V centered molecular orbitals, and the MECPs have M–Sn separations on the order of 4 Å apart, the diradical electron density on the metal resides significantly closer to the metal atom than to the Sn nucleus. Thus it is not altogether surprising that the casset calculations do not predict a heavy atom effect at the MECP; the electrons involved in the spin state change reside in metal-centered orbitals, and the incoming Sn–H (or Si–H) group does not approach closely enough to interact strongly, in the context of SOC, with these metal-centered orbitals.

From this point of view, it seems that different incoming groups will likely behave in largely the same manner in effecting spin state changes in 16-electron photoproducts, so long as they experience similarly long MECP separations. The very similar SOC values calculated by Harvey and Aschi⁷⁹ for Fe(CO)₄ at the dissociation limit and at the MECP located for CO-addition also support this hypothesis; the addition of CO, HSiMe₃, and HSnMe₃ are all predicted to show similar changes in SOC at the MECP geometry. Implicit in the application of this discussion to experimental chemistry is, of course, the assumption that non-adiabatic transition state theory can accurately characterize the reaction through a single MECP geometry.

3.5 Conclusions

The reactivity of three triplet organometallic photoproducts toward the activation of Sn–H bonds has been studied on the picosecond timescale. To our knowledge, this study constitutes the first experimental demonstration of Sn–H bond activation by these three metal carbonyl species, and further exploration into their synthetic utility in this area may be worthwhile. The mechanistic differences between singlet and triplet photoproducts described in studies of silane activation also characterize the activation of Sn–H bonds in tributylstannane. Triplet 16-electron photoproducts do not form alkyl-coordinated intermediates, and, for this reason, are able to diffuse freely through solution. Consistent with previous studies, upon encountering a more coordinating functional group (in this case the Sn–H bond), the triplet photoproducts readily undergo spin crossover, which allows formation of the bond activated product. The similarities

between the present study and that on silane activation support the notion that this description for triplet organometallic reactivity extends to other bond activation reactions as well, with the important implication that a two-state mechanism can significantly accelerate the rate of a reaction by facilitating diffusion of the catalyst to its target functional group. In the case of $\text{CpV}(\text{CO})_3$, the initially formed triplet species can relax to form an alkyl solvated singlet during the vibrational cooling period, partitioning the reactivity of this catalyst into two pathways. The singlet photoproduct forms transiently stable alkyl coordinated intermediates, which slows rearrangement to the bond activated product.

DFT calculations suggest that $\text{CpV}(\text{CO})_3$ activates the Sn–H bond to a lesser extent than $\text{CpCo}(\text{CO})$ or $\text{Fe}(\text{CO})_4$. This difference was also apparent in the results of a previous study on Si–H bond activation by these photoproducts.¹⁸ We have explored changes in SOC at MECP geometries calculated for silane activation, and we find that changes in SOC at the MECP geometry, relative to the dissociation limit, are similar in magnitude for both types of bond activation. The observed trends in reaction rates are consistent with the trends in energy barriers and SOC obtained via calculations. Importantly, our calculations and results show no evidence for the role of an external heavy atom effect. The results of this study extend our understanding of triplet 16-electron reactivity to a new class of bond activation reactions and provide insight into the role, or lack thereof, of external heavy atom effects in two-state organometallic catalysis.

4 Observation of a Solvent Dependent Spin-State Equilibrium in CpCo(CO)

The following chapter is reproduced (adapted) in part with permission from (Lomont, J. P.; Nguyen, S. C.; Schlegel, J. P.; Zoerb, M. C.; Hill, A. D.; Harris C. B. *J. Am. Chem. Soc.* 2012, *134*, 3120-3126.). Copyright (2012) American Chemical Society.

4.1 Introduction

Cyclopentadienyl cobalt dicarbonyl is widely used as a catalyst for the cyclotrimerization of alkynes,^{80,81} and its time-resolved photochemistry has been studied by several authors.^{18,23,24,32,82,83} Experimental and theoretical investigations have established that the primary photoproduct, CpCo(CO), exists in a triplet ground state in the gas phase and in alkane solutions, but that reactivity of CpCo(CO) typically occurs via the singlet state.^{10,18,53} Interestingly, theoretical predictions have shown that a ligand-bound minimum can exist for both the singlet and triplet species,^{10,54} and that the identity of an incoming ligand affects the relative energies of the bound singlet and triplet states. Figure 4.1 illustrates this unique feature of the triplet potential energy surface of CpCo(CO), relative to other triplet photoproducts. Here we use time-resolved infrared spectroscopy (TRIR) to explore whether cases exist in which a solvent coordinated triplet state is preferred over that of a singlet, or whether it is possible to observe two solvated spin states simultaneously.

Previous solution-phase studies on the reactivity of CpCo(CO) and other triplet organometallic photoproducts have suggested that triplet photoproducts interact very weakly with alkyl groups of solvent molecules, and that spin crossover to a singlet state is necessary for the coordination of a solvent molecule to the unsaturated metal center.^{15,17-19,23-30,84} The rate of spin state interconversion depends heavily on the solvent environment, however, and coordinating solvents can increase the rate of spin crossover for unsaturated triplet species.⁵⁴

The lack of solvent coordination to coordinatively unsaturated triplet species has been shown to play an important role in their reactivity, exemplified by studies on the activation of Si-H bonds in triethylsilane.^{15-17,19,28-30,80,81} Because they interact so weakly with alkyl groups, triplets diffuse more rapidly through the alkyl chains in neat triethyl silane solutions than their singlet counterparts. Upon encountering a more coordinating Si-H bond, however, triplets readily undergo spin crossover to allow bond activation. This combination of factors allows triplet photoproducts to activate Si-H bonds much more rapidly than those formed in a singlet state, despite the fact that one might expect these reactions to be spin-blocked.

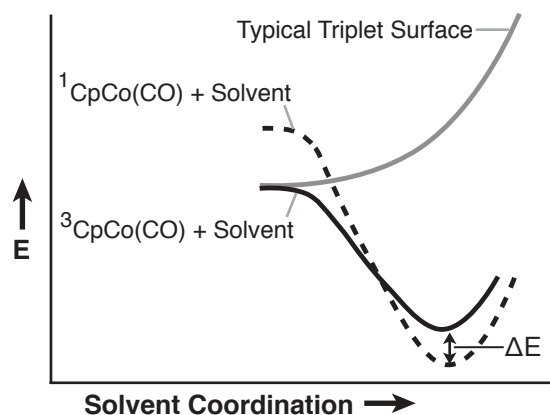


Figure 4.1. Schematic potential energy surfaces for solvent coordination to CpCo(CO) , compared to more typical triplet 16-electron species. Many triplets show a predominantly repulsive potential toward solvent coordination (solid gray line), while the triplet surface for CpCo(CO) shows an attractive potential (solid black line). ΔE designates the energy difference between solvated singlet and triplet states.

Our observation of a solvent coordinated triplet CpCo(CO) species in this study would be consistent with previous computational studies showing that a ligand-bound minimum can exist on the triplet surface.^{10,54} Computational mechanistic studies have also implicated triplet intermediates in alkyne cyclotrimerization reactions catalyzed by this species.^{85–89} To facilitate interpretation of the experimental results, we use density functional theory (DFT) to study each of the solvent coordinated photoproducts observed in this study. We investigate the choice of various density functionals on the relative spin state energies, and, consistent with the earlier careful study by Carreón–Macedo and Harvey,⁵⁴ the BP86 and PW91 functionals appear to give reasonably accurate results for the relative spin state energetics of CpCo(CO) .

4.2 Methods

4.2.1 Sample Preparation

CpCo(CO)_2 was purchased from Strem Chemicals Inc. All solvents were purchased from Sigma–Aldrich Co. All samples and solvents were used without further purification. Dilute solutions of CpCo(CO)_2 were stable in air at ambient temperatures for at least a few hours (verified via FTIR) in all solvents. Samples used to collect TRIR spectra were prepared at a concentration of ca. 5 mM.

4.2.2 Quantum Chemical Modeling

The ground spin state of CpCo(CO) has been investigated previously by several authors.^{10,53,54} In this case we were particularly interested in the relative spin–state energetics of CpCo(CO) coordinated to different solvent molecules, so we carried out geometry optimizations using three different density functionals (BP86,^{37,38} B3LYP,^{37,39} PW91^{40–42}) in the Gaussian09 package.⁴³ The aug-cc-pDVZ basis set^{46–48} was used in all calculations, except those involving 1-iodobutane. Since the aug-cc-pDVZ basis is not defined for iodine, the lanl2dz^{44,45} basis was

used on the iodine atom, while the aug-cc-pDVZ basis was used for all other atoms in these calculations. All geometry optimizations were followed with a frequency analysis for use in interpreting the TRIR results, and also to verify that the calculated geometries were genuine local minima. For the potential energy surface scans shown in Figure 4.5, the distance between the Co atom of CpCo(CO) and the O atom of methanol was held fixed at various distances as the remaining geometrical parameters were optimized. These calculations were performed for both singlet and triplet CpCo(CO) species to locate an approximate minimum energy crossing point (MECP) for the coordination of methanol to CpCo(CO), as described in section III.D.

To investigate the strength of spin-orbit coupling (SOC) between the singlet and triplet spin states, complete active space multiconfigurational self-consistent field (casscf) calculations were carried out in the GAMESS-US package⁵⁶ using Ahlrich's pDVZ basis set⁵⁷ with one additional d function on each C and O atom, and an additional f function on Co. The BP86 geometry for ³CpCo(CO) was used in these calculations (calculated geometries were similar for each choice of DFT functional). The active space of the casscf calculations consisted of 8 electrons in 10 d-type orbitals, constituting an (8,10) active space. The choice to include unoccupied d-type orbitals containing an extra node was made to account for the double-shell effect, which has been shown to be important in transition metal complexes.⁵⁹ Calculations were performed as follows: restricted or restricted open shell Hartree-Fock calculations were performed for singlet and triplet states, respectively, to generate the initial wavefunctions. After inspecting the active space orbitals, the casscf wavefunction was generated for the triplet state. The core orbitals from the triplet casscf wavefunction are then frozen in the subsequent calculation of the singlet casscf wavefunction, as this is necessary for the corresponding orbital transformation necessary to calculate the SOC matrix elements.⁶⁰ Finally, SOC between singlet and triplet states was calculated using the full Breit-Pauli spin-orbit Hamiltonian.⁶¹⁻⁶³ This method of calculating SOC is favorable, as it allows for different molecular orbitals to describe the ground and excited states. The effects of state averaging when generating the casscf wavefunctions were tested, but did not result in a meaningful difference in calculated SOC values, and the reported result is based on wavefunctions that were not state averaged.

4.3 Results and Discussion

The TRIR spectra in the CO stretching region are presented as difference absorbance spectra. Positive absorptions correspond to newly formed species, while negative bands correspond to the depletion of parent molecules. Since the negative parent bands are very similar in each case, the spectra presented focus on the newly formed product peaks.

4.3.1 Ultrafast UV-Pump IR-Probe Spectroscopy in Alkanes and Haloalkanes

The photochemistry of CpCo(CO)₂ in alkane solutions has been studied by several authors.^{18,24,32} In cyclohexane, the carbonyl loss photoproduct, ³CpCo(CO), forms in a triplet ground state with a characteristic IR absorption at 1989 cm⁻¹, and is stable as a triplet for > 1 μs.⁸² We wanted to investigate whether spin crossover and solvent coordination would occur on the picosecond timescale in more coordinating solvent environments, so we carried out the same experiment in a series of haloalkanes: 1-chlorobutane, 1-bromobutane, and 1-iodobutane.

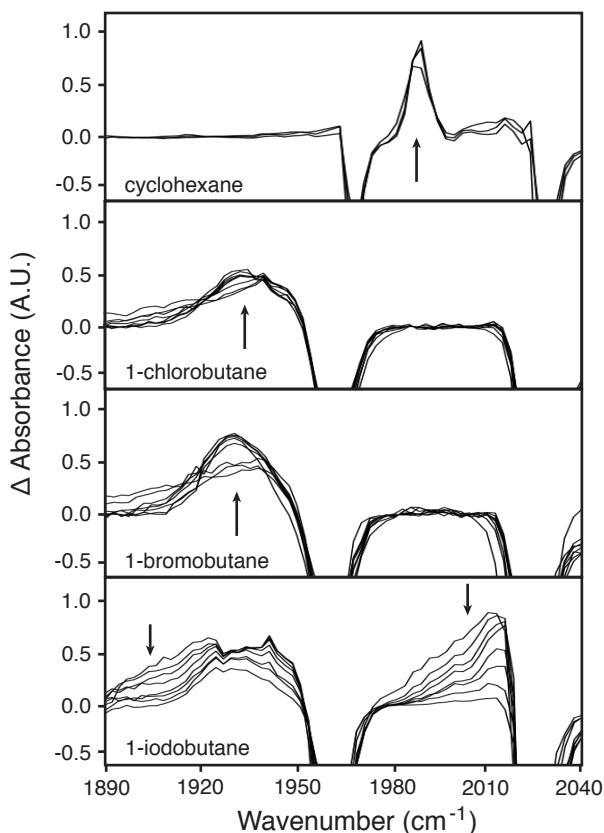


Figure 4.2. TRIR spectra of $\text{CpCo}(\text{CO})_2$ in cyclohexane and haloalkane solvents at 10, 30, and 50 ps (cyclohexane), and 5, 10, 20, 30, 40, 50, 60, and 70 ps (haloalkanes) following 267 nm photolysis (400 nm photolysis was used in the case of 1-iodobutane, which also results in a broad absorption corresponding to an electronically excited state).

In each of these solvents, $^3\text{CpCo}(\text{CO})$ was not directly observed, but instead a product peak at ca. 1935 cm^{-1} was present (Figure 4.2 and Table 4.2). On the basis of electronic structure calculations of the relative spin state energetics of the $\text{CpCo}(\text{CO})$ molecule interacting with each haloalkane (section III.D), we assign this photoproduct to a solvated singlet species. We conclude that spin crossover to a $^1\text{CpCo}(\text{CO})(\text{sol.})$ photoproduct takes place within the first several picoseconds of the formation of the $\text{CpCo}(\text{CO})$ photoproduct in these halogenated solvents, and no evidence of other solvated photoproducts was observed.

For spectra taken in 1-iodobutane solvent, 400 nm excitation was used to avoid a strong UV-absorption band of 1-iodobutane that prevents photolysis of $\text{CpCo}(\text{CO})_2$ using 267 nm pump pulses. This results in the formation of $\text{CpCo}(\text{CO})$ along with an electronically excited state of $\text{CpCo}(\text{CO})_2$ with a lifetime of ca. 50 ps, as can be observed in the spectra in Figure 4.2. TRIR spectra were also recorded in the other solvents using 400 nm photolysis, and the same photochemistry involving the $\text{CpCo}(\text{CO})$ photoproduct was observed in each, indicating that both spectra result in the same CO loss photochemistry and thus can be directly compared. All other spectra are presented using 267 nm excitation.

4.3.2 Ultrafast UV–Pump IR–Probe Spectroscopy in Acetone and DMF

We next studied the photolysis of $\text{CpCo}(\text{CO})_2$ in acetone and dimethylformamide (DMF), which are expected to be more strongly coordinating than haloalkanes via their sp^2 hybridized oxygen atoms. Figure 4.3 shows the TRIR spectra of $\text{CpCo}(\text{CO})_2$ in acetone and DMF.

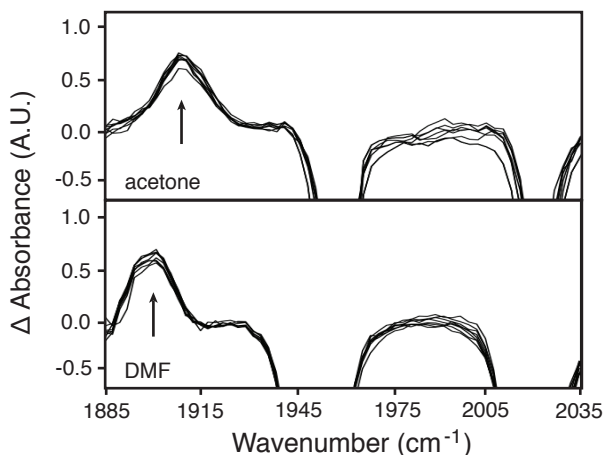


Figure 4.3. TRIR spectra of $\text{CpCo}(\text{CO})_2$ in neat acetone and DMF solvents at 5, 10, 20, 30, 40, 50, 60, and 70 ps following 267 nm photolysis.

In both acetone and DMF, only a single photoproduct is observed. The frequency of this product's absorption is significantly red-shifted compared to the solvated singlet observed in the haloalkane solvents. DFT calculations (section III.D) predict this to be the case for solvated singlet $\text{CpCo}(\text{CO})$, and also confirm that the singlet species is the more stable spin state. On this basis, we assign this photoproduct to a $^1\text{CpCo}(\text{CO})(\text{sol.})$ species.

4.3.3 Ultrafast UV–Pump IR–Probe Spectroscopy in Alcohols and THF

We next wanted to study the photolysis of $\text{CpCo}(\text{CO})_2$ in alcohol and THF solvents, as we felt the sp^3 oxygen atoms in these solvents would provide an interesting comparison to the sp^2 hybridized oxygen atoms in acetone and DMF. Shown in Figure 4.4 are the TRIR spectra of $\text{CpCo}(\text{CO})_2$ in methanol, 1-butanol, 1-hexanol, 1-decanol, and THF.

Interestingly, these spectra reveal the presence of two distinct solvated photoproducts at ca. 1916 and 1942 cm^{-1} . In 1-butanol, 1-hexanol, and 1-decanol, unsolvated $^3\text{CpCo}(\text{CO})$ can also be initially observed via its IR absorption at ca. 1989 cm^{-1} , and this decays within 50 ps. This is readily explained by the fact that the longer alkyl chains require $^3\text{CpCo}(\text{CO})$ to, on average, undergo more diffusion before encountering a $-\text{OH}$ site to which it can coordinate. This is consistent with our previous understanding of the interactions of triplet species with alkyl groups.²⁵ The presence of two peaks at ca. 1916 and 1942 cm^{-1} was surprising, however, and their assignment requires more detailed explanation.

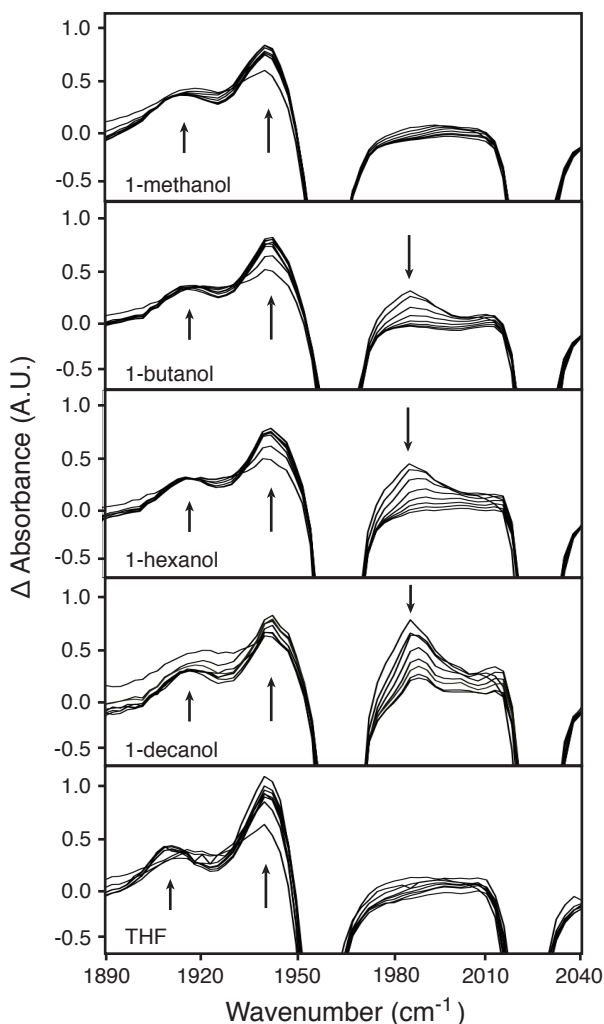


Figure 4.4. TRIR spectra of $\text{CpCo}(\text{CO})_2$ in neat alcohol and THF solvents at 5, 10, 20, 30, 40, 50, 60, and 70 ps following 267 nm photolysis. In 1-butanol, 1-hexanol, and 1-decanol, the initially unsolvated $^3\text{CpCo}(\text{CO})$ species can be observed at ca. 1989 cm^{-1} .

We performed these experiments using both 267 nm and 400 nm pump pulses, and observed that the ratio of peaks at ca. 1916 and 1942 cm^{-1} was independent of the pump wavelength. Comparison to experiments in acetone and DMF (section III.C) confirms that these peaks arise from two distinct chemical species. This information, combined with the observed kinetics in the longer chain alcohol solvents, indicates that the peaks at 1916 and 1942 cm^{-1} correspond to two distinct photoproducts originating from the same precursor, which in this case is $^3\text{CpCo}(\text{CO})$. Though we initially considered that one of these peaks could belong to a ring-slipped species, this is inconsistent with the understanding of why ring-slip takes place. Ring-slippage would only decrease the electron count on an already electron deficient 16 electron metal center, which is inconsistent with observations of ring-slip in the literature.⁹⁰ To determine whether a weak interaction with a second solvent molecule could be responsible for one of the two observed photoproducts species, we also obtained the TRIR spectra in diluted solutions (10 mol% and 50 mol%) of 1-butanol or THF in cyclohexane. These spectra in diluted alcohol solutions showed

essentially the same peak ratios at ca. 1916 and 1942 cm^{-1} , indicating that no weak interaction with a second alcohol or THF molecule, such as hydrogen bonding with the Cp ring, are responsible for the presence of a second species. A solvent hydrogen bond donor is also ruled out by the very similar spectra in both alcohols and THF. Having thus ruled out all other reasonable possibilities, we are able to conclude that the oxygen atom in alcohol and THF solvents is able to coordinate to CpCo(CO) in both singlet and triplet spin states. This conclusion is supported by the results of electronic structure calculations comparing the energetics of each alcohol coordinated to singlet and triplet CpCo(CO) (section III.D). By comparing the observed and calculated frequencies and calculated spin state energy differences for CpCo(CO) in each solvent, we were able to assign the lower frequency peak at ca. 1916 cm^{-1} to $^1\text{CpCo(CO)(sol.)}$, and the higher frequency peak at ca. 1942 cm^{-1} to $^3\text{CpCo(CO)(sol.)}$.

We note that both products form at essentially the same rate from the unsolvated $^3\text{CpCo(CO)}$ precursor, and that they form in the same ratio at which they are present at 1.5 ns within the first ca. 10 ps, or roughly during the vibrational cooling period of the nascent photoproduct. This implies that there is little barrier to spin crossover from the unsolvated $^3\text{CpCo(CO)}$ precursor, and we infer it is likely that both solvated spin states are in equilibrium. We will examine this point in more detail in section III.D.

One previous study²⁴ has investigated the time-resolved IR spectrum of CpCo(CO)₂ in dilute alkane solutions containing THF on the microsecond timescale, but these authors did not report the observation of a second peak at ca. 1916 cm^{-1} , which we have assigned to solvated $^1\text{CpCo(CO)}$. One possible explanation is that $^1\text{CpCo(CO)(sol.)}$ is more reactive than $^3\text{CpCo(CO)(sol.)}$ on longer timescales, and thus it has already reacted prior to the shortest time delay (0.5 μs) reported in that work. This conflicts, however, with the fact that we believe there to be little barrier to equilibration of $^3\text{CpCo(CO)(sol.)}$ and $^1\text{CpCo(CO)(sol.)}$. Looking carefully at the spectra from that work, an alternative explanation is that a peak is, in fact, present at ca. 1920 cm^{-1} , and that the authors did not assign it due the signal-to-noise ratio. Considering the integrated absorption of the lower frequency peak is only ca. 24% that of the higher frequency peak (see Table 4.1), we feel this is the most likely explanation. Our results in 10 mol% THF in cyclohexane solution show the formation of both $^3\text{CpCo(CO)(sol.)}$ and $^1\text{CpCo(CO)(sol.)}$ from the unsolvated $^3\text{CpCo(CO)}$ precursor in the same ratio observed in neat THF solution, and with the same observed frequency for the THF solvated triplet as in the previous study.²⁴

Table 4.1.^a Relative Spin State Populations

Solvent	$^1\text{CpCo(CO)(sol.)}$ (ca. 1916 cm^{-1})	$^3\text{CpCo(CO)(sol.)}$ (ca. 1942 cm^{-1})
methanol	29%	71%
1-butanol	21%	79%
1-hexanol	24%	76%
1-decanol	30%	70%
THF	24%	76%

(a) Percentages denote relative integrated peak areas for each absorption.

Voigt lineshapes were fit to the peaks corresponding to the solvated singlet and triplet species in each neat alcohol solvent and neat THF at a time delay of 200 ps. In the case of the absorption at ca. 1942 cm^{-1} , this also required separating a significant overlapping contribution from the parent bleach at ca. 1965 cm^{-1} , to which a Voigt profile was also fit. Undoubtedly, this introduces some amount of error into our values for the peak areas. We also do not have a reliable way of

knowing the relative extinction coefficients for the solvated singlet and triplet species. Our main interest here lies in comparing relative populations across different solvents, and, since both the singlet and triplet monocarbonyl species have very similar predicted geometries (see DFT calculations), we will make the approximation that the extinction coefficients are equal as we calculate the relative populations of the two species. Table 4.1 lists the relative peak areas, which, using our assumption of equal extinction coefficients, are equivalent to the relative populations of the solvated singlet and triplet species. It is noteworthy that the relative populations of the singlet and triplet species are similar in each of these solvents, implying that coordination of CpCo(CO) to the sp^3 oxygen atom in each of these solvents results in similar changes in free energy. The spin state is clearly sensitive to the identity of the moiety directly coordinated to the metal center however, as demonstrated by the results discussed in sections III.A and III.B.

Table 4.2 summarizes the experimentally observed frequencies for CpCo(CO) photoproducts in each solvent studied.

Table 4.2. Experimental CO-Stretching Frequencies for CpCo(CO) Species

Solvent	Solvated Photoproduct	Observed frequency (cm^{-1})
cyclohexane	$^3CpCo(CO)$	1989
<i>n</i> -octane	$^3CpCo(CO)$	1989
1-chlorobutane	$^1CpCo(CO)(Cl-R)$	1935
1-bromobutane	$^1CpCo(CO)(Br-R)$	1932
1-iodobutane	$^1CpCo(CO)(I-R)$	1932
acetone	$^1CpCo(CO)(O=CR_2)$	1911
DMF	$^1CpCo(CO)(O=CR_2)$	1902
methanol	$^1CpCo(CO)(HO-R)$	1916
	$^3CpCo(CO)(HO-R)$	1942
1-butanol	$^1CpCo(CO)(HO-R)$	1916
	$^3CpCo(CO)(HO-R)$	1942
1-hexanol	$^1CpCo(CO)(HO-R)$	1917
	$^3CpCo(CO)(HO-R)$	1943
1-decanol	$^1CpCo(CO)(HO-R)$	1918
	$^3CpCo(CO)(HO-R)$	1942
THF	$^1CpCo(CO)(O(-R)_2)$	1913
	$^3CpCo(CO)(O(-R)_2)$	1942

4.3.4 Density Functional Theory and ab Initio Calculations

DFT geometry optimizations were carried out to investigate the relative spin state energies of singlet and triplet CpCo(CO) coordinated to each solvent molecule in the study. Each calculation included a single solvent molecule coordinated to the metal center, and thus these are otherwise gas phase calculations of the energies and frequencies for the solvent coordinated species. A careful study of the relative spin state energies for CpCo(CO)⁵⁴ has shown that the BP86 functional gives relatively accurate spin state splitting between singlet and triplet states, so we expect the BP86 results to be the most reliable. We checked these calculations against the PW91 functional, which also gave good results in the previous study, and the B3LYP hybrid functional, which gave an excessively large spin state gap in the previous study.⁵⁴ Table 4.3 summarizes the calculated spin state energy differences and frequencies associated with each solvent molecule coordinated to the CpCo(CO) photoproduct in the singlet and triplet states.

Table 4.3. Results of Density Functional Theory Calculations

CpCo(CO) +	R _{Co-X} (Å) ^a		Frequency (cm ⁻¹)		ΔE _{T-S} ^b (kcal/mol)
	Sing.	Trip.	Sing.	Trip.	
no ligand					
<i>BP86</i>	–	–	1929	1958	-13.0
<i>PW91</i>	–	–	1939	1968	-12.9
<i>B3LYP</i>	–	–	2024	2062	-25.4
1-chlorobutane	X = Chlorine				
<i>BP86</i>	2.25	2.66	1925	1942	7.9
<i>PW91</i>	2.24	2.65	1935	1951	7.7
<i>B3LYP</i>	2.31	2.86	2007	2050	-10.0
1-bromobutane	X = Bromine				
<i>BP86</i>	2.35	2.69	1928	1941	9.4
<i>PW91</i>	2.34	2.68	1937	1949	9.8
<i>B3LYP</i>	2.41	2.91	2008	2046	-8.7
1-iodobutane	X = Iodine				
<i>BP86</i>	2.53	2.83	1928	1944	10.5
<i>PW91</i>	2.52	2.80	1932	1952	11.2
<i>B3LYP</i>	2.58	3.10	2006	2044	-7.8
acetone	X = Oxygen				
<i>BP86</i>	1.88	2.07	1909	1921	11.8
<i>PW91</i>	1.88	2.07	1919	1930	11.9
<i>B3LYP</i>	1.92	2.20	1987	2027	-6.8
DMF	X = Oxygen				
<i>BP86</i>	1.95	2.21	1893	1906	6.6
<i>PW91</i>	1.94	2.20	1903	1916	6.6
<i>B3LYP</i>	1.98	2.22	1975	2029	-8.2
methanol	X = Oxygen				
<i>BP86</i>	2.04	2.24	1914	1927	2.8
<i>PW91</i>	2.03	2.23	1925	1937	2.7
<i>B3LYP</i>	2.03	2.23	2005	2030	-11.5
1-butanol	X = Oxygen				
<i>BP86</i>	2.04	2.29	1919	1927	4.2
<i>PW91</i>	2.04	2.28	1929	1936	4.2
<i>B3LYP</i>	2.04	2.28	2006	2031	-10.2
1-hexanol	X = Oxygen				
<i>BP86</i>	2.04	2.30	1918	1927	4.2
<i>PW91</i>	2.04	2.28	1929	1936	4.3
<i>B3LYP</i>	2.04	2.28	2006	2031	-10.2
1-decanol	X = Oxygen				
<i>BP86</i>	2.04	2.29	1918	1927	4.1
<i>PW91</i>	2.04	2.28	1928	1936	4.1
<i>B3LYP</i>	2.04	2.27	2006	2030	-10.2
THF	X = Oxygen				
<i>BP86</i>	2.02	2.22	1914	1920	4.2
<i>PW91</i>	2.00	2.24	1910	1932	5.8
<i>B3LYP</i>	2.01	2.23	1988	2025	-9.3

(a) Distance between the Co atom and the nearest non-hydrogen ligand atom (X) obtained from optimized geometries. (b) Positive ΔE values indicate the singlet state is favored, while negative values indicate the triplet state is favored.

Similar to the previous study,⁵⁴ we find that the BP86 and PW91 functionals give the best results, while the B3LYP functional consistently overestimates the spin state splitting. We thus focused on the BP86 and PW91 results to draw our conclusions about the observed photoproducts. In the following discussion, results are given as the BP86 value with the PW91 value in parentheses.

Looking first at the results in haloalkanes, the predicted energy splitting is 7.9 (7.7) kcal/mol in favor of a solvated singlet photoproduct. The corresponding frequency is predicted to be 1925 (1935) cm⁻¹. While these unscaled frequencies are not expected to match the experimental values

exactly, we make use of their relative values with different solvent ligands to assist in making spectral assignments. We have attempted to take a holistic view of the observed and predicted frequencies, calculated energy differences, and experimental data into account in making these assignments. On the basis of the calculated relative spin state energies and comparisons to other observed and predicted frequencies, we assign the experimental peaks at ca. 1935 cm^{-1} in each haloalkane to $^1\text{CpCo}(\text{CO})(\text{sol.})$.

In acetone, our calculations predict the solvated singlet species to be favored by 11.8 (11.9) kcal/mol, and the CO stretching frequency is predicted to be 1909 (1919) cm^{-1} . Comparing this calculated frequency to those calculated for the haloalkane solvated complexes, the further red-shifting predicted by coordination to acetone is consistent with the experimentally observed values of ca. 1935 cm^{-1} in haloalkanes and 1911 cm^{-1} in acetone. In DMF, we calculate the solvated singlet to be favored by 6.6 (6.6) kcal/mol, and the predicted frequency is predicted to be even further red-shifted to 1893 (1903) cm^{-1} , again consistent with the experimentally observed frequency of 1902 cm^{-1} .

Moving to the alcohol and THF results, the predicted energy differences for singlet and triplet solvent coordinated species are much smaller. Keeping in mind that these are gas phase calculations, and that entropic contributions are not accounted for, we feel the predicted relative energy differences of ca. 2-4 kcal/mol match the experimental observation of an equilibrium between singlet and triplet spin states reasonably well. We note that none of these functionals include dispersion effects, which could affect the relative stability of singlet and triplet species. Considering the concentration independence and excitation wavelength independence of the observed peak ratios (discussed in section III.B), we were able to independently make the assignment of the two solvated species to $^1\text{CpCo}(\text{CO})(\text{sol.})$ and $^3\text{CpCo}(\text{CO})(\text{sol.})$, and here we seek primarily to determine which peak corresponds to which spin state. DFT calculations suggest that $^1\text{CpCo}(\text{CO})(\text{sol.})$ corresponds to the lower frequency peak, so we tentatively assign solvated singlet CpCo(CO) to the peak at ca. 1916 cm^{-1} , and solvated triplet CpCo(CO) to the peak at ca. 1942 cm^{-1} . By comparison to the spectra and calculations for CpCo(CO) in acetone and DMF, we affirm that the lower frequency absorption at ca. 1916 cm^{-1} corresponds to $^1\text{CpCo}(\text{CO})(\text{sol.})$, and thus the absorption at ca. 1942 cm^{-1} corresponds to $^3\text{CpCo}(\text{CO})(\text{sol.})$.

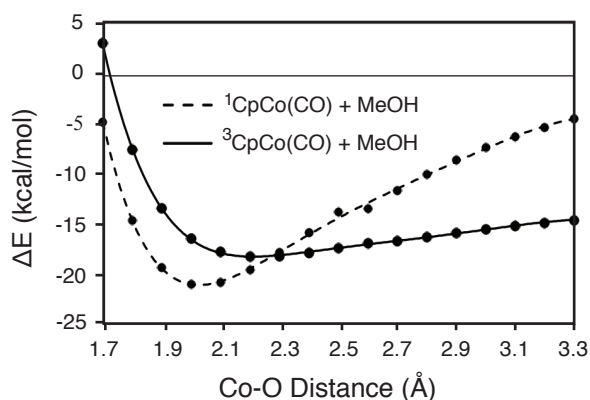


Figure 4.5. DFT energy scans for coordination of methanol to singlet and triplet CpCo(CO). The curves are generated by performing geometry optimizations at fixed Co–O distances. Circles correspond to calculated energies relative to the dissociation limit on the singlet surface, while the lines are fits to the data presented for visualization purposes only.

As mentioned in section III.B, we feel that the alcohol and THF solvated singlet and triplet species are likely in equilibrium prior to any subsequent reactivity that might occur. One piece of evidence supporting this is the calculated spin–orbit coupling constant of 206.2 cm^{-1} (RMS value), which is relatively high among first–row transition metal complexes.^{18,79} Recall that the probability of spin state interconversion should scale approximately with the square of this value.⁹¹ The bound singlet and triplet states in alcohols and THF also possess similar geometries, as evidenced by the optimized internuclear distances in Table 4.3. Looking at the methanol–solvated singlet and triplet structures optimized at the BP86 level, for example, shows an RMSD of only 0.552 \AA ($.400\text{ \AA}$ with H atoms omitted) in coordinates between the two solvated species. We also performed constrained geometry optimizations at various separations between the oxygen atom of MeOH and the Co metal center for both the singlet and triplet species (Figure 4.5). This builds approximate potential energy surfaces for the coordination of methanol to singlet and triplet CpCo(CO), which allows us to locate an approximate minimum energy crossing point (MECP) between the two surfaces.⁵⁵ The MECP is essentially a transition state analogue for reactions occurring on multiple potential energy surfaces, with the added constraint that the electronic state must also change in the vicinity of this geometry. We find the MECP to be located at a Co–O separation of 2.28 \AA , which is also close to the equilibrium separations of 2.24 \AA and 2.04 \AA calculated for the solvated triplet and singlet minima, respectively. The similarity of the MECP to the methanol–solvated minima suggests that crossover between the species is a facile process. Finally, as mentioned above, the experimental spectra show the formation of both photoproducts in their equilibrium ratio from a common unsolvated triplet precursor within the first several picoseconds, strongly suggesting a low barrier to spin state interconversion from the triplet precursor to the solvated singlet species. We feel this is convincing evidence that the two spin states are in equilibrium at ambient temperatures.

4.4 Conclusions

We have shown in this paper that the 16–electron species CpCo(CO) can coordinate to a solvent molecule in either the singlet or triplet spin state. This is in contrast to the previous assertions that triplet 16–electron photoproducts cannot interact strongly with solvent molecules, and adds to our understanding of triplet reactivity in organometallic photoproducts. The existence of transition metal complexes with two thermally accessible spin states is well known,^{92–98} but, to our knowledge, this is the first observation of a transient photoproduct that exhibits an equilibrium between two stable spin states, and also the first observed case in which a solvent molecule has been shown to coordinate to two spin states of the same photoproduct.

In the case of CpCo(CO), spin crossover does not appear to present a significant kinetic barrier to solvent coordination or reactivity of the triplet species, and thus relative thermodynamic stabilities determine the spin state of CpCo(CO) on the picosecond timescale. As electronic structure calculations demonstrate, CpCo(CO) can have favorable interactions with solvent molecules and other ligands in both the singlet and triplet states, and the ability of a solvent ligand to stabilize either state will determine the spin state of the reactant present in solution. These results add to our previous model for triplet reactivity in solution and suggest that the reactivity of triplet photoproducts may depend strongly on how the solvent environment affects the relative spin state energetics. Further experiments are underway to compare the reactivity of solvated singlet and triplet CpCo(CO) as a catalyst in different environments.

5 Characterization of a Short-Lived Triplet Precursor in CpCo(CO)-Catalyzed Alkyne Cyclotrimerization

The following chapter is reproduced (adapted) in part with permission from (Lomont, J. P.; Nguyen, S. C.; Zoerb, M. C.; Hill, A. D.; Schlegel, J. P.; Harris C. B. *Organometallics* 2012, 31, 3582-3587.). Copyright (2012) American Chemical Society.

5.1 Introduction

Cyclopentadienyl cobalt dicarbonyl is well known for its utility as a catalyst in cyclotrimerization and cyclo-oligomerization reactions involving alkynes and alkenes.^{80,81,85-88} Computational studies have suggested the involvement of triplet intermediates in these reactions,^{18,23,24,32,35,82,83,85-88} and the first step in the reaction mechanism is the thermal or photochemical dissociation of a CO ligand to form a reactive, 16-electron monocarbonyl species. Here we report an ultrafast study of the photochemistry of CpCo(CO)₂ in neat 1-hexyne and 1-hexene solutions and find that both singlet and triplet spin states play a role in generating the initially formed alkyne/alkene coordinated species.

The time-resolved photochemistry of CpCo(CO)₂ has been studied previously by several authors. In alkane solvents, the primary photoproduct, ³CpCo(CO), forms in a triplet ground state and is stable for > 1 μs uncoordinated to any alkyl groups.²⁴ Solution-phase studies of CpCo(CO) and other ground-state triplet organometallic photoproducts have suggested that unsaturated triplet species interact very weakly with alkyl groups of solvent molecules, and that intersystem crossing to a singlet state is required for the coordination of a solvent molecule to the metal center.^{10,15-19,23-30,84} In more coordinating solvent environments, spin crossover to a singlet state and solvent coordination take place more rapidly.^{18,24,25,35} CpCo(CO) is somewhat unique in that theoretical work has shown that a ligand-bound minimum can exist for both singlet and triplet states, and their relative energies depend on the identity of the incoming ligand.^{10,54} Using time-resolved infrared (TRIR) spectroscopy, we recently discovered that both the singlet and triplet spin states of this unsaturated complex can coordinate to certain solvent molecules,³⁵ motivating further investigation into the reactivity of this interesting species.

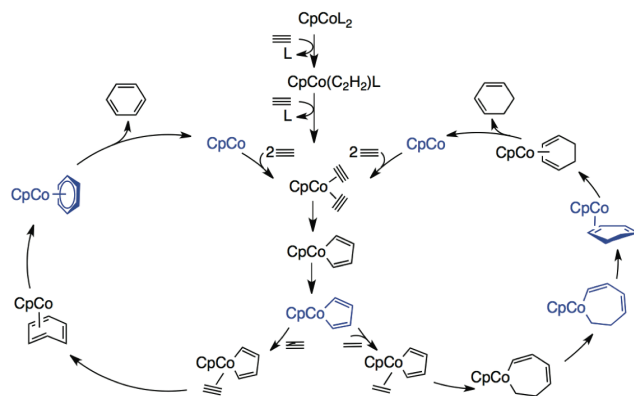


Figure 5.1. Previously proposed catalytic cycles involving triplet intermediates in cobalt-mediated cyclotrimerization and cyclo-oligomerization reactions of alkynes and alkenes. Triplet species are shown in blue.

Previous studies on bond activation in neat triethylsilane solution have established that the differing interactions of singlet and triplet species toward solvent molecules play an important role in their reactivity.^{15–19,84} The diffusion of singlet photoproducts is hindered by their coordination to alkyl groups as token-ligands, slowing the process of rearrangement to form bond-activated products. Since triplets interact so weakly with alkyl groups, they are able to diffuse rapidly through hydrocarbon chains in solution, yet readily undergo spin crossover upon encountering a more coordinating Si–H bond. These differences in weak solvent interactions allow triplets to activate Si–H bonds orders of magnitude faster than their singlet counterparts,¹⁸ despite the fact that triplet reactivity could be slowed by the requirement for a spin state change.

More recently, computational investigations into cobalt mediated cyclotrimerization and cyclo-oligomerization of alkynes and alkenes have implicated triplet intermediates and competing spin conserving and spin crossover pathways at several stages of the reaction mechanisms.^{85–88} Figure 5.1 summarizes pathways involving triplet intermediates proposed in two recent mechanistic studies on these reactions, with triplet species shown in blue.^{87,88} The authors of these studies found several low lying minimum energy crossing points between singlet and triplet surfaces along the reaction path, leading to the proposal of these nonadiabatic mechanisms. Recent work also suggests a two-state mechanism is involved in the activation of Si–H bonds for alkene hydrosilylation by cyclopentadienyl cobalt species.⁸⁹

Each of the aforementioned findings demonstrates the tendency for intersystem crossing between singlet and triplet states to play a role in the reactivity of CpCoL complexes. In the present study, we explore the picosecond dynamics of photochemically generated CpCo(CO) in neat alkyne and alkene solutions. Our goal is to gain insight into the interaction of the initially generated ³CpCo(CO) photoproduct with the unsaturated carbon–carbon bonds in the solvent, specifically looking for the involvement of any solvent coordinated triplet adducts formed between alkynes or alkenes and the CpCo(CO) moiety.

5.2 Methods

5.2.1 Sample Preparation

CpCo(CO)₂ was purchased from Strem Chemicals Inc. 1-Hexene and 1-Hexyne were purchased from Sigma–Aldrich Co. All samples and solvents were used without further purification. Dilute solutions of CpCo(CO)₂ were stable in air at ambient temperatures for at least a few hours (verified via FTIR). Samples used to collect TRIR spectra were prepared at a concentration of ca. 5 mM.

5.2.2 Data Analysis

Kinetic traces were obtained by fitting Voigt bandshapes to each spectral feature (the parent bleach was fit to the static FTIR spectrum), and decay time constants are reported as the decay time constant from fitting an exponential rise and decay function to the kinetic trace. Errors are reported as a 95% confidence interval to the fit.

5.2.3 Density Functional Theory Modeling

Geometry optimizations were carried out using the BP86,^{37,38} B3LYP,^{37,39} and PW91^{40–42} functionals in the Gaussian09 package.⁴³ The aug-cc-pDVZ basis set^{46–48} was used in all calculations. All geometry optimizations were followed with a frequency analysis for use in interpreting the TRIR results, and also to verify that the calculated geometries were genuine local minima.

5.3 Results and Discussion

5.3.1 Ultrafast UV–Pump IR–Probe Spectroscopy in 1-Hexyne and 1-Hexene

Time-resolved infrared (TRIR) spectra of CpCo(CO)₂ in neat 1-hexyne and 1-hexene solutions were collected following 267 nm photolysis. The TRIR spectra in the CO stretching region are presented as difference absorbance spectra. Positive absorptions correspond to newly formed species, while negative bands correspond to the depletion of parent molecules.

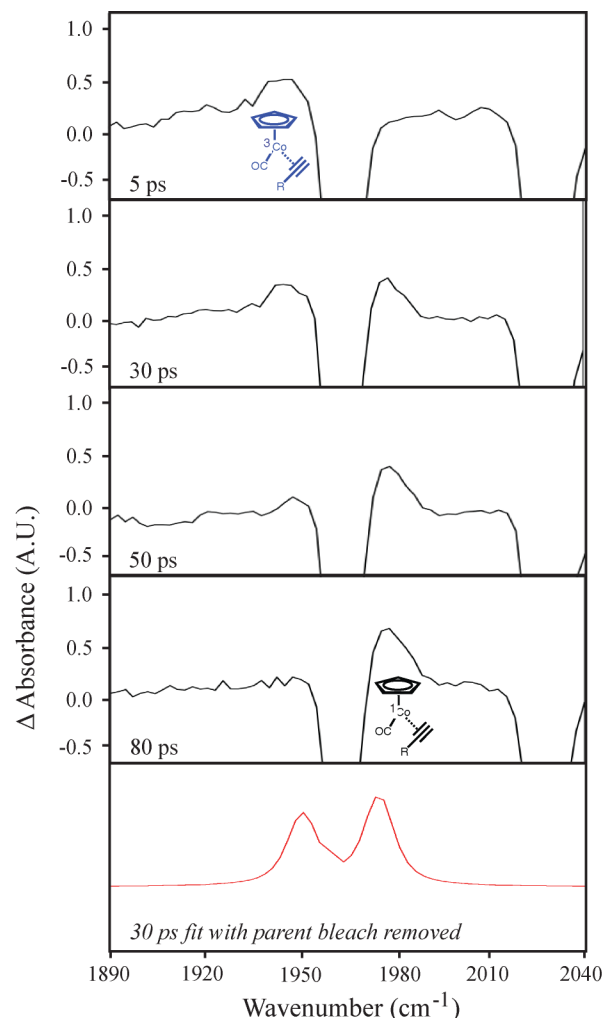


Figure 5.2. TRIR spectra of $\text{CpCo}(\text{CO})_2$ in 1-hexyne following 267 nm photolysis. Structures shown indicate the spectral assignments explained in the text. To extract clear bands corresponding to the two positive absorptions, the lower panel shows Voigt bandshapes fit to the 30 ps TRIR spectrum with the parent bleach subtracted. This fit is plotted at the same resolution as the experimental spectra. The actual ΔOD of the 1979 cm^{-1} absorption at 80 ps is ca. 0.4 before removing the parent bleach.

Figure 5.2 shows the time resolved infrared (TRIR) spectra of $\text{CpCo}(\text{CO})_2$ in neat 1-hexyne solution. Previous studies in alkane solutions have shown that $^3\text{CpCo}(\text{CO})$ exhibits a characteristic IR absorption at 1989 cm^{-1} .^{24,32} No absorption corresponding to the unsolvated $^3\text{CpCo}(\text{CO})$ photoproduct is directly observed in Figure 5.2, but instead the earliest delay times show the formation of a photoproduct peak at 1949 cm^{-1} . This absorption rises during the vibrational cooling period of the nascent photoproduct, and decays in $28 \pm 8\text{ ps}$ with the concomitant rise of a new absorption at 1979 cm^{-1} . The absorption at 1979 cm^{-1} then remains constant in intensity for $> 1\text{ ns}$. We note that the absorption at 1979 cm^{-1} cannot correspond to unsolvated $^3\text{CpCo}(\text{CO})$, as there should be no precursor to the unsolvated triplet. A previous picosecond TRIR study in a mixed 1-hexene/*n*-hexane solvent observed a similar absorption at 1974 cm^{-1} at delay times of hundreds of picoseconds, corresponding to $^1\text{CpCo}(\text{CO})(\eta^2\text{-1-}$

hexene).³² Thus we assign the absorption at 1979 cm⁻¹ in 1-hexyne to ¹CpCo(CO)(η²-1-hexyne), leaving the absorption at 1949 cm⁻¹ unassigned for now. We will revisit the assignment of the absorptions in Figure 5.2 in more detail in the next section.

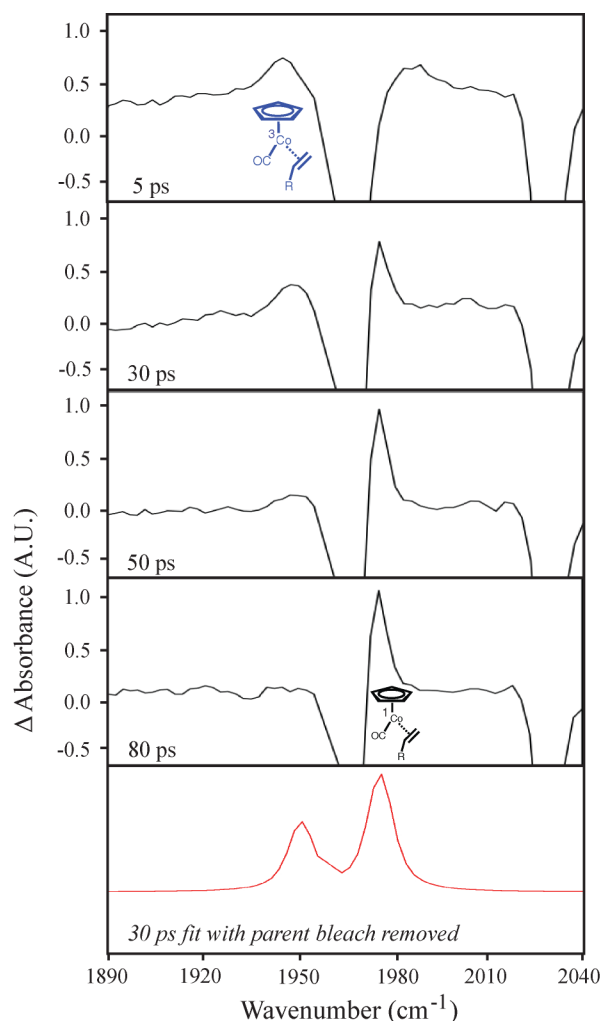


Figure 5.3. TRIR spectra of CpCo(CO)₂ in 1-hexene following 267 nm photolysis. Structures shown indicate the spectral assignments explained in the text. To extract clear bands corresponding to the two positive absorptions, the lower panel shows Voigt bandshapes fit to the 30 ps TRIR spectrum with the parent bleach subtracted. This fit is plotted at the same resolution as the experimental spectra. The actual Δ OD of the 1976 cm⁻¹ absorption at 80 ps is ca. 1.0 before removing the parent bleach.

The photochemistry observed in neat 1-hexene solution is very similar to that in 1-hexyne solution, and the TRIR spectra are shown in Figure 5.3. An initially formed product peak at 1949 cm⁻¹ decays in 43 ± 11 ps along with the rise of an absorption at 1976 cm⁻¹. At early delay times (5 ps in Figure 5.3), some amount of ³CpCo(CO) is also observed at 1989 cm⁻¹. As mentioned in the preceding paragraph, a similar absorption to that at 1976 cm⁻¹ has been observed in an earlier TRIR study⁷ in solutions of 1-hexene in *n*-hexane and was assigned to ¹CpCo(CO)(η²-1-

hexene). The previous account³² did not report an absorption corresponding to the 1949 cm^{-1} peak in the present study.

Before assigning the absorptions at 1949 cm^{-1} , we should address our reasons for assigning this peak to a distinct chemical species, rather than to vibrational cooling of the singlet photoproduct. We have studied the photochemistry of $\text{CpCo}(\text{CO})_2$ following 267 nm excitation in many solvents, so there are ample data for comparison. In cyclohexane, for example, the triplet photoproduct absorption is observed at 1989 cm^{-1} , and this spectrum shows no similar absorptions at lower frequencies that would indicate vibrational cooling should lead to an absorption that is so significantly red-shifted or that persists with a lifetime of 30–40 ps. In other solvents in which a solvated singlet photoproduct is observed (acetone, DMF, THF, and several alcohols and haloalkanes),³⁵ we again did not observe any dynamics similar to those in the present study. Were the dynamics observed in this study simply a result of vibrational cooling, we would have expected to see at least some evidence of similar spectral changes taking place in other solvents. Moreover, were the absorption at 1949 cm^{-1} to arise from hot bands of the solvated singlet, one would expect to simultaneously observe at least some photoproduct intensity at the fundamental absorption frequency (1979/1976 cm^{-1}) of the species giving rise to the hot bands; the early time spectra in both solvents show that this is not the case. Finally, we do observe some hot bands at ca. 1920 cm^{-1} that we attribute to cooling of the species at 1949 cm^{-1} (see 5 and 30 ps spectra in Figures 2 and 3). Were these to arise from vibrational cooling of the solvated singlet at 1979/1976 cm^{-1} , the red-shifting by as much as 60 cm^{-1} would be remarkably larger in magnitude than what was observed in cyclohexane or other solvent environments.³⁵ For these reasons, we assign the observed dynamics to a distinct intermediate species.

To assign the absorptions observed at 1949 cm^{-1} in each solvent, and to direct our efforts using density functional theory to explore the possible peak assignments, we consider what plausible coordination geometries exist for alkynes and alkenes to a metal center. Both end-on and η^2 coordination geometries initially appear to be plausible candidates. A vinylidene species was ruled out, both because a vinylidene complex would not be expected to rearrange to form an η^2 species, and because the spectra in 1-hexyne and 1-hexene are very similar, and formation of a vinylidene from 1-hexene coordination is not possible via a tautomerization mechanism.⁹⁹ A previous study on the picosecond to nanosecond timescale has also shown that vinylidene species are not expected to form on the timescale studied.¹⁰⁰ We therefore directed our DFT investigations to end-on and η^2 coordination geometries, keeping in mind that both singlet and triplet spin states have been shown to be important in the reactivity of CpCoL derivatives.

5.3.2 Density Functional Theory Calculations

Density functional theory (DFT) calculations aid us in assigning the photoproducts observed in the TRIR spectra. Previous studies have shown that the BP86 and PW91 functionals give reasonable singlet–triplet energy differences for the $\text{CpCo}(\text{CO})$ photoproduct,^{35,54} and we also used the B3LYP hybrid functional to further validate the calculated coordination geometries. Initial testing showed that both side-on (η^2) and end-on coordination geometries can be associated with local minima for the 1-hexyne and 1-hexene coordinated photoproducts, so we performed geometry optimizations from a variety of initial configurations. Table 5.1 summarizes the calculated CO stretching frequency for each spin state and coordination geometry, as well as the binding energy for 1-hexyne and 1-hexene coordinated species relative to the dissociated triplet state, along with spectral assignments for the experimentally observed absorptions.

Looking at the experimental spectra, we first assign the absorptions at 1979 cm⁻¹ in 1-hexyne and 1976 cm⁻¹ in 1-hexene to ¹CpCo(CO)(η²-1-hexyne) and ¹CpCo(CO)(η²-1-hexene), respectively. As discussed in the previous section, the assignment of the 1976 cm⁻¹ in 1-hexene to ¹CpCo(CO)(η²-1-hexene) was made in a previous study in solutions of 1-hexene in cyclohexane,⁷ and this assignment is consistent with other cases involving the interaction of alkenes and alkynes with otherwise coordinatively unsaturated metal centers.^{99,100} DFT calculations confirm that the singlet η² species are the most thermodynamically stable. We then consider the 1949 cm⁻¹ absorption, corresponding to the transiently stable intermediate present at early times in each solvent. Comparing the relative energies of the end-on and η² coordinated triplet species (see Table 5.1) allows us to rule out the end-on triplet as a candidate, leaving only the end-on singlet and η² triplet as possibilities. It is not necessarily useful to compare the relative energies of these two species, since the early time photoproduct must form because of a kinetic barrier to reaching the final η² singlet species. Of these two possibilities, only one possesses an easily understandable kinetic barrier to forming the η² singlet; the η² triplet requires a change of spin state. To rule out the end-on singlet, we consider that the relatively open coordination geometry of CpCo(CO) should allow the unsaturated carbon-carbon bond to approach from a distribution of angles, and Hammond's postulate suggests that those geometries leading to form the η² singlet should have more favorable interactions with the metal center. Thus if an end-on singlet were to form at early times, there is no clear reason why this intermediate would be the *only* species initially present (see 5 ps delay times in Figures 5.2 and 5.3) and then rearrange to the η² singlet. This interpretation is also supported by a previous study on the rearrangement kinetics of 16-electron Cr(CO)₅ in 1-hexyne solution, in which no end-on coordinated singlet species was observed. Thus we assign the coordinated intermediate at 1949 cm⁻¹ to an η² triplet.

Table 5.1. Calculated and observed CO stretching frequencies and relative stabilities for η² and end-on isomers

Ligand	Calculated Frequency (cm ⁻¹)		ΔE _{Binding} ^b (kcal/mol)		Experimental Frequency (cm ⁻¹)
	Sing.	Trip.	Sing.	Trip.	
no ligand					
BP86	1929	1958			1989 cm ⁻¹
PW91	1939	1968			³ CpCo(CO)
B3LYP	2024	2062			in cyclohexane ⁸
1-Hexyne (η ²)					
BP86	1950	1941	-34.7	-12.7	1979 cm ⁻¹ η ² -singlet 1949 cm ⁻¹ η ² -triplet
PW91	1961	1949	-37.7	-15.5	
B3LYP	2040	2031	-12.2	-3.3	
1-Hexyne (end-on)					
BP86	1967	1944	-18.6	-7.1	Not observed by experiment
PW91	1977	1952	-20.6	-9.4	
B3LYP ^a	–	–	–	–	
1-Hexene (η ²)					
BP86	1942	1936	-34.9	-6.7	1976 cm ⁻¹ η ² -singlet 1949 cm ⁻¹ η ² -triplet
PW91	1953	1945	-38.1	-9.5	
B3LYP	2031	2035	-12.4	-3.5	
1-Hexene (end-on)					
BP86	1938	1936	-10.8	-6.6	Not observed by experiment
PW91	1949	1946	-13.1	-9.4	
B3LYP ^a	2017	–	10.2	–	

(a) B3LYP geometry optimizations for species with missing entries consistently rearranged to the η^2 geometry. (b) Binding energies are given relative to the dissociated triplet state.

The DFT results for the 1-hexyne coordinated species further support this conclusion, as the end-on singlet is actually predicted to have a higher CO stretching frequency than the η^2 singlet, while the η^2 triplet shows a red-shift in frequency, relative to the η^2 singlet, consistent with the experimental results. The calculations involving 1-hexene do not show this difference, and instead predict similar frequencies for the η^2 triplet and the end-on singlet. While not entirely conclusive on their own, the results of the frequency calculations are thus most consistent with the assignment of the species at 1949 cm^{-1} to the η^2 triplet. Comparing the DFT-calculated frequency differences between the η^2 triplet and η^2 singlet typically shows a roughly 10 cm^{-1} red-shift going from the singlet to the triplet. This trend is reasonably consistent with the experimental results; our fits to the TRIR spectra showed the η^2 triplet absorption red-shifted by ca. 25 cm^{-1} from that of the η^2 singlet.

Having assigned each initially coordinated species to a triplet precursor, it is interesting to consider that the spin state change in this reaction appears to take place more slowly than in alcohol and THF solutions. In a recent study in alcohol and THF solvents,³⁵ we observed both solvated spin states to form concurrently (within 1 ps time resolution), whereas, in the present case, the solvated triplet clearly forms first and then converts to the solvated singlet. Looking at the calculated structures of the coordinated triplet and singlet species (Figure 5.4) provides a possible factor contributing to the slower rate of spin crossover in the present study.

Figure 5.4 summarizes the BP86 calculated coordination geometries and calculated energies for each species assigned to an experimentally observed IR absorption, focusing on the coordination of the unsaturated carbon-carbon bond to the Co center. The η^2 coordinated alkyne and alkene show somewhat different coordination geometries in the triplet and singlet states, as shown in Figure 5.4. The requirement for a rearrangement of the coordination geometry may partially explain the slower rate of intersystem crossing in these species, relative to our recent observations in alcohol and THF solvents. For the alcohol and THF coordinated species, both spin states were calculated to have very similar coordination geometries, which may assist the spin crossover process.

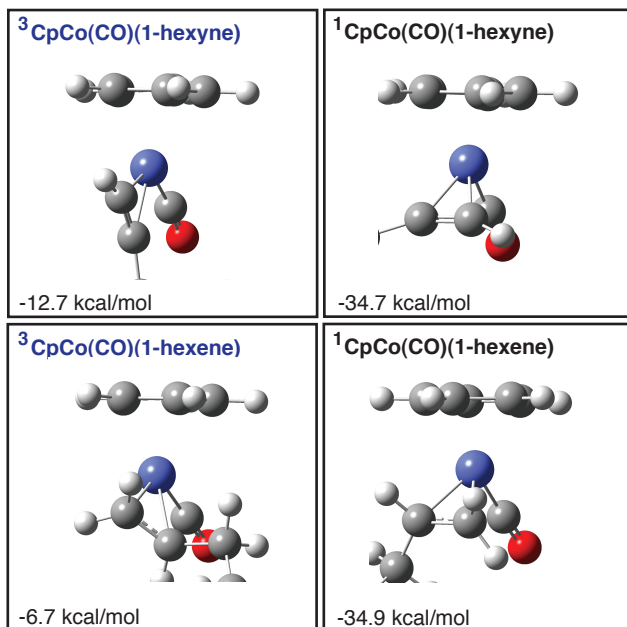


Figure 5.4. Calculated structures for the observed η^2 triplet and singlet 1-hexyne and 1-hexene coordinated species. The graphics focus on the interaction of the Co center with the unsaturated carbon-carbon bond (the full alkyl chains are not shown). Energies listed are the BP86 values, relative to the triplet dissociation limit.

5.4 Conclusions

These results provide new insight into the early mechanistic steps of $\text{CpCo}(\text{CO})_2$ catalyzed cyclotrimerization and cyclo-oligomerization reactions involving alkyne and alkene substrates, as well as a better understanding of the complex reactivity of triplet 16-electron photoproducts on the ultrafast timescale. In terminal alkyne and alkene solutions, $^3\text{CpCo}(\text{CO})$ initially coordinates to the unsaturated carbon-carbon bond *without a change of spin state* to form a $^3\text{CpCo}(\text{CO})(\eta^2\text{-alkyne/alkene})$ intermediate, which subsequently undergoes spin crossover to form the $^1\text{CpCo}(\text{CO})(\eta^2\text{-alkyne/alkene})$ species. We note that this mechanism appears to be the only possible route to formation of the η^2 singlet, as the η^2 triplet is the only solvent-coordinated species observed at early delay times. This result suggests that coordination of alkenes and alkynes to other triplet 16-electron species involved in the reaction mechanisms depicted in Figure 1 may similarly involve coordination of alkenes and alkynes prior to spin crossover from the triplet state. The apparently slower rate of spin crossover involving coordination to alkynes and alkenes, relative to recent observations in alcohol and THF solvents, highlights the influence of the coordinating ligand on rates of spin state changes. Consistent with the previous understanding of the interaction of triplet 16-electron photoproducts with alkyl groups, we do not observe coordination of $^3\text{CpCo}(\text{CO})$ with sp^3 hybridized alkyl groups of 1-hexyne or 1-hexane.

6 Direct Observation of a Bent Carbonyl Ligand in a 19-Electron Transition Metal Complex

The following chapter is reproduced (adapted) in part with permission from (Lomont, J. P.; Nguyen, S. C.; Harris C. B. *J. Phys. Chem. A* 2013, 117, 2317-2324.). Copyright (2013) American Chemical Society.

6.1 Introduction

Though even electron species comprise the majority of organometallic complexes, odd electron complexes have long been known to exist as stable products, or as reactive intermediates, in chemical reactions.¹⁰¹⁻¹⁰⁸ Among odd electron complexes, 17-electron (17e) and 19-electron (19e) radicals are the most commonly encountered. 19e complexes can be powerful reducing agents,¹⁰⁹ and 19e structures have been implicated as transient intermediates¹⁰²⁻¹⁰⁴ and as transition states^{110,111} in chemical reactions. The question often arises of whether a 19e complex is a “true 19e complex” in sense that the metal center has 19 valence electrons, or whether the extra electron density tends to localize onto a ligand. Complexes in which the 19th electron is at least somewhat localized onto a ligand orbital are often termed 18+ δ complexes, where δ describes the amount of radical electron density localized on the metal center.^{101-104,112}

In many cases, transiently lived 19e structures are proposed to involve the rearrangement of a ligand to accommodate the excess electron density at the metal center. A 2-electron donor ligand may rearrange to become a 1-electron donor,^{113,114} an aromatic ring may “slip,” resulting in a lower coordination number,¹¹⁵ or a phosphine or phosphite ligand may adopt a radical electronic configuration.¹¹⁶⁻¹¹⁸ Examples of such structures are shown in Figure 6.1. The theoretical rationale for each of these distortions is that the 19th electron can be moved from a higher energy metal-ligand antibonding orbital into a lower energy ligand-centered orbital. In many cases, the experimental evidence for the mechanistic role of these species has originated from investigations into the reactivity of radical complexes, and thus many of the proposed structures have not been directly observed.

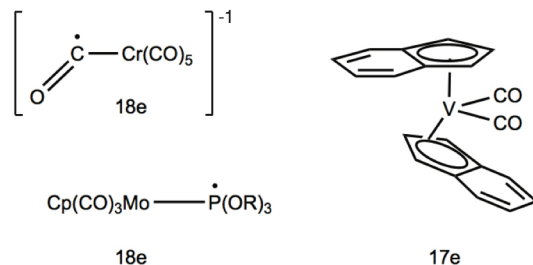


Figure 6.1. Examples of ligand rearrangements that avoid a 19-electron metal center.

In this chapter, picosecond time-resolved infrared (TRIR) spectroscopy is used to characterize a 19e species in which a single CO ligand adopts a bent conformation to reduce

excess electron density at the metal center. Specifically, photolysis of $[\text{CpRu}(\text{CO})_2]_2$ in a 1:4 molar $\text{P}(\text{OMe})_3:\text{CH}_2\text{Cl}_2$ solution leads to formation of 17e $\text{CpRu}(\text{CO})_2$ radicals, which coordinate the Lewis base $\text{P}(\text{OMe})_3$ to form a 19e adduct with a bent CO ligand. The bending of this ligand is demonstrated by comparison of the CO-stretching frequencies observed in the TRIR spectra of $[\text{CpRu}(\text{CO})_2]_2$ to analogous experiments on $[\text{CpFe}(\text{CO})_2]_2$, combined with density functional theory (DFT) calculations. DFT geometry optimizations provide evidence for the likely geometry adopted by $\text{CpRu}(\text{CO})_2\text{P}(\text{OMe})_3$, which involves a bent Ru–C–O bond angle of ca. 143–153°. Bending of the CO ligand presumably allows this complex to avoid a genuine 19e configuration at the metal center, similar in spirit to the structures shown in Figure 6.1. No evidence for subsequent reactivity or decay of the 19e adduct is observed within 1 ns of its formation.

The results of this study also provide insight into the mechanism of formation of a bridged $[\text{CpRu}(\text{CO})]_2(\mu\text{-CO})$ photoproduct that has been observed in previous experiments on longer timescales.^{119,120} Interestingly, the bridged species is not observed to form on the picosecond timescale, indicating that it does not form directly from photolysis of the parent complex at 267 or 400 nm in neat CH_2Cl_2 solution. This suggests that the mechanism of its formation likely involves diffusive reactions of 17e radicals occurring on longer timescales. It cannot be ruled out that different excitation wavelengths or different solvent conditions could allow for its formation directly from photolysis of the parent dimer.

6.2 Methods

6.2.1 Sample Preparation

$[\text{CpRu}(\text{CO})_2]_2$, $[\text{CpFe}(\text{CO})_2]_2$, $\text{P}(\text{OMe})_3$, and CH_2Cl_2 were purchased from Sigma-Aldrich Co. All samples and solvents were used without further purification. Dilute solutions of all samples were stable in air at ambient temperatures (verified via FTIR). Samples used to collect TRIR spectra were prepared at concentrations of ca. 5 mM.

6.2.2 Data Analysis

Kinetic data in this work result from spectra measured at delay times between 0 and 1000 ps between the UV/visible-pump and IR-probe pulses. Kinetic traces for each spectral feature were obtained by integrating a narrow spectral region (ca. 4 cm^{-1} wide) surrounding the reported frequency. The kinetic data were then fit to exponential curves using Origin Pro 8 software. To obtain fits with exponential rise and decays, a separate, home-written, fitting program was used. Errors on experimental time constants are reported as 95% confidence intervals.

6.2.3 Density Functional Theory Modeling

Geometry optimizations were carried out using the BP86,^{37,38} B3LYP,^{37,39} B3P86,^{37,38} B3PW91,^{37,40–42} B97D,¹²¹ LC-wPBE,^{122–125} M06,¹²⁶ PW91,^{40–42} wB97,¹²⁷ and wB97XD¹²⁸ functionals in the Gaussian09 package.⁴³ The 6-31+G(d,p) basis^{129,129,130} set was used for all atoms except Fe and Ru, and the lanl2dz^{44,45} basis was used for Fe and Ru. Unless otherwise noted, all calculations for odd-electron complexes were performed in a doublet spin state. All geometry optimizations were followed with a frequency analysis for use in interpreting the TRIR

results. Constrained geometry optimizations (described in section III B) were performed with the BP86 functional by fixing the M–C–O bond angle for a single carbonyl ligand at various angles and optimizing the remaining geometric parameters. Frequency calculations were also carried out for each partially optimized structure.

6.3 Results and Discussion

TRIR spectra in the CO stretching region are presented as difference absorbance spectra. Positive absorptions correspond to newly formed species, while negative bands correspond to the depletion of parent molecules.

6.3.1 Time-Resolved Infrared Spectroscopy

In polar solutions, $[\text{CpRu}(\text{CO})_2]_2$ exists as a mixture of *cis* and *trans* bridged isomers, as well as two non-bridged isomers.^{131–134} With regard to existing studies on the photochemistry of this complex, IR spectroscopy has been used to examine its reactivity following continuous irradiation in solution and in matrix isolation,^{119,135} and UV-Vis spectroscopy has been used to study its photochemistry following continuous irradiation and flash photolysis in solution.¹²⁰ Reactivity studies involving spin trapping and EPR spectroscopy have also been used to follow the reactivity of 17e radicals and carbonyl-loss products.¹³⁶ Density functional theory has been used to study the structural isomers of the parent molecule and the corresponding carbonyl loss products.¹³⁵ The results of all of these studies suggest that both 17e radicals, and a bridging CO-loss complex, $[\text{CpRu}(\text{CO})_2(\mu\text{-CO})]$, may result from photolysis of $[\text{CpRu}(\text{CO})_2]_2$.

Figure 6.2A shows picosecond TRIR spectra of $[\text{CpRu}(\text{CO})_2]_2$ in neat CH_2Cl_2 solution following 400 nm photolysis. Positive absorptions at 1933 and 2003 cm^{-1} are assigned to the 17e $\text{CpRu}(\text{CO})_2$ radical, and similar formation of 17e radicals has been observed previously for the Fe congener of this species.¹³⁷ While only one parent bleach band in the terminal region is not obscured by product bands, examination of the FTIR spectrum of $[\text{CpRu}(\text{CO})_2]_2$ in CH_2Cl_2 solution indicates that both photoproduct bands overlap other parent bleach bands.

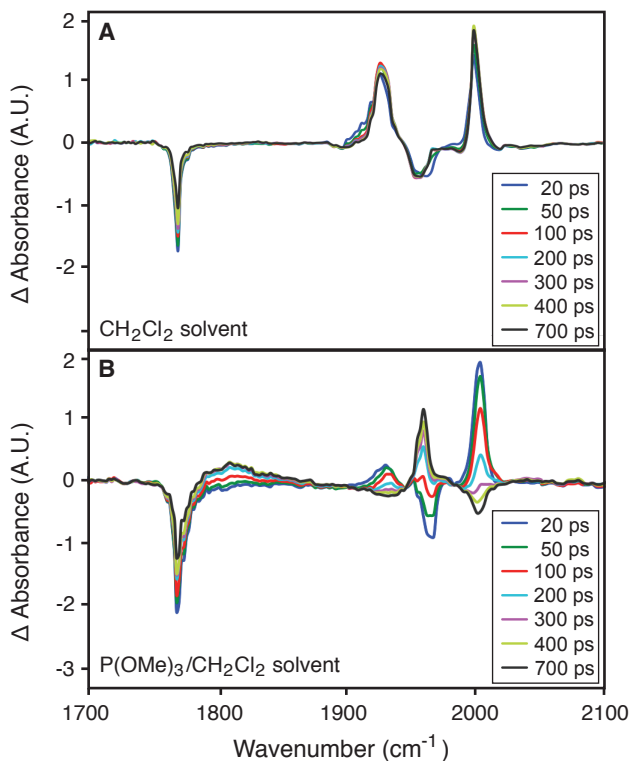


Figure 6.2. TRIR spectra of $[\text{CpRu}(\text{CO})_2]_2$ following 400 nm excitation in neat CH_2Cl_2 solution (panel A) and 1:4 molar $\text{P}(\text{OMe})_3:\text{CH}_2\text{Cl}_2$ solution (panel B).

Figure 6.2B shows TRIR spectra of $[\text{CpRu}(\text{CO})_2]_2$ in 1:4 molar $\text{P}(\text{OMe})_3:\text{CH}_2\text{Cl}_2$ solution. This solvent was chosen based on previous studies that have shown 17e radicals can coordinate the Lewis base $\text{P}(\text{OMe})_3$ on the picosecond timescale under these conditions.^{138,139} Absorptions at 1930 and 2003 cm^{-1} , assigned to 17e $\text{CpRu}(\text{CO})_2$, decay with the concomitant rise of new absorptions at 1810 and 1959 cm^{-1} . The decay time constants for the absorptions at 1930 and 2004 cm^{-1} are 190 ± 4 and 206 ± 9 ps, respectively, while the rise time constants for the bands at 1810 and 1959 cm^{-1} are 221 ± 7 and 192 ± 16 ps, respectively; thus two kinetically correlated species are present. Based on the correlated time constants for decay of the 17e species and rise of the new product peaks, we assign the absorptions at 1810 and 1959 cm^{-1} to the 19e $\text{CpRu}(\text{CO})_2\text{P}(\text{OMe})_3$ adduct. This is supported by the downshift in frequency of the CO-stretching absorptions, as well as the fact that the new species also shows two strong CO-stretching bands, ruling out the possibility that $\text{P}(\text{OMe})_3$ has substituted a CO ligand to form a monocarbonyl product.

Before proceeding, we wish to make abundantly clear the reasons the absorption at 1810 cm^{-1} cannot belong to the dimetallic bridged species $[\text{CpRu}(\text{CO})_2]_2(\mu\text{-CO})$, which has been observed previously in a 3-methylpentane matrix at 1772 cm^{-1} .¹¹⁹ First, no analogous absorption is present in the spectra collected in neat CH_2Cl_2 solution, clearly indicating that a reaction with the Lewis base $\text{P}(\text{OMe})_3$ is responsible for generating the species observed at 1810 cm^{-1} . Were the band at 1810 cm^{-1} to correspond to a dimetallic bridged complex, we would expect to observe the same complex in neat CH_2Cl_2 solution. Second, the time constants for the rise of the bands at 1810 and 1959 cm^{-1} correlate well with one another, indicating that they belong to the same species, and also correlate well with the decay of the bands at 1930 and 2004 cm^{-1} , indicating that $\text{CpRu}(\text{CO})_2$

is clearly the species which reacts to form the species observed at 1810 and 1959 cm^{-1} . There is no reason that the presence of the Lewis base $\text{P}(\text{OMe})_3$ should cause recombination of $\text{CpRu}(\text{CO})_2$ fragments to form a dimetallic complex. Moreover, existing ultrafast studies of $[\text{CpW}(\text{CO})_3]_2$ in phosphine and phosphite solutions^{138,139} have amply demonstrated that a Lewis base reacts with individual 17e $\text{CpW}(\text{CO})_3$ fragments to form adducts containing a single metal center, analogous to what we assign here. In the studies of the $[\text{CpW}(\text{CO})_3]_2$ dimer, no evidence was found to suggest that the presence of a Lewis base caused geminate recombination of the nascent 17e fragments to form a dimetallic complex. Having examined this spectral assignment in detail, we will next consider the structure of the $\text{CpRu}(\text{CO})_2\text{P}(\text{OMe})_3$ adduct more closely.

The observed frequency of 1810 cm^{-1} for the antisymmetric stretching mode is unusually low and is more consistent with the frequency one would expect for a bent or bridging carbonyl stretching mode than for a terminal carbonyl stretching mode. Additional evidence that this frequency is lower than expected is provided by comparing the present results to previous studies involving 17e and 19e photoproducts of $[\text{CpW}(\text{CO})_3]_2$.^{138,139} In that study, roughly equal frequency shifts were observed for the lower frequency and higher frequency absorption bands when moving from the 17e to 19e products ($\Delta\nu = 30$ and 28 cm^{-1} , respectively), while in the present study the antisymmetric mode redshifts significantly more ($\Delta\nu = 120 \text{ cm}^{-1}$) than the symmetric mode ($\Delta\nu = 44 \text{ cm}^{-1}$) when moving from the 17e to 19e ruthenium products. Even at the longest delay times, the terminal carbonyl parent bleaches are still not strongly visible, indicating that some quantity of 17e photoproduct remains overlapped with these bands. This suggests that an equilibrium is established between 17e $\text{CpRu}(\text{CO})_2$ and 19e $\text{CpRu}(\text{CO})_2\text{P}(\text{OMe})_3$.

This is consistent with observations made in a previous picosecond study on $[\text{CpW}(\text{CO})_3]_2$ in similar solvent environments, in which an equilibrium was established between 17e $\text{CpW}(\text{CO})_3$ and 19e $\text{CpW}(\text{CO})_3\text{L}$ ($\text{L} = \text{P}(\text{OMe})_3, \text{PPh}_3, \text{PBu}_3$) on the picosecond timescale.^{138,139} While the experiments on photolysis of the $[\text{CpW}(\text{CO})_3]_2$ dimer observed a picosecond disproportionation mechanism, the results of the present study cannot be explained by a disproportionation mechanism: were a disproportionation mechanism to take place, additional cationic and anionic products would be observed, requiring a total of at least six positive product bands (two for each of the 17e and 19e species, and at least one for each of the anionic and cationic products) in the picosecond TRIR spectra.

To provide additional evidence that this frequency is significantly lower than one would typically expect for the formation of a 19e adduct, we also examined the TRIR spectra of the iron congener, $[\text{CpFe}(\text{CO})_2]_2$. TRIR spectra of $[\text{CpFe}(\text{CO})_2]_2$ were collected following 400 nm photolysis in 1:4 molar $\text{P}(\text{OMe})_3:\text{CH}_2\text{Cl}_2$ solution, and these spectra are shown in Figure 6.3. Similar to the results with the ruthenium dimer, absorptions at 1918 and 1998 cm^{-1} , assigned to the 17e $\text{CpFe}(\text{CO})_2$ radical, are observed to decay with the concomitant rise of absorptions at 1895 and 1954 cm^{-1} , assigned to the 19e $\text{CpFe}(\text{CO})_2\text{P}(\text{OMe})_3$ adduct. An isosbestic point at ca. 1907 cm^{-1} is observed between the antisymmetric stretching modes of the 17e and 19e complexes. Note that the frequency shift of the antisymmetric mode upon coordination of $\text{P}(\text{OMe})_3$ to form the 19e adduct is only 23 cm^{-1} , while this same frequency shifts by 120 cm^{-1} for the ruthenium congener. This difference further demonstrates that the frequency of the antisymmetric CO stretching mode of $\text{CpRu}(\text{CO})_2\text{P}(\text{OMe})_3$ is unusually low, and also indicates that the structures of the iron and ruthenium 19e products differ significantly. The product band at ca. 1820 cm^{-1} in Figure 6.3 corresponds to the CO-loss product $\text{Cp}_2\text{Fe}_2(\mu\text{-CO})_3$, and this species has been reported previously.¹⁴⁰ It is worth pointing out that previous reports have

indicated $\text{CpFe}(\text{CO})_2\text{L}$ ($\text{L} = \text{CO}, \text{PPh}_3$) to adopt an $\eta^4\text{-Cp}$ coordination geometry, thus displacing the radical electron density onto the Cp ring.^{109,141,142} The TRIR spectra reported in this study do not provide any direct structural information to support or disprove such a coordination geometry, and the DFT investigations (*vide infra*) do not predict a ring slipped geometry.

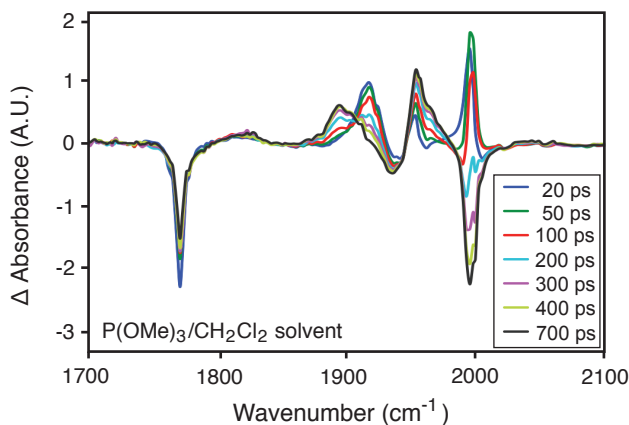


Figure 6.3. TRIR spectra of $[\text{CpFe}(\text{CO})_2]_2$ following 400 nm excitation in 1:4 molar $\text{P}(\text{OMe})_3:\text{CH}_2\text{Cl}_2$ solution.

We were also interested in the possible effects of the solvent on the structure of the 19e $\text{CpRu}(\text{CO})_2\text{P}(\text{OMe})_3$ adduct, so TRIR spectra of $[\text{CpRu}(\text{CO})_2]_2$ were collected following 400 nm excitation in 1:4 molar $\text{P}(\text{OMe})_3:n\text{-heptane}$ solution. These spectra were similar to those obtained in 1:4 molar $\text{P}(\text{OMe})_3:\text{CH}_2\text{Cl}_2$ solution, with bands at 1940 and 2009 cm^{-1} observed for the 17e $\text{CpRu}(\text{CO})_2$ photoproduct, and frequencies of 1826 and 1956 cm^{-1} observed for the 19e $\text{CpRu}(\text{CO})_2\text{P}(\text{OMe})_3$ adduct. The antisymmetric band of the 19e complex at 1826 cm^{-1} exhibited a narrower bandwidth in the *n*-heptane solution than in the CH_2Cl_2 solution. The similarity of the spectra in these two solvents suggests that the polarity of the surrounding solvent does not substantially affect the structure of the 19e adduct.

As mentioned in the introduction, previous studies have demonstrated that formation of 19e adducts may involve rearrangement of a two electron donor ligand to a one electron donor to avoid a 19e count at the metal.^{113,114} In this case, the spectroscopic evidence appears to suggest that, for $\text{CpRu}(\text{CO})_2\text{P}(\text{OMe})_3$, a CO ligand rearranges to a bent conformation such that it behaves as a 1-electron donor. Density functional theory calculations were carried out to investigate the structure of the $\text{CpRu}(\text{CO})_2\text{P}(\text{OMe})_3$ and $\text{CpFe}(\text{CO})_2\text{P}(\text{OMe})_3$ complexes.

A final note with regard to the TRIR spectra in neat CH_2Cl_2 solution: previous FTIR studies following continuous irradiation of $[\text{CpRu}(\text{CO})_2]_2$ in a 3-methylpentane matrix have observed a bridging carbonyl absorption at 1772 cm^{-1} , and the authors assigned this absorption to a singly bridged $[\text{CpRu}(\text{CO})_2]_2(\mu\text{-CO})$ photoproduct.¹³⁵ In the picosecond TRIR spectra in neat CH_2Cl_2 (Figure 6.2A), no absorptions corresponding to bridging carbonyl photoproducts are observed following either 400 or 267 nm excitation, indicating that no significant quantity of $[\text{CpRu}(\text{CO})_2]_2(\mu\text{-CO})$ is formed. The most likely explanation would appear to be that the singly bridged species forms through a mechanism that does not follow directly from photolysis of the parent complex, perhaps involving subsequent reactivity of the 17e radical photoproducts on longer timescales. It is also possible that the singly bridged species does not form in CH_2Cl_2

solution, or that an unobserved, transient precursor to its formation is unable to form in CH_2Cl_2 solution. Similarly, the absence of bridging carbonyl photoproduct peaks indicates that the triply bridged species $\text{Cp}_2\text{Ru}_2(\mu\text{-CO})_3$ is not formed; analogues to this species have been observed previously following photolysis of $[\text{CpFe}(\text{CO})_2]_2$ ¹⁴⁰ and $[\text{Cp}^*\text{Ru}(\text{CO})_2]_2$ ^{120,135} ($\text{Cp}^* = \text{C}_5(\text{CH}_3)_5$).

6.3.2 Density Functional Theory Modeling

DFT geometry optimizations were carried out for each of the 17e and 19e species mentioned in the preceding section. Interestingly, even when the Opt=VeryTight convergence criteria were used, two different local minima could be located for $\text{CpRu}(\text{CO})_2\text{P}(\text{OMe})_3$ depending on whether the input structure involved approximately linear Ru–C–O angles or one bent Ru–C–O angle. This observation held true for all 10 of the functionals tested. Table 6.1 lists the relative energies and vibrational frequencies obtained for the two minima located with each functional, and Comparing the energies of these minima, it is clear that the minimum involving a bent Ru–C–O bond angle is the overall minimum energy structure. For $\text{CpFe}(\text{CO})_2\text{P}(\text{OMe})_3$, only a single minimum with approximately linear Fe–C–O bond angles was located. The calculated BP86 structures of the minima for each 19e species are shown in Figure 6.4.

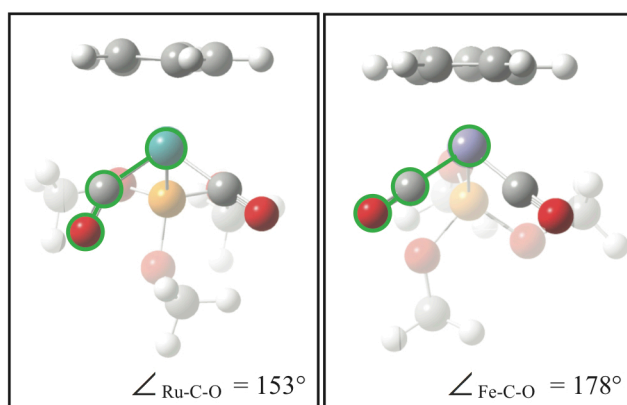


Figure 6.4. Structures of the minima located for $\text{CpRu}(\text{CO})_2\text{P}(\text{OMe})_3$, and $\text{CpFe}(\text{CO})_2\text{P}(\text{OMe})_3$ using the BP86 functional. The M–C–O angle in question is highlighted in green.

Table 6.1. Calculated energies and vibrational frequencies for each of the CpRu(CO)₂P(OMe)₃ minima located using each density functional. The terms Bent and Unbent are used to distinguish between the two local minima located with each functional. The angles indicated for each structure correspond to the set of atoms indicated in Figure 6.4.

Functional	Structure	Ru-C-O Angle (°)	Vib. Freqs. (cm ⁻¹)	ΔE _{Bent-Unbent} ^a (kcal/mol)
BP86	Bent	153	1849, 1949	-3.31
	Unbent	177	1924, 1980	
B3LYP	Bent	151	1918, 2031	-1.70
	Unbent	177	2007, 2068	
B3P86	Bent	150	1927, 2056	-3.57
	Unbent	177	2032, 2093	
B3PW91	Bent	150	1927, 2052	-3.25
	Unbent	177	2028, 2089	
B97D	Bent	152	1854, 1954	-4.80
	Unbent	177	1935, 1996	
LCWPBE	Bent	146	1939, 2124	-3.44
	Unbent	177	2097, 2158	
M06	Bent	147	1941, 2053	-3.26
	Unbent	178	2029, 2095	
PW91	Bent	152	1856, 1961	-4.04
	Unbent	177	1942, 2001	
WB97	Bent	143	1923, 2095	-3.09
	Unbent	177	2068, 2130	
WB97XD	Bent	147	1947, 2094	-3.42
	Unbent	177	2064, 2128	

(a) Negative ΔE values indicate that the bent conformation is favored.

In comparing the calculated and experimental vibrational frequencies, we were primarily interested in the predicted *difference* in frequency between the symmetric and antisymmetric modes. Using the BP86 functional, the difference in frequency between the symmetric and antisymmetric CO stretching modes for CpFe(CO)₂P(OMe)₃ is 53 cm⁻¹, while for CpRu(CO)₂P(OMe)₃ this difference is predicted to be 100 cm⁻¹. The fact that the calculated and experimental frequencies for each complex are in reasonable agreement supports the notion that the calculated structures can be considered to provide a reasonable description of those observed experimentally. Thus, it appears that the structure of CpFe(CO)₂P(OMe)₃ involves approximately linear M–C–O bond angles, while CpRu(CO)₂P(OMe)₃ involves a bent CO ligand.

Constrained geometry optimizations were carried out with the BP86 functional to further investigate the potential energy surface along the coordinate for bending of a M–C–O bond in both the ruthenium and iron centered 19-electron adducts, and these were performed by freezing one M–C–O bond angle at angles ranging from 120 to 180 while optimizing the remaining geometrical parameters. The vibrational frequencies and energies of the bent complexes are plotted in Figure 6.5.

The results of the frequency calculations shown in Figure 6.5 indicate that, as the M–C–O angle is bent away from a linear geometry, the frequencies of both the symmetric and antisymmetric CO stretching modes are predicted to shift. In terms of comparing the results of these calculations to the experimental data, it is especially relevant that the difference in frequency between the symmetric and antisymmetric modes increases significantly as the M–C–O bond angle is lowered. From the plotted energies, it is clear that the minimum energy structure for CpRu(CO)₂P(OMe)₃ is predicted to involve a bent CO ligand, while that for CpFe(CO)₂P(OMe)₃ is predicted to involve both CO ligands bonded in the traditional, 2-electron

donor fashion. As shown in Table 6.1, the value of the Ru–C–O angle is predicted to be approximately 143–153°, depending on which density functional theory method is used. The leveling off in the potential energy surface of the CpRu(CO)₂P(OMe)₃ complex (Figure 6.5, top panel) provides a likely explanation for why two local minima were located in the direct geometry optimizations for this complex; when the Ru–C–O bond angle is approximately linear, there is essentially no local gradient in energy along the Ru–C–O bending coordinate.

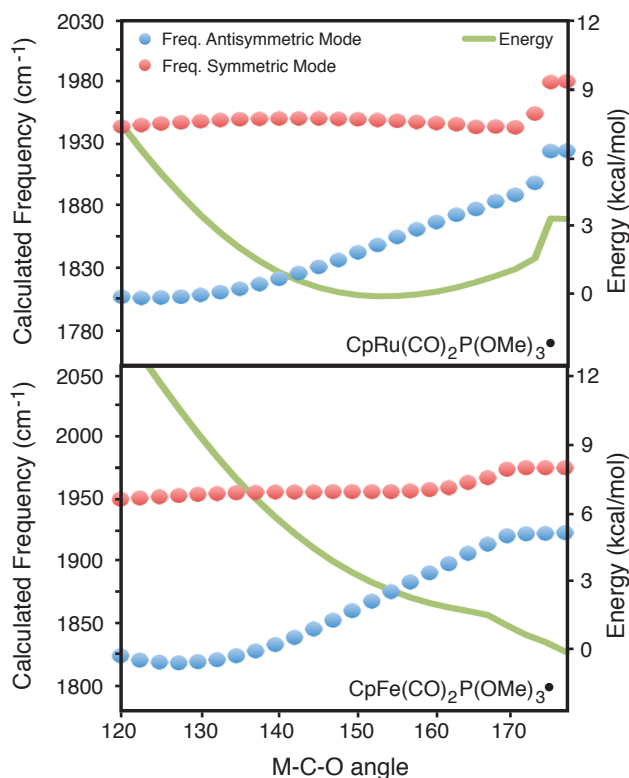


Figure 6.5. Vibrational frequencies calculated using the BP86 functional for the symmetric (red dots) and antisymmetric (blue dots) modes of the two CpM(CO)₂P(OMe)₃ species, along with their energies (green lines) as a function of the M–C–O angle.

In addition to the calculations described thus far, we also performed geometry optimizations to search for local minima other than those shown in Figure 6.4, and we will describe these briefly. One type of geometry we considered was a local minimum involving a bridging carbonyl ligand bridging the Ru and P atoms in the 19e CpRu(CO)₂P(OMe)₃ adduct; however, no corresponding minimum could be located. We also attempted geometry optimizations for the CpRu(CO)₂P(OMe)₃ species in a quartet (as opposed to a doublet) spin state; these resulted in structures in which the Cp ring distorted to coordinate the metal via a single carbon atom, and the energies were significantly (> 35 kcal/mol) higher in energy than the doublet minima. Constrained geometry optimizations were performed in which both Ru–C–O bond angles were simultaneously constrained to a bent conformation, and the frequencies of these species were also calculated. The results indicated that bending of both carbonyls simultaneously led to species with too small of a splitting between the symmetric and antisymmetric CO stretching modes to be consistent with the experimental observations. The “double-bent” structures

calculated were also consistently higher in energy than the “single-bent” minima reported. For example, constraining both M-C-O angles to 160° led to structures ca. 3 kcal/mol higher in energy than the single bent minima, while constraining both M-C-O angles to 150° led to structures ca. 6 kcal/mol higher in energy than the single bent minima, and further constraining both M-C-O angles to 140° led to structures ca. 13 kcal/mol higher in energy than the single bent minima (these values obviously vary somewhat with the choice of functional the values listed here correspond to those calculated using the BP86 functional). Geometry optimizations beginning from “ring-slipped” conformations returned to the local minimum shown in Figure 6.4. The fact that no other minima were located further supports assignment of the 19e CpRu(CO)₂P(OMe)₃ adduct to the structure containing a bent CO ligand.

Considering that the 19e iron and ruthenium species possess identical ligands, and share the same d-electron configuration, it is somewhat surprising that DFT methods correctly predict this significant structural difference. The fact that all 10 DFT methods tested correctly distinguished between the structures of CpFe(CO)₂P(OMe)₃ and CpRu(CO)₂P(OMe)₃ speaks to the power of DFT for studying organometallic complexes. We were pleasantly surprised at this result, and, indeed, it provided much of the motivation for choosing to test so many functionals. Certainly though, DFT methods do not always predict geometries consistent with experimental observations. In a study on the FeO₂⁻ anion, for example, nine of ten tested DFT methods predicted a bent geometry for this odd electron complex, while only one predicted the linear doublet ground state that matches experimental observations.¹⁴³

While the observation of a bent 19e CO complex is surprising, the literature contains other reports of bent CO ligands in a variety of contexts. As was mentioned in the introduction, the bending of a ligand to avoid a 19e configuration at the metal has been reported previously.^{113,114} A number of experimental and computational studies have been carried out on CO bound myoglobin, and the Fe-C-O angle has been debated and reported to take on a wide range of values from completely bent to completely linear.¹⁴⁴⁻¹⁵¹ Similarly, bridging carbonyls have been reported that span the entire range of symmetrically bridging to completely nonbridging.¹⁵² As early as the 1960's, unsymmetrical bridging CO ligands were reported, and Cotton suggested these semi-bridging CO ligands provide a mechanism for a metal with excessive electron density to transfer some of that electron density onto to a CO group bonded to a metal center with less electron density.¹⁵³⁻¹⁵⁶ The existence of bent nitrosyl ligands is also well known.¹⁵⁷⁻¹⁵⁹ In the case of CpRu(CO)₂P(OMe)₃ we believe the 19e metal center transfers its excess electron density onto a CO ligand, causing it to adopt a bent conformation.

Of course, the ability to predict which 19e complexes will adopt a bent CO ligand conformation would be a powerful tool. Unfortunately, it remains difficult to make such predictions from arguments based solely on the identity of the metal center or its ligands. However, our results demonstrate that DFT methods are able to correctly predict that the CpRu(CO)₂P(OMe)₃ adduct will have a bent CO ligand in its minimum energy conformation, while the CpFe(CO)₂P(OMe)₃ complex will not. The fact that the DFT results matched the experimental results closely in this study was very pleasing to us, and thus, at this point in time, DFT geometry optimizations seem to offer the best method for predicting whether a given 19e adduct will contain a bent CO ligand. We expect that future experimental studies characterizing the structures of 19e adducts will help to develop predictive ability regarding the structures of these species.

6.4 Conclusions

In this paper, we have used picosecond TRIR spectroscopy to demonstrate the formation of a 19e $\text{CpRu}(\text{CO})_2\text{P}(\text{OMe})_3$ adduct with a bent CO ligand. DFT calculations and comparison to experimentally observed vibrational frequencies for $\text{CpFe}(\text{CO})_2\text{P}(\text{OMe})_3$ were used to assign the experimental TRIR spectra. Presumably, the CO ligand bends due to donation of excess electron density from the 19e metal center into a carbon-centered orbital, which allows the metal center to redistribute some of the unpaired electron density. The observation of a bent CO ligand in $\text{CpRu}(\text{CO})_2\text{P}(\text{OMe})_3$ provides new insight into the solution-phase structure of this 19e complex, and this information helps to develop a clearer picture of 19e reactivity.

In addition to reporting the observation of a bent CO ligand in the $\text{CpRu}(\text{CO})_2\text{P}(\text{OMe})_3$ adduct, this study also represents the first ultrafast investigation into the photochemistry of the $[\text{CpRu}(\text{CO})_2]_2$ dimer. It is significant that no singly bridged CO complex was observed in neat CH_2Cl_2 solution following 267 or 400 nm irradiation. This suggests that the singly bridged $[\text{CpRu}(\text{CO})]_2(\mu\text{-CO})$ complex that has been reported previously does not form as a direct result of photolysis at either excitation wavelength, suggesting that it forms via a diffusive mechanism on timescales longer than 1 ns. It remains possible that this species may form on the picosecond timescale under other conditions.

7 Insights Into the In-Cage Photochemical Disproportionation of Transition Metal Dimers

The following chapter is reproduced (adapted) in part with permission from (Lomont, J. P.; Nguyen, S. C.; Harris C. B. *J. Phys. Chem. A* 2013, 117, 3777-3785.). Copyright (2013) American Chemical Society.

7.1 Introduction

While the majority of organometallic complexes contain an even number of valence electrons, the importance of odd electron species has long been known.^{101–108,160} Among these, the most commonly encountered odd electron complexes are 17-electron (17e) and 19-electron (19e) species. Electron rich 19e complexes have been implicated in electron transfer reactions as well as catalytic processes.^{102–104} In the present study, we focus our attention on the reactivity of 17e and 19e complexes toward radical disproportionation on the picosecond timescale.

In the reactions studied in this paper, photochemical cleavage of the metal-metal bond in a transition metal dimer leads to the initial formation of a 17e radical pair, and these 17e radicals may coordinate a Lewis base to form a 19e adduct. A 17e and 19e radical pair may then undergo disproportionation, transferring an electron to yield two 18e complexes. Previous picosecond studies on the photolysis of $[\text{CpW}(\text{CO})_3]_2$ in the presence of Lewis bases have demonstrated that radical disproportionation between 17e and 19e species can occur prior to diffusion out of the solvent cage.^{138,139} Here we investigate the role of the identity of the transition metal complex in these reactions, and we find that different transition metal complexes exhibit markedly different reactivity with regard to picosecond disproportionation and the formation of 19e adducts.

For 19e complexes, a distinction is often made between “true” 19e complexes, in which the 19th electron is localized at the metal center, and $18 + \delta$ complexes, in which the 19th electron localizes on a ligand away from the metal center.^{101–104,112} For example, we recently discovered that the 19e adduct $\text{CpRu}(\text{CO})_2\text{P}(\text{OMe})_3$ is an $18 + \delta$ complex containing a bent CO-ligand.¹⁶¹ There also exists evidence that $\text{CpFe}(\text{CO})_2\text{P}(\text{OMe})_3$ is likely to be an $18 + \delta$ complex with an η^4 Cp ligand.^{109,141,142}

Tyler et al. studied the photochemically initiated radical disproportionation of $[\text{CpM}(\text{CO})_3]_2$ (M = Cr, Mo, W) into $\text{CpM}(\text{CO})_3^-$ and $\text{CpM}(\text{CO})_3\text{L}^+$ (L = phosphine, phosphite), and their originally proposed mechanism is shown in Figure 7.1, panel C.^{162–165} More recent TRIR studies^{138,139,166,167} on $[\text{CpW}(\text{CO})_3]_2$ in phosphite and phosphine solutions ranging from picosecond through microsecond timescales led to the proposal of the two additional mechanisms, shown in Figure 7.1, panels A and B.

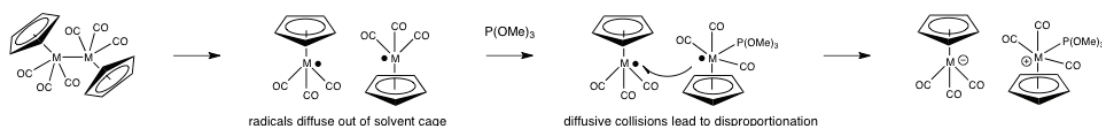
The disproportionation mechanism in panel A occurs on the picosecond timescale, prior to diffusion of the 17e and 19e radicals out of the solvent cage. This will be referred to as the “in-cage” mechanism. It is also possible that a pair of 17e radicals diffuses apart prior to formation of a 19e intermediate, or that a 17e and 19e radical pair do not form disproportionation products prior to diffusion out of the solvent cage. In this case, the 17e and 19e species may subsequently react with other radicals via diffusive encounters in the bulk solvent. This mechanism, shown in Figure 7.1B, will take place on longer timescales ranging from nanoseconds to milliseconds (or longer) and has been termed the “radical mechanism.”¹⁶⁷ Finally, there is the disproportionation

mechanism originally proposed by Tyler et al,^{162,164,164,165} shown in Figure 7.1C. This mechanism postulates that a 19e complex reacts via diffusive collisions with a parent dimer molecule to form the disproportionation products. This mechanism was supported by observations of a quantum yield greater than unity, consistent with a radical chain mechanism.

A. in-cage mechanism



B. radical mechanism



C. dimer mechanism

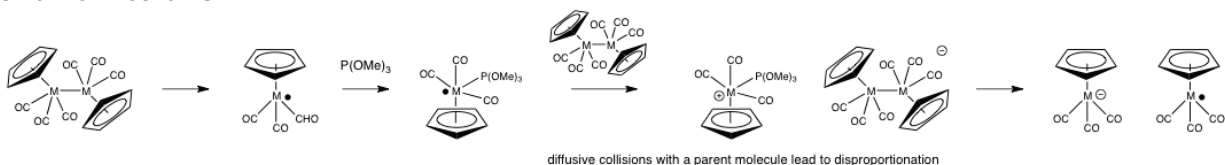


Figure 7.1. A summary of three mechanisms proposed for radical disproportionation

Presumably, mechanisms similar to those in Figure 7.1 also describe plausible disproportionation mechanisms following photolysis of other transition metal dimers. The present study uses picosecond time-resolved infrared (TRIR) spectroscopy to elucidate details surrounding the in-cage mechanism. The results described in this paper present new insights into its applicability of the in-cage mechanism and the factors that dictate whether this mechanism, or a diffusive one, will characterize electron transfer reactions in these complexes. These results also explore the tendency of the 17e radicals generated to form 19e photoproducts in the presence of Lewis bases, and provide insight into the oxidizing and reducing properties of the 17e and 19e complexes studied.

7.2 Methods

7.2.1 Sample Preparation

$\text{Mn}_2(\text{CO})_{10}$, $\text{Re}_2(\text{CO})_{10}$, $[\text{CpFe}(\text{CO})_2]_2$, $[\text{CpRu}(\text{CO})_2]_2$, $[\text{CpMo}(\text{CO})_3]_2$, $\text{P}(\text{OMe})_3$, and CH_2Cl_2 were purchased from Sigma-Aldrich Co. All samples and solvents were used without further purification. Dilute solutions of all samples, except $[\text{CpMo}(\text{CO})_3]_2$ in phosphite/ CH_2Cl_2 solution, were stable in air at ambient temperatures (verified via FTIR). Samples used to collect TRIR spectra were prepared at concentrations of ca. 5 mM. In the case of phosphite/ CH_2Cl_2 solutions of $[\text{CpMo}(\text{CO})_3]_2$, the dimer was observed to decay on the timescale of several hours, presumably due to the fact that the flow pump setup is not rigorously air-free. For this reason,

fresh samples of identical concentration were prepared every 30 minutes, and data files were checked to ensure that no evidence of parent species decay was present in the TRIR spectra.

7.2.2 Data Analysis

Kinetic data in this work result from spectra measured at delay times between 0 and 1000 ps between the UV/visible-pump and IR-probe pulses. Kinetic traces for each spectral feature were obtained by integrating a narrow spectral region (ca. 3 cm^{-1} wide) surrounding the reported frequency. The kinetic data were then fit to exponential curves using Origin Pro 8 software. To obtain fits with exponential rise and decays, a separate, home-written, fitting program was used. Errors on experimental time constants are reported as 95% confidence intervals.

7.2.3 Density Functional Theory Modeling

Density functional theory (DFT) calculations have been carried out to facilitate assignment of the absorptions observed in the TRIR spectra for $[\text{CpMo}(\text{CO})_3]_2$. Calculations were carried out using the BP86^{37,38} functional in the Gaussian09⁴³ package using the lan12dz basis^{44,45} for Mo and the 6-31+G(d,p)^{129,129,130} basis for all other atoms. Geometry optimizations were followed by a frequency analysis to ensure that all geometries were genuine local minima and for use in interpreting the TRIR results.

7.3 Results and Discussion

TRIR spectra in the CO stretching region are presented as difference absorbance spectra. Positive absorptions correspond to newly formed species, while negative bands correspond to the depletion of parent molecules.

7.3.1 Reactivity of $\text{Mn}(\text{CO})_5$ and $\text{Re}(\text{CO})_5$ Radicals

$\text{Mn}_2(\text{CO})_{10}$ has been demonstrated to undergo disproportionation under thermal or photochemical conditions in the presence of amines^{168–171} and other Lewis bases, including THF and acetonitrile.^{172–175} Previous studies have also provided strong evidence that $\text{Mn}(\text{CO})_5$ and $\text{Re}(\text{CO})_5$ coordinate phosphines, phosphites, and other ligands via an associative mechanism to form a 19e intermediate.^{176–180} However, it is notable, especially in the context of the present study, that the corresponding parent dimers are not believed to undergo disproportionation reactions with monodentate phosphines or phosphites.^{181–183} In the few studies in which disproportionation was observed in the presence of these ligands, it has been shown that the disproportionation reaction could be attributed to the presence of other donor solvents.¹⁸⁴ The 18-electron complexes $\text{Mn}(\text{CO})_5\text{Cl}$ and $\text{Mn}(\text{CO})_4\text{PPh}_3\text{Cl}$ have been observed via FTIR spectroscopy,¹⁷⁹ but, to our knowledge, 19e products formed by coordination of a phosphite or phosphine to $\text{Mn}(\text{CO})_5$ have not been directly observed. Irradiation of $\text{Re}_2(\text{CO})_{10}$ in pyridine and DMF solution led to the observation of $\text{Re}(\text{CO})_5^-$, suggesting that disproportionation does take place in these solvents.¹⁸⁵ In acetonitrile, the anionic product was not observed, suggesting that disproportionation did not take place in acetonitrile solution.¹⁶³ The cationic products were not addressed in either of these studies.

TRIR spectra of $\text{Mn}_2(\text{CO})_{10}$ and $\text{Re}_2(\text{CO})_{10}$ in 1:4 molar solutions of $\text{P}(\text{OMe})_3$ in CH_2Cl_2 were obtained in order to observe the reactivity of the corresponding 17e radical fragments. This solvent was selected since it was used previously to demonstrate the in-cage disproportionation mechanism with $[\text{CpW}(\text{CO})_3]_2$, thus allowing us to directly compare the results of that study to the present observations. Figure 7.2 shows the TRIR spectra obtained for $\text{Mn}_2(\text{CO})_{10}$ following 400 nm excitation. Based on comparisons to previous picosecond TRIR studies in alkane and alcohol solutions,¹⁸⁶ the positive absorption band at 1985 cm^{-1} is assigned to the 17e species $\text{Mn}(\text{CO})_5$. The lack of dynamic changes for this absorption, combined with the absence of any other absorption bands, indicates that no other products are formed on the picosecond timescale. Thus, no 19e adducts or disproportionation products are observed in these spectra.

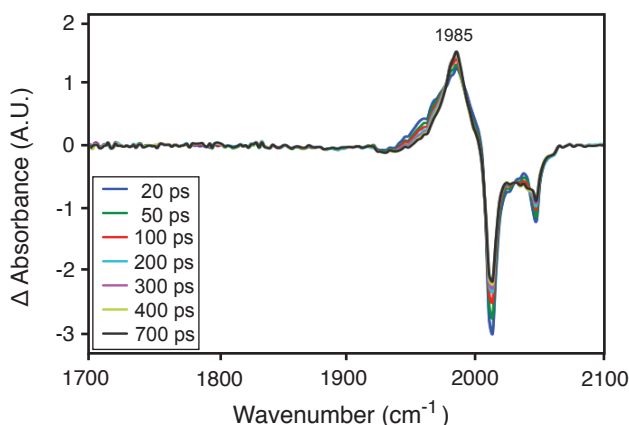


Figure 7.2. TRIR spectra of $\text{Mn}_2(\text{CO})_{10}$ following 400 nm photolysis in 1:4 molar $\text{P}(\text{OMe})_3:\text{CH}_2\text{Cl}_2$ solution.

Picosecond TRIR spectra of $\text{Re}_2(\text{CO})_{10}$ have been reported previously in alkane and carbon tetrachloride solution.^{187,188} 400 nm photolysis of this dimer does not lead to significant formation of 17e radicals via cleavage of the Re-Re bond, so 267 nm photolysis was instead used to generate 17e radicals from this parent species. The corresponding TRIR spectra are shown in Figure 7.3. Previous investigations using 295 nm excitation observed the formation of both 17e radicals and CO-loss products,^{187,188} and similar results were observed in the present experiments. Absorption bands at ca. 1930, 1950, and 2051 cm^{-1} (marked with asterisks in Figure 7.3) are assigned to CO-loss products, while the absorption band at 1989 cm^{-1} is assigned to the 17e species $\text{Re}(\text{CO})_5$. We attribute the spectral changes with delay time to solvation of CO-loss complexes and geminate recombination, but no 19e species are observed on the picosecond timescale. Were a 19e complex to form, we would expect to see the growth of a new product band red-shifted from the band at 1989 cm^{-1} , along with significant decay of the band at 1989 cm^{-1} corresponding to the 17e $\text{Re}(\text{CO})_5$ photoproduct. Since this peak decays slightly on the picosecond timescale, but no other product peaks are formed, we attribute the decay of this band to overlap with a band of the unsolvated CO-loss complex, which redshifts upon solvent coordination.

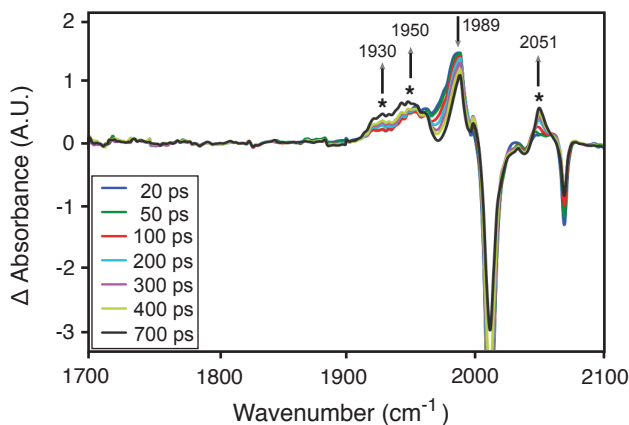


Figure 7.3. TRIR spectra of $\text{Re}_2(\text{CO})_{10}$ following 267 nm photolysis in 1:4 molar $\text{P}(\text{OMe})_3:\text{CH}_2\text{Cl}_2$ solution. Asterisks denote absorptions due to the CO-loss product $\text{Re}_2(\text{CO})_9$.

Considering that the mechanism for ultrafast in cage disproportionation (Figure 7.1A) relies on the formation of 19e adducts, and that no 19e adducts are observed, it is not surprising that disproportionation products are also not observed to form. This lack of reactivity is in contrast to that reported previously for $\text{CpW}(\text{CO})_3$ radicals in the same solvent, which readily coordinate $\text{P}(\text{OMe})_3$ to form a 19e species and establish a 17e/19e equilibrium on the picosecond timescale. Since previous studies have shown that both $\text{Mn}(\text{CO})_5$ and $\text{Re}(\text{CO})_5$ coordinate phosphines, phosphites, and other ligands via an associative mechanism proceeding through a 19e intermediate,^{176–180} the lack of reactivity of these 17e complexes on the picosecond timescale implies that an energetic barrier to coordination of $\text{P}(\text{OMe})_3$ may exist. While unexpected, this would not be a terribly surprising result when considering that previous studies have demonstrated rates of associative ligand substitution reactions to 17e complexes to span a wide range and depend heavily on the identity of the metal center.^{189,190} Of course, it is also possible that an equilibrium between the $\text{M}(\text{CO})_5$ and $\text{M}(\text{CO})_5\text{P}(\text{OMe})_3$ adducts is established rapidly, but that it strongly favors the 17e species, such that the 19e adducts are formed in such low yields that they cannot be detected. Since the 19e intermediate is needed to generate the disproportionation product, this would also explain the lack of observed disproportionation products.

7.3.2 Reactivity of $\text{CpFe}(\text{CO})_2$ and $\text{CpRu}(\text{CO})_2$ Radicals

$[\text{CpFe}(\text{CO})_2]_2$ has been shown to undergo thermal and photochemical disproportionation in the presence of phosphines and phosphites,^{109,191} and these early experiments played a role in developing the mechanism shown in Figure 7.1C. The disproportionation chemistry of $[\text{CpRu}(\text{CO})_2]_2$ has been reported to be similar to that of the iron congener.¹⁹² TRIR spectra of $[\text{CpFe}(\text{CO})_2]_2$ have been reported on the femtosecond though microsecond timescales, and 400 nm photolysis leads to the formation of 17e $\text{CpFe}(\text{CO})_2$ radicals, as well as a triply bridged CO-loss complex, $\text{Cp}_2\text{Fe}_2(\mu\text{-CO})_3$.^{193–195} The photochemistry of $[\text{CpRu}(\text{CO})_2]_2$ has been investigated previously by flash photolysis and continuous irradiation experiments in solution^{120,135,136} and by continuous irradiation in frozen matrices.¹³⁵ Density functional theory calculations^{119,135} have also been used to study this complex and its derivatives.

TRIR spectra of each of these dimers in 1:4 molar $\text{P}(\text{OMe})_3:\text{CH}_2\text{Cl}_2$ solution were collected as part of a recent study on the observation of a bent CO-ligand in the 19e $\text{CpRu}(\text{CO})_2\text{P}(\text{OMe})_3$ adduct,¹⁶¹ and we reproduce them here to discuss their implications for in-cage radical disproportionation. In these spectra, the formation of 19e adducts (in an equilibrium with the corresponding 17e species) was observed on the picosecond timescale, but no disproportionation products were observed. We will briefly revisit these results here.

Figure 7.4A shows the TRIR spectra of $[\text{CpFe}(\text{CO})_2]_2$ collected following 400 nm photolysis in 1:4 $\text{P}(\text{OMe})_3:\text{CH}_2\text{Cl}_2$ solution. Positive absorptions at 1918 and 1998 cm^{-1} correspond to 17e $\text{CpFe}(\text{CO})_2$, and these decay with the concomitant rise of absorptions at 1895 and 1954 cm^{-1} (rise time of 315 ± 38 ps for the 1895 cm^{-1} band), assigned to the 19e complex $\text{CpFe}(\text{CO})_2\text{P}(\text{OMe})_3$. The weak positive absorption at ca. 1820 cm^{-1} is assigned to the triply-bridged CO-loss product $\text{Cp}_2\text{Fe}_2(\mu\text{-CO})_3$. In these spectra, we observe no evidence indicating the formation of disproportionation products. If disproportionation products were to form, we would at least one additional band at a frequency lower than that of the antisymmetric stretching mode of $\text{CpFe}(\text{CO})_2\text{P}(\text{OMe})_3$ (which would correspond to the anionic product), as well as at least one absorption at a frequency higher than that of the symmetric stretching mode of $\text{CpFe}(\text{CO})_2$ (which would correspond to the cationic disproportionation product). These expected frequency regimes are based on comparisons to previous experiments on the $[\text{CpW}(\text{CO})_3]_2$ dimer, as well as to present results on the $[\text{CpMo}(\text{CO})_3]_2$ dimer (*vide infra*).

TRIR spectra of $[\text{CpRu}(\text{CO})_2]_2$ in 1:4 $\text{P}(\text{OMe})_3:\text{CH}_2\text{Cl}_2$ solution are shown in Figure 7.4B. Absorptions at 1930 and 2003 cm^{-1} , assigned to 17e $\text{CpRu}(\text{CO})_2$, decay with the concomitant rise of new absorptions at 1810 and 1959 cm^{-1} (rise time of 192 ± 16 ps for the 1959 cm^{-1} band),¹⁶¹ which were assigned to 19e $\text{CpRu}(\text{CO})_2\text{P}(\text{OMe})_3$. Our recent investigation into the unusually low frequency of the antisymmetric stretching mode at 1810 cm^{-1} demonstrated that this low frequency can be attributed to the presence of a bent CO ligand.¹⁶¹ Similar to the situation with the iron congener, we observe no evidence indicating the formation of disproportionation products in these spectra.

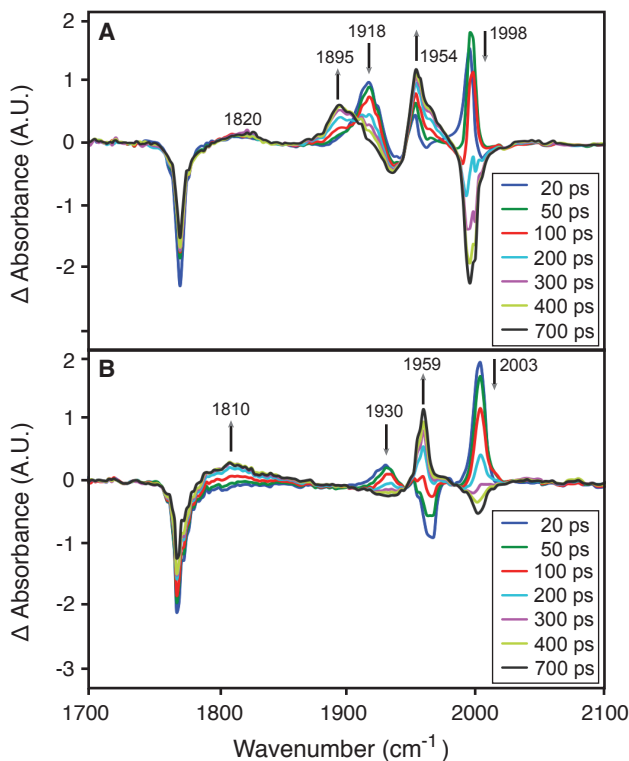


Figure 7.4. TRIR spectra of $[\text{CpFe}(\text{CO})_2]_2$ (Panel A) and of $[\text{CpRu}(\text{CO})_2]_2$ (Panel B) following 400 nm photolysis in 1:4 molar $\text{P}(\text{OMe})_3:\text{CH}_2\text{Cl}_2$ solution.

The CO ligand presumably distorts to a bent conformation in order to distribute charge away from the metal center, and thus this 19-electron adduct is best described as an $18 + \delta$ complex. The lowered charge density at the metal center may explain its poorer ability to act as a reducing agent, relative to the 19e tungsten complex, $\text{CpWCO}_3\text{P}(\text{OMe})_3$, studied previously.^{138,139}

Interestingly, reports have indicated that $\text{CpFe}(\text{CO})_2\text{L}$ ($\text{L} = \text{CO}, \text{PPh}_3$) complexes adopt an η^4 coordination geometry for the Cp ligand, thus displacing the radical electron density onto the Cp ring.^{141,142} For this reason, it seems likely that $\text{CpFe}(\text{CO})_2\text{P}(\text{OMe})_3$ may similarly redistribute charge away from the metal center onto the Cp ring, making it a poorer reducing agent. The fact that $\text{CpFe}(\text{CO})_2\text{P}(\text{OMe})_3$ does not undergo disproportionation on the picosecond timescale is, itself, evidence that this species is a poorer reducing agent than the 19e $\text{CpW}(\text{CO})_3\text{L}$ ($\text{L} = \text{PPh}_3, \text{P}(\text{OMe})_3, \text{PBu}_3$) complexes with which the in-cage mechanism was originally observed. Delocalization of the 19th electron onto the Cp ring would seem to provide the most likely explanation for the lack of disproportionation reactivity in this case.

7.3.3 Reactivity of $\text{CpMo}(\text{CO})_3$ Radicals

As described in the introduction, the disproportionation reactivity of $[\text{CpMo}(\text{CO})_3]_2$, as well as its chromium and tungsten congeners, has been studied previously.¹⁶²⁻¹⁶⁵ These experiments led to the proposal of the disproportionation mechanism shown in Figure 7.1C. In polar solvents, $[\text{CpMo}(\text{CO})_3]_2$ exists as a mixture of trans and gauche isomers, with no bridging carbonyls present in either structure.^{196,197} The nanosecond TRIR spectra of $[\text{CpMo}(\text{CO})_3]_2$ have been reported previously in *n*-heptane solution following 532 nm excitation.^{198,199} 532 nm photolysis

leads to the formation of 17e $\text{CpMo}(\text{CO})_3$ radicals, with no evidence for the formation of CO-loss products.^{198–201}

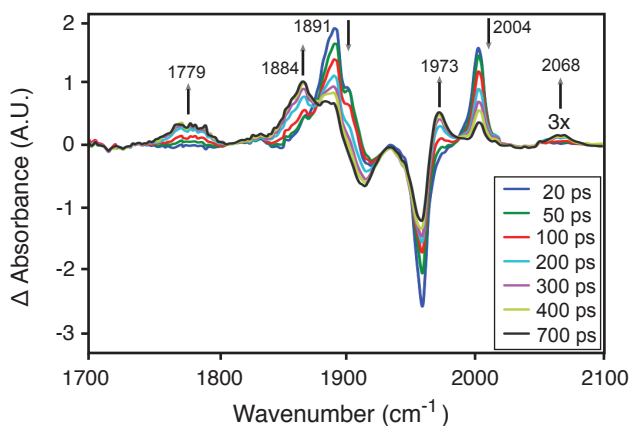


Figure 7.5. TRIR spectra of $[\text{CpMo}(\text{CO})_3]_2$ following 400 nm photolysis in 1:4 molar $\text{P}(\text{OMe})_3:\text{CH}_2\text{Cl}_2$ solution.

Figure 7.5 shows the TRIR spectra of $[\text{CpMo}(\text{CO})_3]_2$ collected following 400 nm photolysis in 1:4 molar $\text{P}(\text{OMe})_3:\text{CH}_2\text{Cl}_2$ solution. These spectra are similar to those obtained previously for $[\text{CpW}(\text{CO})_3]_2$ in the same solvent.^{138,139} Photoproduct absorptions at 1891 and 2004 cm^{-1} are assigned to the 17e species $\text{CpMo}(\text{CO})_3$. These decay with the concomitant rise of absorptions at 1884 and 1973 cm^{-1} , assigned to the 19e species $\text{CpMo}(\text{CO})_3\text{P}(\text{OMe})_3$. A decay constant of 196 ± 5 ps is observed for the band at 2004 cm^{-1} , and a rise time of 184 ± 8 ps is observed for the absorption at 1973 cm^{-1} , suggesting that the two species are kinetically correlated. An isosbestic point is also observed at ca. 1877 cm^{-1} .

Absorptions at ca. 1779 and 2068 cm^{-1} are also observed to grow in with time constants of 193 ± 11 and 299 ± 67 ps, respectively. The broad lower frequency band at ca. 1779 cm^{-1} is assigned to the anionic disproportionation product, $\text{CpMo}(\text{CO})_3^-$, while the higher frequency band at 2068 cm^{-1} is assigned to the cationic disproportionation product, $\text{CpMo}(\text{CO})_3\text{P}(\text{OMe})_3^+$ (the intensity of this absorption has been magnified by a factor of 3 for visualization purposes). Note that these absorptions should exhibit identical rise times, as they correspond to products formed simultaneously in the same chemical process. The lower intensity of the 2068 cm^{-1} absorption makes it difficult to obtain a quality fit, so we feel the rise time for the band at 1779 cm^{-1} likely provides the most accurate time constant that we can offer for this process. The anionic product has been observed previously in pyridine solution and displays a similar absorption frequency (1770 cm^{-1} in pyridine), as well as another at 1895 cm^{-1} , which likely overlaps with the 1891 cm^{-1} band of $\text{CpMo}(\text{CO})_3$ in the present study.^{185,202} The observed frequencies for these species are consistent with those observed for the analogous disproportionation products with the tungsten analogue.

Table 7.1. Experimentally observed vibrational frequencies for each photoproduct in 1:4 molar P(OMe)₃:CH₂Cl₂ solution.

Complex	e ⁻ count	Observed Frequency (cm ⁻¹)
Mn(CO) ₅	(17e)	1985
Re(CO) ₅	(17e)	1989
CpFe(CO) ₂	(17e)	1918, 1998
CpFe(CO) ₂ P(OMe) ₃	(19e)	1895, 1954
CpRu(CO) ₂	(17e)	1930, 2003
CpRu(CO) ₂ P(OMe) ₃	(19e)	1810, 1959
CpMo(CO) ₃	(17e)	1891, 2004
CpMo(CO) ₃ P(OMe) ₃	(19e)	1884, 1973
CpMo(CO) ₃ ⁻	(18e)	1779
CpMo(CO) ₃ P(OMe) ₃ ⁺	(18e)	2068

To our knowledge, the cationic disproportionation product, CpMo(CO)₃P(OMe)₃⁺, has not previously been characterized, so DFT calculations were used to predict its vibrational frequencies. Using the BP86 functional, bands are predicted at 1988, 2002, and 2056 cm⁻¹ (see Table 7.2). Assuming that the band predicted at 2056 cm⁻¹ corresponds to that observed experimentally at 2068 cm⁻¹, the lower frequency bands likely overlap with those of the 17e and/or 19e photoproducts. DFT calculations were similarly carried out on the anionic product for the purpose of comparing the oscillator strengths predicted for the absorptions monitored experimentally. The calculated vibrational frequencies and intensities are listed in Table 7.2. Note that two degenerate bands are predicted at 1806 cm⁻¹, which correspond to the band observed experimentally at 1779 cm⁻¹. The calculated intensities, after summing those for the degenerate modes at 1806 cm⁻¹, predict the absorption observed experimentally at 1779 cm⁻¹, corresponding to the anionic product, to be ca. 4.7 times stronger than that of the cationic product at 2068 cm⁻¹. Considering that these are gas phase calculations, the calculated intensities seem to agree, at least qualitatively speaking, with those observed experimentally.

Table 7.2. Calculated vibrational frequencies and intensities for photoproducts arising from photolysis of [CpMo(CO)₃]₂.

Complex	e ⁻ count	Calculated Frequencies (cm ⁻¹) and intensities (km/mol)
CpMo(CO) ₃	(17e)	1913 (1242), 1916 (802), 1989 (626)
CpMo(CO) ₃ P(OMe) ₃	(19e)	1886 (954), 1901 (743), 1972 (883)
CpMo(CO) ₃ ⁻	(18e)	1806 (1293), 1806 (1307), 1894 (764)
CpMo(CO) ₃ P(OMe) ₃ ⁺	(18e)	1988 (967), 2002 (395), 2056 (549)

7.3.4 Comparison to Previous Ultrafast Disproportionation Studies

The most striking result of this study is that the in-cage disproportionation mechanism previously observed following photolysis of [CpW(CO)₃]₂ in P(OMe)₃/CH₂Cl₂ solution does not occur for four out of the five complexes investigated. Only the molybdenum congener of the [CpW(CO)₃]₂ dimer reacts according to the in-cage disproportionation mechanism under the conditions tested.

As mentioned in section IIIA, the fact that 17e $\text{Mn}(\text{CO})_5$ and $\text{Re}(\text{CO})_5$ radicals do not form 19e complexes via coordination of $\text{P}(\text{OMe})_3$ as a ligand on the picosecond timescale suggests that either an energetic barrier exists for coordination of a $\text{P}(\text{OMe})_3$ ligand to these complexes, or that the 17e/19e equilibrium heavily favors the 17e species. Given that no 19e photoproducts are observed, it is not surprising that disproportionation products do not form on the picosecond timescale, since the in cage mechanism requires a 19e complex as the reducing agent in the disproportionation reaction.

$\text{CpFe}(\text{CO})_2$ and $\text{CpRu}(\text{CO})_2$ behave similarly in that both 17e radicals do coordinate $\text{P}(\text{OMe})_3$ as a ligand on the picosecond timescale, but neither of the corresponding 17e/19e radical pairs is observed to undergo in-cage disproportionation. A recent study by us¹⁶¹ into the structure of $\text{CpRu}(\text{CO})_2\text{P}(\text{OMe})_3$ provides evidence for why this 19e complex is unlikely to serve as a strong reducing agent; the excess charge from the metal center delocalizes onto a CO ligand, weakening the capacity for this complex to behave as a reducing agent. Previous studies on the iron congener have suggested that $\text{CpFe}(\text{CO})_2\text{L}$ complexes adopt an η^4 Cp coordination geometry, similarly delocalizing excess charge away from the metal center. The fact that neither of these complexes is expected to genuinely have a 19e configuration at the metal center provides the most likely explanation for why these species are not strong enough reducing agents to participate in disproportionation reactions on the picosecond timescale.

The only complex for which photolysis led to disproportionation on the picosecond timescale was $[\text{CpMo}(\text{CO})_3]_2$. The results were very similar to those observed in previous studies on $[\text{CpW}(\text{CO})_3]_2$. We infer that both the $\text{CpMo}(\text{CO})_3\text{P}(\text{OMe})_3$ and $\text{CpW}(\text{CO})_3\text{P}(\text{OMe})_3$ 19e adducts have sufficient 19e character at metal to behave as a reducing agent on the picosecond timescale. Similar to the results observed for the tungsten photoproducts, the formation of in-cage molybdenum disproportionation products is complete within the first few hundred picoseconds; decay of the 17e and 19e species does not continue significantly at later delay times, demonstrating that their diffusion apart limits the timescale over which the in-cage disproportionation mechanism can operate. As was discussed in the existing studies on the tungsten dimer, the timescale of ca. 200 ps for formation of the disproportionation products thus corresponds to the timescale for diffusion of the nascent 17e/19e radical pair out of the solvent cage. This timescale determines the extent to which disproportionation can occur on the picosecond timescale. Previous infrared spectroelectrochemical studies observed that the electrochemical and spectroscopic characteristics of $[\text{CpMo}(\text{CO})_3]_2$ are nearly identical to those of $[\text{CpW}(\text{CO})_3]_2$,²⁰³ which is consistent with the results observed in the present study.

Taking all of the available data into account, membership in the same periodic group appears to provide the best predictor of reactivity toward the formation of 19e products and disproportionation on the picosecond timescale. A previous study by Tyler et al. investigated whether a heavy atom effect could be observed in a study on geminate recombination of 17e $\text{CpFe}(\text{CO})_2$ and $\text{CpMo}(\text{CO})_3$ radicals, and found no evidence for a spin barrier to recombination.²⁰⁴ In the present study, we observe no clear trends in reactivity for metal centers of differing atomic number, supporting the notion that spin barriers also do not play a role in the tendency of these 17e/19e pairs to undergo disproportionation. While there is only limited evidence in this study to further support this assertion, spin state changes frequently play an important role in the reactivity of transition metal complexes, so we feel this is an important point to consider.

7.4 Conclusions

In this paper we have reported an investigation into the picosecond photochemical disproportionation reactivity of several transition metal dimers in the presence of the Lewis base $\text{P}(\text{OMe})_3$. Our observations indicate that the reactivity of the 17e photoproducts studied follows periodic trends in terms of their tendency to form 19e products and to undergo disproportionation reactions. Interestingly, the in-cage disproportionation mechanism, originally reported in photochemical studies on the $[\text{CpW}(\text{CO})_3]_2$ dimer, does not take place with four of the five transition metal dimers studied. The results demonstrate that in-cage disproportionation can only occur in cases where both 19e product formation (in significant quantities) and electron transfer are fast, relative to diffusion of the nascent radical photoproducts.

The observations made with regard to in-cage disproportionation carry implications for the initiation of radical chain reactions catalyzed by transition metal dimers in the presence of Lewis bases.^{205–209} The in-cage mechanism serves as an early termination step to a radical chain pathway, implying that those transition metal dimers which do not undergo in-cage disproportionation may serve as better initiators of radical chain pathways. This is a somewhat counterintuitive notion, since the factors that promote in-cage disproportionation (i.e. the facile formation of 19e adducts, and, in particular, 19e adducts that are strong reducing agents) are the same factors one might expect to promote an efficient radical chain pathway. We should also point out that delocalized $18 + \delta$ adducts are likely to be inefficient initiators of these reactions, and that many radical pathways can be efficiently initiated by 17e photoproducts in non-coordinating solvents (in the absence of a Lewis base).

The results of this study reveal that in-cage disproportionation may, in fact, be a relatively uncommon process, emphasizing the importance of other disproportionation pathways, such as those shown in Figures 7.1B and 7.1C. Future work will focus on elucidating the role of the Lewis base on the strength of the 19e reducing agent formed in these reactions.

8 Reactivity of the TEMPO Radical Toward 16- and 17-Electron Organometallic Reaction Intermediates

The following chapter is reproduced (adapted) in part with permission from (Lomont, J. P.; Nguyen, S. C.; Harris C. B. *J. Am. Chem. Soc.* 2013, 135, 11266-11273.). Copyright (2013) American Chemical Society.

8.1 Introduction

(2,2,6,6-tetramethylpiperidin-1-yl)oxyl (TEMPO) is a stable nitroxyl radical with a remarkably broad range of applications in chemistry, including numerous examples in the field of organometallic catalysis. TEMPO is a popular reagent for the oxidation of alcohols,²¹⁰⁻²¹⁴ and TEMPO-based catalysts have been employed for various industrial applications, often with environmental and health benefits over alternative methods.^{215,216} Further applications of TEMPO include catalysis of the Pauson-Khand reaction,²¹⁷ oxidative couplings of arenes,²¹⁸ nitration of olefins,²¹⁹ and the synthesis of monodisperse cobalt oxide nanoparticles.²²⁰ TEMPO is also commonly used as a radical trap and polymerization reagent²²¹⁻²²⁹ and as a structural probe of biological systems via EPR measurements.²³⁰⁻²³⁵

The behavior of TEMPO as a ligand is a topic of significant interest, as its bonding and reactivity carry mechanistic implications for the myriad of chemical processes mentioned above. Literature reports have established three distinct modes of coordination of TEMPO to individual metal centers (see Figure 8.1), as well as additional examples involving TEMPO as a bridging ligand between pairs of metal centers,²³⁶ demonstrating that its behavior as a ligand is as varied as its chemical applications. In the present study, we use picosecond time-resolved infrared (TRIR) spectroscopy to directly characterize the reactivity of TEMPO as a ligand toward coordinatively unsaturated 16-electron (16e) and 17-electron (17e) organometallic photoproducts, which are representative of commonly encountered intermediates in organometallic reaction mechanisms. Our observations make use of the structurally sensitive CO-stretching frequencies of the metal-carbonyl photoproducts to monitor the reaction with TEMPO.

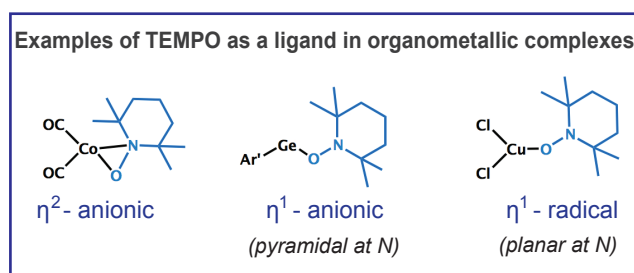


Figure 8.1. Representative examples of coordination geometries for TEMPO adducts

TEMPO may coordinate to individual metal centers with either η^1 or η^2 hapticity, with two possibilities for the electronic structure of the η^1 coordinated TEMPO ligand. η^1 TEMPO ligands

may either effectively undergo an internal oxidation-reduction process with the metal center, resulting in an anionic TEMPO ligand, or they may behave as radical 1e donors, with no oxidation/reduction taking place.²³⁶⁻²⁴² This distinction is more than a mere issue of electron counting, as the two situations result in clearly distinguishable bonding geometries at the nitroxyl nitrogen atom; anionic TEMPO ligands are characterized by a nitrogen atom that adopts a pyramidal geometry, while the radical TEMPO ligand maintains a planar geometry about the nitrogen center. These differences have been established by characterization of the crystal structures of various TEMPO adducts involving metals including Li, Na, Mg,²³⁶ Ti,^{237,239} Ga,²³⁸ Pd,²⁴⁰ Cu,^{241,242} Fe,²⁴³ and Al.^{238,243} Examples of η^2 coordinated TEMPO adducts include the 16-electron (16e) complexes (TEMPO)Co(CO)₂ and (TEMPO)Mn(CO)₃, or the 14-electron (14e) complex (TEMPO)V(CO)₃, which are formed via reactions with Co₂(CO)₈,²⁴⁴⁻²⁴⁶ Mn₂(CO)₁₀,²⁴⁷ or V(CO)₆ (a 17e complex),²⁴⁸ respectively. The reactions with metal carbonyl dimers presumably proceed via homolysis of the metal-metal bond.

While the mechanisms of TEMPO catalyzed oxidation reactions have been studied by several authors,²⁴⁹⁻²⁵² the coordination chemistry of TEMPO has been much less thoroughly investigated, and many key reaction intermediates have never been directly observed. There still remains substantial debate in the literature regarding the mechanism of alcohol oxidations.^{241-243,253-257} At present, there exist no clear rules for predicting the nature of coordination of a TEMPO ligand in a given complex. In this study, we use ultrafast TRIR spectroscopy to directly characterize the adducts formed following the reaction of TEMPO with coordinatively unsaturated 16e and 17e metal carbonyl reaction intermediates in solution. Density functional theory calculations are used to facilitate interpretation of the experimental results. Metal carbonyl complexes represent one of the most widely used classes of organometallic reagents and catalysts, and thus the reactivity of TEMPO toward these species is broadly relevant to chemists working with this increasingly popular, coordinatively versatile reagent. For each of the 16e and 17e intermediates studied, TEMPO coordination is observed to take place with concomitant oxidation of the metal center, yielding adducts containing anionic TEMPO ligands. No other ligand substitutions or distortions are observed. The similar reactivity of TEMPO with each of the intermediates studied suggests that these observations are representative of TEMPO's reactivity toward low-valent transition metal complexes in general.

8.2 Methods

8.2.1 Sample Preparation

CpCo(CO)₂, Fe(CO)₅, [CpFe(CO)₂]₂, Mn₂(CO)₁₀, (2,2,6,6-tetramethylpiperidin-1-yl)oxyl (TEMPO), and cyclohexane were purchased from Sigma-Aldrich Co. All samples and solvents were used without further purification. Dilute solutions of all samples were stable in air at ambient temperatures for at least a few hours (verified via FTIR).

8.2.2 Data Analysis

Kinetic data in this work result from spectra measured at delay times between 0 and 1000 ps between the visible-pump and IR-probe pulses. Kinetic traces for each spectral feature were obtained by integrating a narrow spectral region (ca. 5 cm⁻¹ wide) surrounding the reported

frequency. The kinetic data were then fit to exponential curves using Origin Pro 8 software. Errors on experimental time constants are reported as 95% confidence intervals.

8.2.3 Density Functional Theory Modeling

Density functional theory (DFT) calculations have been carried out to facilitate assignment of the absorptions observed in the TRIR spectra. Calculations were carried out using the BP86,^{37,38} B3LYP,^{37,39} M06,¹²⁶ PBE0,^{258–260} PW91,^{40–42} and WB97¹²⁷ functionals in the Gaussian09⁴³ package using the 6-311+g(d,p) basis^{261–264} for all atoms. Geometry optimizations were followed by a frequency analysis for use in interpreting the TRIR results and to ensure that all geometries were genuine local minima. As DFT methods are known to have difficulties accurately predicting bond enthalpies for TEMPO and other radicals, we use only the calculated frequencies in interpreting the experimental observations.^{265–269}

8.3 Results and Discussion

TRIR spectra in the CO stretching region are presented as difference absorbance spectra. Positive absorptions correspond to newly formed species, while negative bands correspond to the depletion of parent molecules. Data were collected using 400 nm excitation, as initial experiments indicated that the relative absorption cross sections of TEMPO and the metal carbonyl species, combined with the weaker 267 nm pump power, rendered collection of quality TRIR spectra at the 267 nm excitation wavelength infeasible (see SI for the UV-Vis spectrum of TEMPO in cyclohexane solution).

8.3.1 Ultrafast reactivity of TEMPO toward 16-electron photoproducts

Beginning from a stable 18e organometallic complex, thermal or photochemical dissociation of a 2e ligand leads to the formation of a relatively reactive 16e species. In this study, we have characterized the reactivity of the TEMPO radical toward the 16e CpCo(CO) and Fe(CO)₄ photoproducts, which serve as representative examples of 16e intermediates in organometallic reaction mechanisms. The literature contains ample reports on the reactivity of these prototypical 16e photoproducts, which facilitates interpretation of the experimental results in cyclohexane/TEMPO solution. Spectra were collected at varied TEMPO concentrations; the spectra collected at lower TEMPO concentrations generally yielded better signal-to-noise, and here we present spectra collected at concentrations that allow clear visualization of the conversion of each photoproduct to the corresponding TEMPO adduct, while maintaining quality signal-to-noise ratios.

Reactivity of TEMPO toward CpCo(CO)

In alkane solution, 400 nm photolysis of CpCo(CO)₂ leads to formation of ³CpCo(CO), characterized by its absorption band at 1989 cm⁻¹, along with excitation into an electronically excited state of the parent molecule that relaxes completely within the first 100 ps. Figure 8.2 shows TRIR spectra of CpCo(CO)₂ collected following 400 nm excitation in a 0.16 M solution of TEMPO in cyclohexane solvent. At early delay times (see 5 ps spectrum), the positive features in the spectra are dominated by broad absorption bands due to the electronically excited

parent complex. The negative bleaches at 1967 and 2029 cm^{-1} correspond to depletion of the parent $\text{CpCo}(\text{CO})_2$ complex. The band at 1989 cm^{-1} , corresponding to $^3\text{CpCo}(\text{CO})$, decays with a time constant of 274 ± 32 ps ($k_{\text{bimol}} = 2.3 \times 10^{10} \text{ M}^{-1}\text{s}^{-1}$), with the concomitant rise of a new band at 2025 cm^{-1} , attributed to the TEMPO adduct. Data collected at higher TEMPO concentrations (e.g. 0.32 M TEMPO) shows complete conversion of $^3\text{CpCo}(\text{CO})$ at a 1 ns delay time.

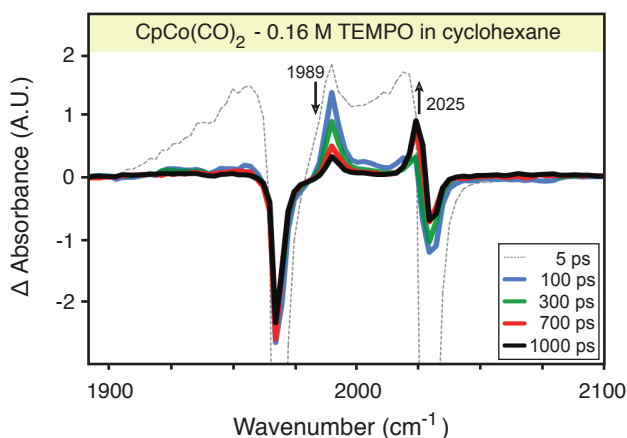


Figure 8.2. TRIR spectra of $\text{CpCo}(\text{CO})_2$ in 0.16 M TEMPO/cyclohexane solution following 400 nm photolysis.

It is noteworthy that this new CO absorption band is at a higher frequency than that of $^3\text{CpCo}(\text{CO})$; coordination of a solvent molecule as a token ligand to $\text{CpCo}(\text{CO})$ typically results in a decreased CO stretching frequency for the lone carbonyl ligand, presumably due to increased pi-backbonding from the Co center.^{23,25,35,270,271} In the spectra shown in Figure 8.2, we interpret the increase in CO-stretching frequency to suggest a decrease in pi-backbonding to the CO ligand upon coordination of the TEMPO ligand, suggesting a decrease in electron density at the Co center.

As was mentioned in the introduction, TEMPO can coordinate to a single metal center with either η^1 or η^2 hapticity, with either an anionic or radical electronic configuration in the η^1 geometry. To coordinate to 16e $\text{CpCo}(\text{CO})$ with an η^2 geometry and not exceed an 18e count at the metal center, either the carbonyl ligand would have to dissociate, or the Cp ring would have to distort. Considering that the observed TEMPO adduct clearly contains a CO ligand, and that the observation of a stable a ring-slipped product in the solution phase would be exceedingly rare,⁹⁰ we conclude an η^1 coordination geometry for TEMPO. Of the two possibilities for η^1 coordination, only the anionic coordination mode would be expected to reflect an oxidation of the metal center, consistent with the relatively high frequency of the IR absorption band observed for the $\text{CpCo}(\text{CO})(\text{TEMPO})$ adduct. This strongly suggests that the TRIR results indicate an anionic TEMPO ligand. Density functional theory (DFT) calculations were carried out to further investigate the structure of this adduct.

Geometry optimizations and frequency calculations were carried out using six DFT functionals (see Table 8.1), including both hybrid and pure density functionals. Previous investigations into the ability of various DFT functionals to accurately predict the difference in energy between the singlet and triplet states for 16e $\text{CpCo}(\text{CO})$ have demonstrated that pure density functionals (e.g. BP86 or PW91) are better able to predict this energy gap.^{25,35,270,271}

Upon coordination of the doublet TEMPO ligand to $^3\text{CpCo}(\text{CO})$, our results suggest that a doublet ground state is favored by 8 to 20 kcal/mol, relative to a quartet.

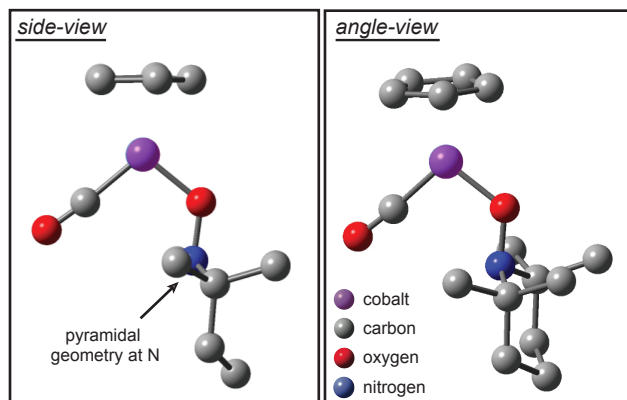


Figure 8.3. DFT (B3LYP) calculated structure for the $\text{CpCo}(\text{CO})(\text{TEMPO})$ adduct (H-atoms omitted for clarity).

Geometry optimizations indicate that TEMPO coordinates to the metal center in a η^1 fashion (see Figure 8.3), consistent with our aforementioned reasoning. As discussed in the introduction, previous work has established that anionic TEMPO ligands are characterized by a pyramidal geometry at the nitroxyl nitrogen, while a radical TEMPO ligand maintains a planar geometry at the nitrogen center. With each functional tested, the nitrogen atom of the $\text{CpCo}(\text{CO})(\text{TEMPO})$ adduct clearly adopts a pyramidal geometry, indicating the presence of an anionic TEMPO ligand. The sum of the bond angles about the nitrogen atom is 336.1° (B3LYP value). For comparison, calculations on the free (non-metal-coordinated) TEMPO ligand were also carried out, and each functional also correctly predicts a nearly planar geometry for the free TEMPO radical. Reduction of the TEMPO ligand, and thus oxidation of the Co center, is consistent with the experimentally observed blue-shift in the CO stretching frequency upon TEMPO coordination; whereas coordination of most 2e donor ligands results in a decrease in the experimentally observed CO stretching frequency, the fact that coordination of TEMPO results in an increase in the CO stretching frequency suggests decreased pi-backbonding from the Co center to the CO ligand.

Table 8.1. Experimental and calculated frequency shifts upon coordination of TEMPO (nitroxyl group) to $^3\text{CpCo}(\text{CO})$. Previous results for coordination of 1-butanol are provided for comparison.

Functional	$\Delta\nu_{\text{TEMPO}}^{\text{a}}$ (cm^{-1})	$\Delta\nu_{\text{Butanol,si}}^{\text{a}}$ nglet^{a} (cm^{-1})	$\Delta\nu_{\text{Butanol,tri}}^{\text{a}}$ plet^{a} (cm^{-1})
B3LYP	22	-59	-35
BP86	5	-43	-36
M06	23	-56	-36
PBE0	48	-56	-37
PW91	5	-43	-37
WB97	36	-66	-42
Experiment:	36	-73	-42

(a) Calculated frequency shifts are reported relative to the CO-stretching frequency calculated for $^3\text{CpCo}(\text{CO})$. No scaling factors were used.

Indeed, the calculated CO-stretching frequencies predict an increase in CO-stretching frequency upon coordination of TEMPO (Table 8.1). For comparison, the analogous experimental and calculated values are also shown for both the singlet and triplet 1-butanol-coordinated adducts observed in a previous study;³⁵ these are provided to demonstrate the ability of DFT calculations to reproduce experimentally observed changes in CO-stretching frequencies. While these calculated frequency shifts are not expected to be quantitatively accurate, it is striking that the changes in experimentally observed CO-stretching frequencies upon coordination to TEMPO and 1-butanol are qualitatively well-reproduced by the DFT calculations. These calculated frequencies, in conjunction with the experimental results and calculated geometries, support assignment of TEMPO in the CpCo(CO)(TEMPO) adduct as an anionic TEMPO ligand (refer to Figure 8.1), effectively resulting in a Co(II) complex. As was mentioned earlier, the simple fact that the experimental CO stretching frequency increases upon coordination of TEMPO provides strong, stand-alone evidence that TEMPO has oxidized the metal center. The good agreement between calculation and experiment in this spectroscopically straightforward adduct (i.e. containing a single CO oscillator) supports the notion that DFT methods are useful for predicting the behavior of TEMPO as it reacts with coordinatively unsaturated organometallic intermediates.

Reactivity of TEMPO toward Fe(CO)₄

Photolysis of Fe(CO)₅ at 400 nm in cyclohexane solution leads to formation of ³Fe(CO)₄, characterized by absorption bands at 1965 and 1987 cm⁻¹, along with a small amount of ¹Fe(CO)₄(cyclohexane), characterized by absorption bands at 1950, 1970, and 1986 cm⁻¹.³⁰ TRIR spectra of Fe(CO)₅ collected following 400 nm excitation in a 0.32 M solution of TEMPO in cyclohexane solvent are shown in Figure 8.4. A higher concentration of TEMPO was used in this case so that the conversion of photoproducts to TEMPO-coordinated adducts could be observed more clearly on the picosecond timescale. Bands at 1965 and 1987 cm⁻¹ decay with increasing decay time, accompanied by the growth of new bands at ca. 1985 and 2041 cm⁻¹, attributed to formation of an Fe(CO)₄(TEMPO) adduct; note that the band at 1987 cm⁻¹ appears to shift as it decreases in intensity due to its overlap with the band of the TEMPO adduct at 1985 cm⁻¹. The relatively static absorption band at 1949 cm⁻¹ is attributed to ¹Fe(CO)₄(cyclohexane). At a 0.32 M concentration of TEMPO, the rise time of the band at 2041 cm⁻¹ is 634 ± 102 ps (*k*_{bimol} = 4.9 × 10⁹ M⁻¹s⁻¹). Based on comparisons to previous time-resolved studies on Fe(CO)₄ photoproducts,³⁰ the TEMPO adduct may also have a weak absorption band near 1965 cm⁻¹ overlapping that of ³Fe(CO)₄. Multiple CO-dissociation processes can be ruled out, as the incident photon energy at 400 nm is too weak to lead directly to multiple CO-loss in the solution phase, and previous studies have examined the spectra of ligand induced multiple CO-loss for this photoproduct and the presence of the band at 2041 cm⁻¹ is inconsistent with such a process.²⁵

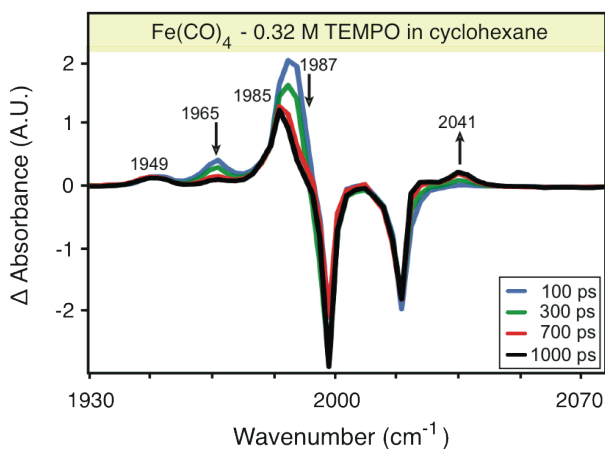


Figure 8.4. TRIR spectra of $\text{Fe}(\text{CO})_4$ in 0.32 M TEMPO/cyclohexane solution following 400 nm photolysis.

Changes in geometry and the coupling of local modes upon TEMPO coordination make it less straightforward to assign an oxidation state to the TEMPO ligand based purely on the experimental data than in the case of the $\text{CpCo}(\text{CO})(\text{TEMPO})$ adduct. However, it is useful to compare the present spectra to those observed in a previous solution phase study on $\text{Fe}(\text{CO})_4$ adducts formed with the 2e donor PET_3 , or with alcohol solvents.²⁵ For $\text{Fe}(\text{CO})_4\text{PET}_3$, the major CO-stretching absorptions are located at 1932 and 2047 cm^{-1} , and for $\text{Fe}(\text{CO})_4(\text{alcohol})$ these are located at 1950 and 2047 cm^{-1} . In each case, the lower frequency bands most likely correspond to an overlapping combination of the B_1 and B_2 bands, with the higher frequency band assigned to an A_1 mode. The notably higher frequency of the B_1/B_2 band (1985 cm^{-1}) in the TEMPO adduct may suggest that the Fe center is less able to effectively pi-backbond, though the similar frequencies of the A_1 modes in all three cases are not as conclusive. For this reason, DFT geometry optimizations and frequency calculations were also used to study the oxidation state of the TEMPO ligand in this adduct.

Table 8.2. Experimental and calculated frequency gap for the A_1 and B_1 modes of $^2\text{Fe}(\text{CO})_4(\text{TEMPO})$

Functional	$\Delta\nu$ [$A_1 - B_1$ modes] (cm^{-1})
B3LYP	54
BP86	65
M06	57
PBE0	55
PW91	67
WB97	54
Experiment:	55

Using each of the six functionals tested, the DFT calculated geometries show a pyramidal coordination geometry about the nitrogen center (sum of bond angles equal to 334.1° with B3LYP), indicating that TEMPO is reduced to an anionic ligand. To check for consistency with the experimentally observed IR spectra, frequency calculations were carried out. We have used the calculated frequency gap between the highest frequency CO-stretching (A_1) mode and the next highest frequency (B_1) mode to compare with the splitting between the experimentally observed bands (Table 8.2). As is evident from the values in Table 8.2, these calculated

frequency gaps are consistent with the gap observed experimentally, supporting assignment of the experimentally observed TEMPO adduct to anionic TEMPO ligand adduct. It is reassuring to note that all six functionals uniformly predict a distinctly pyramidal coordination geometry about nitrogen.

From these results, we thus conclude that both of the 16e photoproducts studied react to form adducts containing anionic TEMPO ligands (refer back to Figure 8.1), effectively increasing the oxidation state of the metal centers by one. The bimolecular rate constants demonstrate that the reactions between these 16e species and TEMPO occur at or near the diffusion limited rate.

8.3.2 Ultrafast reactivity of TEMPO toward 17-electron radicals

In addition to the 16e photoproducts described thus far, we also explored the reactivity of the TEMPO radical toward odd-electron reaction intermediates. Photolysis of $[\text{CpFe}(\text{CO})_2]_2$ and $\text{Mn}_2(\text{CO})_{10}$ at 400 nm readily yields the corresponding 17e radicals, which serve as representative examples of 17e intermediates in organometallic reaction mechanisms. Note that we have elected to present spectra at higher TEMPO concentrations for these 17-electron photoproducts, so that formation of the corresponding TEMPO adduct could be readily observed on the ultrafast timescale.

Reactivity of TEMPO toward $\text{CpFe}(\text{CO})_2$

In alkane solution, photolysis of $[\text{CpFe}(\text{CO})_2]_2$ at 400 nm leads to formation of 17e $\text{CpFe}(\text{CO})_2$ radicals, characterized by absorption bands at 1935 and 2006 cm^{-1} (which shift slightly in the data in 0.64 M TEMPO solution shown in Figure 8.5). A CO loss product, $\text{Cp}_2\text{Fe}_2(\mu\text{-CO})_3$ is also formed and shows an absorption band at 1820 cm^{-1} (not shown);¹⁴⁰ this species did not show dynamic changes with delay time. Figure 8.5 shows TRIR spectra of $[\text{CpFe}(\text{CO})_2]_2$ collected following 400 nm excitation in a 0.64 M solution of TEMPO in cyclohexane solvent. As the delay time increases, the bands at 1931 and 2003 cm^{-1} , corresponding to $\text{CpFe}(\text{CO})_2$ (shifted slightly from those in neat cyclohexane), decay with the concomitant rise of new bands at 1972 and 2020 cm^{-1} , assigned to a $\text{CpFe}(\text{CO})_2(\text{TEMPO})$ adduct. The fact that two bands are present in this adduct indicates that both CO ligands are still present. Note that the $\text{CpFe}(\text{CO})_2$ band at 2003 cm^{-1} overlaps a parent bleach band at ca. 2005 cm^{-1} , which is not readily visible due to overlap with the more intense positive band. At a 0.64 M concentration of TEMPO, formation of the TEMPO adduct is not substantially complete within the experimentally accessible time delays, indicating that formation of the TEMPO adduct from $\text{CpFe}(\text{CO})_2$ is notably slower than with either of the 16e photoproducts studied. It does not appear that an equilibrium is reached on the timescale studied, as the peaks continue to show dynamic changes at delay times >1000 ps. In addition to the observed frequencies themselves, the fact that dynamic changes continue to occur beyond the first ca. 200 ps rules out the possibility of recombination of the nascent fragments to incorporate a bridging TEMPO ligand, as previous studies have demonstrated that picosecond bimolecular reactions involving the fragments cease after diffusion out of the solvent cage, which is complete within the first ca. 200 ps.

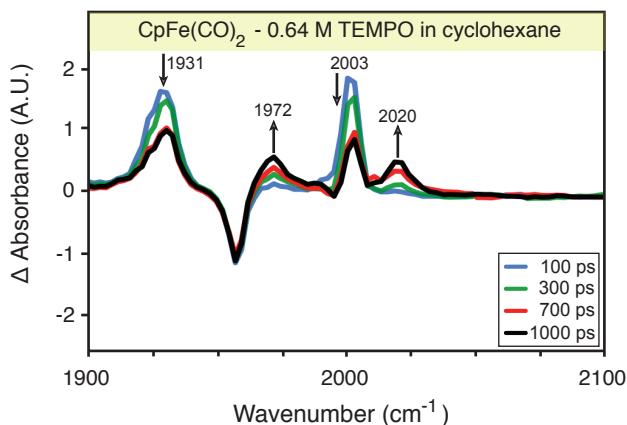


Figure 8.5. TRIR spectra of $\text{CpFe}(\text{CO})_2$ in 0.64 M TEMPO/cyclohexane solution following 400 nm photolysis.

Noting that both the frequencies of the symmetric and antisymmetric CO-stretching modes of the $\text{CpFe}(\text{CO})_2$ species increase upon coordination of the TEMPO ligand, it appears that the amount of electron density at the Fe has decreased (i.e. that the metal center has been oxidized by coordination of TEMPO). For comparison, coordination of the strong 2e donor ligand $\text{P}(\text{OMe})_3$ to $\text{CpFe}(\text{CO})_2$ results in a decrease of the CO stretching frequencies, indicative of an increase in pi-backbonding to the CO-ligands. Thus the experimental results in this case again point to an anionic TEMPO ligand. DFT calculations show a calculated pyramidal geometry at nitrogen for this adduct using all six functionals tested (sum of angles equal to 336.5° with B3LYP), also indicating an anionic TEMPO ligand.

As shown in Table 8.3, DFT results with each of the hybrid functionals predict an increase in the CO-stretching frequencies of both modes upon coordination of TEMPO to $\text{CpFe}(\text{CO})_2$, consistent with the experimental results. The pure DFT functionals tested (BP86 and PW91) instead predict similar frequencies for $\text{CpFe}(\text{CO})_2$ and $\text{CpFe}(\text{CO})_2(\text{TEMPO})$. Considering that the experimentally observed frequencies are clearly higher for the TEMPO adduct, consistent with the anionic ligand (whose geometry was correctly predicted by all of the functionals tested), this difference indicates that the pure DFT functionals do a poor job of describing the changes in vibrational frequencies for $\text{CpFe}(\text{CO})_2$ upon coordination of a TEMPO ligand.

Table 8.3. Experimental and calculated frequency shifts for CO-stretching modes upon coordination of TEMPO (nitroxyl group) to $\text{CpFe}(\text{CO})_2$

Functional	$\Delta\nu_{\text{symmetric}} (\text{cm}^{-1})$	$\Delta\nu_{\text{antisymmetric}} (\text{cm}^{-1})$
B3LYP	40	22
BP86	6	-2
M06	40	21
PBE0	41	23
PW91	6	-3
WB97	59	37
Experiment	41	17

Reactivity of TEMPO toward $Mn(CO)_5$

400 nm photolysis of $Mn_2(CO)_{10}$ yields a pair of $Mn(CO)_5$ radicals, characterized by an absorption band at 1985 cm^{-1} in alkane solution.^{186,272} Figure 8.6 shows TRIR spectra of $Mn_2(CO)_{10}$ collected following 400 nm excitation in a 0.64 M solution of TEMPO in cyclohexane. The bands at ca. 1985 cm^{-1} decrease with increasing delay time, along with the rise of bands at 2021-2033 (broad) and 2052 cm^{-1} , assigned to an $Mn(CO)_5(TEMPO)$ adduct. The possibility of concomitant CO-loss (from $Mn(CO)_5$) to yield species with fewer CO ligands was assessed via DFT frequency calculations, and these predicted a strong red-shift (ca. $50\text{-}80\text{ cm}^{-1}$) of the strongest CO-stretching absorption band, relative to bare $Mn(CO)_5$, in each case, thus ruling out potential CO-loss structures. Similar to the situation with $[CpFe(CO)_2]_2$, the fact that dynamic changes take place on timescales longer than that for diffusion out of the solvent cage eliminate the possibility of recombination to form an adduct with a bridging TEMPO ligand. Considering the delocalization of the vibrational modes of $Mn(CO)_5$, and lack of existing TRIR results on the coordination of ligands to $Mn(CO)_5$, it is not necessarily straightforward to correlate the experimentally observed frequency shifts to changes in the amount of electron density at the Mn center. DFT calculations were thus used to investigate the oxidation state of the metal center to check for consistency between the experimentally observed and calculated CO-stretching absorptions.

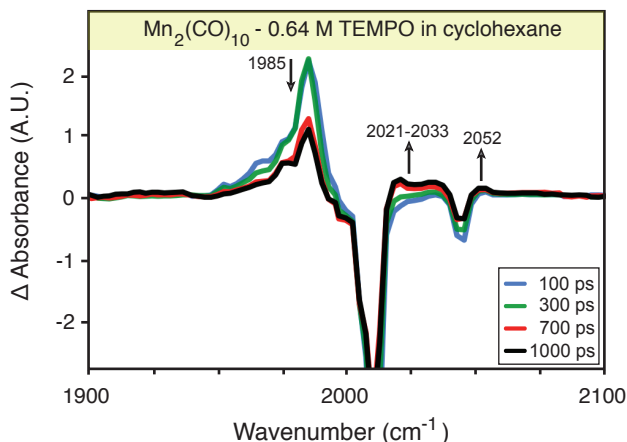


Figure 8.6. TRIR spectra of $Mn(CO)_5$ in 0.64 M TEMPO/cyclohexane solution following 400 nm photolysis.

Similar to each of the other adducts in this study, all six functionals tested indicate that the $Mn(CO)_5(TEMPO)$ adduct adopts a pyramidal geometry about the nitrogen center (sum of angles = 333.8° using the B3LYP functional), again indicating an anionic TEMPO ligand. The calculated frequency shifts for $Mn(CO)_5(TEMPO)$, relative to bare $Mn(CO)_5$, are in good agreement with those observed experimentally; the highest intensity absorption band (observed experimentally at 1985 cm^{-1}) is predicted to remain at a similar frequency and decrease in intensity, with higher frequency bands becoming IR active at frequencies blue-shifted by ca. $20\text{-}85\text{ cm}^{-1}$ relative to the band at 1985 cm^{-1} . On the basis of comparison between the DFT results and the experimental spectra, we conclude that $Mn(CO)_5(TEMPO)$ is characterized by an anionic TEMPO ligand.

We point out that 17e complexes are typically relatively unreactive toward many 2e donor ligands, relative to their 16e counterparts, and that only strong Lewis bases (e.g. phosphines, phosphites) have been previously observed to undergo associative reaction mechanisms with 17e photoproducts on the ultrafast timescale.^{138,139,187} Even among 17e photoproducts, Mn(CO)₅ is particularly unreactive in this regard, as a recent study demonstrated that it does not react to any detectable extent in concentrated P(OMe)₃ solutions on the picosecond timescale.²⁷³ Also of relevance to the Mn(CO)₅(TEMPO) adduct are previous studies that have isolated a final product of Mn(CO)₃(TEMPO) from the reaction of TEMPO with Mn₂(CO)₁₀, with TEMPO behaving as an η^2 anionic ligand (refer back to Figure 8.1) in the 16e Mn(CO)₃(TEMPO) complex.²⁴⁷ This implies that to ultimately achieve the more thermodynamically stable product, Mn(CO)₅(TEMPO) must lose two additional carbonyl ligands and rearrange its TEMPO ligand to an η^2 coordination geometry.

A final point we wish to make is that the fact the metal centers are clearly oxidized upon reaction with TEMPO (which is clear from the experimental data alone in the case of CpCo(CO) and CpFe(CO)₂) is indication that the dynamic changes observed in the TRIR spectra cannot be the result of an electron transfer process independent of TEMPO coordination. Were this to be the case (i.e. were electron transfer to cause oxidation of the metal centers), electron transfer would need to occur from an already electron deficient metal center to TEMPO, and electron transfer *from* a species which is already electron deficient *to* a species which is stable under ambient conditions would be unprecedented. Were such a rare event to be observed, there is furthermore no reason it should take place with all four of the photoproducts studied. The timescales observed for this reaction at the concentrations studied are consistent with the body of existing literature surrounding bimolecular reactions involving electron deficient organometallic photoproducts on the picosecond timescale, and the DFT results further indicate both that TEMPO should coordinate to these metal centers as an anionic ligand, and that, upon coordination, the frequencies should shift in a manner consistent with the experimental observations.

8.4 Conclusions

In this study we have examined the reactivity of the TEMPO radical toward coordinatively unsaturated 16e and 17e metal carbonyl reaction intermediates. In each case, we observe that this coordinatively versatile ligand *coordinates to the metal center associatively with a concurrent internal oxidation-reduction process, yielding adducts with anionic TEMPO ligands*. The oxidation state of each metal center has thus increased by one, and these adducts are characterized by a pyramidal geometry at the nitroxyl nitrogen atom. Overall, the 16e complexes appear to react more readily with TEMPO than the 17e complexes, despite the fact that TEMPO is a radical species. The fact that TEMPO coordinates to each of these intermediates similarly, as an anionic ligand, suggests that these results can be considered generally representative of the reactivity of TEMPO toward coordinatively unsaturated 16e and 17e reaction intermediates of low-valent complexes. In light of this result, one can rationalize the tendency for the TEMPO ligand to adopt an anionic character by the low-valency of the metal center, making the internal oxidation-reduction process facile.

This result is relevant to existing studies on TEMPO catalyzed reaction mechanisms. For example, Sheldon *et. al.* have suggested a reaction mechanism in which TEMPO coordinates to a Cu(I) complex as an anionic ligand to yield a Cu(II) intermediate, which subsequently effects

alcohol oxidation.^{274,275} An alternative mechanism for this same reaction suggests a different role for the metal complex, where disproportionation of TEMPO yields a hydroxylamine which is then oxidized by the metal complex to yield the active catalytic species, an oxoammonium TEMPO cation.^{253,276–285} The latter mechanism has been proposed to characterize the same reaction catalyzed by a variety of other metals as well. While the present results do nothing to rule out the possibility of the latter mechanism, they clearly demonstrate that TEMPO can react as proposed in the former mechanism, via anionic coordination to a low-valent metal center. Similar anionic coordination of TEMPO has also been proposed previously in other situations, such as a C-H arylation mechanism in which two TEMPO molecules coordinate as anionic ligands to a low-valent Rh(I) complex yielding a Rh(III) intermediate.²¹⁸ Additional (different) mechanisms have been proposed for reactions involving higher-valent metal complexes.

The structure and reactivity of organometallic TEMPO adducts is important to developing a clear understanding of their mechanistic role in a wide range of chemical processes, including the oxidation of alcohols, oxidative arene coupling, free radical polymerization, and radical trapping experiments. In addition to the insight gained into the chemistry of this important ligand, we have demonstrated that time-resolved infrared spectroscopy, combined with electronic structure calculations, allows for direct characterization of the structure of organometallic TEMPO adducts in the solution phase. Continued studies into the reactivity of well-characterized TEMPO complexes will help to further elucidate the mechanistic details and patterns governing TEMPO-mediated organometallic reactivity.

9 Direct Observation of a Metal-Ketene Formed by Photoexcitation of a Fischer-Carbene Using Ultrafast IR Spectroscopy

The following chapter is intended to be published in an American Chemical Society Journal and thus we claim no copyright for the text or figures contained in this chapter.

9.1 Introduction

Fischer carbene transition-metal complexes have been developed as reagents for a variety of reactions which form new carbon-carbon bonds and which exploit the chemistry of the formal double bond between the metal and the carbene carbon.^{286,287} The carbon atom is electrophilic and readily undergoes nucleophilic addition reactions, resulting, for example, in benzannulation between unsaturated alkoxy-carbenes and alkynes.²⁸⁸ These types of thermal reactions are a long-standing area of investigation; however, Fischer carbenes are also useful for an entirely different set of unique but poorly understood photoinduced reactions.

Hegedus and coworkers discovered that photoexcitation of group 6 Fischer carbenes leads to products consistent with the reactivity expected from ketenes.²⁸⁹⁻²⁹² For example, carbenes readily react with imines after visible photoexcitation to form β -lactams, the four-membered ring common to all penicillin antibiotics. This reactivity led Hegedus to propose an intermediate metal-ketene structure in which a carbonyl has inserted into the metal-carbene bond (a process termed photocarbonylation, see Scheme 1) to form the ketene moiety. Nevertheless, there exists no direct evidence for a metal-ketene structure despite previous attempts to observe these species in cryogenic matrices and with microsecond time-resolved spectroscopy.^{293,294} Interestingly, this reactivity was observed for group 6 complexes of Cr and Mo, but not W.²⁸⁹

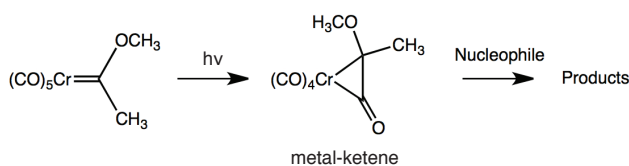


Figure 9.1. Photocarbonylation reaction step proposed for Cr and Mo Fischer carbene complexes

For many years after the seminal report by Hegedus in 1982, the mechanistic details surrounding the reactivity of the group 6 Fischer carbenes remained elusive. Recent work by Fernández et. al. led to the proposal of a mechanism for the photocarbonylation reaction involving initial excitation into a triplet state which undergoes a solvent-induced spin crossover to yield a metal-ketene solvated at the vacant coordination site.²⁹⁵⁻²⁹⁷ Photochemical investigations into both Cr and W carbenes characterized the anti \rightarrow syn isomerization of the methoxy substituent as one of the primary photochemical processes, with CO-loss occurring to a lesser extent.^{297,298} Despite these insights, the photocarbonylation mechanism has, until now, never been experimentally observed.

9.2 Results and Discussion

We report picosecond TRIR measurements on the group 6 Fischer carbene complexes $\text{Cr}(\text{CO})_5[\text{CCH}_3(\text{OCH}_3)]$ (A) and $\text{W}(\text{CO})_5[\text{CCH}_3(\text{OCH}_3)]$ (B) following visible photoexcitation (see SI for experimental details). For the Cr complex, we show the first conclusive evidence of metal-ketene intermediates in the reaction mechanism; both short-lived and long-lived metal ketene intermediates are observed to form upon visible excitation. For the W complex, no metal-ketene products were observed, demonstrating that the lack of synthetic utility of W-based Fischer carbenes is due to a lack of reactivity in the key photocarbonylation step.

Figure 1 shows TRIR difference spectra and kinetic traces for A dilute in cyclohexane following 400 nm excitation. Negative signals, referred to as bleaches, result from species depleted by the 400 nm excitation pulse and correspond to the absorptions of A, while positive signals result from new species present after photoexcitation.

At early delay times, two strong positive features are observed at 1777 cm^{-1} and 1990 cm^{-1} , which both decay with similar time constants of $33 \pm 5\text{ ps}$ and $36 \pm 1\text{ ps}$, respectively. The 1777 cm^{-1} band exhibits a rise time of $\sim 5\text{ ps}$. Based on the relatively low frequency of the 1777 cm^{-1} band, the strong features observed at early delay times are assigned to the formation of an excited state metal-ketene intermediate (refer to scheme 1), which has been postulated to form en-route to generating a longer-lived metal-ketene species.²⁹⁵⁻²⁹⁷ The similar time constants for the decay of the 1777 and 1990 cm^{-1} bands, along with DFT calculations indicating the terminal CO-stretching modes of a metal ketene are consistent with the frequency of the transient band at 1990 cm^{-1} , suggest that these bands correspond to the same transiently-lived metal-ketene. Bands at 1771 and 1791 cm^{-1} , which are visible at early times but persist beyond the decay of the 1777 cm^{-1} band, are correspondingly assigned to long-lived metal-ketene structures. The parent bleaches recover substantially on the same timescale ($33 \pm 2\text{ ps}$), indicating that the primary relaxation pathway for the excited state metal-ketene is reversion to the parent complex, though it likely also exhibits a non-negligible branching ratio to formation of the longer-lived metal-ketenes, as has been suggested previously.^{295,296,299} Our DFT calculations (*vide infra*) indicate that the presence of the two bands at 1771 and 1791 cm^{-1} is likely due to two distinct ketene structures, as a single metal-ketene structure would not be expected to give rise to two bands in this region. These metal-ketenes have never before been observed experimentally and are the species that have long been postulated to be responsible for the synthetically useful photochemistry of Fischer carbenes.

Other bands observed at 1930 , 1953 and 2070 cm^{-1} are assigned to the known anti \rightarrow syn isomerization for the methoxy substituent of A.^{297,298} Weaker bands observed at 1899 and 2044 cm^{-1} are assigned to the formation of a CO-loss product. Interestingly, neither the bands corresponding to the triplet nor the singlet metal-ketene species are observed following 267 nm excitation, indicating that irradiation at this wavelength does not lead to formation of metal-ketenes. When the analogous TRIR experiments were carried out in methanol, the transiently lived metal ketene was still observed, but no long-lived singlet metal-ketene species were detected. Considering the low yield of long-lived metal-ketenes, it may simply be that peak broadening in the more polar solvent places these bands below our detection threshold. Alternatively, there may be a solvent-dependent branching ratio to formation of the long-lived metal ketenes.

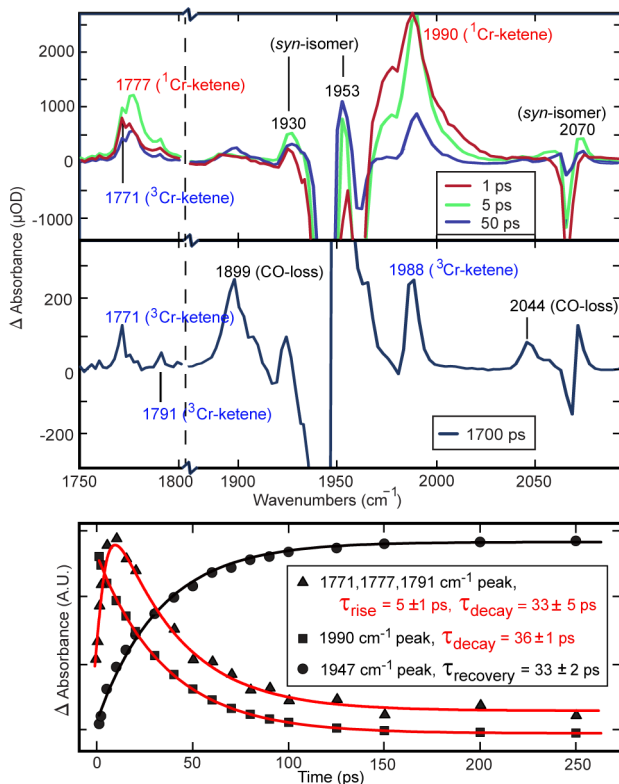


Figure 9.2. TRIR spectra of $\text{Cr}(\text{CO})_5[\text{CCH}_3(\text{OCH}_3)]$ following 400 nm excitation in cyclohexane solution along with corresponding kinetic traces.

DFT calculations⁴³ were carried out to investigate the structures of the metal-ketene intermediates observed experimentally. A recent DFT study of Cr carbene complexes by Fernández et al. showed that the lowest lying triplet state possesses a metal-ketene structure,^{295,296} suggesting that this state is responsible for the unique photochemistry of the compounds. Typically the difference in the spin-state and geometry between T_1 and S_0 would cause the triplet state to be long-lived, persisting for hundreds of picoseconds or more. The fact that the transiently lived metal-ketene relaxes in ca. 33 ps suggests that this species is a singlet.

We performed DFT calculations on the singlet (S_0) and triplet (T_1) states of A and found two nearly isoenergetic triplet geometries with metal-ketene structures (insets 1 and 2 of Figure 2). The calculated metal ketene stretching frequencies for the two triplet structures were 1749 and 1772 cm^{-1} , which are in quite good agreement with the experimentally observed frequencies for the long-lived metal-ketene structures. The calculated terminal CO-stretching frequencies for both structures also agree reasonably well with the experimentally observed band at 1988 cm^{-1} , suggesting that these two triplet structures may represent the two long-lived metal-ketenes observed experimentally.

Time-dependent DFT calculations show five electronic levels accessible with the energy of a 400 nm photon (71.5 kcal/mol): three triplet states (T_1 , T_2 , T_3) and two singlet states (S_1 , S_2), as shown in Figure 2. Because spin-allowed absorption cross sections are typically larger than for spin-forbidden excitations, photoexcitation should promote A to a singlet electronic state (S_1 or S_2), and the molecule can subsequently relaxes to the lowest triplet state (T_1).

Scans of the potential energy surface (PES) of the T_1 and S_0 states along the carbene-chromium-carbonyl C–Cr–C bond angle reveal a downhill pathway for formation of the two nearly isoenergetic triplet metal-ketene structures (Figure 2). This bond angle changes by 43° between S_0 structure A (inset 4) and T_1 metal-ketene structures (insets 1 and 2), and the distance between the carbene carbon and carbonyl carbon shortens from 2.75 to 1.63 Å. PES scans in the S_0 state indicate that this state approaches the T_1 state at the metal-ketene geometries, but no crossing was identified. Were the triplet minima to relax to a singlet state, the PES scans suggest that the S_0 state will revert to the parent complex. This very likely explains the short lifetime of the transient metal-ketene observed at early delay times.

The ~ 5 ps rise of the excited state ketene band most likely corresponds to the timescale for insertion of a CO into the metal-carbene bond. Considering that the peak at 1990 cm^{-1} shows no rise, but is broad at early time delays, this band likely results from a distribution of photoexcited A molecules which may or may not have not yet formed the metal-ketene structure, but already possess terminal CO absorptions in this spectral region. The fact that spectral signatures of the long lived bands at 1771 and 1791 cm^{-1} are visible at early delay times (see 1 ps and 5 ps spectra in Figure 1) suggests that the long-lived species can be formed quite rapidly after photoexcitation. Thus the initially populated excited singlet state can relax to either the singlet ground state or to the long-lived triplet state, and the branching ratio between these two relaxation pathways will determine the yield for formation of the long-lived metal-ketenes.

Though this interpretation appears to provide a fairly straightforward explanation for the experimental results, it is worth considering the suggestion of Fernández et. al. that solvent coordination and relaxation to a singlet spin state may produce the metal-ketene intermediate responsible for the chemistry of the group 6 carbenes.^{295,296,299} Accordingly, we also carried out DFT calculations in which an alkane solvent molecule coordinates to the vacant coordination site of a singlet metal-ketene structure. Local minima were located involving solvent-coordinated metal-ketene structures, though PES scans along the coordinate for alkane de-coordination indicate a very low barrier (ca. 3 kcal/mol) to solvent de-coordination, at which point the ground state singlet should relax back to the parent structure (see Figure 2). Thus while we cannot conclusively rule out the possibility that the long-lived metal-ketenes observed experimentally correspond to solvent-coordinated singlet structures, we favor the interpretation of the data suggested by our DFT results, as it provides an intuitively reasonable and internally consistent explanation for the experimental observations. Similar DFT scans indicate that decoordination of methanol from the hypothetical solvated singlet metal-ketene may involve a higher barrier, on the order of ca. 10 kcal/mol.

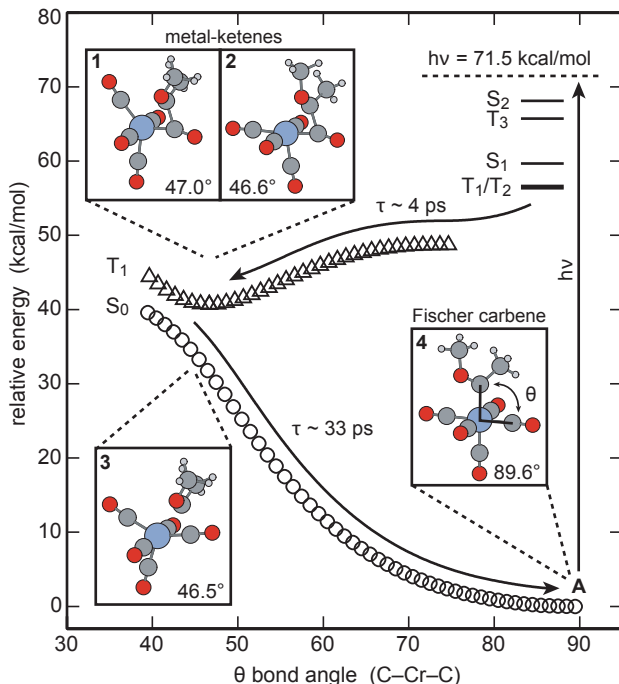


Figure 9.3. DFT energetics as a function of the carbene-chromium-carbonyl C–Cr–C bond angle for the S_0 and T_1 electronic levels involved in photoexcitation of $\text{Cr}(\text{CO})_5[\text{CCH}_3(\text{OCH}_3)]$ (A). Insets show the calculated molecular structures at various points on the PESs, and the associated bond angles are given in the lower corners of the insets. Data points for T_1 correspond to the structure shown in inset 2. The relative energies of singlet (S_1 , S_2) and triplet (T_1 , T_2 , T_3) excited states within the energy of a 400 nm photon are shown.

To summarize, the TRIR results for the photochemistry of $\text{Cr}(\text{CO})_5[(\text{CCH}_3(\text{OCH}_3))]$ following 400 nm excitation can be interpreted as follows: initial excitation into a singlet state results in the formation of both a transiently lived singlet metal-ketene intermediate, along with two long-lived triplet metal ketene intermediates. Another primary photoexcitation pathway involves the previously characterized to anti \rightarrow syn isomerization of the methoxy substituent. The long-lived triplet metal-ketenes are the species responsible for the well-known, synthetically useful photochemistry of Fischer carbenes. CO-loss also occurs to a minor extent.

We next sought to investigate the analogous W carbene, and these TRIR difference spectra following 400 nm excitation in cyclohexane are shown in Figure 3. The most notable difference between these spectra and those collected for the Cr carbene is the lack of any bands in the bridging-CO region (ca. $1750\text{--}1850\text{ cm}^{-1}$) that would indicate the formation of a metal-ketene structure. Thus, we can immediately see that no metal-ketene intermediate is formed upon visible excitation of the W Fischer carbene. Transient broad bands are observed at ca. 1930 , 1970 and 2060 cm^{-1} , assigned to an excited state of the parent complex, B, which decay on the timescale of $23 \pm 1\text{ ps}$. Long lived bands are also observed at 1938 , 1948 , 1985 (weak) and 2069 (weak) cm^{-1} , and these are assigned to anti \rightarrow syn isomerization that takes place upon photoexcitation, analogous to the process observed for the Cr congener.^{297,298} The bands of the two isomers of B overlap strongly, influencing the observed band positions. Analogous experiments carried out using 267 nm excitation also observed additional bands at 1892 , 1905 , 1995 , and 2044 cm^{-1} ,

corresponding to a CO-loss species (not observed following 400 nm excitation), but again found no evidence for any metal-ketene structure.

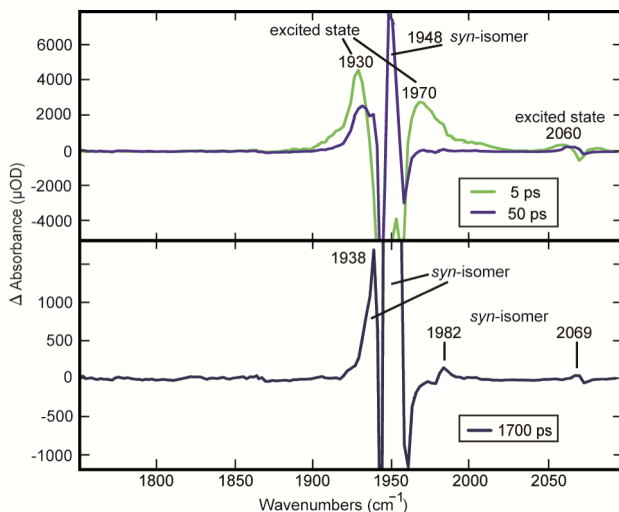


Figure 9.4. TRIR spectra of $W(CO)_5[CCH_3(OCH_3)]$ following 400 nm excitation in cyclohexane solution.

The absence of formation of a metal-ketene intermediate is consistent with the lack of photochemical reactivity typically observed for tungsten Fischer carbenes in synthetic applications. It has been suggested that high occupation of the p_z atomic orbital of the carbene carbon may inhibit photoinsertion of the CO-ligand, making photocarbonylation either unfavorable or presenting a substantial kinetic barrier.²⁹⁹

9.3 Conclusions

In conclusion, we have monitored the formation of the metal-ketene intermediates formed upon visible excitation of the Fischer carbene $Cr(CO)_5[CCH_3(OCH_3)]$. Photoexcitation leads to rapid formation of both singlet and triplet metal-ketene structures, with the singlet metal-ketene primarily relaxing to reform the parent complex in tens of picoseconds, and potentially also contributing to the population of the two long-lived triplet metal-ketenes, which are responsible for the synthetically useful photochemistry of these complexes. Another major photochemical pathway involves anti \rightarrow syn isomerization of the parent carbene, with CO-loss being a minor pathway. The analogous tungsten-based Fischer carbene was also studied, and while photoisomerization and CO-loss pathways were observed, no metal-ketenes were formed. This is consistent with the observed lack of reactivity of tungsten-based Fischer carbenes in synthetic applications.

10 Picosecond Time-Resolved Infrared Studies of the Photochemistry of $M_3(CO)_{12}$ ($M = Fe, Os$) Clusters in Solution

The following chapter is reproduced (adapted) in part with permission from (Lomont, J. P.; Shearer, A. J.; Nguyen, S. C.; Harris, C. B. *Organometallics*, 2013, 32, 2178-2186.). Copyright (2013) American Chemical Society.

10.1 Introduction

Transition metal carbonyl clusters of the type $M_3(CO)_{12}$ ($M = Fe, Ru, Os$) serve as common synthetic precursors to other organometallic complexes.^{300–317} Their structures, fluxional ligand rearrangement mechanisms, and chemical reactivity patterns have served as a model for the behavior of other transition metal carbonyl complexes. In this paper, we report an investigation into the picosecond photochemical dynamics of the $Fe_3(CO)_{12}$ and $Os_3(CO)_{12}$ clusters in the solution phase. A previous picosecond time-resolved infrared (TRIR) study on the photochemistry of the $Ru_3(CO)_{12}$ congener³¹⁸ demonstrated that each of the observed photoproducts contained a bridging carbonyl ligand, while the parent complex itself contains no bridging carbonyl ligands. In the present study, we find that no cluster photoproducts containing bridging carbonyls form as a result of metal-metal bond cleavage from the non-bridged iron or osmium clusters, providing an interesting contrast to the previous results.

Both $Fe_3(CO)_{12}$ and $Os_3(CO)_{12}$ have found wide applications in chemical catalysis and as synthetic precursors to other organometallic complexes. These clusters have been shown to catalyze olefin hydrogenation, alkene isomerization, hydrosilation, and carbonylation reactions.^{319–323} The reactivity of both complexes toward ligand substitution and declusterification has been investigated, as has the subsequent reactivity of the derivatives formed in these reactions.^{324–332} Their catalytic behavior when adsorbed onto various surfaces has also been studied,^{333–349} and surface adsorbed adducts of each cluster have been shown to catalyze the Fischer-Tropsch reaction^{350–354} and the water gas shift reaction.³⁵⁵ The mechanisms of fluxional ligand rearrangements in the $Fe_3(CO)_{12}$ cluster have been a topic of substantial discussion in the literature, and these mechanisms serve as a model for the fluxional processes at work in other M_3L_{12} species.^{356–367}

Several studies have investigated the photochemistry of these clusters in the solution phase and in alkane glasses.^{368,368–370} Regarding the carbonyl-loss complexes observed in glasses, $Fe_3(CO)_{11}$ adopts a structure containing two bridging carbonyls, while $Os_3(CO)_{11}$ contains no bridging carbonyl.^{368,369} It is worth noting that, in alkane glasses, the parent $Fe_3(CO)_{12}$ species contains bridging carbonyls, while $Os_3(CO)_{12}$ does not. Photochemical cleavage of a metal-metal bond in either complex is believed to lead to formation of bridging carbonyl rearrangement isomers, though the evidence for the existence of these species is less direct.^{371,372} While non-bridged metal-metal bond cleavage photoproducts are expected to be short lived, isomers containing bridging carbonyls have been proposed to be relatively stable, accounting for the photochemical reactivity of these clusters on diffusion limited timescales and beyond.³⁷¹ To our knowledge, the only existing picosecond time-resolved study on the photochemistry of either of

these clusters was performed using 590 nm pump and 720, 760, or 800 nm probe wavelengths to study the photochemistry of $\text{Fe}_3(\text{CO})_{12}$.³⁷² This study concluded that metal-metal bond cleavage products, some containing bridging carbonyls, were observed to form on the picosecond timescale, as were carbonyl-loss products. By probing the photochemistry of these clusters using ultrafast TRIR spectroscopy, we seek to directly monitor the structure and stability of the products formed following photochemical excitation, which will allow for a better understanding of their subsequent roles in chemical reactions.

In this paper we report an investigation into the photochemistry of the $\text{Fe}_3(\text{CO})_{12}$ and $\text{Os}_3(\text{CO})_{12}$ clusters following 267 nm and 400 nm excitation wavelengths in solution. The results of this study provide new insight into the role of transiently lived metal-metal bond cleavage intermediates, bridging carbonyl species, fragmentation products, and CO-dissociation products in trimetallic clusters.

10.2 Methods

10.2.1 Sample Preparation

$\text{Fe}_3(\text{CO})_{12}$ and $\text{Os}_3(\text{CO})_{12}$ were purchased from Fisher Scientific, and cyclohexane and methanol were purchased from Sigma–Aldrich Co. All samples and solvents were used without further purification. Dilute solutions of $\text{Fe}_3(\text{CO})_{12}$ and $\text{Os}_3(\text{CO})_{12}$ were stable in air at ambient temperatures for at least a few hours (verified via FTIR) in each solvent. Samples of $\text{Fe}_3(\text{CO})_{12}$ used to collect TRIR spectra were prepared at a concentrations of ca. 4 mM. The $\text{Os}_3(\text{CO})_{12}$ sample was prepared as a saturated solution in cyclohexane, since the solution appeared to be saturated at a concentration of less than 1 mM.

10.2.2 Data Analysis

Kinetics traces in this work result from spectra measured at delay times between 0 and 1000 ps between the UV/visible-pump and IR-probe pulses. Kinetic traces for each spectral feature were obtained by integrating a narrow spectral region (ca. 4 cm^{-1} wide) surrounding the reported frequency. The kinetic data were then fit to exponential curves using Origin Pro 8 software. Most photoproducts were observed to be completely formed within 1 ps, or roughly the duration of the excitation pulse. For these products, exponential decay functions were fit to data beginning at a delay time of 2 ps. In cases where an exponential rise and decay function was needed, a separate, home-written, fitting program was used. Errors on experimental time constants are reported as 95% confidence intervals.

10.2.3 Density Functional Theory Modeling

Density functional theory (DFT) calculations have been carried out to attempt to facilitate assignment of the species observed in the TRIR experiments. All calculations were carried out using the BP86^{37,39} functional in the Gaussian09⁴³ package. The 6-31+G(d,p) basis^{129,130,373} set was used for all atoms except Fe and Os, for which the lanl2dz^{44,45} basis was used. Each geometry optimization was followed by a frequency analysis to ensure that all geometries were genuine local minima. While most structures in this study were identified by interpretation of the infrared spectra and comparison to literature results, DFT calculations were used for predicting

the strengths of interactions with solvent molecules, as well as to search for local minima corresponding to the short-lived metal-metal bond cleavage transients.

10.3 Results and Discussion

Time-resolved infrared (TRIR) spectra of $\text{Fe}_3(\text{CO})_{12}$ and $\text{Os}_3(\text{CO})_{12}$ have been recorded in the CO stretching region following 400 and 267 nm excitation. Spectra for $\text{Fe}_3(\text{CO})_{12}$ were collected in cyclohexane and methanol solutions, while the low solubility of $\text{Os}_3(\text{CO})_{12}$ in polar solvents limited our study to cyclohexane solution for that species. TRIR spectra are presented as difference absorbance spectra, in which positive absorptions correspond to newly formed species, and negative bands correspond to the depletion of parent molecules.

10.3.1 Picosecond Time-Resolved IR Spectroscopy of $\text{Fe}_3(\text{CO})_{12}$

Cyclohexane Results

TRIR spectra of $\text{Fe}_3(\text{CO})_{12}$ collected in cyclohexane solution following 400 nm and 267 nm excitation are shown in Figure 10.1 and the time constants for exponential fits to the data are listed in Table 10.1. A previous study into the electronic structure of a single crystal sample of $\text{Fe}_3(\text{CO})_{12}$ indicated that absorption bands at 437 and 602 nm correspond to $\sigma \rightarrow \sigma^*$ and $\sigma^* \rightarrow \sigma^*$ transitions (with respect to metal-metal bonding/antibonding orbitals), respectively, while a band at 263 nm was assigned to an MLCT state associated with charge transfer to a carbonyl ligand.³⁷⁴ In solution, $\text{Fe}_3(\text{CO})_{12}$ exists as a mixture of non-bridged and bridged (C_{2v}) isomers, with the non-bridged isomer present in significantly larger quantities (see Figure 10.2, structures A and B).^{364,375-386} While the exact quantity of the bridged isomer in solution is not known, it has been suggested to be in the range of 5-10%, depending on the solvent.³⁷⁸ As can be seen in the FTIR spectrum in Figure 10.1, the bridging carbonyl absorption is very weak relative to the absorptions in the terminal region. We will focus first on interpreting the bands in the terminal carbonyl stretching region.

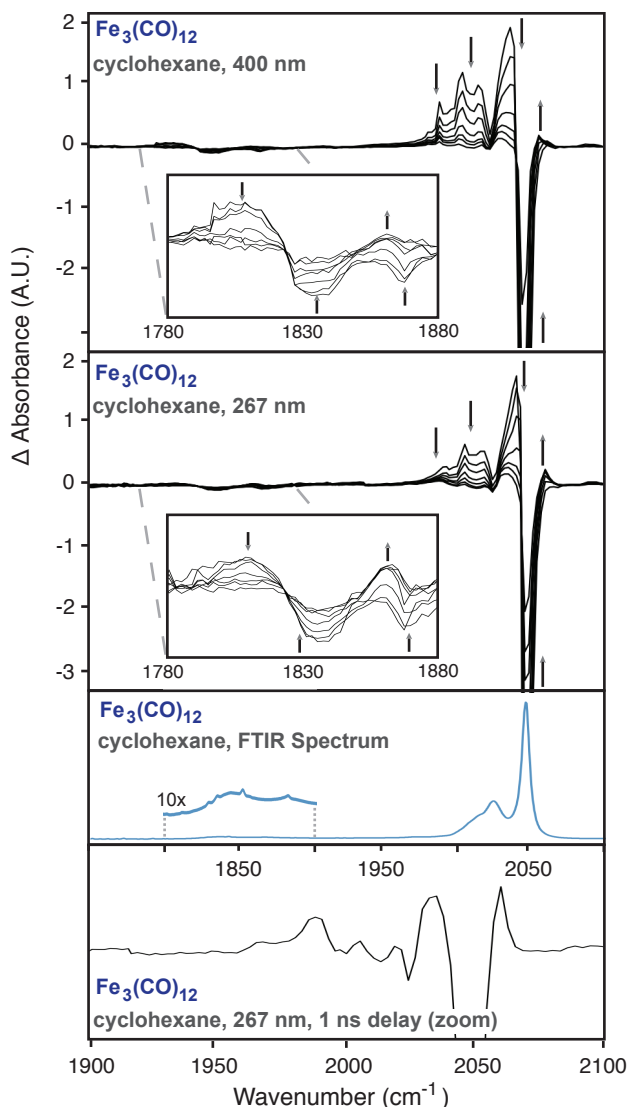


Figure 10.1. TRIR spectra of $\text{Fe}_3(\text{CO})_{12}$ following 400 nm and 267 nm excitation in cyclohexane solution at delay times of 20, 50, 100, 200, 300, 400, and 700 ps, along with the FTIR spectrum. An enlarged version of the terminal carbonyl region of the 267 nm excitation spectrum at a delay time of 1 ns is shown in the bottom panel.

Following 400 nm excitation, the strongest product absorption band at 2036 cm^{-1} exhibits a decay time constant of $133 \pm 23\text{ ps}$. The time constants for decay of the other positive terminal carbonyl absorptions at ca. 1990, 2005, and 2017 cm^{-1} are similar to that for the 2036 cm^{-1} band, suggesting that these bands correspond to the same species. A previous study following 590 nm excitation in cyclohexane reported a similar decay time constant of 150 ps for the transient photoproducts.³⁷² In that work, the photoproduct absorptions were assigned to a mixture of unsaturated and bridging $\text{Fe}_3(\text{CO})_{12}$ isomers. In both this study and the previous study, a fast decay component of ca. 10 to 25 ps is observed, and we attribute this to vibrational cooling of overlapping bands of the nascent photoproduct. The short, picosecond lifetime of this transient species suggests that it is a metal-metal bond cleavage isomer that exists uncoordinated to any

solvent molecules. Were a solvent molecule to coordinate as a token ligand to one of the metal centers, we would expect the solvent-coordinated photoproduct to exhibit a significantly longer lifetime.

The fact that the only observable bridging carbonyl product bands at 1807 and 1861 cm^{-1} do not recover on the same timescale as those in the terminal region, along with their significantly weaker intensity, suggests that the species that contribute dominantly to the terminal region do not contain any bridging carbonyls. As we will discuss shortly, the band at 1861 cm^{-1} does not decay on the timescale studied, and only becomes visible as the parent bleaches recover. Thus we assign the strong bands at 1990, 2005, 2017, and 2036 cm^{-1} in the terminal carbonyl region species to a non-bridged metal-metal bond cleavage photoproduct, similar to structure C in Figure 10.2. We point out that the bridged photoproducts observed via a band at 1807 and 1861 cm^{-1} will also have weak overlapping contributions in the terminal CO-stretching region (*vide infra*).

Table 10.1. Time constants for transient product bands and bleach recoveries of $\text{Fe}_3(\text{CO})_{12}$ in cyclohexane following 400 and 267 nm excitation

Absorption (cm^{-1})	$\tau_{400 \text{ nm}}$ (ps)	$\tau_{267 \text{ nm}}$ (ps)
Product decay time constants in cyclohexane ^a		
1807	293 ± 87	327 ± 186
1990	10 ± 2	11 ± 2
	141 ± 32	167 ± 38
2005	10 ± 2	13 ± 2
	145 ± 9	159 ± 17
2017	24 ± 4	11 ± 2
	152 ± 13	125 ± 12
2036	4 ± 3 (rise)	16 ± 15 (rise)
	133 ± 23	156 ± 17
Parent bleach recovery time constants in cyclohexane		
1835	276 ± 57	222 ± 138
1867	191 ± 52	240 ± 173
2047	100 ± 12	21 ± 3
		187 ± 22

(a) Only absorptions that decay on the picosecond timescale are listed in this table.

We attempted to use DFT geometry optimizations to study the structure of the metal-metal bond cleavage product. Previous DFT investigations studies on $\text{Fe}_3(\text{CO})_{12}$ have shown that the calculated minimum energy structure corresponds to the C_{2v} geometry observed in the crystalline phase, which is not the predominant form observed in solution. Our initial attempts to locate a non-bridged metal-metal bond cleavage product were carried out by performing geometry optimizations beginning from input geometries in which a single Fe-Fe bond distance had been elongated from a non-bridged, D_{3h} geometry, or from the C_{2v} , bridged geometry. These optimizations each returned to the C_{2v} equilibrium structure, or to a higher energy non-bridged structure with equal Fe-Fe bond distances. We thus feel it is likely that the transiently lived, non-bridged $\text{Fe}_3(\text{CO})_{12}$ photoproduct may not correspond to a genuine local minimum on the potential energy surface and that the ca. 150 ps lifetime corresponds to the timescale for rearrangement of the metal-metal cleavage product to reform the parent complex.

To investigate the nature of potential metal-metal bond cleavage products arising from the non-bridged isomer, we began with a D_{3h} structure obtained from a symmetry-constrained geometry optimization, and performed single-point frequency calculations for structures with

one, two, or all three metal-metal bonds elongated, searching for structures whose predicted IR absorption bands red-shift ca. 10 cm^{-1} relative to the D_{3h} structure (to, at least qualitatively, match the experimentally observed transient). We found that elongating a single Fe-Fe bond did not lead to significant changes in the predicted observed IR frequencies, while symmetrically elongating either two or three Fe-Fe bonds led to predicted red-shifts in the IR bands that were reasonably consistent with our experimental spectra. For example, symmetrically elongating two Fe-Fe bonds to 4.4 \AA leads to predicted red shifts of $4\text{-}9\text{ cm}^{-1}$ for the strongest observed bands, while symmetrically elongating all three Fe-Fe bonds to 4.0 \AA leads to predicted red-shifts of $10\text{-}11\text{ cm}^{-1}$, with the pattern of band intensities resembling that of the ground state structure in both cases. Thus our DFT results suggest that the non-bridged transient species likely corresponds to a structure in which either two or three Fe-Fe bonds are elongated, relative to the ground state structure.

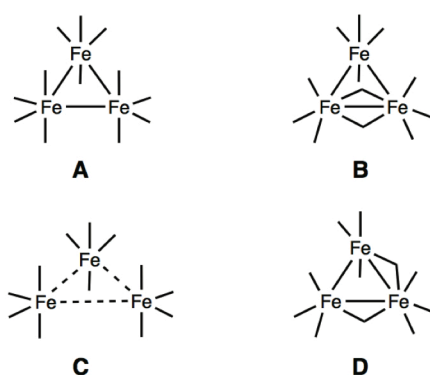


Figure 10.2. Species A and B depict the non-bridging and bridging isomers of the parent $\text{Fe}_3(\text{CO})_{12}$ complex. C shows the transient metal-metal bond cleavage product arising from photolysis of A, while D shows the carbonyl-loss product believed to form following ligand dissociation from B.

Looking next at the absorptions in the bridging carbonyl region of Figure 10.1, these exhibit decay rates longer than those observed for the terminal carbonyl bands. From Figure 10.1, it is evident that the bridging carbonyl bleach bands at 1835 and 1867 cm^{-1} are similar in intensity to the transient bridging photoproduct band at 1807 cm^{-1} . Despite the rather large errors on some of the time constants due to the weak band intensities, the kinetics of the bleach recoveries also correlate well with those for decay of the bridged photoproduct. These facts suggest that only the C_{2v} bridging isomer gives rise to photoproducts containing bridging carbonyl ligands. Were the non-bridged isomer to give rise to a photoproduct containing bridging CO-ligands, we would expect the corresponding bands to be substantially larger in intensity than those observed, since the non-bridged parent isomer is present in significantly larger concentration than the bridged parent structure. This point is further demonstrated by the correlated kinetics for decay seen in the transient band at 1807 cm^{-1} and the recovery of the parent bleaches in the bridging region. The picosecond lifetime of the bridging carbonyl absorption observed at 1807 cm^{-1} indicates that the observed absorption cannot correspond to a carbonyl loss or fragmentation product, as the absorptions of such products would not be expected to recover on the picosecond timescale. We thus assign the band at 1807 cm^{-1} to a metal-metal bond cleavage transient arising from cleavage of an Fe-Fe bond in the C_{2v} bridged parent molecule.

DFT geometry optimizations calculations were again used to search for local minima involving the cleavage of a metal-metal bond (and/or rearrangement of the bridging carbonyls) from the C_{2v} bridged complex. These attempts either returned to the C_{2v} parent complex, or to a higher energy non-bridged minimum. Similar to the case with the non-bridged isomer, no local minima with an extended Fe-Fe bond were located. Single-point DFT calculations were again performed involving the elongation of one or two Fe-Fe bonds (the CO-bridged Fe pair was not extended), and, similar to the results with the all-terminal structures, only structures in which two Fe-Fe bonds were elongated led to red-shifts that appear reasonably consistent with the experimental observations. For example, symmetrically elongating the two non-bridged Fe-Fe bonds to 4.4 Å leads to red shifts of 2-9 cm^{-1} in the observable IR band frequencies, with the pattern of band intensities again resembling that of the ground state structure in each case. We thus assign the transient bridging rearrangement intermediate to a geometry involving two extended Fe-Fe bonds, though we cannot say whether a bridging carbonyl may also rearrange. The short (picosecond) lifetimes for reversion of both transient species to their parent complexes implies that they play little role in the photochemistry of $\text{Fe}_3(\text{CO})_{12}$ in reactions occurring on diffusion limited (or longer) timescales.

A weak positive absorption is also present at ca. 1861 cm^{-1} ; this is more clearly visible at longer delay times when the overlapping bleach intensity at 1867 cm^{-1} has recovered. In the TRIR spectra, the band at 1861 cm^{-1} is more prominent in the spectra obtained following 267 nm excitation, consistent with the notion that shorter excitation wavelengths will favor excitation into a dissociative MLCT state. A previous study in alkane glasses reported the formation of bridged CO-loss photoproduct D (Figure 10.2) at a frequency of 1858 cm^{-1} .³⁶⁸ We thus assign the absorption at 1861 cm^{-1} in the present study to structure D. Again, the comparably weak intensities of this photoproduct band and those of the bridged parent bleaches suggests that the bridged isomer likely gives rise to this complex, though it cannot be ruled out that this species may form in low quantum yield from photolysis of the non-bridged parent isomer. Likewise, we cannot rule out the possibility that the C_{2v} bridged parent isomer may also undergo fragmentation to yield $\text{Fe}(\text{CO})_4$ and $\text{Fe}_2(\text{CO})_8$; our conclusions in this regard are based on the disparate intensity scales observed for 1) the (weaker) bridging isomer parent bleaches and bridging CO-loss photoproduct intensities, and 2) the (stronger) all-terminal isomer bleach and fragmentation photoproduct intensities.

In general, the spectra and kinetics observed following 267 nm excitation are qualitatively similar to those observed following 400 nm excitation. However, it is noteworthy that a greater amount of parent bleach intensity remains at longer delay times following 267 nm excitation. If we compare the 2047 cm^{-1} parent bleach intensity at 1 ns relative to its maximum value at early delay times (ca. 2 ps), this absorption maintains ca. 12% of its maximum intensity following 267 nm excitation, but only 6% following 400 nm excitation. While these numbers are only intended to provide a qualitative comparison, it is clear that more photoproducts remain at longer delay times following 267 nm excitation.

This is also apparent by looking at the positive product bands following 267 nm excitation. At a delay time of 1 ns, absorption bands are visible at 1967, 1988, 2033, and 2060 cm^{-1} ; these appear to remain relatively constant in intensity as the overlapping transient metal-metal bond cleavage products decay. The bands at 1967 and 1988 cm^{-1} are assigned to $\text{Fe}(\text{CO})_4$,^{29,30,387} and those at 2033 and 2060 cm^{-1} are assigned to the bridged isomer of $\text{Fe}_2(\text{CO})_8$,^{31,388} based on comparisons to literature values. The literature demonstrates that bridged $\text{Fe}_2(\text{CO})_8$ also displays weak bands in the bridging region, but these appear to be below our detection limit. Some reports

assign a very weak a' transition at 1857 cm^{-1} , and all reports assign another weak a'' band at ca. $1815\text{-}1820\text{ cm}^{-1}$.^{388,389} While both bands are weak, the a'' band should be several times stronger than the a' band, so the fact that we do not observe an a'' band in the $1815\text{-}1820\text{ cm}^{-1}$ region for this species indicates that the band at 1861 cm^{-1} does not correspond to the a' mode of bridged $\text{Fe}_2(\text{CO})_8$, confirming our earlier assignment of the 1861 cm^{-1} band to $\text{Fe}_3(\text{CO})_{11}$. DFT calculations indicate that interactions between $\text{Fe}_2(\text{CO})_8$ and an alkyl group are only weakly favorable (ca. 0.25 kcal/mol) and thus we do not believe that $\text{Fe}_2(\text{CO})_8$ coordinates to an alkyl group as a token ligand. The band at 2060 cm^{-1} appears to rise with increasing delay time; we attribute this to the band's weak intensity and overlap with the more intense recovering parent bleach. Thus it appears that 267 nm excitation leads to fragmentation products in addition to the metal-metal bond cleavage products. The bands at 2033 and 2060 cm^{-1} are also weakly visible in the spectra following 400 nm excitation, suggesting that a small amount of fragmentation also occurs at this wavelength. While it is possible that carbonyl-loss products are also formed (in fact, the very weak absorption at 1861 cm^{-1} does suggest that a small amount are formed), the spectra appear to be well-explained by fragmentation products and metal-metal bond cleavage transients, and thus we find no clear evidence suggesting significant formation of carbonyl loss, $\text{Fe}_3(\text{CO})_{11}$ photoproducts from the all-terminal isomer of $\text{Fe}_3(\text{CO})_{12}$. In previous solution-phase continuous irradiation studies, it was observed that photofragmentation dominated the net photochemistry of $\text{Fe}_3(\text{CO})_{12}$.³⁶⁸ Considering the short lifetimes of the transient rearrangement products, the fragmentation photoproducts are likely responsible for subsequent reactivity on longer timescales.

Recent X-ray scattering studies on the ruthenium congener have shown that two-carbonyl loss products must be invoked to obtain a quality fit to the X-ray scattering data.^{390,391} Such di-carbonyl loss products arising from single photon absorption are believed to be rare, though their existence has been established following excitation of $\text{Fe}(\text{CO})_5$ at 267 nm .^{29,30,387} In the present study, the band positions observed at longer delay times all appear to correspond to known photoproducts, and thus we do not believe any di-carbonyl loss products are observed in this study.

Methanol Results

TRIR spectra of $\text{Fe}_3(\text{CO})_{12}$ collected in methanol solution following 400 nm excitation are shown in Figure 10.3, and the corresponding time constants for the decay of each absorption feature are listed in Table 10.2. We were interested to see if differences in the quantities of bridging photoproducts would be observed in the more polar methanol solvent, since the bridging $\text{Fe}_3(\text{CO})_{12}$ isomer is present in larger quantities in more polar solutions.³⁷⁹ Similar to the data collected in cyclohexane solution, it is evident that disparate absorption intensity scales characterize the bridging and terminal carbonyl regions in these spectra.

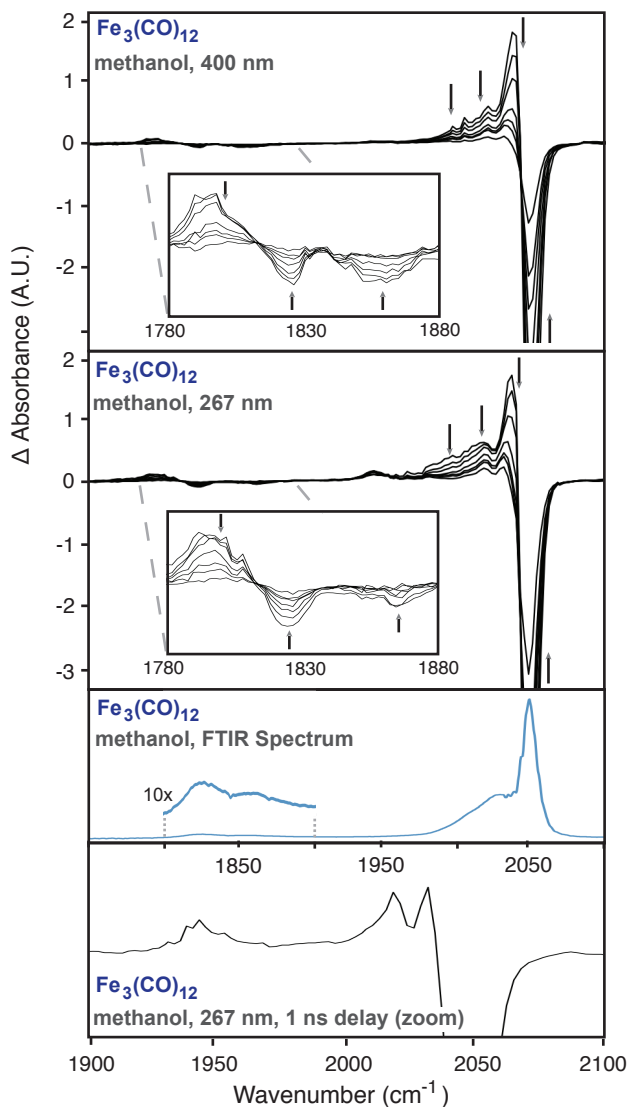


Figure 10.3. TRIR spectra of $\text{Fe}_3(\text{CO})_{12}$ following 400 nm and 267 nm excitation in methanol solution at delay times of 20, 50, 100, 200, 300, 400, and 700 ps, along with the FTIR spectrum. An enlarged version of the terminal carbonyl region of the 267 nm excitation spectrum at a delay time of 1 ns is shown in the bottom panel.

Looking first at the terminal carbonyl stretching region, the absorptions at 2002, 2020, and 2037 cm^{-1} decay at similar rates following excitation at either 400 or 267 nm irradiation. The lifetimes of these absorptions are slightly (ca. 30%) longer than those of the terminal carbonyl bands in cyclohexane solution. Based on the similar decay constants of each band in this region, it appears that a single transiently lived photoproduct is observed in this region of the spectrum. Again, the picosecond lifetime of this species implies that it exists uncoordinated to solvent molecules. For comparison, a previous study on the photochemistry of $\text{Ru}_3(\text{CO})_{12}$ observed a THF-solvated isomer with a lifetime of 50 ms,³⁹² which is several orders of magnitude longer than the lifetime of the species observed in the present study. The relatively similar lifetime in

each solvent supports the notion that there is no major difference in the behavior of this transient rearrangement intermediate in cyclohexane or methanol solvents.

In the bridging region of the spectrum, the photoproduct band at 1794 cm^{-1} is red-shifted relative to the frequency observed in cyclohexane. The comparable intensity scale and correlated kinetics between this absorption and the bridged parent bleaches again suggests that the bridged parent species gives rise to the bridged transient photoproduct. It is somewhat interesting that the lifetime of the bridged photoproduct is actually shorter in methanol, perhaps indicating that the more polar solvent decreases the stability of the bridged metal-metal bond cleavage product, relative to the situation in cyclohexane. The absorption for the bridged carbonyl loss product D is not clearly visible in these spectra, presumably due to its overlap with the parent bleaches and broadening of the absorptions in the more polar solvent, combined with its already very weak intensity.

Comparing the spectra obtained following 267 and 400 nm excitation again reveals the presence of fragmentation photoproducts. Looking at the TRIR spectra at a delay of 1 ns shows the presence of bands at 1944, 1982, 2018, and 2032 cm^{-1} . Based on comparison to literature values, the band at 1944 cm^{-1} is assigned to $\text{Fe}(\text{CO})_4$, whose absorption frequencies are known to shift upon coordination to methanol.³⁸⁷ To our knowledge, the IR spectrum of $\text{Fe}_2(\text{CO})_8$ in polar solutions has not been reported previously. However, based on our observations in cyclohexane, as well as the fact that one would expect $\text{Fe}_2(\text{CO})_8$ to be formed concomitantly along with $\text{Fe}(\text{CO})_4$, we attribute the bands at 2018, and 2032 cm^{-1} to $\text{Fe}_2(\text{CO})_8$. Considering the shift in the observed frequencies, relative to cyclohexane solvent, it seems likely that $\text{Fe}_2(\text{CO})_8$ also exists coordinated to a solvent molecule. Our DFT calculations indicate that bridged $\text{Fe}_2(\text{CO})_8$ does coordinate to a methanol molecule with a favorably enthalpy of ca. 12 kcal/mol.

Table 10.2. Time constants for transient product bands and bleach recoveries of $\text{Fe}_3(\text{CO})_{12}$ in methanol following 400 and 267 nm excitation

Absorption (cm^{-1})	$\tau_{400 \text{ nm}}$ (ps)	$\tau_{267 \text{ nm}}$ (ps)
Product decay time constants in methanol ^a		
1794	9 ± 19 (rise)	30 ± 15 (rise)
	194 ± 42	135 ± 48
2002	13 ± 5	8 ± 1
	222 ± 36	205 ± 23
2020	203 ± 38	221 ± 76
2037	174 ± 17	186 ± 19
Parent bleach recovery time constants in methanol		
1826	186 ± 28	170 ± 31
1864	9 ± 4	11 ± 7
	133 ± 25	141 ± 44
2050	22 ± 5	12 ± 1
	260 ± 36	219 ± 17

(a) Only absorptions that decay on the picosecond timescale are listed in the table.

10.3.2 Picosecond Time-Resolved IR Spectroscopy of $\text{Os}_3(\text{CO})_{12}$

In the solution phase, $\text{Os}_3(\text{CO})_{12}$ is known to adopt a non-bridged, approximately D_{3h} geometry.^{375,377} Unfortunately, the very low solubility of $\text{Os}_3(\text{CO})_{12}$ in polar solvents prevented us from obtaining TRIR spectra in methanol or other alcohols. Unlike the iron congener, the parent osmium cluster does not contain any detectable fraction of an isomer containing bridging

carbonyls. Transitions in the electronic absorption spectrum of $\text{Os}_3(\text{CO})_{12}$ at 330 and 385 nm have been assigned to $\sigma \rightarrow \sigma^*$ and $\sigma^* \rightarrow \sigma^*$ transitions (with respect to metal-metal bonding/antibonding orbitals), respectively, with another band at 240 nm assigned to an MLCT state associated with charge transfer to a carbonyl ligand.²⁶ A remaining band centered at 280 nm has not been assigned.²⁶

The TRIR spectra of $\text{Os}_3(\text{CO})_{12}$ collected in cyclohexane following 400 nm excitation are shown in Figure 10.4, and the time constants for the decay of each absorption feature are listed in Table 10.3. In this case, no bridging carbonyl photoproducts were observed to form at either excitation wavelength, and thus the spectra shown focus on the terminal carbonyl stretching region.

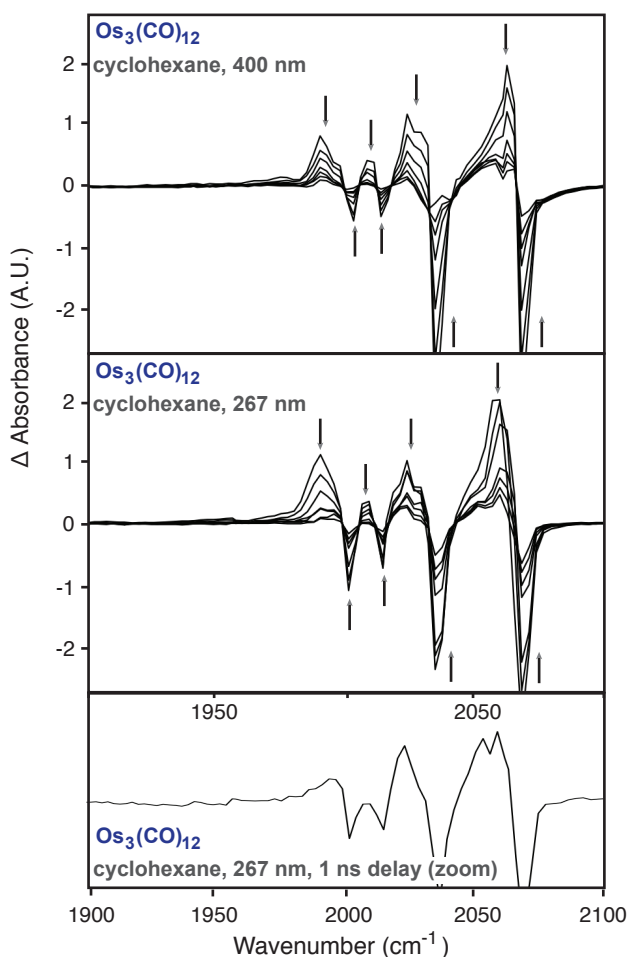


Figure 10.4. TRIR spectra of $\text{Os}_3(\text{CO})_{12}$ following 400 nm (top panel) and 267 nm (bottom panel) excitation in cyclohexane solution at delay times of 20, 50, 100, 200, 300, 400, and 700 ps. An enlarged version of the 267 nm excitation spectrum at a delay time of 1 ns is shown in the bottom panel.

Following 400 nm excitation in cyclohexane solution, product bands were observed to form at 1991, 2010, 2028, and 2062 cm^{-1} , as were parent bleaches at 2001, 2015, 2036, and 2069 cm^{-1} . The product bands are observed to decay on a timescale of ca. 150 ps (see Table 10.3), with time

constants that are similar to one another within the errors of the fits. Considering that no bridging carbonyls are present, and that most of the product absorptions decay on the picosecond timescale, we assign the major photoproduct to a metal-metal bond cleavage transient, similar to that observed for the iron congener (see structure C in Figure 10.2). DFT geometry optimizations were again unable to locate a local minimum with an extended metal-metal bond and returned to the ground state geometry calculated for Os₃(CO)₁₂. To investigate the structure of the transient metal-metal bond cleavage intermediate, single-point DFT frequency calculations were performed for structures beginning from the ground state structure with one, two, or all three Os-Os bonds elongated. Similar to the case with the Fe₃(CO)₁₂ cluster, only structures involving two or three Os-Os bonds elongated led to red-shifting of the calculated frequencies to produce results in reasonable accord with the observed spectra. For example, symmetric elongation of two Os-Os bonds to 4.4 Å yielded predicted red-shifts of 6-9 cm⁻¹ in the observable IR bands, while symmetric elongation of all three Os-Os bonds to 4.4 Å predicted red-shifts of 10-11 cm⁻¹, with the pattern of band intensities again resembling that of the ground state structure in each case. Our DFT results thus indicate that the structure of the transient rearrangement intermediate likely involves two or three elongated Os-Os bonds.

Table 10.3. Time constants for product band and bleach recoveries of Os₃(CO)₁₂ in cyclohexane following 400 and 267 nm excitation

Absorption (cm ⁻¹)	$\tau_{400 \text{ nm}}$ (ps)	$\tau_{267 \text{ nm}}$ (ps)
Product decay time constants in cyclohexane		
1991	5 ± 1	10 ± 3
	174 ± 35	129 ± 15
2010	12 ± 3	184 ± 16
	156 ± 16	
2028	5 ± 1	18 ± 4 (rise)
	126 ± 14	186 ± 32
2062	8 ± 3	14 ± 4 (rise)
	145 ± 14	164 ± 43
Parent bleach recovery time constants in cyclohexane		
2001	5 ± 1	153 ± 11
	136 ± 18	
2015	2 ± 1	13 ± 11 (rise)
	141 ± 6	183 ± 43
2036	6 ± 1	184 ± 14
	117 ± 9	
2069	6 ± 1	125 ± 18
	126 ± 17	

Considering that each of the transient bands assigned to metal-metal bond cleavage products (for both the Fe and Os clusters) present spectra that somewhat resemble those of the corresponding parent complex, but red-shifted by ca. 10 cm⁻¹, we should address the possibility that these bands could also correspond to already recovered ground state molecules (i.e. with all three metal-metal bonds intact) that are still vibrationally hot. While this possibility cannot be definitively ruled out, the available evidence suggests this is not the case. Our DFT results indicate that the metal-metal bond cleavage transients yield spectra with similarly red-shifted frequencies and are thus in accord with the spectral assignment of these bands to metal-metal bond cleavage products. Moreover, were the transient bands due primarily/entirely to vibrational cooling of ground state molecules, we would expect to observe significant band narrowing and blue-shifting of each of the positive bands observed in all of the spectra in Figures 10.1, 10.3,

and 10.4 with increasing delay time; this not the case. The majority of the transient bands observed remain at a relatively constant bandwidth and stable center frequency with increasing delay time, which is not consistent with spectral dynamics we would expect from vibrational cooling. The only band for which a dynamic blue-shift is clearly observed is the highest intensity positive transient band following 267 nm excitation of $\text{Os}_3(\text{CO})_{12}$. By contrast, the highest intensity bands in the spectra of $\text{Fe}_3(\text{CO})_{12}$ in both solvents at both excitation wavelengths actually appear to red-shift slightly with increasing delay time, probably due to their overlap with the neighboring parent bleach band. Certainly, vibrational cooling of the transient photoproducts affects these spectra; for example, several of the kinetic fits in Tables 10.1-10.3 display a fast early time component that is influenced by, or entirely due to, vibrational cooling. However, considering the agreement between the DFT calculated transient metal-metal bond cleavage products, and the lack of consistent band narrowing and blue-shifting that would be expected if the positive bands were due entirely to vibrational cooling, we feel the evidence supports assignment of the transient bands (i.e. those bands that recover on the picosecond timescale) to metal-metal bond cleavage products.

Comparison of the spectra following 267 and 400 nm excitation in Figure 10.4 shows similar band positions and rates for decay of the transient species. Making the same qualitative comparison of the parent bleach intensities as was made for the iron congener, the parent bleach at 2069 cm^{-1} maintains ca. 11% of its initial maximum intensity at 1 ns following 267 nm excitation, but only ca. 5% of its initial maximum intensity following 400 nm excitation. We interpret this to indicate that more long-lived (fragmentation or carbonyl-loss) photoproducts are formed following 267 nm excitation, as one would expect when shifting to higher excitation wavelengths. Monitoring the yield of CO-loss photoproducts by integrating the overlapping transient and CO-loss photoproduct positive bands shows the same general trend as was observed by monitoring the relative fraction of remaining parent bleach intensity. We point out that it is difficult to visualize the differences in the amount of CO-loss photoproducts at the different excitation wavelengths, as the y-axes of these spectra have been normalized to account for differences in transient band intensity due to differing extinction coefficients and pump powers at the two excitation wavelengths. Note also that the maximum intensity for transient bands is typically observed at delay times of only a few picoseconds, while the earliest delay time plotted is 20 ps (which contributes to why it is difficult to visualize the relative quantities of photoproducts remaining at longer delay times). A few of the photoproduct and bleach bands were observed to exhibit rise times that extended for 13-18 ps, and we believe this is due to vibrational cooling processes and the overlap of product and bleach bands at early delay times.

Unlike the situation for the iron congener, the photoproducts present at long delay times in these spectra do not correlate well to the absorptions for potential fragmentation products. $\text{Os}(\text{CO})_4$ would be expected to display bands at ca. 1948, 1966, 2010, and 2097 cm^{-1} ,³⁹³ which does not match the observed TRIR spectra. $\text{Os}_2(\text{CO})_8$ has been observed previously in a CH_4 matrix to show bands at 2004, 2024, and 2056 cm^{-1} ,³⁹⁴ and, while these band positions may at first appear reasonably consistent with some of the observed absorptions, there are a few pieces of evidence which are inconsistent with the formation of $\text{Os}_2(\text{CO})_8$. First, the band at 2002 cm^{-1} decays completely on the picosecond timescale, which is inconsistent with formation of a fragmentation product. Also, two bands are present at 2052 and 2060 cm^{-1} , rather than the single band in this region that would be expected for $\text{Os}_2(\text{CO})_8$. Finally, $\text{Os}_2(\text{CO})_8$ and $\text{Os}(\text{CO})_4$ would be expected to form concomitantly, and thus the absence of $\text{Os}(\text{CO})_4$ is further evidence that $\text{Os}_2(\text{CO})_8$ does not form. While the IR spectrum of $\text{Os}(\text{CO})_3$ has not, to our knowledge, been

reported, the IR spectrum of $\text{Os}_2(\text{CO})_9$ is known to exhibit bands at 1778, 2013, 2024, 2038, and 2080 cm^{-1} in alkane solution.^{395,396} These bands are clearly inconsistent with the observed TRIR spectra, demonstrating that fragmentation to yield $\text{Os}_2(\text{CO})_9$ does not occur. Thus for $\text{Os}_3(\text{CO})_{12}$, fragmentation does not appear to take place. We therefore attribute the long-lived photoproduct intensity at 1993, 2023, 2052, and 2060 cm^{-1} to carbonyl-loss products. The similarity between the band positions at both excitation wavelengths suggests that no di-carbonyl loss (i.e. $\text{Os}_3(\text{CO})_{10}$) photoproducts are observed in these spectra, as the lower energy 400 nm excitation is not expected to yield such species.

A previous study at 90 K in methylcyclohexane glass containing ^{13}C O suggested that an equatorial CO ligand is initially dissociated, followed by rearrangement to an axially vacant form.³⁶⁹ IR absorptions for this species were reported at 1970 (weak), 1996, 2021, 2051, and 2060 cm^{-1} , which, considering the difference in the experimental conditions, match the bands observed at longer delay times in the current spectra well. We thus assign the species observed at longer delay times in the present study to axially vacant $\text{Os}_3(\text{CO})_{11}$. Our DFT calculations suggest that coordination of an alkane as a token ligand at the axial site of $\text{Os}_3(\text{CO})_{11}$ is not favorable; geometry optimizations were attempted with a propane molecule occupying the vacant axial site of $\text{Os}_3(\text{CO})_{11}$, and these led to minima involving the propane molecule expelled from the axial site.

10.4 Conclusions

In this study, we have investigated the ultrafast solution-phase photochemistry of the $\text{Fe}_3(\text{CO})_{12}$ and $\text{Os}_3(\text{CO})_{12}$ clusters following 267 and 400 nm excitation. Significantly, no formation of bridging carbonyl cluster photoproducts from non-bridging parent molecules was observed. This observation appears to hold true for rearrangement isomers arising from metal-metal bond cleavage, as well as the carbonyl-loss photoproducts, of either the iron or osmium congeners. This is in direct contrast to the observations made previously for $\text{Ru}_3(\text{CO})_{12}$, in which two distinct types of bridging photoproducts formed from the all-terminal parent complex. In that study, no transient species without bridging carbonyls were experimentally observed. In the present study, the only transient trimetallic photoproducts observed to contain bridging carbonyls were the rearrangement isomer and carbonyl-loss product that we believe arise from photolysis of the C_{2v} bridging isomer of $\text{Fe}_3(\text{CO})_{12}$.

The photochemistry of $\text{Fe}_3(\text{CO})_{12}$ differs from that of its ruthenium and osmium congeners in that UV irradiation leads to fragmentation of the cluster into $\text{Fe}(\text{CO})_4$ and $\text{Fe}_2(\text{CO})_8$ moieties. For $\text{Ru}_3(\text{CO})_{12}$ ⁴ and $\text{Os}_3(\text{CO})_{12}$, fragmentation of the cluster does not occur, and carbonyl loss products are the only photoproducts arising from dissociation of the cluster. While it remains difficult to offer a simple explanation for why the all-terminal ruthenium cluster is the only in this series to yield photoproducts containing bridging carbonyls, the observation of fragmentation products for the iron cluster alone can likely be explained by differences in the strength of the metal-metal bonding interactions. Previous reports have demonstrated that the strength of metal-metal interactions among the homometallic group 8 metal carbonyl clusters tend to increase with increasing atomic number, and thus are expected to be weakest in the iron species.^{385,397,398}

These observations carry implications for the species involved in the photochemical reactivity of these clusters on longer timescales; the transient metal-metal bond cleavage products recover on the picosecond timescale, implying that these cannot participate in reactions

occurring on diffusion limited timescales. Thus the fragmentation and carbonyl-loss photoproducts of the iron and osmium clusters, respectively, will dictate the photochemistry of these clusters on longer timescales. It is interesting that, despite their analogous structures, each of the homoleptic group 8 transition metal carbonyl clusters exhibits unique photochemistry on the ultrafast timescale. The photochemistry of the group 8 clusters thus appears to be quite nuanced and not easily generalized.

11 Picosecond time-resolved infrared and DFT studies of the photochemistry of $\text{Co}_4(\text{CO})_{12}$ in solution

The following chapter is reproduced (adapted) in part with permission from (Lomont, J. P.; Nguyen, S. C.; Harris, C. B. *Organometallics*, 2012, 31, 4031-4038.). Copyright (2013) American Chemical Society.

11.1 Introduction

The chemistry of transition metal carbonyl clusters, including their structure, fluxional dynamics, and thermal and photochemical reactivity, is a subject of considerable interest in the chemical sciences.^{311,317,399-401} Among these, clusters of the group 8 and group 9 metals of the type $\text{M}_3(\text{CO})_{12}$ ($\text{M} = \text{Fe}, \text{Ru}, \text{Os}$) and $\text{M}_4(\text{CO})_{12}$ ($\text{M} = \text{Co}, \text{Rh}, \text{Ir}$), respectively, have served as models for the behavior of other transition metal clusters. We present an investigation into the photochemical behavior of $\text{Co}_4(\text{CO})_{12}$ in polar and nonpolar solvents using picosecond time-resolved infrared (TRIR) spectroscopy. Ultrafast studies on the photochemistry of $\text{M}_3(\text{CO})_{12}$ clusters have provided insight into their rearrangement and ligand dissociation dynamics,^{318,372} but, to our knowledge, this constitutes the first investigation into the photochemistry of an $\text{M}_4(\text{CO})_{12}$ complex on the ultrafast timescale.

Though it was the first tetranuclear cluster ever prepared,⁴⁰² the structure of $\text{Co}_4(\text{CO})_{12}$ remained unclear for several decades. A number of NMR investigations have addressed the structure of the cluster using ^{13}C , ^{17}O , and ^{59}Co resonances.⁴⁰³⁻⁴¹² ^{13}C NMR studies initially yielded controversial results, but the structure of this species in alkane solutions and in the solid state is now known to be of C_{3v} symmetry.⁴⁰⁹⁻⁴¹⁶

Though its catalytic activity has been investigated to a lesser extent than that of many other metal carbonyl clusters, $\text{Co}_4(\text{CO})_{12}$ has been used as a catalyst in hydroformylation and hydroesterification reactions.^{417,418} Synthetic chemists working on the $\text{Co}_2(\text{CO})_8$ catalyzed Pauson-Khand reaction (PKR) originally suggested that the formation of $\text{Co}_4(\text{CO})_{12}$ was an impediment to the PKR,^{419,420} though in the past decade $\text{Co}_4(\text{CO})_{12}$ has actually gained significant attention for its role as a catalyst in the PKR in both organic and aqueous solutions.⁴²¹⁻⁴²⁵ At a CO pressure of 10 atm, $\text{Co}_4(\text{CO})_{12}$ was demonstrated to achieve higher catalytic efficiency than the more widely used $\text{Co}_2(\text{CO})_8$ catalyst.⁴²¹

Existing studies on the photochemistry of $\text{Co}_4(\text{CO})_{12}$ are somewhat limited. Interestingly, UV photolysis of either $\text{Co}_4(\text{CO})_{12}$ or $\text{Co}_2(\text{CO})_8$ has been shown to significantly impede the catalytic hydroformylation of alkenes, relative to the thermally catalyzed reaction.⁴²⁶ Recent studies have also shown that $\text{Co}_4(\text{CO})_{12}$ in CH_2Cl_2 solution can serve, under thermal or photochemical conditions, as a precursor to cobalt-carbon clusters with a cubane structure, which act as single-molecule magnets.⁴²⁷⁻⁴²⁹ The strongest absorptions in the electronic spectrum of $\text{Co}_4(\text{CO})_{12}$ are centered at 340 and 375 nm. Both have been assigned to multiple overlapping transitions, which are predicted to result primarily in weakening of the metal-metal bonding between the apical and basal Co atoms.^{430,431} Considering the results of a previous study on the trimetallic $\text{Ru}_3(\text{CO})_{12}$ cluster, it initially seemed likely that 267 nm excitation would also lead to CO-loss products via MLCT excitations.³¹⁸

In this study we investigate the photochemically induced rearrangement dynamics of $\text{Co}_4(\text{CO})_{12}$, which may serve as a model for the photochemistry of other M_4L_{12} clusters. The observed photochemistry in cyclohexane and CH_2Cl_2 solvents is compared at 267 and 400 nm excitation wavelengths, and DFT calculations are used to facilitate interpretation of the experimental spectra.

11.2 Methods

11.2.1 Sample Preparation

$\text{Co}_4(\text{CO})_{12}$ was purchased from Strem Chemicals Inc. Cyclohexane and CH_2Cl_2 were purchased from Sigma–Aldrich Co. All samples and solvents were used without further purification. Dilute solutions of $\text{Co}_4(\text{CO})_{12}$ were stable in air at ambient temperatures for at least a few hours (verified via FTIR) in each solvent. Samples used to collect TRIR spectra were prepared at a concentration of ca. 2 mM.

11.2.2 Data Analysis

Kinetic data in this work result from spectra measured at delay times between 0 and 1100 ps between the UV/visible-pump and IR-probe pulses. Kinetic traces for each spectral feature were obtained by integrating a narrow spectral region (ca. 3 cm^{-1} wide) surrounding the reported frequency. The kinetic data were then fit to exponential curves using Origin Pro 8 software. To obtain fits with exponential rise and decays, a separate, home-written, fitting program was used. Errors on experimental time constants are reported as 95% confidence intervals.

11.2.3 Density Functional Theory Modeling

Density functional theory (DFT) calculations have been carried out to facilitate assignment of the absorptions observed in the TRIR experiments. All calculations were carried out using the BP86,^{37,38} B3LYP,^{37,39} and PW91^{40–42} functionals in the Gaussian09⁴³ package using the lanl2dz^{44,45} basis on Co and the aug-cc-pDVZ basis^{46–48} set on all other atoms. Each geometry optimization was followed by a frequency analysis to ensure that all geometries were genuine local minima. Beyond checking for reasonable consistency between the experimentally observed spectra and the calculated structures, we did not find the calculated frequencies to be particularly helpful in assigning the experimental spectra. Many species show similar predicted CO-stretching frequencies, and the errors in the absolute frequencies are too large to make quantitative comparisons between calculated and observed values.

11.3 Experimental Results

TRIR spectra in the CO stretching region are presented as difference absorbance spectra. Positive absorptions correspond to newly formed species, while negative bands correspond to the depletion of parent molecules.

11.3.1 TRIR in Cyclohexane Solution

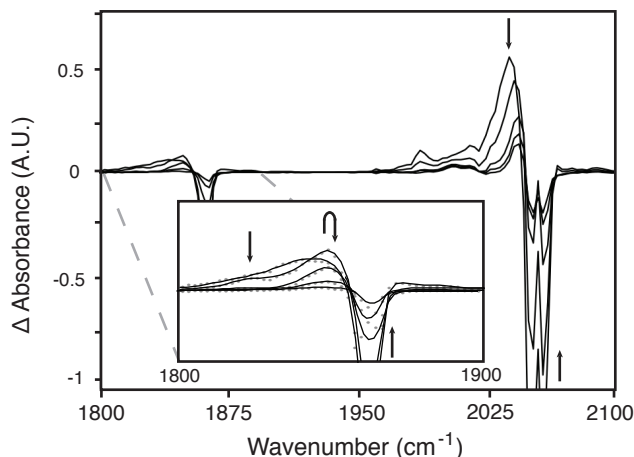


Figure 11.1. TRIR spectra at UV-IR delay times of 10, 40, 200, 400, and 1000 ps obtained following 400 nm photolysis in cyclohexane solution. The inset magnifies the 1800-1900 cm^{-1} spectral region. In the inset, gray dots are actual data points while black lines are fits to the data.

Figure 11.1 shows TRIR spectra of $\text{Co}_4(\text{CO})_{12}$ in cyclohexane following 400 nm excitation. Broad absorptions between ca. 1975 and 2050 cm^{-1} correspond to terminal CO-stretching modes of the photoproducts, while those between 1800 and 1855 cm^{-1} correspond to bridging CO-stretching modes. Parent bleaches are observed at 1863, 2054, and 2062 cm^{-1} . Overlapping peaks of the terminal CO-stretching modes of different species make it difficult to separate their kinetics in the terminal region of the spectrum, but the bridging region contains absorptions at ca. 1824 cm^{-1} and ca. 1849 cm^{-1} that clearly display distinct kinetics, suggesting that two distinct species must be present. Kinetic traces of the absorptions at 1824, 1849, and 1863 cm^{-1} are shown in Figure 11.2.

While the 1824 cm^{-1} region decays to baseline on the timescale studied, we observe some intensity at ca. 1850 cm^{-1} even at longer delay times. We interpret this to suggest that the 1824 cm^{-1} absorption results solely from metal-metal bond cleavage products, while the absorption at 1849 cm^{-1} has contributions from both metal-metal cleavage and CO-loss products. A weak absorption is also present at ca. 1880 cm^{-1} , but the weak intensity and overlap with the parent bleach make it difficult to obtain reliable kinetics in this region.

Table 11.1. Experimental Time Constants for Product Peaks and Bleach Recoveries in Cyclohexane at 400 and 267 nm

Absorption (cm^{-1})	$\tau_{400 \text{ nm}}$ (ps)	$\tau_{267 \text{ nm}}$ (ps)
Product decay time constants in cyclohexane		
1824	95 ± 4	119 ± 9
1849	36 ± 5 (rise)	54 ± 8 (rise)
	170 ± 9	152 ± 15
2010 ^a	5 ± 1	8 ± 1
	114 ± 10	166 ± 24
2031 ^a	13 ± 1	17 ± 2
	140 ± 8	173 ± 24
2040 ^a	26 ± 4	17 ± 6
	156 ± 13	191 ± 22
Parent bleach recovery time constants in cyclohexane		
1863 ^a	15 ± 1	11 ± 2
	157 ± 2	158 ± 4
2052 ^a	19 ± 3	15 ± 2
	154 ± 4	183 ± 18
2060 ^a	16 ± 2	22 ± 5
	164 ± 8	237 ± 39

(a) The fast decay components of these absorptions may correspond to vibrational or electronic relaxation processes, or to fast recombination of transiently dissociated complexes.

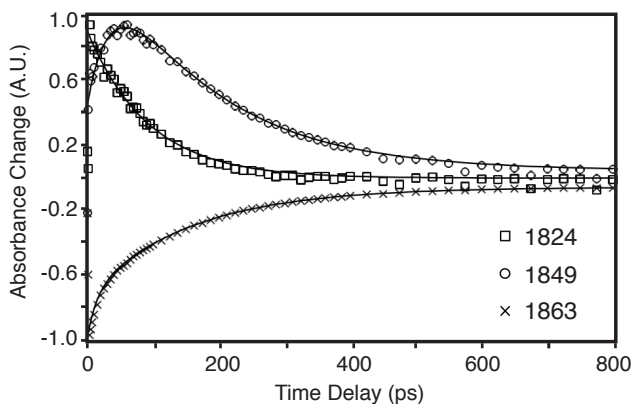


Figure 11.2. Kinetic traces obtained at 1824, 1849, and 1863 cm^{-1} following 400 nm excitation in cyclohexane. Lines represent exponential functions fit to the experimental data points.

TRIR spectra collected using 267 nm excitation are qualitatively similar to those obtained using 400 nm excitation. Kinetic traces of the CO-stretching absorptions following both excitation wavelengths are summarized in Table 11.1. The most noteworthy difference between the spectra obtained with the two excitation wavelengths is the amount of parent bleach intensity remaining at longer delay times; it is clear that more long-lived photoproducts are present following 267 nm excitation, relative to when 400 nm excitation is used. If we compare the 2060 cm^{-1} parent bleach intensity at 1 ns relative to its maximum value at early delay times (ca. 2 ps), this absorption maintains 21% of its initial maximum intensity using 267 nm excitation, but only 10% following 400 nm excitation. While these numbers are only intended to provide a qualitative comparison of the quantum yields for photochemical processes, it is clear that more photoproducts remain at longer delay times following 267 nm excitation than with 400 nm excitation. As will be discussed later, we can interpret this in terms of the branching ratio for

formation of CO-loss vs. metal-metal bond cleavage products. Overall, the observed photoproducts exhibit only small downshifts in frequency relative to the parent complex. One possible explanation for this is that, in a tetrametallic cluster, the changes in electron density as bonds are broken or formed are spread over several metal centers, whereas in complexes containing only a single metal center, the changes in electron density are localized to the lone metal, and thus tend to affect the CO stretching frequencies more significantly.

11.3.2 TRIR in CH₂Cl₂ Solution

TRIR difference spectra of Co₄(CO)₁₂ following 400 nm excitation in CH₂Cl₂ are shown in Figure 11.3. Absorptions from ca. 1950-2045 cm⁻¹ again reflect terminal carbonyl stretches of transient photoproducts, and absorptions in the 1800-1850 cm⁻¹ region correspond to bridging CO-stretching modes. These spectra are qualitatively similar to those obtained in cyclohexane, and kinetic fitting parameters for the various absorptions are given in Table 11.2. Two time scales for product decay are again observed in the bridging region, as can be seen from the kinetic traces at 1825 and 1840 cm⁻¹ in Figure 11.4. Relative to the decay times observed in cyclohexane, the transient species have longer lifetimes in CH₂Cl₂. The significantly different decay times of the absorptions at 1824 cm⁻¹ in cyclohexane and 1825 cm⁻¹ in CH₂Cl₂ clarify the fact that this absorption is not simply the result of vibrational cooling of the absorptions at 1849 cm⁻¹ in cyclohexane or 1840 cm⁻¹ in CH₂Cl₂. This solidifies the assignment of these kinetically uncorrelated absorptions to two distinct chemical species. Also supporting this notion is the fact that we do not observe evidence of significant blue shifting of the terminal carbonyl frequencies.

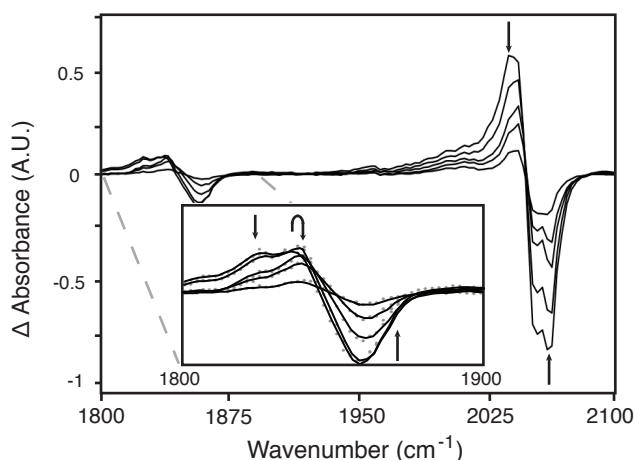


Figure 11.3. TRIR spectra at UV-IR delay times of 10, 40, 200, 400, and 1000 ps obtained following 400 nm photolysis in CH₂Cl₂ solution. The inset magnifies the 1800-1900 cm⁻¹ spectral region. In the inset, gray dots are actual data points while black lines are fits to the data.

Spectra and kinetics obtained following 267 nm excitation are similar to those obtained following 400 nm excitation, with more photoproduct intensity at longer delay times again observed following 267 nm excitation, relative to when 400 nm excitation is used. In this case, the 1 ns spectrum following 267 nm excitation shows that the parent bleach at 2062 cm⁻¹ maintains 20% of its initial maximum intensity, while this fraction decreases to 7% when 400 nm

excitation is used. These fractions are similar to those observed in cyclohexane solution. In both solvents, and with both excitation wavelengths, the higher frequency bridging product absorption exhibits a rise time of ca. 50 ps. We believe there are two reasonable explanations for this rise. The first is vibrational cooling of the corresponding photoproduct, as this process would not be expected to show a significant solvent dependence. An alternative possibility is that, since this peak overlaps with the parent bleach, the faster recovery of the lower frequency absorption at 1824/1825 cm^{-1} leads to significant parent bleach recovery at early times, causing the higher frequency kinetic trace to increase in intensity at early times.

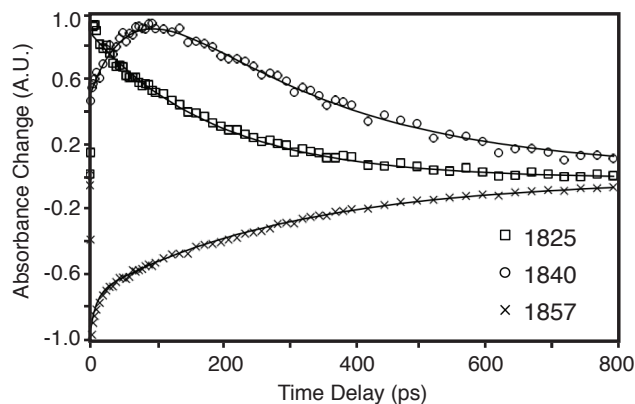


Figure 11.4. Kinetic traces obtained at 1825, 1840, and 1857 cm^{-1} following 400 nm excitation in CH_2Cl_2 . Lines represent exponential functions fit to the experimental data points.

Table 11.2. Experimental Time Constants for Product Peaks and Bleach Recoveries in CH_2Cl_2 at 400 and 267 nm

Absorption (cm^{-1})	$\tau_{400 \text{ nm}}$ (ps)	$\tau_{267 \text{ nm}}$ (ps)
Product decay time constants in CH_2Cl_2		
1825	276 ± 12	322 ± 23
1840	48 ± 10 (rise)	52 ± 6 (rise)
	390 ± 72	435 ± 34
2015 ^a	9 ± 1	7 ± 2
	190 ± 18	116 ± 17
2035 ^a	18 ± 1	28 ± 6
	220 ± 10	173 ± 56
2045 ^a	29 ± 3	25 ± 19
	319 ± 18	188 ± 15
Parent bleach recovery time constants in CH_2Cl_2		
1857 ^a	9 ± 1	7 ± 3
	307 ± 11	302 ± 12
2054 ^a	20 ± 1	22 ± 2
	245 ± 9	283 ± 27
2062 ^a	18 ± 1	26 ± 3
	256 ± 6	353 ± 31

(a) The fast decay components of these absorptions may correspond to vibrational or electronic relaxation processes, or to fast recombination of transiently dissociated complexes.

In determining whether the observed kinetic traces in both solvents correspond to ground state rearrangement products, vibrationally excited products, or electronically excited species, we can compare the data collected at different excitation wavelengths and different solvents to gain

important insights. The fact that the spectra in a given solvent are qualitatively very similar and show similar kinetics at different excitation wavelengths indicates that the observed dynamics are not the result of electronically excited species; if electronically excited species did account for any of the observed dynamics, we would expect to observe differences in the TRIR spectra as a function of excitation wavelength. Comparing the data in different solvents, the differing lifetimes of the transient rearrangement intermediates indicate that the observed lifetimes are not due to vibrational relaxation; if, for example, the lower frequency bridging absorption was merely a vibrationally hot species, we would not expect its lifetime to change so significantly between solvents. This same reasoning holds for the other absorption features. For these reasons, we assign the observed dynamics to ground state species.

11.4 DFT Results and Discussion

To facilitate interpretation of the experimental results, we have carried out geometry optimizations and frequency calculations for $\text{Co}_4(\text{CO})_{12}$ and several potential photoproducts resulting from metal-metal bond cleavage or CO-loss. Due to the large number of overlapping absorptions from CO-stretching modes, our assignments of the experimentally observed species must rely strongly on the DFT results. As we will describe, however, the results we have obtained appear to match with, and explain, the experimental data quite well.

In accord with previous studies, our calculations yield a ground state C_{3v} structure for the parent complex, shown from several angles in Figure 11.5a. Looking at what non-dissociative rearrangement products can be formed from excitation of the parent molecule, there initially appeared to be two possibilities. One is cleavage of a metal-metal bond between the apical Co and any of the three equivalent basal Co atoms, while the other is rearrangement of a bridging CO between any pair of basal Co atoms to become a terminal CO, which would also likely involve the concurrent cleavage of a metal-metal bond between the two formerly bridged Co atoms. Previous studies into the electronic spectrum have suggested that cleavage of an apical-basal Co-Co bond is most likely. We investigated both of these possible pathways using DFT calculations.

11.4.1 Rearrangement Pathways

Rearrangement of a bridging CO along with cleavage of a metal-metal bond between any of the three basal Co atoms did not lead to any stable unsolvated local minima, nor did it lead to any stable alkane or CH_2Cl_2 solvated geometries (see SI for details of these calculations). Attempts at geometry optimizations following from this pathway returned to the parent species with the solvent molecule, if present, expelled from $\text{Co}_4(\text{CO})_{12}$ cluster. We interpret this to indicate that no stable local minimum exists that follows in a simple fashion from cleavage of a basal-basal Co-Co bond and/or rearrangement of a bridging CO-ligand. Following this initial dissociation pathway, no clear description arose to explain the observed rearrangement dynamics.

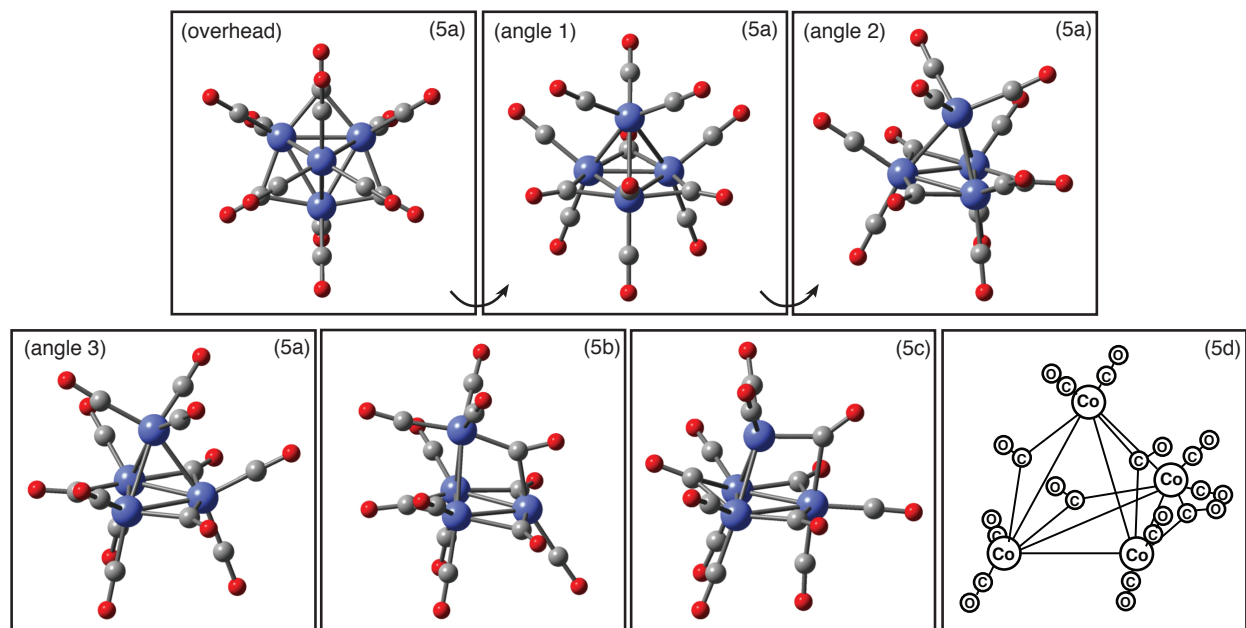


Figure 11.5. Calculated BP86 structures for the parent $\text{Co}_4(\text{CO})_{12}$ (5a) shown at several angles, as well as the two rearrangement products (5b and 5c) formed via cleavage of an apical-basal Co-Co bond, along with a line drawing representation of the D_{2d} structure proposed by Cotton in Ref. 26 (5d).

Following the metal-metal cleavage pathway involving an apical-basal Co-Co bond did lead to two stable rearrangement geometries. Two different products can readily form, since either an apical or basal CO ligand can rearrange to bridge the cleaved metal-metal bond (5b and 5c). We believe these species correspond to the rearrangement products observed experimentally.

Our attempts to locate alkane and CH_2Cl_2 solvent coordinated minima for structure 5b showed that the solvent molecule may coordinate only weakly via a basal Co atom (5-alkyl and 5b- CH_2Cl_2 in Table 11.3). We were unable to locate any solvated minima for structure 5c, presumably due to increased steric crowding. Table 11.3 lists the energies of each of these complexes. While converged geometries were obtained for 5b-alkyl and 5b- CH_2Cl_2 , it is noteworthy that the binding energies to these solvents are weakly favorable at best; in several cases these are even calculated to have higher energies than the dissociated solvent and cluster moieties.

Attempts to locate other plausible rearrangement structures were unsuccessful; these are described in more detail in the SI of the published manuscript, and we will briefly address just one other relevant result here. Despite evidence for a C_{3v} crystal structure, Cotton once suggested that a structure of D_{2d} symmetry may actually correspond to the solution phase geometry at ambient temperature (see Figure 11.5d).⁴³² Attempts to locate a structure corresponding to this geometry were unable to locate a corresponding local minimum, and instead led to a structure that differs significantly from the C_{3v} parent complex or either of the other rearrangement structures. This new structure contained 6 bridging and 6 terminal carbonyl ligands. To reach this structure from the parent complex would require the breaking and formation of many chemical bonds, thus it does not appear to be a plausible rearrangement intermediate for the species observed in our experiments.

To relate the calculated structures to our experimental spectra, we first consider that 2 distinct species were observed to recover on the picosecond timescale in each solvent. The decay time constants in either solvent are on the timescale of hundreds of picoseconds, which is far shorter than would be expected for a solvent-coordinated rearrangement product. For comparison, a previous study on $\text{Ru}_3(\text{CO})_{12}$ observed a THF solvated complex with a lifetime of 50 ms,³⁹² which is ca. 10^8 times longer than the lifetimes of the transient rearrangement products observed in the present study. The frequency shift of the product absorptions between cyclohexane and CH_2Cl_2 solvents is also relatively small, consistent with a difference in dielectric constants between solvents, and not indicative of differences in solvent coordination between the two solvent environments. These observations agree with the results of our calculations, which indicate solvation of the rearrangement intermediates is weakly favorable at best. We thus assign the two species observed experimentally in each solvent to unsolvated 5b and 5c. While we cannot rule out the existence of other rearrangement products, the experimental results demonstrate the presence of two species, and only two reasonable rearrangement geometries could be located, supporting the notion that 5b and 5c are the predominant rearrangement products formed upon photoexcitation. It is, of course, worth noting that the specific bonding arrangements of the structures assigned to the experimental rearrangement products are obtained from the results of the DFT calculations. If more subtle conformational changes, such as the reversible opening of a bridging CO ligand, were at work, DFT calculations may fail to locate a corresponding minimum.

To assign which of the experimentally observed absorptions corresponds to each of 5b and 5c, we first looked to the DFT calculated frequencies; however these are predicted to be similar for both compounds. Each is predicted to exhibit 2 relatively strong absorptions in the bridging region, and the absolute calculated frequencies are not necessarily useful, as the typical errors are on the order of the separation of the experimentally observed absorptions. As only two distinct kinetic traces are observed, it is likely that each species has an overlapping absorption with the parent complex. An alternative possibility is that the DFT calculated frequencies overestimate the separation of the two absorptions for each species, and in reality each species has two absorptions at similar frequencies.

Table 11.3. Relative Energies Calculated for $\text{Co}_4(\text{CO})_{12}$ and Rearrangement Complexes

Species	ΔH relative to Parent (kcal/mol)		
	BP86	PW91	B3LYP ^a
5a	0	0	0
5b	29.2	29.1	28.1
5b-alkyl	30.6	27.5	-
5b- CH_2Cl_2	26.4	24.3	29.8
5c	2.0	1.2	5.3

(a) No stable minimum could be located for 5b coordinated to propane.

To assess which species is expected to have a larger barrier to rearrangement back to the parent complex, we located transition states beginning from species 5b or 5c returning to 5a, and the associated energies are given in Table 11.4. 5c is calculated to have the larger barrier to rearrangement back to the parent complex, which suggests that this species is the longer-lived rearrangement isomer corresponding to the kinetic trace at 1849 cm^{-1} in cyclohexane (1840 cm^{-1} in CH_2Cl_2). Considering these are gas phase calculations, the low calculated barriers for return to the parent complex are in reasonable agreement with the observed lifetimes of the rearrangement

species. Species 5b is thus assigned to the kinetic trace at 1824 cm⁻¹ in cyclohexane (1825 cm⁻¹ in CH₂Cl₂).

Table 11.4. Calculated Energy Barriers for Rearrangement to the Parent Complex

Transition State	ΔH^\ddagger to Return to Parent Complex (kcal/mol)		
	BP86	PW91	B3LYP
5b → 5a	0.30	0.61	0.50
5c → 5a	1.51	1.65	0.79

While it remains difficult to conclusively assign which of 5b and 5c correspond to which kinetic trace, we feel the fact that only these two structures could be located, despite great effort to search for others, provides strong support for our assignment of the two observed rearrangement products as species 5b and 5c. Both have lifetimes on the same order of magnitude and are present in comparable quantities, which is not surprising, given the parallel nature of their formation and recovery via ligand rearrangements. We attribute the solvent dependence of the lifetimes of both rearrangement products to stabilization of the rearrangement intermediates in the more polar CH₂Cl₂ solvent.

11.4.2 Carbonyl-Loss Products

Looking at the absorptions that remain present at longer delay times, the similarities between the quantities of these species in each solvent, combined with the observed excitation wavelength dependence of their formation, suggests that these absorptions correspond to CO-loss products rather than to solvated rearrangement intermediates. Were a solvated rearrangement species present, we expect that its formation should be solvent dependent, and thus cause a noticeable difference in the quantity of long-time parent bleach intensity in the different solvents; this is not the case. The wavelength dependence thus indicates that the higher energy of the 267 nm photons leads to a greater fraction of CO-loss products. We also do not believe these absorptions correspond to fragmentation products, such as Co(CO)₄ or Co₂(CO)₈. Co(CO)₄ has a characteristic absorption at 2011 cm⁻¹, and Co₂(CO)₈ has absorptions at 1857, 2023, 2041, and 2070 cm⁻¹ in *n*-heptane.⁴³³ While we do observe photoproduct intensity near 2010 cm⁻¹, there appears to actually be more than one absorption present in this region. Another possible set of fragmentation products we considered were the odd electron fragments Co(CO)₃ and Co₃(CO)₉, the IR spectra of which, to our knowledge, have not been reported. For this reason, we can only rely on DFT calculations to assess the presence of these intermediates. DFT results predict three strong terminal CO stretching modes for Co₃(CO)₉ between 2000-2020 cm⁻¹ (BP86 values). Co(CO)₃ is calculated to have two strong, distinct IR bands downshifted ca. 40-60 cm⁻¹ from those of the terminal stretching modes calculated for Co₃(CO)₉, and we would expect these to be relatively sharp, compared to those of a cluster. Since the two species would have to form from cleavage of a common precursor, Co₄(CO)₁₂, we would also expect the strong CO-stretching bands of each species to exhibit comparable intensities. These predictions are clearly not consistent with the observed spectra at long delay times, and for this reason we ruled out fragmentation to Co(CO)₃ and Co₃(CO)₉ as a possible pathway. The data are thus most consistent with the formation of a CO-loss product. This is similar to the results of a previous TRIR study on Ru₃(CO)₁₂ using the same excitation wavelengths, which observed CO-loss products but no evidence for fragmentation of the cluster.³¹⁸

To investigate the nature of the CO-loss products, we carried out geometry optimizations following loss of one of each of the 4 types of CO ligands (apical, basal bridging, and 2 types of basal terminal) from the parent complex. Deletion of an apical or either type of basal terminal CO ligand led to the structures shown in Figure 11.6, while deletion of a bridging ligand led to rearrangement of an apical CO to become a bridging CO, resulting in structures very similar to 6a. Geometry optimizations were carried out for alkane and CH_2Cl_2 solvated versions of each.

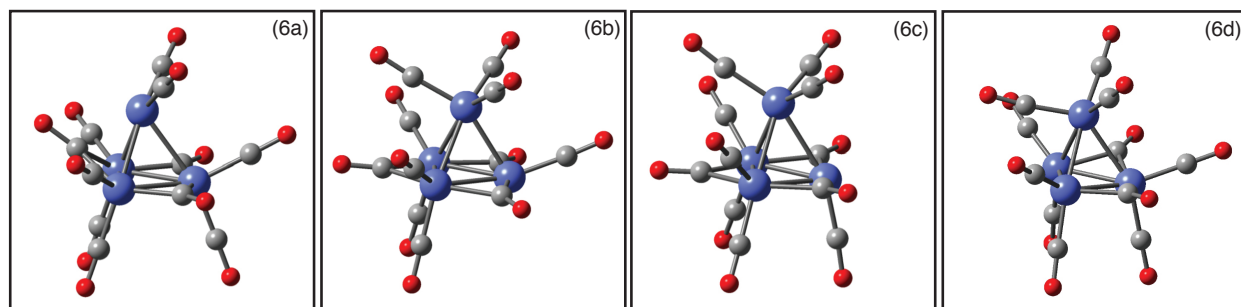


Figure 11.6. Calculated BP86 structures CO-loss products formed from dissociation of a carbonyl ligand from the parent species (5a). Since a local minimum could not be located for the unsolvated bridging CO-loss complex, the structure shown in panel (d) was obtained from the CH_2Cl_2 -solvated bridging loss complex with the solvent molecule not shown.

The relative stabilities of these species are given in Table 11.4. In the case of the bridging-loss complexes, alkane and CH_2Cl_2 solvated species were located, but these geometries could only be converged when the BP86 functional was used.

While calculations and experiments cannot tell us which of the CO ligands is dissociated, we seek to determine which CO-loss product(s) is (are) most stable, since rearrangement to the most stable isomer is likely to determine the subsequent chemistry of these complexes. Among the unsolvated CO-loss species, the apical CO-loss structure (6a) is most stable. Using the BP86 functional, which generally gave intermediate results between those of the B3LYP and PW91 functionals, 6a is favored by at least 8.3 kcal/mol over each other CO-loss species. Calculated structures for alkyl and CH_2Cl_2 solvated structures showed more favorable binding energies for coordination at either of the two terminal CO-loss sites, but this is weighed against the higher intrinsic stability of the apical CO-loss complex. The energies calculated for each complex, measured relative to unsolvated 6a, are given in Table 11.5.

Among the alkyl-solvated complexes, the apical CO-loss complex (6a-alkyl) is calculated to be the most stable. However, the binding energy of only ca. 1-4 kcal/mol is notably lower than values of ca. 11-13 kcal/mol that have been measured experimentally for coordination of an alkane as a token ligand to unsaturated 16-electron complexes,⁴³⁴⁻⁴³⁶ thus we tentatively assign the CO-loss photoproduct observed in cyclohexane to 6a-alkyl, though it also seems reasonable that unsolvated 6a may be present in solution.

Among the CH_2Cl_2 solvated complexes, the apical CO-loss species (6a- CH_2Cl_2) is again calculated to be the most stable. While CO-loss at the apical site leads to a product that is intrinsically more stable, the fact that this photoproduct does not interact as strongly with CH_2Cl_2 as the basal-terminal CO-loss products (6b- CH_2Cl_2 and 6c- CH_2Cl_2) leaves it only ca. 1.5-2.5 kcal/mol more stable than these isomers. The calculated frequencies for 6a- CH_2Cl_2 , 6b- CH_2Cl_2 , and 6c- CH_2Cl_2 are similar, making it difficult to unambiguously assign the CO-loss product in CH_2Cl_2 solution, thus our assignment to 6a- CH_2Cl_2 remains tentative.

Table 11.5. Relative Energies Calculated for CO-loss Photoproducts

Species	ΔH relative to Parent (kcal/mol)		
	BP86	PW91	B3LYP
6a	0	0	0
6b	9.5	9.5	8.3
6c	10.0	9.8	9.6
6a-alkyl	-1.6	-4.2	-1.1
6b-alkyl	1.8	-1.2	2.5
6c-alkyl	2.2	-1.0	3.4
6d-alkyl ^a	10.0	-	-
6a-CH ₂ Cl ₂	-3.9	-7.2	-2.7
6b-CH ₂ Cl ₂	-2.2	-5.3	-1.4
6c-CH ₂ Cl ₂	-2.3	-5.5	-0.9
6d-CH ₂ Cl ₂ ^a	10.2	-	-

(a) No stable minimum could be located for 6d-alkyl or 6d-CH₂Cl₂ with the PW91 or B3LYP functionals

While DFT calculations allow us to identify the most stable CO-loss structures, energy differences of only a few kcal/mol may fall within the errors of the calculations, so conclusions regarding these complexes remain tentative. It is reassuring that all three functionals result in the same qualitative trends in energy differences.

In the context of the photochemistry of Co₄(CO)₁₂, it is noteworthy that 267 and 400 nm excitation wavelengths lead to only transient rearrangement products and CO-loss complexes, with no evidence for fragmentation to form Co(CO)₄ or Co₂(CO)₈. This is important, because knowledge of the photoproducts formed via direct excitation of the parent complex facilitates our understanding of the subsequent chemistry of these complexes. In previous studies on cobalt catalyzed hydroformylation and hydroesterification reactions, and the Pauson-Khand reaction, the catalytically active species were believed to be Co₂(CO)₈ or species derived from Co₂(CO)₈, such as HCo(CO)₄ or HCo(CO)₃.^{437,438} The present study suggests that photochemical formation of Co(CO)₄ radicals, hydrides, Co₂(CO)₈, or any other fragmentation products must occur through subsequent thermal or photochemical reactions of the Co₄(CO)₁₁ CO-loss complexes. Another possibility is that the yield of fragmentation products is quite low, but that their concentration accumulates over time. The short (sub-nanosecond) lifetimes of the rearrangement products (5b and 5c) indicate that these are not likely to play an important role in reactivity occurring on diffusion limited, or longer, timescales in dilute solution.

11.5 Conclusions

The photochemical dynamics of Co₄(CO)₁₂ were studied using picosecond TRIR spectroscopy. In both cyclohexane and CH₂Cl₂ solvents, 267 and 400 nm excitation result primarily in cleavage of an apical-basal Co–Co bond and formation of two new bridged intermediates, 5b and 5c. The formation of these species involves rearrangement of either a basal (5b) or an apical (5c) carbonyl to bridge the cleaved Co–Co bond. Both species exhibit a solvent dependent lifetime, and both decay on the timescale of hundreds of picoseconds. These lifetimes indicate that neither forms a solvent-coordinated complex in either cyclohexane or CH₂Cl₂ solvent. We thus interpret the solvent dependence of the lifetimes to be caused by the differing

solvent polarities, with the more polar CH_2Cl_2 solvent stabilizing the rearrangement intermediates relative to the cyclohexane solvent. It is important to emphasize the specific structural assignments of these species rely heavily on the DFT results. In the process of performing DFT calculations to search for other potential rearrangement intermediates, we found no stable minimum corresponding to the D_{2d} geometry once proposed by Cotton,⁴³² implying that this structure does not likely play a role in the thermal or photochemical reactivity of $\text{Co}_4(\text{CO})_{12}$.

Carbonyl loss accounts for a minor, but important photochemical pathway, with a greater fraction of CO-loss products forming following 267 nm excitation, relative to when 400 nm excitation is used. In cyclohexane or other alkane solvents, DFT calculations suggest that the alkyl-solvated apical-CO-loss species is the most stable, though coordination to alkyl groups should be weak. In CH_2Cl_2 , the solvent-coordinated apical-CO-loss species $6a\text{-CH}_2\text{Cl}_2$ is calculated to be the most stable.

Importantly, we do not observe evidence for the formation of $\text{Co}(\text{CO})_4$, $\text{Co}_2(\text{CO})_8$, $\text{Co}(\text{CO})_3$, or $\text{Co}_3(\text{CO})_9$ arising directly from photoexcitation of the parent species. Taking into account the picosecond lifetimes observed for the rearrangement complexes, photoproducts involving loss of a single CO ligand from the $\text{Co}_4(\text{CO})_{12}$ parent molecule are most likely to dictate the subsequent reactivity in solution. To our knowledge, this work represents the first investigation into the photochemistry of an M_4L_{12} complex on the picosecond timescale. The experimental and computational results probe the role of bridging carbonyl intermediates and formation of CO-loss products, which provide insight relevant to existing and future studies on the chemistry of tetrametallic clusters.

12 Exploring the Utility of Thermal-Photochemical CO-Delivery with CORM-2

The following chapter is intended to be published in an American Chemical Society Journal and thus we claim no copyright for the text or figures contained in this chapter.

12.1 Introduction

Once considered a dangerous toxin, nitric oxide has since become widely recognized for its critical role as a signaling molecule.⁴³⁹ Similarly, research on the biological role of the CO, the “silent killer,” uncovered that many crucial physiological and cellular processes are governed by CO through its roles in vasodilation, circadian rhythms, and anti-apoptotic, anti-proliferative, and anti-inflammatory functions.⁴⁴⁰

In cells CO is generated by heme-oxygenases.⁴⁴¹ Administering exogenous CO gas as a form of medical treatment has been explored in several clinical trials on human subjects,^{442–445} but this approach carries inherent problems, since inhalation exposes the gas (which readily outcompetes oxygen in binding to hemoglobin) to the body’s entire blood supply, poisoning and potentially even killing the patient. Thus administering CO as a solution via a molecular release process has become an ever-intensifying areas of research. Early attempts at developing CO-releasing molecules (CO-RMs) sought to tune the CO-release properties of boroncarboxylates^{446,447} but this approach proved unsuccessful, and metal carbonyl complexes have since proved to be the most promising class of CO-RMs.^{448–453}

A large number of metal carbonyl CO-RMs have been synthesized and explored for their CO-release properties. Several well-known metal carbonyls of long-standing interest, such as $\text{Fe}(\text{CO})_5$ or $\text{Mn}_2(\text{CO})_{10}$, have also been explored as CO-RMs.⁴⁴⁸ Synthetic approaches to designing new CO-RMs often employ organic ligands that allow for improved solubility, targeting of specific organs, and hopefully lower toxicity such that they can be safely processed and excreted from the body.^{454,455} One notable candidate CO-RM in this regard is $\text{Ru}(\text{CO})_3\text{Cl}(\text{glycinate})$ (CORM-3),^{456,457} though numerous other organometallic CO-RMs with improved aqueous solubility have been developed, and this remains an area of active exploration.

$\text{Ru}_2\text{Cl}_4(\text{CO})_6$ (CORM-2) is among the most widely studied CO-RMs, and its physiological efficacy has been investigated in a wide variety of contexts, resulting in over 150 articles published to date on its biological applications.⁴⁵³ A primary challenge in developing useful metal carbonyl CO-RMs is their solubility, as most metal carbonyl complexes have very limited solubility in aqueous solution. As such, CORM-2 has traditionally been “solubilized” in DMSO, as is common practice in many small molecule screening studies. As we will elaborate on in this paper, the term “solubilized” is misleading in this context, since the CORM-2 dimer reacts readily with DMSO to generate DMSO-ligated monomeric ruthenium products. Mann et al. have previously studied this reaction using CNMR spectroscopy,⁴⁵⁸ and we have used FTIR spectroscopy to monitor the same reaction in DMSO, the dynamics of which are visible on the timescale of minutes to days after dissolving CORM-2 in DMSO. We find similar behavior to that reported previously, though monitoring the reaction via FTIR was helpful for developing a clearer picture of the timescale over which the reactions take place and the reactivity of the DMSO-ligated products in different solvent environments.

While CORM-2 has traditionally been used to liberate CO spontaneously upon injection into living tissue, many other CO-RMs do not spontaneously release CO and have been explored as photochemical CO-release agents.⁴⁴⁸ It is convenient that CORM-2 releases CO spontaneously, yet despite possessing 6 CO ligands, an average of only 0.9 moles of CO is released to myoglobin per mole of CORM-2 used.⁴⁵³ Thus it would appear that CO-loss from CORM-2 may lead to the formation of products which do not themselves undergo further spontaneous CO-loss in living tissue, motivating our desire to explore its photochemical CO-release properties in the spirit of developing a tandem thermal/photochemical CO-delivery method.

We have used FT-IR spectroscopy to characterize the reactivity of CORM-2 in DMSO solutions, observing the mixture of monomeric DMSO-ligated products that form upon dissolution. We then explored the behavior of both the CORM-2 parent dimer and the major DMSO-ligated monomeric products with regard to CO-release in a biologically relevant solvent environment: mouse serum. The relatively uncongested organometallic CO-stretching region of the infrared spectrum in mouse serum allows for direct monitoring of these complexes via FT-IR spectroscopy in this solvent environment. While the parent CORM-2 dimer readily liberates CO in mouse serum, the major DMSO-ligated products do not. The photochemical CO-release properties of the species observed in DMSO and in mouse serum were also examined, and photoexcitation does readily liberate CO, demonstrating that a tandem thermal/photochemical approach may significantly improve the efficacy of CORM-2 for biological applications. Indeed, such an approach can very likely be generally applied to a wide range of CO-RMs. Of relevance to the practical application of this approach in living organisms are existing studies in which non-thermally active CO-RMs (those which have failed to produce an effect *in-vivo* in the absence of light) have successfully been used to liberate CO to yield a physiological response in the presence of a cold light source.^{458,459} Finally, ultrafast time-resolved infrared (TRIR) spectroscopy was used to look at the primary photochemical dynamics of the monomeric species formed in DMSO solution, demonstrating that CO-loss is the only primary photochemical process leading to the formation of long-lived products (thus, CO ligand dissociation occurs selectively over that of Cl ligands).

12.2 Methods

12.2.1. Sample Preparation

$\text{Ru}_2\text{Cl}_4(\text{CO})_6$ (CORM-2), all solvents, and mouse serum were obtained from Sigma-Aldrich Co. and were used as supplied.

12.2.2 FT-IR Spectroscopy and CW Photolysis

FTIR Spectra were collected on a Nicolett 6700 FT-IR Spectrometer (Thermo Scientific). Where continuous-wave irradiation was used, the source was a 254 nm Pen-Ray® lamp (Ultra-Violet Products Ltd.) providing an intensity at the sample of ca. 4.5 mW/cm^2 . Samples were contained in a stainless steel cell (Harrick Scientific) fitted with 2 mm thick CaF_2 windows separated by spacers ranging from 25 to $390 \mu\text{m}$ in thickness. The solvent spectrum has been subtracted as the background in all FT-IR spectra.

12.2.3 DFT Modeling

Density functional theory (DFT) calculations have been carried out to facilitate assignment of the absorptions observed in the infrared spectra. Calculations were carried out using the BP86,^{37,38} and B3LYP,^{38,39} functionals in the Gaussian09⁴³ package using the lan12dz^{44,460} basis for Ru and the 6-311+g(d,p) basis^{261–264} for all other atoms. Geometry optimizations were followed by a frequency analysis for use in interpreting the TRIR results and to ensure that all geometries were genuine local minima.

12.3 Results and Discussion

12.3.1 Structures Present in Solutions of CORM-2

The structure of CORM-2 has been investigated previously using a variety of techniques including X-ray diffraction,⁴⁶¹ infrared spectroscopy,^{462,463} and density functional theory calculations.^{464,465} Its structure in the solid state and the solution phase is believed to correspond to the isomer of C_{2h} symmetry shown in Figure 12.1. Our DFT calculations carried out for this study also find that this isomer is predicted to be the most stable.

Many small molecule screen studies use DMSO to dissolve a potential drug before injection into a living organism, and this has been the approach taken in the numerous preclinical investigations into the biological applications of CORM-2. As Mann and co-workers noted previously,⁴⁵⁸ CORM-2 reacts with DMSO to form DMSO-ligated monomers. Similar observations have also been made with regard to other oxygen-containing solvents.⁴⁶² Using CNMR spectroscopy, Mann and co-workers observed that the parent complex readily reacts in DMSO to form species **A**, **B**, and **C** after warming for 5 minutes and allowing the sample to sit overnight. Interestingly, in that study the parent complex CORM-2 was not observed, nor was it reported in a spectrum collected within 23 minutes of dissolution in DMSO, suggesting that it reacts rapidly when dissolved in DMSO.⁴⁵⁸ Fortunately the infrared spectra of complexes **A**, **B**, and **C**, and of the related monocarbonyl **D**, have been characterized previously,⁴⁶⁶ facilitating their assignment via FT-IR spectroscopy in our study.

We have used FT-IR spectroscopy to follow the reaction of CORM-2 with DMSO on timescales ranging from minutes to days after dissolution in neat DMSO (Figure 13.1). Within a few minutes of dissolving the complex, it is clear that several species are present in solution. Bands initially observed at ca. 1955, 2043, 2120, and 2131 cm^{-1} decay as several new bands are observed to grow in. These initially observed bands do somewhat resemble the FTIR spectrum of intact CORM-2, though a careful comparison of these bands to the FTIR spectrum of CORM-2 in other solvents suggests that it has likely already undergone a reaction upon dissolution, and thus we have labeled these bands RI (reactive intermediates).⁴⁶⁷ This also explains the notably higher solubility of CORM-2 in DMSO, relative to other solvents. The bands at 2062 and 2121 cm^{-1} are assigned to complex **A**, those at 2011 and 2075 cm^{-1} to complex **B**, and those at 2033 and 2089 cm^{-1} to complex **C** (note that **B** and **C** are structural isomers). Since the infrared frequencies of these complexes have each been previously reported in the literature in chloroform solution,⁴⁶⁶ the identity of each of these species was readily verified by diluting aliquots of the DMSO solution with chloroform and then collecting the FT-IR spectrum. After several days had passed, no further significant spectral changes were observed, and complexes **B** and **C** were the primary species present in solution, with a small amount of the tricarbonyl

species **A** also visible. Voigt fits to the bands at 2011 and 2033 cm^{-1} used in conjunction with the calculated band intensities indicate the ratio of **B**:**C** is roughly 3:2. It remains entirely possible that the small amount of species **A** present continues to undergo CO-substitution by DMSO at slow rate to form additional **B** and **C**, though our data do not allow us to conclude this with certainty. A relatively weak band at ca. 1975 cm^{-1} is assigned to the monocarbonyl species **D**.

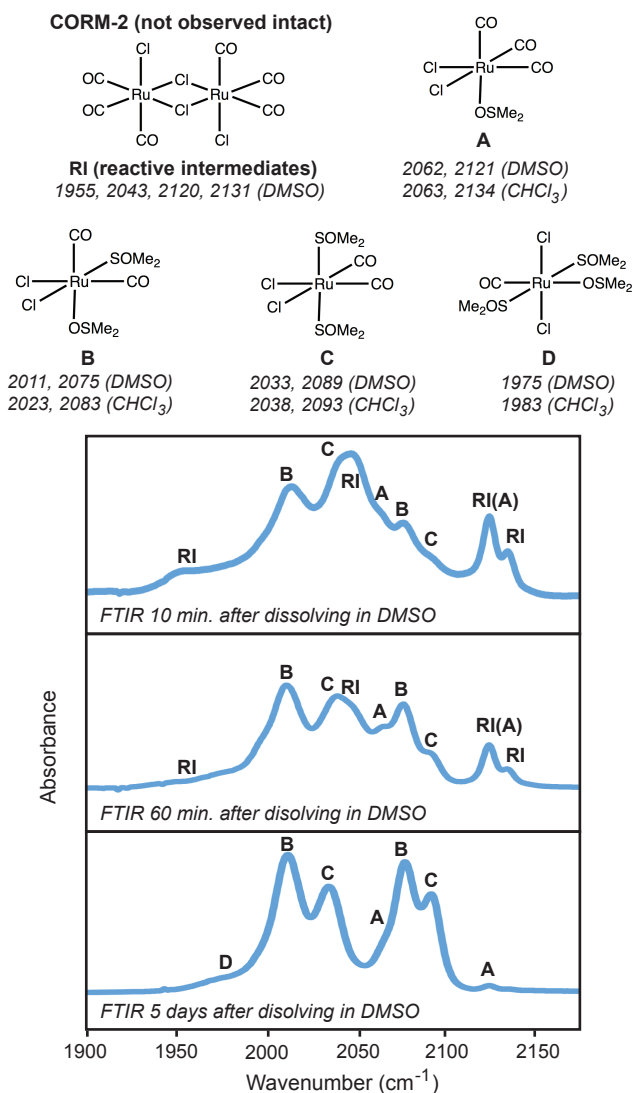


Figure 12.1. FTIR spectra of CORM-2 in DMSO at varying times after preparing the solution. The frequencies observed for product species in CHCl_3 solvent are also listed.

It is thus clear that the mixture of structures present in DMSO solutions of CORM-2 evolves significantly on the timescale of hours to days. That this reaction occurs spontaneously and takes days to complete bears on the large body of existing (and future) physiological studies on CORM-2; careful attention should be paid to characterizing the solution being tested in such studies.

12.3.2 Thermal and Photochemical CO-Release Properties of CORM-2 Derivatives in Mouse Serum

Considering that the CORM-2 parent molecule and the monomeric species formed in DMSO solutions may exhibit different behavior with regard to spontaneous CO-release, we next sought to characterize the behavior of these species in a biologically relevant solvent environment: mouse serum. Since an average of only 0.9 moles of CO are delivered per mole of CORM-2 used (despite its 6 CO ligands),⁴⁵³ it seemed that CO loss from CORM-2 may lead to the formation of products which do not themselves undergo further spontaneous CO loss. While absorptions from proteins and biomolecules heavily obscure the region of the infrared spectrum corresponding to the CO vibrations in organic molecules, the higher frequency region in which organometallic CO-stretching modes are observed is relatively uncongested, making FT-IR characterization of these species in mouse serum possible.⁴⁶⁸

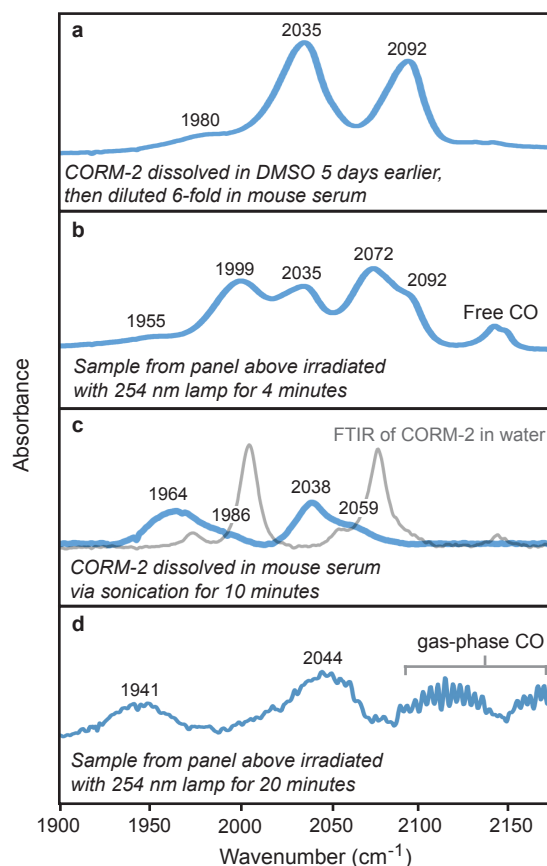


Figure 12.2. FTIR spectra of: (a) CORM-2 prepared in DMSO 5 days earlier (thus consisting primarily of species **B** and **C**) diluted 6-fold in mouse serum (b) the sample from the previous panel following 254 nm irradiation (c) pure CORM-2 dissolved in mouse serum via sonication for 10 minutes along with the spectrum in pure water for comparison (d) the sample from the previous panel following 254 nm irradiation.

Figure 12.2a shows the FTIR spectrum obtained when a solution of CORM-2 dissolved 5 days earlier in DMSO is diluted in mouse serum. The spectrum appears qualitatively similar to that in neat DMSO, with the bands appearing more coalesced than in mouse serum, possibly due to spectral broadening or shifting, or to a different balance of isomers **B/C** in the new solvent environment. Water may also coordinate to replace DMSO as a ligand.⁴⁶⁷ The spectrum shows no changes upon standing, indicating that the species present are stable in this environment. *Thus the DMSO-ligated monomers do not spontaneously release CO in mouse serum, suggesting that a significant fraction of the CO-delivery agent being introduced in DMSO solutions is inactive.*

Considering that many CO-RMs are only active photochemically (i.e. they only produce a physiological effect *in-vivo* in the presence of applied light),^{448,453,458,459,469} and that CO-loss is commonly observed upon UV excitation of metal carbonyls,³³² CW irradiation ($\lambda=254$ nm) of the sample from Figure 12.2a was carried out in the spirit of liberating CO from the otherwise inactive CO-RM derivatives. Figure 12.2b shows a spectrum collected after 4 min. of photolysis. A reaction has clearly taken place, and free CO is detected in this spectrum. Bubbles of CO gas are also visible in the sealed IR cell and by translating the cell such that the beam in the FTIR instrument passes through these bubbles, the rovibrational spectrum of CO gas can be observed. *Thus the inactive DMSO-ligated CORM-2 derivatives can be activated for CO release photochemically.*

Having investigated the behavior of the DMSO-ligated derivatives in mouse serum, we next sought to do the same for the parent molecule. CORM-2 was thus dissolved in mouse serum via sonication for 10 minutes. The corresponding FTIR spectrum is shown in Figure 12.2c, along with that in water for comparison, and it is clear that CORM-2 has undergone a reaction. The spectrum shows no changes upon standing, indicating that the species present are stable in this environment. The timescale for which we can neatly monitor the stability of the species present under these conditions appears to be limited to ca. 2-3 hours, as the mouse serum solution begins to congeal, presumably due to lower solubility causing the organometallic species to crash out of solution.⁴⁷⁰ We observe no detectable decay of the species present, nor release of free CO, in the sample stored inside the FTIR cell.

While it was not possible to observe free CO here, since it can escape during sonication, additional evidence (*vide infra*) confirms that CO is released. We were curious to see which components of the mouse serum promoted its decomposition. A previous study used osmometry experiments to demonstrate that CORM-2 decomposes in various solvents, evidenced by a reduction in the average molecular mass of the species present in solution, though the timescale over which these changes took place was not discussed.⁴⁶² Sonication for 3 min. in phosphate buffered saline (PBS) yields a solution with an FTIR spectrum similar (albeit less broadened) to that in mouse serum. Sonication in saline for 3 minutes produced similar spectral changes, but the reaction was less complete and continued in the sealed FTIR cell; in this case free CO was detected. The fact that the same products form in saline, and CO release is observed, demonstrates that CO was indeed evolved during sonication in PBS and mouse serum. It appears that NaCl promotes the release of CO, and that phosphate ions accelerate the reaction. This is consistent with earlier work by Motterlini et. al. who observed that saline promotes CO loss from CORM-3, with PBS resulting in even more rapid CO loss.⁴⁷¹ If enough time is allowed to pass, the formation of similar products can be observed to begin in pure water, suggesting that the product(s) formed in each solution may involve substitution of water for CO ligands.

We note that the absorption for free CO appears fairly strong, despite the fact that the oscillator strength for free CO is typically lower than that of CO in an organometallic complex,

and we attribute this to the fact that formation of small pockets of pure CO may affect the relative signal strengths observed in the FTIR spectrum. It is also worth pointing out that the band for pure CO appears broadened near the center, as if two distinct free CO absorptions are present. This is not altogether surprising, as numerous matrix isolation studies of CO have demonstrated that multiple absorption bands can arise for free CO due to interactions with surrounding molecules (in this case, likely water in the mouse serum).⁴⁷²⁻⁴⁷⁵ Analogous experiments involving the solution of CORM-2 dissolved 5 days earlier in DMSO were also carried out where pure water was used in place of mouse serum, and generally similar results were obtained in this case (see SI of published manuscript, Figures S1 and S3).

Since the products formed in mouse serum showed no further reaction over the course of several hours, photolysis of the solution in Figure 12.2c was also carried out in the interest of promoting additional CO loss. CO was readily liberated, as demonstrated by the spectral changes and observation of free CO gas in Figure 12.2d.

To briefly recap: both the products of the reaction of CORM-2 with DMSO, and with mouse serum itself, are stable in mouse serum (i.e. they do not spontaneously liberate CO at an appreciable rate). In both cases, UV irradiation promotes rapid photochemical CO-release, which can thereby significantly increase the yield of CO-delivery by CORM-2.

12.3.3 Picosecond Time-Resolved Infrared Studies on the Primary Photochemistry of the DMSO-ligated Derivatives (**B** & **C**)

Since the photochemistry of the DMSO-ligated derivatives **B** and **C** have now been demonstrated to be of practical interest, we also undertook ultrafast TRIR spectroscopic studies of these species to gain insight into their primary photochemistry.

Picosecond TRIR experiments were used to characterize the primary photochemistry upon excitation of the DMSO-ligated species that form upon dissolution of CORM-2 in DMSO. The sample used for the TRIR experiments was prepared by allowing CORM-2 to react in DMSO at room temperature for 5 days, such that the primary species present in solution are **B** and **C** (in a roughly 3:2 ratio). The positive photoproduct signals observed are thus expected to correspond to products formed upon excitation of the mixture of species **B** and **C**. Figure 12.3 shows the FTIR spectrum of this sample (reproduced from the lower panel of Figure 1), along with the TRIR spectra obtained at delay times of 5 and 1700 ps.

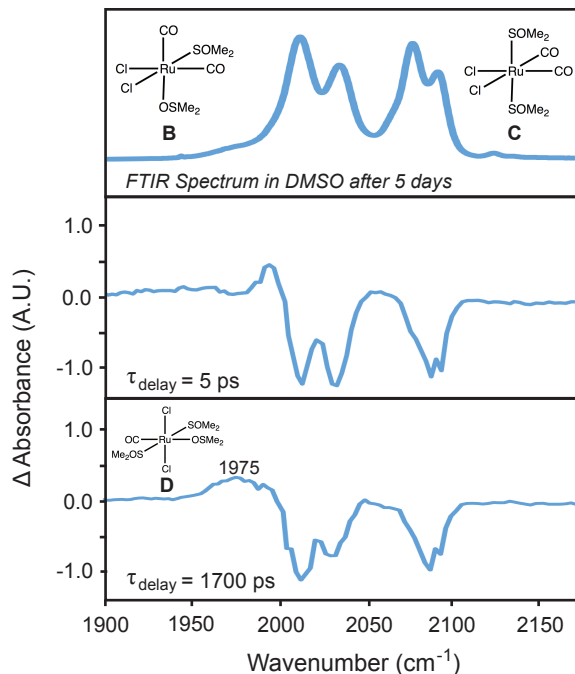


Figure 12.3. (top) FTIR spectrum of CORM-2 dissolved in DMSO 5 days earlier, reproduced from the lower panel of Figure 1. (middle and bottom) TRIR spectra of this sample collected in neat DMSO solution following 267 nm excitation at delay times of 5 ps and 1700 ps.

The TRIR spectra at early times show a weak, broad absorption lower frequencies, likely corresponding to vibrationally excited photoproducts (see spectrum at 5 ps). A sharper band at ca. 1995 cm⁻¹ observable at early times may correspond to an electronically excited state, to an unsolvated complex, or to an isomer of the final photoproduct undergoing a geometric rearrangement. The TRIR spectra at intermediate delay times ranging from ca. 50 to 1700 ps appear similar to that shown at 1700 ps, with a static absorption band centered at ca. 1975 cm⁻¹.

Either isomer (**B** or **C**) present in this mixture could in principle lose a CO, a Cl, or a DMSO ligand. The fact that the solvent is DMSO rules out the possibility that any photoproduct signals at delay times greater than a few tens of picoseconds are due to loss of a DMSO ligand, as DMSO can readily re-coordinate to a vacant coordination site under these conditions. In this case, loss of a Cl ligand would result in two observable photoproduct bands for the symmetric and asymmetric stretching modes of the two would-be remaining carbonyl ligands. DFT calculations were used to verify this, and such bands would be expected to differ in frequency by ca. 50-100 cm⁻¹ and thus should readily be resolved in the photoproduct spectra. This is not the case, and as such we can see that a Cl ligand is not lost, thus indicating that CO is lost.

It is also worth pointing out that the approximate strengths of a Ru-CO bond and Ru-Cl bond are 31^{476,477} and 77⁴⁷⁸ kcal/mol, respectively. Thus while both fall within the 267 nm photon energy of 107 kcal/mol, the CO is much more weakly bound and thus is the ligand clearly expected to be preferentially dissociated, in line with the observations in the TRIR spectra.

Some of the potential monocarbonyl products that form upon CO loss in DMSO solution (i.e. those which coordinate another DMSO molecule at the vacant coordination site) have been characterized previously,⁴⁶⁶ and the infrared band observed at ca. 1975 cm⁻¹ is consistent with that reported previously in chloroform solution for species **D**, which was also observed in DMSO

solution in the FT-IR spectra shown in Figure 12.1. Thus we tentatively assign the photoproduct observed in the 1700 ps TRIR spectrum to the monocarbonyl species **D**, though it remains possible that another structural isomer or stereoisomer of **D** exhibits a similar infrared frequency, or that a mixture of monocarbonyl isomers is observed.

The principle result obtained from the TRIR experiments is that loss of CO occurs selectively over loss of Cl upon photoexcitation of the mixture of **B** and **C**. In biological environments it remains possible, and indeed likely, that DMSO will also be dissociated from **B** and **C**, either due to photochemical dissociation or to substitution by water or other molecules/ions present in solution.

12.4. Conclusions

To date, CORM-2 has been used in a large number of physiological studies to release CO under thermal conditions. As we have explored in this study, dissolution of CORM-2 in DMSO leads to a reaction of the parent CORM-2 molecule to form monomeric DMSO-ligated ruthenium complexes on the timescale of hours to days. While the parent complex readily liberates CO under thermal conditions in mouse serum, the two primary dicarbonyl products formed in DMSO solution do not exhibit the same CO-release behavior. For this reason, one can expect the physiological efficacy of a DMSO solution of CORM-2 to depend sensitively on the time elapsed between dissolution of the complex and administration of the complex into a living organism.

There exist several CO-RMs which will not release CO readily under thermal conditions, and are instead used as photochemical CO-delivery agents. This approach can even offer advantages in terms of site-specificity and timed control of CO-release. Our exploration into the photochemistry of CORM-2 demonstrates that both the parent complex and the mixture of DMSO-ligated monomers formed in DMSO solution readily liberate CO upon photochemical excitation. Taken in conjunction with the observation that the DMSO-ligated species do not release CO thermally in mouse serum (while the parent does), we suggest that CORM-2 may be an ideal candidate for a combined thermal-photochemical CO-delivery approach in biological specimens. Though such an approach has not, to our knowledge, been taken with any CO-RM to date, this idea may very well extend to any number of thermally active CO-RMs which do not quantitatively liberate CO under physiological conditions.

13 A TRIR/DFT Mechanistic Study of Ring-Slipped Intermediates via Photolysis of $(\eta^1\text{-C}_5\text{Cl}_5)\text{Mn}(\text{CO})_5$

The following chapter is intended to be published in an American Chemical Society Journal and thus we claim no copyright for the text or figures contained in this chapter.

13.1 Introduction

Since the synthesis and characterization of ferrocene in the early 1950's,^{479–481} the cyclopentadienyl ligand and its analogues have become among the most widely-used ligands in organometallic chemistry. A variety of coordination geometries have been characterized for this coordinatively versatile ligand, and a subset of representative structures are shown in Figure 13.1. Isomerization, or “ring-slippage” between these different coordination geometries, particularly those of η^5 , η^3 , and η^1 hapticity, are known to be important mechanistic components in the reactivity of many cyclopentadienyl complexes. In a previous communication by our group, we reported several intermediates formed following the “reverse ring-slip” processes occurring in $(\eta^1\text{-C}_5\text{Cl}_5)\text{Mn}(\text{CO})_5$ following 295 nm and 325 nm excitation.⁴⁸² Here we report on our continued exploration of this complex, examining the wavelength dependence of its photochemistry and also characterizing the solvation dynamics of photoproducts formed in a more polar, coordinating solvent (methylene chloride). Of particular interest with regard to solvent-solute interactions is the monocarbonyl-loss photoproduct, which features an unusual, stabilizing three-center M-C-Cl interaction at the metal center. Density Functional Theory (DFT) calculations are used to explore the experimentally observed intermediates, as well as to examine the relevance of the experimental results to related complexes containing the more extensively utilized Cp (C_5H_5) and Cp* (C_5Me_5) ligands.

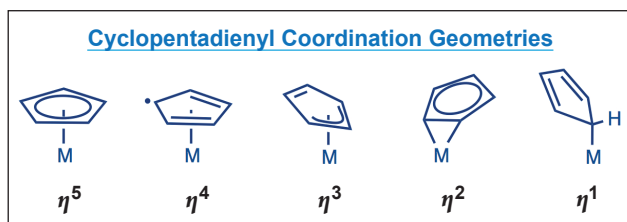


Figure 13.1. Coordination geometries for cyclopentadienyl ligands with η^5 through η^1 hapticity

The concept of cyclopentadienyl ring-slippage was first proposed to explain differences in rates of CO-substitution between cyclopentadienyl containing complexes and their homoleptic metal-carbonyl counterparts,⁴⁸³ the underlying rationale being that a temporary distortion to lower hapticity allows the metal center to avoid an excessively high electron count during the course of a nucleophilic displacement reaction. Ring-slippage can occur analogously with other aromatic ligands including benzyl, indenyl, fluorenyl, fulvalene, etc.^{90,484} Evidence for this ligand distortion has been observed in a wide-range of chemical transformations, including ligand substitutions, alpha-hydrogen abstractions, beta-hydrogen eliminations, bond insertion reactions, and reactions involving transfer of an aromatic ligand.⁹⁰

Cyclopentadienyl complexes of reduced hapticity (relative to the η^5 geometry) have been characterized previously using X-ray crystallography,^{170,485–497} NMR measurements,^{491,495–501} and via infrared absorption bands,^{83,502,503} as well as by less direct evidence based on infrared characterization and electron counting.^{504–507} Similar observations have been made for complexes containing other aromatic ligands. It remains more difficult to characterize the *changes* in hapticity that occur during the course of a chemical reaction, as the transient structures associated with ring-slip processes are typically very short lived. Indeed, the first proposals of ring-slip in the literature were based on inferences from kinetic and mechanistic studies.⁴⁸³

In this study, we seek to circumvent the traditional difficulties associated with probing ring-slipped geometries by characterizing the species of various hapticity that form via photochemical dissociation of one or two carbonyl ligands from an η^1 parent complex. Picosecond time-resolved infrared (TRIR) spectroscopy and density functional theory calculations are used to explore the reverse ring-slip processes associated with the wavelength dependent photochemistry of $(\eta^1\text{-C}_5\text{Cl}_5)\text{Mn}(\text{CO})_5$. In particular, we explore the mechanism of the relatively rare single-photon, dicarbonyl-loss process observed for this complex with a focus on the role of the reverse ring-slip in effecting loss of the second CO. Experiments in CH_2Cl_2 solvent are used to explore the behavior of the monocarbonyl-loss species in polar, coordinating solvents, and additional density functional theory calculations are used to further explore the implications of the experimental results toward other species less amenable to ultrafast investigations.

13.2 Methods

13.2.1 Sample Preparation

$(\eta^1\text{-C}_5\text{Cl}_5)\text{Mn}(\text{CO})_5$ was synthesized according to literature protocol,⁵⁰⁸ and *n*-pentane and methylene chloride (Sigma-Aldrich Co.) were used without further purification.

13.2.2 Data Analysis

Kinetic data in this work result from spectra measured at delay times between 0 and 1000 ps between the visible-pump and IR-probe pulses. Kinetic traces for each spectral feature were obtained by integrating a narrow spectral region (ca. 5 cm^{-1} wide) surrounding the reported frequency. The kinetic data were fit using a home-written fitting program. Errors on experimental time constants are reported as 95% confidence intervals.

13.2.3 DFT Modeling

Density functional theory (DFT) calculations have been carried out to facilitate assignment of the absorptions observed in the TRIR spectra. Calculations were carried out using the BP86,^{37,38} and B3LYP,^{37,39} functionals in the Gaussian09⁴³ package using the lanl2dz^{44,45} basis for Mn and the aug-cc-pvdz basis^{46–48} for all other atoms. Geometry optimizations were followed by a frequency analysis for use in interpreting the TRIR results and to ensure that all geometries were genuine local minima.

13.3 Results and Discussion

13.3.1 Ultrafast photochemistry in *n*-pentane

In a previous communication by our group,⁴⁸² TRIR results on $(\eta^1\text{-C}_5\text{Cl}_5)\text{Mn}(\text{CO})_5$ in *n*-pentane solution following 295 and 325 nm excitation were reported. We have further explored the photochemistry following 267 and 400 nm excitation to investigate the wavelength dependence of the photochemical processes observed previously, with a particular focus on the rare dicarbonyl-loss process observed in the earlier study.

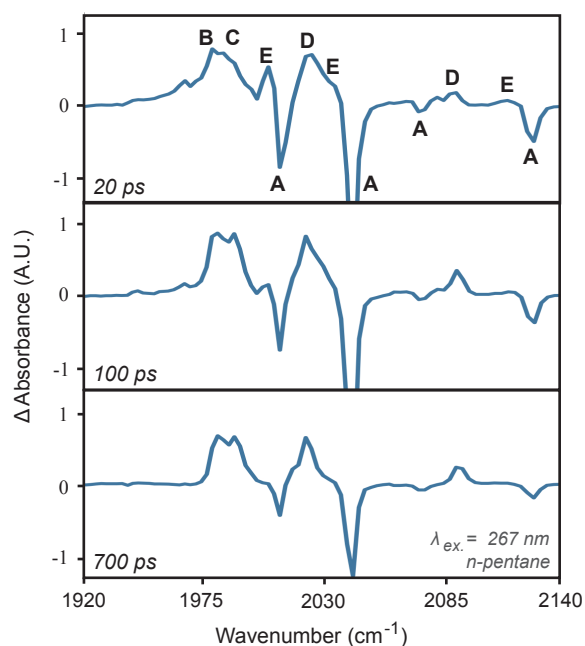


Figure 13.2. TRIR spectra of $(\eta^1\text{-C}_5\text{Cl}_5)\text{Mn}(\text{CO})_5$ in *n*-pentane solution following 267 nm excitation. (A.U. = arbitrary units)

Figure 13.2 shows the TRIR spectra collected following 267 nm excitation in *n*-pentane solution. Comparison to our group's previous report⁴⁸² and to the literature⁵⁰⁸ allows assignment of species **B** (1982 cm^{-1}) to the di-carbonyl-loss product $(\eta^5\text{-C}_5\text{Cl}_5)\text{Mn}(\text{CO})_3$, **C** (1989 cm^{-1}) to $\text{Mn}(\text{CO})_5$, **D** ($2020, 2092\text{ cm}^{-1}$) to a monocarbonyl-loss C-Cl coordinated product $(\text{C}_5\text{Cl}_5)\text{Mn}(\text{CO})_4$, and the bands labeled **E** to an electronically excited state which relaxes completely within the first ca. 200 picoseconds. Bleaches at $2011, 2044, 2075,$ and 2128 cm^{-1} correspond to the parent complex, $(\eta^1\text{-C}_5\text{Cl}_5)\text{Mn}(\text{CO})_5$ (**A**) (note that the weak parent bleach at 2075 cm^{-1} was not observed in the previous study, though it was reported by Reimer and Shaver⁵⁰⁸). Species **B** has been isolated previously,⁴⁸² while **C**, **D**, and the excited state **E** have been characterized in earlier TRIR studies.^{186,482,508,509} The monocarbonyl-loss product, **D**, is known to rearrange to $(\eta^2\text{-C}_5\text{Cl}_5)\text{Mn}(\text{CO})_4$, **F**, on the timescale of 136 ns,⁴⁸² but the relative quantities of **B**, **C**, and **D** at a given excitation wavelength remain constant over the timescale studied.

Note that species **B** exhibits IR bands at 1982 and 2048 cm^{-1} in cyclohexane solution (reported previously⁵⁰⁸), but in the present TRIR study, we do not observe the higher frequency (2048 cm^{-1}) band due to its overlap with the parent bleach at 2044 cm^{-1} . In the previous TRIR study, a band at 2046 cm^{-1} was attributed to **B** in *n*-pentane, but repeated attempts have been unable to reproduce this band in the TRIR spectra. The most likely explanation appears to be that the 2046 cm^{-1} band previously attributed to **B** was in fact a result of a spectral artifact or baseline drift, as the signal-to-noise of the present system is significantly higher than that used in the earlier study.⁵¹⁰ Indeed, the observed frequency of the parent bleach at 2044 cm^{-1} in *n*-pentane suggests that it should likely overlap the 2046 cm^{-1} band of **B** in *n*-pentane in the TRIR spectra. The signal-to-noise ratio is clearly better in the present spectra, as the parent bleach at 2075 cm^{-1} was also not observed in the previous study.

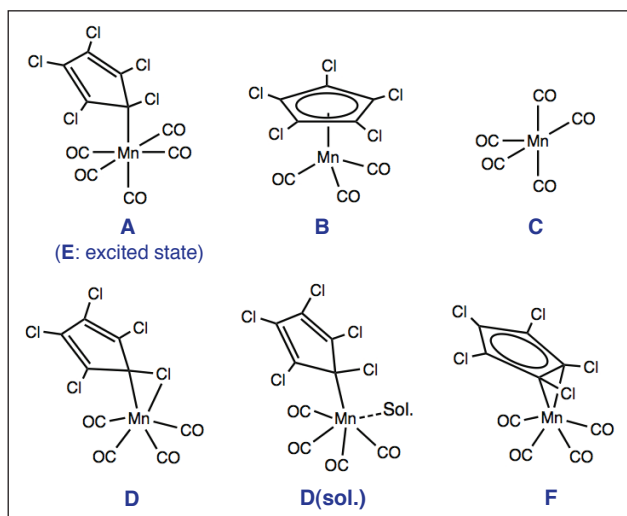


Figure 13.3. Chemical structures of the various intermediates observed in the TRIR spectra

In the previous report⁴⁸² the highest frequency parent bleach at 2127 cm^{-1} , and the neighboring transient product band at ca. 2116 cm^{-1} , were not characterized, though the short lifetime of the 2116 cm^{-1} band indicates that it also corresponds to the transient electronically excited state labeled **E**.

Figure 13.4 shows the TRIR spectra in *n*-pentane following 400 nm excitation. Examination of the spectrum at 400 nm shows bands corresponding to an electronically excited state, **E*** (labeled with an asterisk as this may likely correspond to a different excited state, or mixture of excited states, than that observed following 267 nm excitation), along with the ring dissociation product $\text{Mn}(\text{CO})_5$ (**C**) as the only major long-lived photoproduct. No detectable quantities of carbonyl dissociation products were observed. From this data, we see that longer wavelength irradiation leads to highly selective, preferential dissociation of the η^1 - C_5Cl_5 ligand, leaving the metal-carbonyl bonds intact. This demonstrates the relatively labile nature of η^1 coordinated cyclopentadienyl ligands relative to those of greater hapticity.

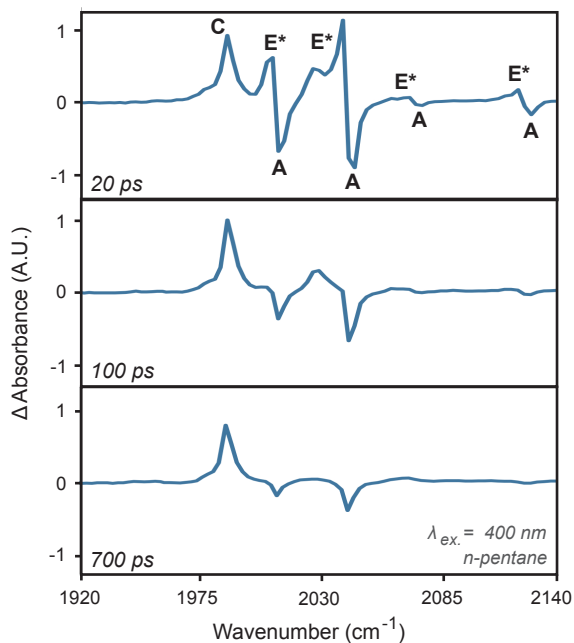


Figure 13.4. TRIR spectra of $(\eta^1\text{-C}_5\text{Cl}_5)\text{Mn}(\text{CO})_5$ in *n*-pentane solution following 400 nm excitation.

With the picosecond TRIR spectra of this complex at four excitation wavelengths in hand (267 and 400 nm data from this study, 295 and 325 nm data from our group's earlier study⁴⁸²), we can now compare the relative quantities of the major photoproducts formed (species **B**, **C**, and **D**) across the different excitation wavelengths. In view of the rarity of single-photon-induced dicarbonyl-loss processes occurring in the solution phase,^{29,30,387,390,511} the observation of species **B** was initially surprising; the generally held expectation is that excess photoexcitation energy, beyond that needed to dissociate the first carbonyl ligand will dissipate to the solvent before a second carbonyl is lost. In this case, the wavelength dependence observed for the ratio of monocarbonyl-loss to dicarbonyl-loss product is striking; 267 nm excitation leads to a lower relative proportion of dicarbonyl-loss product (**B**), relative to the amount of monocarbonyl-loss product (**D**), than excitation at either 295 or 325 nm (Table 14.1). The relative amount of ring-loss product, **C**, increases with increasing wavelength. It is not surprising that no dicarbonyl-loss product is observed at 400 nm, as this excitation wavelength also does not yield any monocarbonyl-loss species. Table 1 lists the relative peak areas for absorption bands corresponding to species **B**, **C**, and **D**. Note that these values are normalized with regard to the total integrated intensity for a given infrared band at a given wavelength, and thus these values do not indicate the absolute quantum yield for a species nor have these values been weighted by the absorption coefficient of the infrared absorption (as these values are not known). Nonetheless, these provide information on the *relative* yields of species **B**, **C**, and **D** formed at each wavelength.

Table 13.1. Relative integrated (normalized) intensities of photoproduct absorptions as a function of excitation wavelength^a

Species (freq.)	267 nm	295 nm ^b	325 nm ^b	400 nm
B (1980 cm ⁻¹)	0.34	0.34	0.25	0
C (1989 cm ⁻¹)	0.31	0.57	0.71	1
D (2020 cm ⁻¹)	0.35	0.09	0.04	0

(a) Integrated band intensities were measured at delay times >600 ps, after vibrational cooling and relaxation of excited states is complete, (b) 295 and 325 nm excitation results were adapted from the previous study by our group.

Looking at Table 13.1, we find that the relative yield of the dicarbonyl-loss photoproduct, **B**, is relatively constant across the excitation wavelength regime of 267 nm to 325 nm, and that the relative fraction of monocarbonyl-loss product actually decreases going from 267 nm to 295 nm. While it is not entirely clear why relatively less monocarbonyl-loss product is observed, this trend nonetheless clearly indicates that the dicarbonyl-loss process is not occurring due simply to excess remaining photoexcitation energy after the first carbonyl is dissociated. Were that the case, one would expect the relative fraction of **D** to **B** to increase with decreasing excitation energy, as dissociation of the second carbonyl would be a chance event, the probability of which should only increase with at shorter excitation wavelengths. The data in Table 13.1 show that this is clearly not the case. However, there exists another possible explanation; the reverse ring-slippage may facilitate ejection of the second CO-ligand.

To explore this possibility, we carried out DFT calculations to determine the exothermicity associated with the reverse ring-slip going from the monocarbonyl-loss complex to form the dicarbonyl-loss product. We discovered that formation of the dicarbonyl loss product (**B**) from the monocarbonyl loss product (**D**) is actually calculated to be *exothermic* by 3.6 kcal/mol (BP86 value). The Mn-CO bond dissociation enthalpy from **D** is calculated to be 37.9 kcal/mol, while the favorable enthalpy change from the reverse ring slip is calculated to be 41.5 kcal/mol (see Figure 13.5). We point out that the thermodynamic values associated with ejection of the second CO are measured here relative to the most stable monocarbonyl-loss structure calculated; in actuality, the fast (< 1 ps) formation time of the dicarbonyl-loss product suggests that the dicarbonyl-loss reaction path never passes through the stable intermediate **D**, but instead likely proceeds more directly through the vibrationally (or electronically) excited parent or monocarbonyl-loss species.

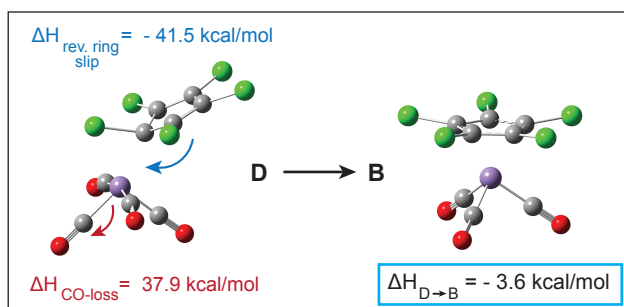


Figure 13.5. Energetics associated with the reverse ring slip and carbonyl dissociation reaction of monocarbonyl-loss product **D** to form dicarbonyl loss product **B**.

The fact that the ejection of a second CO-ligand is exothermic provides an explanation for the relatively constant yield for ejection of a second CO-ligand across the 267-325 nm wavelength regime.⁵¹² This also elucidates an interesting feature of the chemistry of ring-slipped complexes that has not, to our knowledge, been discussed previously. *Namely, a slipped ring can possess “stored energy,” not unlike a compressed spring, which can be released to facilitate the ejection of another ligand, particularly when the value of the energy stored is in excess of the binding energy of another ligand.* This behavior can be expected to be completely general among ring-slipped intermediates and will be explored further in section III C.

Indeed, there exist examples in the literature suggestive of similar behavior.^{494,513} Figure 13.6 shows two such examples (adapted from references^{494,513}). Species **1** reacts with $\text{P}(\text{CH}_3)_3$ to yield intermediate **2**, which can then proceed to add a second phosphine to yield **3**, or undergo carbonyl-loss to yield **4**. The loss of CO from **2** to form **4** is almost undoubtedly driven by the increase in hapticity of the Cp ligand (as no other explanation for why this reaction would proceed spontaneously is readily apparent). The reaction of **2** to form **3** (under thermal or photochemical conditions) is reversible, with the equilibrium favoring the higher hapticity species in the absence of an excess of the phosphine reagent. The same is true for the reaction of **5** to form **6** (although this reaction was reported only under photochemical conditions). Similar to the present observation of the ejection of a second CO-ligand from $(\eta^1\text{-C}_5\text{Cl}_5)\text{Mn}(\text{CO})_5$, the reversible nature of these reactions (i.e. the fact that the phosphine ligands can be ejected to reform the reactant) can very likely be attributed to the favorable enthalpy associated with the reverse ring-slip process. This is almost certainly true when such reactivity is observed under thermal conditions (the reversible nature of the reaction of **2** to **3**), although when photochemical conditions are used it is also, of course, possible that photochemical excitation drives dissociation of the phosphine ligand (the reversible nature of the reaction of **5** to **6**).

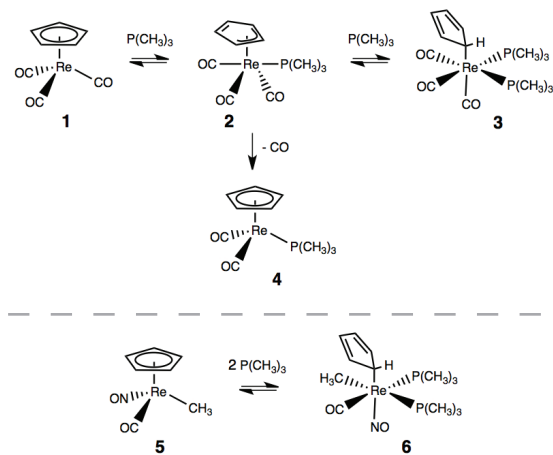


Figure 13.6. Examples of ligand dissociation reactions from the literature likely driven by the favorable enthalpy change associated with reverse ring-slippage.

Returning our focus to the results of the present study, it must be noted that a net exothermic reaction for the reverse ring-slip/ligand-ejection process is not, itself, enough to dictate that the reaction will proceed forward. Indeed the observation of any quantity of the monocarbonyl-loss product **D** is clear evidence that a kinetic barrier must exist to ejection of the second CO-ligand.

D is known to rearrange to an η^2 coordinated complex **F** on the timescale of 136 ns, with no observation of an increase in the amount of dicarbonyl-loss product. Based on the time constant of 136 ns for the rearrangement of **D** to **F**, we obtain a lower limit of 8.1 kcal/mol for the ground state barrier for CO-ejection. The lack of formation of **B** from **D** at longer delay times indicates that the dicarbonyl-loss process is coupled to the relaxation processes occurring following the initial photoexcitation event. Thus formation of **B** from an (electronically or vibrationally) excited state of **D** is still tied to the relaxation processes occurring after photoexcitation, though the lack of a straightforward relationship between the excitation energy and the relative yields for **B** and **D** shown in Table 13.1 suggest that the relative quantities of each species formed depend in a detailed manner on the electronic structure of the species involved. The energy stored in the initially slipped ring, which is released during the reverse ring-slip processes occurring after photoexcitation, helps to account for the lack of a straightforward wavelength dependence in the relative yields of the mono- and dicarbonyl loss products observed experimentally.

13.3.2 Ultrafast Photochemistry in Methylene Chloride

The structure of the monocarbonyl loss product **D** has been proposed to involve a three-center M-C-Cl interaction with an η^1 coordinated ring,⁴⁸² and the calculations carried out for the present study also confirm this as the most likely structure for **D** (see Figure 13.5). This unusual proposed coordination geometry for this ring to the metal center prompted us to experimentally investigate the dynamics of **D** in a more coordinating solvent, in which a solvent molecule might be expected to coordinate to the metal center and thus disrupt this unusual interaction. Information on the dynamics of such a process would provide insight into the overall effects of this interaction on the reactivity of **D** in solution. TRIR experiments were also thus carried out in CH₂Cl₂ solution following 267 nm excitation (see Figure 14.7), and the dynamics of each photoproduct discussed previously were examined.

The majority of the observed bands appear similar to those observed in *n*-pentane solution, although broadened in the more polar solvent. The bands of species **B** and **C** are overlapped and visible in the 1975-1990 cm⁻¹ region, with species **D** observed at 2029 and 2091 cm⁻¹, along with the decaying bands of the electronically excited state **E**. Note that in CH₂Cl₂ solvent, the lower frequency parent bleach is no longer visible at later delay times, suggesting that other photoproduct bands overlap this bleach; these may be a combination of transient bands of the excited state **E**, bands of photoproducts **B** or **C** that shift in the new solvent environment, and/or bands of a solvated photoproduct (*vide infra*). One clear difference is observed relative to the experiments in *n*-pentane; *as the delay time increases, the 2091 cm⁻¹ band of D decays, and a new band becomes visible at 2103 cm⁻¹* (see Figure 5). Though the lower frequency (2029 cm⁻¹) band of **D** also exhibits dynamics, this band may overlap the excited state **E** at early times (evidenced by the results shown in Figure 1) and may also be influenced by the dynamics in the vicinity of the neighboring parent bleach. Thus the kinetic trace shown in Figure 13.7 was generated using the band at 2091 cm⁻¹.

Considering that this new species at 2103 cm⁻¹ is observed to form in the more coordinating CH₂Cl₂ solvent, but not in alkane solvents, we assign this species to a CH₂Cl₂-coordinated monocarbonyl-loss product, **D(sol)**. **D(sol)** may also exhibit a band at ca. 2005-2025 cm⁻¹, as the bleach of **A** in this region is no longer visible at later delay times, and this may also influence the dynamics of the band observed for **D** at 2029 cm⁻¹. Spectral overlap of the bands of the electronically excited state **E** with that of **D(sol)** at 2103 cm⁻¹ during the first few hundred

picoseconds make it difficult to accurately fit a rise to the formation of **D(sol)**, so we used the decay of **D** to fit a time constant to the solvation process **D** \rightarrow **D(sol)**, obtaining a time constant of 680 ± 300 ps.

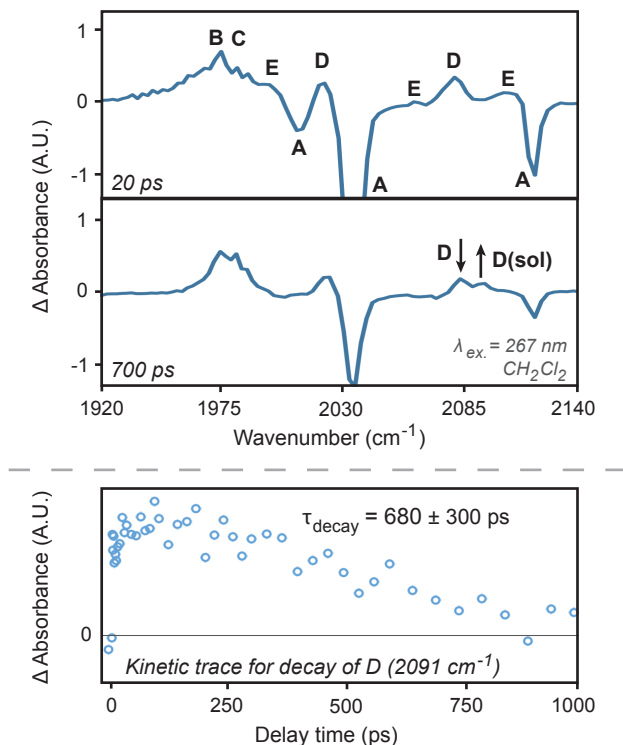


Figure 13.7. TRIR spectra of $(\eta^1\text{-C}_5\text{Cl}_5)\text{Mn}(\text{CO})_5$ in CH_2Cl_2 solution following 267 nm excitation.

DFT calculations were used to scan the potential energy surface associated with coordination of a CH_2Cl_2 molecule to the metal center, and, a barrier on the order of 6-9 kcal/mol is predicted relative to the dissociation limit (infinite separation) as the C_5Cl_5 ring rearranges to accommodate the incoming solvent molecule. Note that these calculations were performed in the “gas phase” for coordination of **D** with a single CH_2Cl_2 molecule. In fact, DFT calculations indicate that **D** + CH_2Cl_2 at the dissociation limit is actually calculated to be lower in energy than the solvated minimum for **D(sol)**, although coordination of CH_2Cl_2 to the metal center is calculated to be favorable relative to dissociated intermolecular distances relevant in the solution phase (ca. 3.5 Å). Thus the calculated barrier is also smaller when referenced against⁵¹⁴ intermolecular distances relevant in the solution phase, and overall the presence of a few kcal/mol barrier to solvent coordination compares favorably with the experimentally observed time constant of 680 ps. Taken together, these results also provide additional support for the proposed geometry of **D**, involving a three center M-C-Cl coordination. The coordination geometry of the C_5Cl_5 ring is calculated to differ in the solvated and unsolvated complexes; the Mn center in **D(sol)** coordinates to the C_5Cl_5 ring via only a single carbon atom (refer to Figure 13.4).

The results of the TRIR experiments and DFT calculations indicate that the type of three center M-C-Cl interaction present in **D** can be disrupted by coordinating solvents, allowing coordination of a molecule as a token ligand at the metal center. There is a barrier to this process on the order of a few kcal/mol. Coordinating ligands are thus also expected to be able to react via an associative mechanism with the metal centers of such complexes. With regard to the subsequent reactivity of any solvated complex containing a Cp ligand, it is relevant to point out that substitution at weakly solvated Cp-metal complexes has been shown to proceed via dissociative or interchange mechanisms, while only the displacement of stronger ligands will proceed via ring-slip processes.⁵¹⁵ Of course, in the case of a solvated η^1 complex, subsequent reactivity cannot involve any further ring-slippage without dissociating the ring completely.

TRIR spectra collected following 400 nm excitation in CH_2Cl_2 were very similar to those collected in *n*-pentane solution, with species **C** as the only long-lived photoproduct observed. The selective dissociation of the C_5Cl_5 at longer excitation wavelengths is thus preserved when changing to a polar solvent, which is not a surprising result.

13.3.3 Exploring the related $\text{CpMn}(\text{CO})_n$ and $\text{Cp}^*\text{Mn}(\text{CO})_n$ Complexes via DFT

In order to explore the applicability of the results for $(\eta^1\text{-C}_5\text{Cl}_5)\text{Mn}(\text{CO})_5$ to other cyclopentadienyl ligands, DFT calculations were carried out to investigate the analogous Cp (C_5H_5) and Cp* (C_5Me_5) species. While $(\eta^1\text{-C}_5\text{Cl}_5)\text{Mn}(\text{CO})_5$ is particularly amenable to studies of ring-slipped intermediates formed via the photochemically induced reverse ring-slip processes, independent consideration of the Cp and Cp* analogues helps to extend the applicability of this investigation to the expansive range of Cp- and Cp*-ligated organometallic complexes.

Though η^5 complexes represent the most commonly encountered Cp/Cp* complexes, η^1 -Cp complexes have been known to exist for almost as long as η^5 -Cp complexes,⁵⁰⁵ and thus we could expect to readily locate local minima for the Cp/Cp* analogues of **A** using DFT geometry optimizations. After optimizing structures for the $\eta^1\text{-CpMn}(\text{CO})_5$ and $\eta^1\text{-Cp}^*\text{Mn}(\text{CO})_5$ parent analogues, we performed a search for Cp and Cp* analogues of each of experimentally observed species. Carbonyl-loss and dicarbonyl-loss structures were optimized for each compound. The monocarbonyl-loss derivatives, D_{Cp} and D_{Cp^*} , involved rearrangement of the ring to an η^2 geometry, analogous to that in species **F** for the C_5Cl_5 ligated compounds (see Figure 13.8). Unlike **A**, the Cp and Cp* derivatives do not possess localized lone electron pairs (as the Cl atoms of the C_5Cl_5 ring of **A** do) to allow a coordination geometry analogous to that observed for species **D**. While an η^2 coordination geometry leaves the Mn center electron deficient (essentially a 17e species), η^3 coordination geometries in Cp complexes are quite rare.⁹⁰ As Cotton pointed out long ago, geometry clearly dictates that a regular pentagon with three vertices equidistant from a given point necessarily must have all five vertices equidistant from that point,⁴⁸⁴ thus an η^3 coordinated ring would necessarily have to distort its bond lengths or angles from those of an η^5 ring to an appreciable extent.

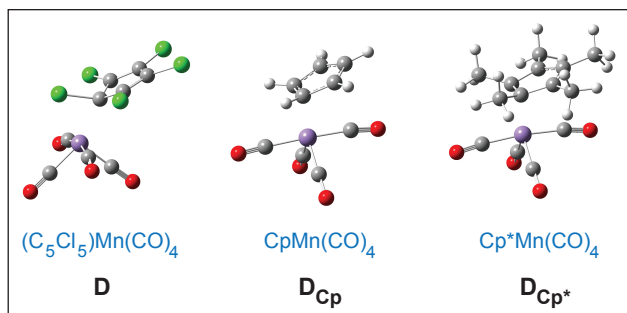


Figure 13.8. Structures of the monocarbonyl-loss products arising from the parent complex (A) and its Cp and Cp* analogues.

The dicarbonyl loss products for the Cp and Cp* derivatives, \mathbf{B}_{Cp} and \mathbf{B}_{Cp^*} , were analogous to \mathbf{B} , as both are characterized by η^5 rings coordinated to the metal center. For both \mathbf{B}_{Cp} and \mathbf{B}_{Cp^*} , the loss of a carbonyl ligand from \mathbf{D}_{Cp} or \mathbf{D}_{Cp^*} (monocarbonyl-loss) to form the dicarbonyl-loss complex is calculated to be *even more exothermic* than in the case with the C_5Cl_5 ring, highlighting the fact that the η^2 Cp/Cp* rings are less stabilized than that in \mathbf{D} involving a three center M-C-Cl interaction at the metal center. The enthalpy changes for the reactions of the $\mathbf{D}_{\text{Cp}} \rightarrow \mathbf{B}_{\text{Cp}} + \text{CO}$ and $\mathbf{D}_{\text{Cp}^*} \rightarrow \mathbf{B}_{\text{Cp}^*} + \text{CO}$ were calculated to be -15.8 kcal/mol and -20.8 kcal/mol, respectively (BP86 values). This result is significant, as it demonstrates *that the mechanistic paradigm involving ring-facilitated ligand ejection is expected to be even more prevalent in complexes of the more widely utilized Cp and Cp* ligands.*

To further explore the intrinsic stability of the various possible coordination geometries, we performed calculations beginning from the calculated minima for \mathbf{B}_{Cp} , and \mathbf{B}_{Cp^*} in which a single metal-carbon (a Cp/Cp* ring carbon) distance was extended in small steps away from the ground state minimum structure. Interestingly, at no point during these scans of the potential energy surfaces did we locate a minimum energy structure corresponding to anything resembling an η^3 coordination geometry. This suggests that neutral η^3 Cp/Cp* complexes will likely be quite rare, as other structures were consistently found to be energetically preferred over the η^3 geometry, which, as was already mentioned, would require a significant distortion of the cyclopentadienyl ring were it to exist.

13.4 Conclusions

In this study we have investigated the reverse ring slip processes that occur following photoexcitation of $\eta^1\text{-(C}_5\text{Cl}_5\text{)Mn(CO)}_5$. As was uncovered via the wavelength dependent study and accompanying and DFT investigation into the dicarbonyl-loss process, ring-slipped geometries can possess stored potential energy relative to their η^5 counterparts, which can facilitate ejection of a ligand from the metal center. This result is likely general among ring-slipped complexes, as examples suggesting similar behavior appear to already exist in the literature.

The monocarbonyl-loss product \mathbf{D} is characterized by a three center M-C-Cl interaction geometry with the C_5Cl_5 ring. The investigation in methylene chloride solvent explored the reactivity of this species toward coordination to a solvent molecule and uncovered that a CH_2Cl_2 molecule can coordinate to the metal center, disrupting the three center interaction. An energetic

barrier is associated with rearrangement of the ring coordination geometry to accommodate coordination of a CH₂Cl₂ solvent molecule. These results provide insight into the nature of the three center M-C-Cl coordination geometry and its implications for the reactivity of **D**, which may also be applicable to other complexes characterized by similar coordination geometries.

Excitation at 400 nm results in highly selective dissociation of the C₅Cl₅ ligand from (η¹-C₅Cl₅)Mn(CO)₅, demonstrating the labile nature of η¹-coordinated cyclopentadienyl ligands.

Additional DFT investigations explored the structure and reactivity of complexes analogous to those studied experimentally, in which the more widely-encountered Cp and Cp* ligands replaced the C₅Cl₅ ligand. Significantly, the mechanistic paradigm in which reverse ring-slip can facilitate ejection of a ligand also characterizes the reactivity of Cp- and Cp*-ligated complexes.

Taken together, these results present new and significant insights into cyclopentadienyl ring-slippage, which are widely applicable toward a broad range of organometallic complexes.

14 Primary Photochemical Dynamics of Triply-Bonded Metal Carbonyl Dimers Probed Via Ultrafast Infrared Spectroscopy

The following chapter is intended to be published in an American Chemical Society Journal and thus we claim no copyright for the text or figures contained in this chapter.

14.1 Introduction

The photochemistry of transition metal carbonyl dimers is a topic of longstanding interest, as these complexes serve both as catalysts for synthetically useful reactions and as model systems for understanding the photochemistry of other transition metal dimers and clusters.^{163,516,517} The majority of such complexes whose photochemistry has been characterized in detail contain a metal-metal (M-M) single bond, and photochemical excitation typically leads to a wavelength dependent mixture of M-M bond homolysis and CO-dissociation products.⁵¹⁸ The photochemical reactivity of homoleptic metal carbonyl dimers of Mn,^{171,172,186,519} Re,^{177,187,188} and Co,⁴⁴⁹ have been characterized in detail, as has that of the cyclopentadienyl carbonyl-complexes of Mo,^{198,520} W,^{138,521} Fe,^{137,140,522-524} and Ru.^{119,120,135,161}

Only a limited number of investigations have been made into the photochemistry of tetracarbonyl group VI dimers, $[\text{CpM}(\text{CO})_2]_2$. The structures of these complexes are distinct from those of the other aforementioned metal carbonyl dimers in that the group VI tetracarbonyl dimers are characterized by higher order M-M bonds of bond order three. Thus the photochemistry of the group VI tetracarbonyl dimers may be expected to differ significantly from that of the more well-characterized species bound by M-M single bonds. In this spirit we sought to investigate the photochemistry of $[\text{Cp}^*\text{Cr}(\text{CO})_2]_2$ (**1**) ($\text{Cp}^* = \text{C}_5\text{Me}_5$) in solution using ultrafast time-resolved infrared (TRIR) spectroscopy. Investigations into the photochemistry of the molybdenum congener, $[\text{Cp}^*\text{Mo}(\text{CO})_2]_2$, (**6**) were also carried out, though a detailed interpretation of these data was hindered by the lack of stability of the Mo complex in solution.

The structure of **1** is characterized by a triple bond linking the Cr atoms and four terminal CO ligands, which are bent slightly over the $\text{Cr}=\text{Cr}$ bond^{525,526} and have been described as semi-bridging CO ligands.⁵²⁷ The tendency of the d^5 $[\text{CpM}(\text{CO})_2]_2$ dimers to adopt bridging or semi-bridging CO-ligand conformations has been explored using a fragment molecular orbital theory approach.⁵²⁷ Initial studies into the photochemistry of **1** demonstrated CO-loss but found no evidence of $\text{Cr}=\text{Cr}$ cleavage products, presumably due to the strength of the $\text{Cr}=\text{Cr}$ triple bond.⁵²⁸ Subsequent infrared characterization of the CO-loss product in PVC matrices observed a single broad band in the bridging CO-stretching region,⁵²⁹ suggesting a triply-bridged structure of D_{3h} symmetry for $\text{Cp}^*_2\text{Cr}_2(\mu\text{-CO})_3$ (**2**), analogous to that of the triplet iron complex $\text{Cp}_2\text{Fe}_2(\mu\text{-CO})_3$ (see Figure 14.1).⁵²⁴ Turner and coworkers then characterized the solution-phase photochemistry of **1** using nanosecond to microsecond TRIR spectroscopy and made the surprising observation that the bridging CO band of **2** is actually two separate bands split by 11 cm^{-1} in n-heptane at room temperature.⁵³⁰ On this basis it was determined the structure of **2** must involve a distortion from D_{3h} symmetry, either due to a particularly strong interaction of the $(\mu\text{-CO})_3$ group with the Cp^* rings, effectively lowering the symmetry to C_{2v} or to a non-linear $\text{Cp}^*\text{-Cr-Cr-Cp}^*$

arrangement, lowering the symmetry of the $(\mu\text{-CO})_3$ group to C_s (at most). Studies into the reactivity of **2** with CO demonstrate a bimolecular rate constant ca. 1000 times greater than that observed for the reaction of the triplet $\text{Cp}_2\text{Fe}_2(\mu\text{-CO})_3$ with CO, suggesting that **2** may be a singlet.⁵³⁰ A subsequent DFT study concluded that **2** is a singlet on the basis of comparison of calculated and experimental infrared frequencies, though the triplet was predicted to be energetically favored by more than 10 kcal/mol.⁵³¹ The reaction of **2** with THF to form **3** has also been observed,^{529,530} although **2** does not appear to react with PPh_3 .^{528,530}

The structure of the molybdenum congener of **1**, $[\text{Cp}^*\text{Mo}(\text{CO})_2]_2$ (**6**) is generally similar to that of **1**, with differences in the bonding angles.⁵³² Existing knowledge on the photochemistry of **6** is limited, and this can likely be at least partially attributed to its lower solution-phase stability (vide infra).

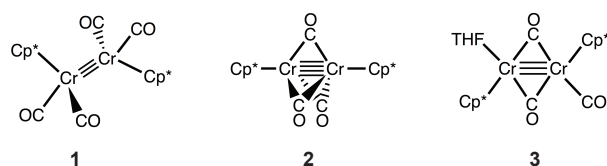


Figure 14.1. Structures of $[\text{Cp}^*\text{Cr}(\text{CO})_2]_2$ and relevant photoproducts observed in previous studies.

It has been suggested that a single-electron excitation should not be capable of cleaving a doubly or triply bonded dimeric transition metal complex,⁵²⁸ since promotion of a single electron from a bonding to an antibonding orbital should lower the effective bond order by, at most, one. For this reason, we do not expect to observe products arising from M-M bond homolysis in this study. This notion is consistent with the lack of observed M-M cleavage products for **1**^{198,528} and its Cp analogue⁵²⁸ in previous studies. Similarly, CO-loss, and not M-M bond cleavage, has been observed as the primary photochemical process upon excitation of $\text{Cp}_2\text{V}_2(\text{CO})_5$, which can be described as containing a $\text{V}=\text{V}$ double bond.⁵³³

In this study we have used ultrafast TRIR spectroscopy to characterize the primary photochemical dynamics of **1**. Upon visible or UV excitation of **1**, the principal photoproduct observed is a transiently lived rearrangement isomer, which DFT calculations suggest exists in a triplet spin state. This species reverts to the parent complex on the timescale of ca. 380 ps and is not involved in formation of the CO-loss product. The structure of this transient appears to distort somewhat between THF and cyclohexane solutions, though the lifetime in each solvent is fairly similar. The triply-bridged CO-loss product, **2**, does not react with THF in neat THF solution on the picosecond time scale, although it is known to do so in dilute solutions of THF on longer time scales. We also briefly discuss the results of analogous studies on the Mo congener, **6**, and although the instability of this species in solution limited our ability to carry out a comprehensive analysis of the TRIR data, this species does not form excited state bridged intermediates analogous to those formed by **1**.

14.2 Methods

14.2.1 Sample Preparation

[Cp*Cr(CO)₂]₂ was purchased from Santa Cruz Biotechnology Inc., [Cp*Mo(CO)₂]₂ was purchased from Fischer Scientific, and solvents were obtained from Sigma-Aldrich Co. All were used as supplied. Samples were prepared at concentrations of ca. 10 mM.

14.2.2 DFT Modeling

Density functional theory (DFT) calculations have been carried out to facilitate assignment of the absorptions observed in the infrared spectra. Calculations were carried out using the BP86,^{37,38} and B3LYP,^{37,39} functionals in the Gaussian09⁴³ package using the 6-311+g(d,p) basis^{261–264} for all atoms. H atoms were substituted for CH₃ groups on the Cp* rings of both complexes studied experimentally. Geometry optimizations were followed by a frequency analysis for use in interpreting the TRIR results and to ensure that all geometries were genuine local minima.

14.3 Results and Discussion

Time-resolved infrared (TRIR) spectra of **1** have been recorded in the CO-stretching region following 400 and 267 nm excitation in cyclohexane and THF solvents. TRIR spectra for the molybdenum congener, **6**, were also collected in cyclohexane, though these solutions contained an impurity due to the instability of **6** in solution. TRIR spectra are presented as difference absorbance spectra, where positive features correspond to newly-formed photoproduct species and negative features (bleaches) correspond to depletion of the parent complex.

14.3.1 Picosecond TRIR Spectroscopy of [Cp*Cr(CO)₂]₂ in Cyclohexane Solution

TRIR spectra of **1** in cyclohexane solution following 400 nm excitation are presented in Figure 14.2. Three transient bands are observed at 1770, 1900, and 2007 cm⁻¹, each of which decay on the time scale of 378 ± 15 ps (as measured for the 1770 cm⁻¹ band, see Figure 14.3) along with concomitant recovery of the parent bleach bands. Weaker, but long-lived photoproduct bands are also observed at ca. 1785 and 1795 cm⁻¹, and these are assigned to the previously characterized CO-loss product **2**.⁵³⁰ These appear less well-resolved in our data, relative to the previous report,⁵³⁰ though it is clear that two distinct bands are present. The bands of **2** are visible at the earliest delay times of only a few picoseconds (as would be expected for a CO-dissociation product) and do not detectably increase in intensity as the transient decays; as such it is clear that the decay of the transient complex is unrelated to the formation of **2**. TRIR spectra collected following 267 nm excitation appeared qualitatively similar to those obtained following 400 nm excitation. At both excitation wavelengths it is clear that the majority of photoexcited **1** molecules relax to reform the parent complex on the picosecond timescale, and thus that CO-dissociation is associated with a relatively small quantum yield, which was not necessarily evident from the previous study on the nanosecond to microsecond time scales.⁵³⁰

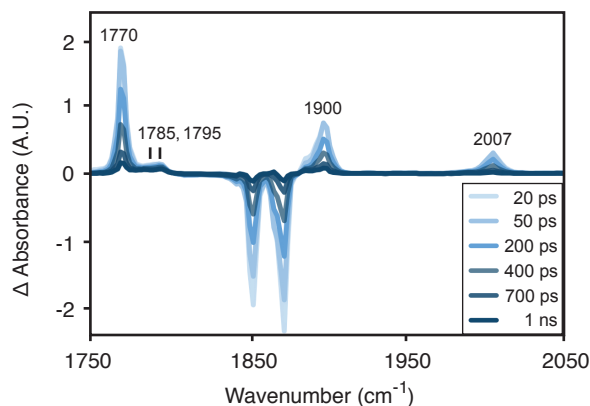


Figure 14.2. TRIR spectra of **1** in cyclohexane solution following 400 nm excitation. (A.U. = Arbitrary Units)

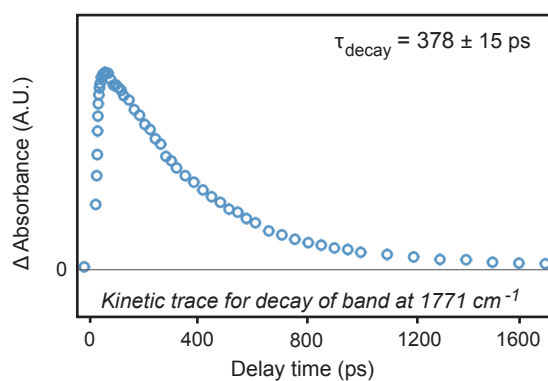


Figure 14.3. Kinetic trace for decay of the transient intermediate observed in cyclohexane solution following 400 nm excitation. (A.U. = Arbitrary Units)

With regard to the transient, a few details relating to its structure are readily apparent. First, the transient complex is not a CO-loss adduct, as it readily reverts to the parent complex on the picosecond time scale, evidenced by concomitant recovery of the parent bleaches along with its decay. Thus it is expected to be a rearrangement/structural isomer of **1**. The fact that two terminal and one bridging CO bands are observed indicates that the transient contains at least two terminal CO-ligands and either one or two bridging CO-ligands. The fact that any bridging ligands are observed signifies a lowering of the Cr≡Cr bond order, as without a weakening of this bond there would be no impetus for the rearrangement of terminal CO ligands to a bridging conformation.

The observation of this transient species complements the earlier, nanosecond to microsecond time scale TRIR study⁵³⁰ on this complex in two ways. First, we have uncovered that the principal (highest quantum yield) photochemical process upon UV/visible excitation of **1** is actually a photoisomerization reaction. Second, despite the lack of M-M homolysis products, the photochemistry of **1** does appear similar in spirit to that of other metal carbonyl dimers; the primary photochemical pathway does involve weakening of the M-M bond. The difference in

this case is that the higher bond order of the Cr≡Cr bond, along with the transient formation of bridging CO-ligands, prevents overall homolysis of the metal-metal bond.

A more detailed discussion of the structure of the transient intermediate will be presented in Section 14.3.3.

14.3.2 Picosecond TRIR Spectroscopy of [Cp*Cr(CO)₂]₂ in THF Solution

TRIR spectra of **1** collected in THF solution following 400 nm excitation are shown in Figure 14.4. Similar to the observations in cyclohexane solution, the major photochemical pathway involves formation of a transient intermediate that decays to reform the parent complex on the picosecond time scale. However, in THF solution four transient bands are observed at 1769, 1790, 1890, and 2010 cm⁻¹. The presence of an additional transient band, along with fact that these transient photoproduct bands don't all simply shift in the same direction, relative to those observed in cyclohexane, suggests that the changes in frequencies reflect at least a minor change in the structure, and perhaps also a change in the delocalization of the vibrational modes in the THF solvent. The relative band intensity of the highest frequency band (2010 cm⁻¹) also appears lower in THF solution, though this may also be influenced by broadening in the more polar solvent. The transient again reverts to the parent complex on the picosecond time scale, with a lifetime of 344 ± 17 ps in THF solution (Figure 14.5), which is fairly similar to the lifetime of the transient observed in cyclohexane solvent. THF does not appear to trap the transient intermediate to any detectable extent, as evidenced by the slightly shorter lifetime in THF solution.

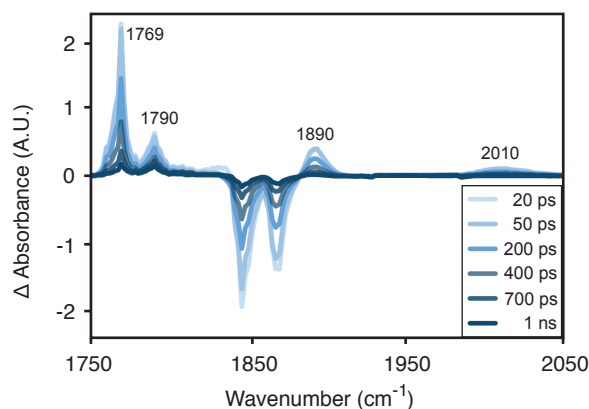


Figure 14.4. TRIR spectra of **1** in THF solution following 400 nm excitation. (A.U. = Arbitrary Units)

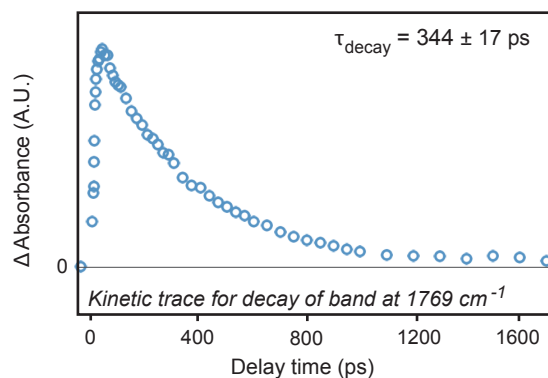


Figure 14.5. Kinetic trace for decay of the transient intermediate observed in THF solution following 400 nm excitation. (A.U. = Arbitrary Units)

The CO-loss product **2** is more difficult to observe in THF solvent (though it is of course still expected to be present), and indeed its bands may overlap those of the much stronger transient absorptions, whose bands are still visible at the longest experimentally accessible delay times. This is true for the data collected at both 400 nm and 267 nm excitation wavelengths, which again appear qualitatively similar to one another. Broadening of the bands of **2** in neat THF very likely also contributes to the difficulty in resolving these bands from those of the transient rearrangement photoproduct. Though the previous TRIR study on this complex observed **2** to react with THF to form **3**, no products arising from the reaction of **2** with THF are detected in the present picosecond experiments in neat THF. Bands of **3** were observed at ~ 1740 , 1774 , and 1881 cm^{-1} (in *n*-heptane solution containing dilute THF) in the previous study, and **3** was estimated to form at a rate near the diffusion limit.⁵³⁰ While the bands at 1774 and 1881 cm^{-1} may partially overlap (and thus be masked by) the strong transient band at 1769 cm^{-1} and the higher frequency parent bleach at ca. 1869 cm^{-1} , respectively, data was collected to frequencies as low as 1720 cm^{-1} with good signal-to-noise and no evidence was observed for any absorption at ca. 1740 cm^{-1} , nor to frequencies as low as 1720 cm^{-1} . Thus, it would appear that **3** does not form within $\sim 1\text{ ns}$ of CO-dissociation from **1** in neat THF solution, thus implying a kinetic barrier of at least several kcal/mol for the addition of THF to **2**.

To explore the structure of the transient intermediate observed experimentally, DFT calculations were carried out for a variety of potential rearrangement isomers of the parent complex. These included structures with elongated Cr \equiv Cr bonds, rotations about the Cr \equiv Cr bond, and rearrangement of either one or two terminal CO ligands to bridging conformations. Each calculation was carried out using both the B3LYP and BP86 functionals, and both singlet and triplet spin states were tested for each calculation. A previous DFT study on the CO-loss photoproducts of **1** noted that each of these functionals yielded similar results, with improved accuracy for the calculated (absolute, unscaled) vibrational frequencies using the BP86 functional.⁵³¹ Our observations were similar in this regard. Although the B3LYP functional predicted greater relative stability for the triplet rearrangement isomers than did the BP86 functional, the results were qualitatively quite similar in terms of the calculated energetics and the local minima located.

With regard to the singlet state rearrangement isomer calculations, despite beginning geometry optimizations from a wide variety of input structures, all singlet calculations reverted

to the ground state parent structure. Thus no singlet minima containing bridging COs (as would be required to match the experimental data) could be located.

When the spin state was changed to a triplet, four distinct local minima were readily located, and these are shown in Figure 14.6. Each of these structures contains two semi-bridging and two terminal CO ligands, with structures **4-trans** and **5-trans** characterized by a *trans* arrangement of the terminal COs, and structures **4-cis** and **5-cis** characterized by a *cis* arrangement of the terminal COs. In each case, the bridging CO ligands are asymmetrical, each interacting more strongly with one Cr atom than the other, hence these CO groups may more accurately be described as semi-bridging ligands. The relative energies, Cr-Cr distances, and vibrational frequencies of each structure calculated using the BP86 functional are provided in Table 14.1. Though the absolute calculated vibrational frequencies are not expected to be quantitatively accurate, trends in the number, ordering, and relative intensities of the infrared bands can be compared to the experimental data to assess the consistency of each structure with that of the transient rearrangement isomer observed experimentally.

14.3.3 DFT Studies

To explore the structure of the transient intermediate observed experimentally, DFT calculations were carried out for a variety of potential rearrangement isomers of the parent complex. These included structures with elongated Cr≡Cr bonds, rotations about the Cr≡Cr bond, and rearrangement of either one or two terminal CO ligands to bridging conformations. Each calculation was carried out using both the B3LYP and BP86 functionals, and both singlet and triplet spin states were tested for each calculation. A previous DFT study on the CO-loss photoproducts of **1** noted that each of these functionals yielded similar results, with improved accuracy for the calculated (absolute, unscaled) vibrational frequencies using the BP86 functional.⁵³¹ Our observations were similar in this regard. Although the B3LYP functional predicted greater relative stability for the triplet rearrangement isomers than did the BP86 functional, the results were qualitatively quite similar in terms of the calculated energetics and the local minima located.

With regard to the singlet state rearrangement isomer calculations, despite beginning geometry optimizations from a wide variety of input structures, all singlet calculations reverted to the ground state parent structure. Thus no singlet minima containing bridging COs (as would be required to match the experimental data) could be located.

When the spin state was changed to a triplet, four distinct local minima were readily located, and these are shown in Figure 14.6. Each of these structures contains two semi-bridging and two terminal CO ligands, with structures **4-trans** and **5-trans** characterized by a *trans* arrangement of the terminal COs, and structures **4-cis** and **5-cis** characterized by a *cis* arrangement of the terminal COs. In each case, the bridging CO ligands are asymmetrical, each interacting more strongly with one Cr atom than the other, hence these CO groups may more accurately be described as semi-bridging ligands. The relative energies, Cr-Cr distances, and vibrational frequencies of each structure calculated using the BP86 functional are provided in Table 14.1. Though the absolute calculated vibrational frequencies are not expected to be quantitatively accurate, trends in the number, ordering, and relative intensities of the infrared bands can be compared to the experimental data to assess the consistency of each structure with that of the transient rearrangement isomer observed experimentally.

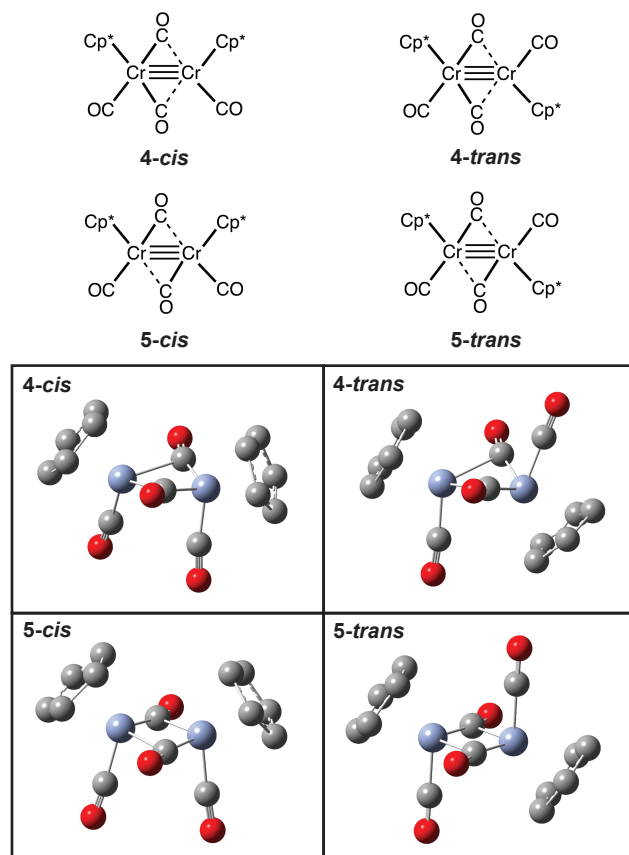


Figure 14.6. Structures of the triplet rearrangement isomers identified as local minima using DFT calculations. The structures shown were obtained using the BP86 functional. H atoms were substituted for CH₃ groups in the calculations, and these have been omitted for clarity of visualization in the graphics above.

Table 14.1. DFT (BP86) calculated energies, Cr-Cr bond distances, and CO-stretching mode frequencies and intensities for each of the triplet structures shown in Figure 14.6.

Structure	ΔE (kcal/mol) ^a	Cr-Cr (Å)	ν_{CO} (cm ⁻¹ , km/mol) ^b
4-cis	24.6	2.57	1781 (812), 1814 (425), 1903 (393), 1960 (1174)
4-trans	19.5	2.53	1823 (1012), 1840 (114), 1893 (1275), 1944 (571)
5-cis	26.4	2.45	1811 (1145), 1817 (109), 1901 (842), 1969 (1246)
5-trans	21.6	2.45	1810 (1133), 1817 (0), 1902 (2029), 1336 (0)

(a) Energies measured relative to the ground state singlet parent structure. (b) Values in parentheses report the calculated intensities for each CO-stretching absorption.

In this regard, structure **4-trans** appears in reasonable agreement with the transient observed in the TRIR spectra in cyclohexane solution (refer to Table 14.1). In order of increasing

frequency, a relatively intense bridging CO band is predicted, accompanied next by a relatively intense terminal CO band, and then a final, highest frequency terminal CO band of notably lower intensity. Based on the low intensity calculated for the 1840 cm^{-1} mode for **4-trans**, it is reasonable that this band could not be detected in the TRIR experiment in cyclohexane, or it may also overlap one band of the CO-loss species, **2**. The ordering of the bands calculated for structure **4-cis** is qualitatively different. Again in order of increasing frequency, a relatively intense bridging CO band is again predicted, followed by a second bridging CO band of just over half the intensity of the first, followed by a slightly weaker terminal CO band, and finally a highest frequency terminal CO band of the largest overall intensity. The prediction of the highest frequency terminal CO stretching band being the most intense in the spectrum is at stark odds with the experimental observations. The same is true of **5-cis**, ruling out this structure as well. **5-trans** is only expected to show two IR-active bands in the CO-stretching region, and is thus also inconsistent with the experimentally observed transient in the TRIR spectra.

The CO stretching vibrations of the transient observed in THF are qualitatively similar to those observed in cyclohexane, with the exception of a second bridging CO absorption, blue-shifted relative to that observed in cyclohexane and at roughly one third the intensity of the first bridging absorption band. For the same reasons described in the preceding paragraph, structures **4-cis**, **5-cis**, and **5-trans** are inconsistent with the experimentally observed spectra in THF, while **4-trans** again provides a qualitatively correct description of the spectrum observed. The only caveat is that the second, lower intensity bridging CO absorption in **4-trans** (that listed at 1840 cm^{-1} in Table 15.1) must become more intense in THF solution, presumably due to a distortion of the structure in the more polar solvent. Nonetheless, **4-trans** again provides the only qualitatively correct description of the CO-stretching region of the spectrum observed experimentally.

Thus the structure of the transient observed experimentally in both cyclohexane and THF solvents is assigned to a structure of the form of the triplet species **4-trans**, containing two semi-bridging CO ligands and a trans configuration of the two terminal CO ligands. It is worth taking note that the agreement between the experimental and calculated spectra is only qualitative at best, and the precise structural details will likely differ from those calculated for **4-trans**. It is also worth pointing out once more that no singlet minima other than the parent complex could be located, and thus the transient observed experimentally is assigned to an excited state triplet intermediate.

Similar to the parent complex, **1**, the triplet transient rearrangement isomer appears to also favor a conformation involving semi-bridging CO-ligands, suggesting that the tendency to adopt semi-bridging CO-ligand conformations for this chromium d^5 complex persists even in its excited state structures.

14.3.4 Picosecond TRIR Spectroscopy of $[\text{Cp}^*\text{Mo}(\text{CO})_2]_2$ in Cyclohexane Solution

We were also interested to study the primary photochemistry of the molybdenum congener, $[\text{Cp}^*\text{Mo}(\text{CO})_2]_2$ (**6**). However, we found that this complex was unstable when dissolved in solution, decaying on the timescale of a few hours in cyclohexane, and more rapidly in THF solution, as monitored via FTIR spectroscopy. Figure 14.7 shows FTIR spectra of $[\text{Cp}^*\text{Mo}(\text{CO})_2]_2$ at 10 minutes and 3 hours following dissolution in cyclohexane solution (the sample vessel contained air, though was sealed after preparing the solution). The parent bands of

6 at 1844 and 1869 cm^{-1} decay with the rise of bands at 1882, 1903, and 1938 cm^{-1} corresponding to a decay product (or, perhaps, multiple decay products) of the parent complex.

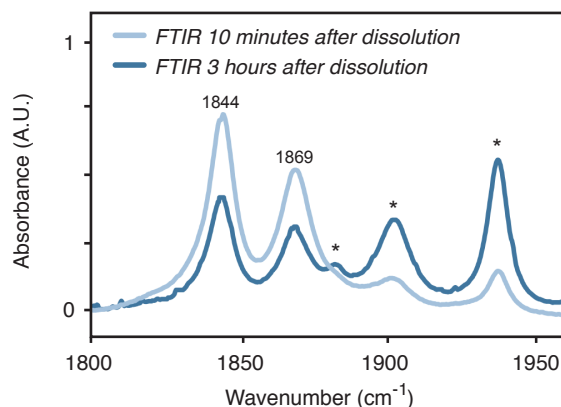


Figure 14.7. FTIR spectra of **6** in cyclohexane solution at times of 10 minutes and 3 hours following dissolution. Asterisks (*) denote bands corresponding to decay products of **6**, which become increasingly intense as more time elapses following dissolution.

TRIR spectra of a cyclohexane solution of **6** collected over the course of ca. 1-2 hours (the time period used for collection of data in this experiment before preparing a fresh sample) thus amount to spectra monitoring a mixture of both the parent complex and its decay product(s) simultaneously. These TRIR spectra collected following 267 nm excitation are shown in Figure 14.8. Clearly, interpretation of the observed product bands is confounded by the presence of a mixture of species present in solution, making it difficult or impossible to draw definitive structural conclusions about the nature of the long-lived products formed. Nonetheless, inspection of the bridging CO-stretching region of the spectrum allows us to observe a clear difference between the photochemistry of **6** and that of **1**; no bridging carbonyl absorption bands are observed in the spectra for the molybdenum species. This fact indicates that no bridged photoproducts are formed from the parent complex, nor from its uncharacterized decay product(s), though our present focus is on the photochemistry of the parent molecule. Short-lived bands at ca. 1832 and 1859 cm^{-1} appear to correspond to the vibrationally excited parent complex, as these bands greatly resemble the IR spectrum of **6** simply red shifted by ca. 10 cm^{-1} , consistent with a vibrationally excited parent species. These transient bands have a lifetime on the order of tens of picoseconds, significantly shorter than those of the transient observed for the Cr complex, and again consistent with relaxation/cooling of a vibrationally excited parent species. These transient bands decay with concomitant recovery of the bleaches of **6**, indicating that **6** is reformed as the vibrationally excited species decays. The bleaches of the impurities (marked with asterisks in Figure 14.8), do not recover, indicating that their depletion leads to long-lived products, presumably CO-loss products.

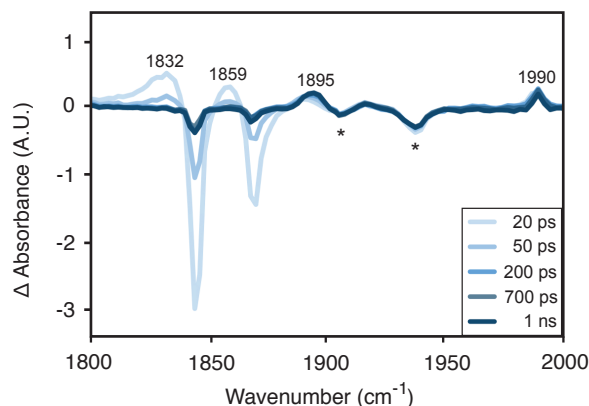


Figure 14.8. TRIR spectra of **6** in cyclohexane solution following 267 nm excitation collected over the course of ca. 1-2 hours before preparing a fresh sample. Since **6** is unstable in solution and decays to form another species (refer to Figure 14.6), these TRIR spectra are best regarded as representing the primary photochemistry of both **6** and the decay product of **6** that forms upon dissolution in cyclohexane solution. Asterisks (*) denote bleach bands corresponding to the decay product of **6**. (A.U. = Arbitrary Units)

The longer lived bands observed at 1895 and 1990 cm^{-1} are difficult to assign due to the presence of the decay product(s) of **6** in the sample. Thus here we simply report the frequencies observed for these long-lived bands and only tentatively discuss their assignment. These almost certainly correspond to CO-dissociation products of **6** and its decay products, as cleavage of the Mo \equiv Mo bond in **6** is unexpected to occur via a single photon excitation. However we will not attempt to assign a definitive molecular structure to these bands, and again emphasize that our primary motivation in discussing these results is to simply show that no bridged transients or photoproducts are formed from the Mo complex. This highlights that the photochemistry of the Cr and Mo complexes differs in their tendency to form both transient and long-lived photoproducts containing bridged CO ligands, with the Cr complex favoring bridging CO-ligands between the two metal centers.

14.4 Conclusions

The picosecond photochemistry of $[\text{Cp}^*\text{Cr}(\text{CO})_2]_2$ in alkane and THF solution has been studied using TRIR spectroscopy. Visible or UV excitation leads predominantly to formation of a transiently lived (378 ± 15 ps) rearrangement isomer with a weakened Cr \equiv Cr bond and two terminal carbonyl ligands rearranged to bridging conformations. This species reverts to the parent complex on the picosecond timescale and does not appear to be involved in formation of the CO-loss product. DFT calculations indicate that this transient is characterized by a triplet spin state and that the two terminal CO ligands adopt a trans conformation about the Cr \equiv Cr bond. Photolysis in neat THF solution does not trap the transient intermediate, and its lifetime (344 ± 17 ps) is similar in either solution. The structure of the transient appears qualitatively similar in THF, though some structural differences must exist between the transient structure observed in the two solvents, evidenced by the observation of a second bridging CO-stretching band in THF solution.

The previously characterized CO-loss species of the Cr dimer, which adopts an asymmetric arrangement of the three bridging CO ligands, is not observed to react with THF (again in neat THF solution) on the picosecond time scale. This suggests that a kinetic barrier to formation of the previously observed THF adduct (**3**, refer to Figure 14.1) exists. The present study also makes clear that CO-dissociation is a relatively low quantum yield event, with formation of the transient being the major photochemical pathway.

The molybdenum congener, $[\text{Cp}^*\text{Mo}(\text{CO})_2]_2$, was found to be unstable in solution, decaying on the time scale of a few hours in cyclohexane solution, and more rapidly in THF. TRIR spectroscopy was used to investigate the potential formation of bridged intermediates in the photochemistry of this Mo congener, and no bridged species, transient nor long-lived, were observed. This indicates that the photochemistry of the molybdenum complex does not involve the formation of CO-bridged intermediates to the same extent observed for the chromium complex.

Overall, these results provide some of the first insight to date on the primary photochemical dynamics of transition metal dimers containing multiple metal-metal bonds (i.e. metal-metal bonds of order two or higher). These species will likely display significantly different photochemistry than the body of existing transition metal dimers characterized to date (i.e. complexes with metal-metal single bonds), as the lower tendency to undergo metal-metal bond cleavage for the former class of complexes will lead to a greater tendency for the solution phase photochemistry of these complexes to be dictated by ligand-dissociation pathways.

15 Should External Heavy Atom Effects be Expected in Transition Metal Complexes?

The following chapter is intended to be published in an American Chemical Society Journal and thus we claim no copyright for the text or figures contained in this chapter.

15.1 Introduction

The influence of spin state changes on the rates of chemical reactions is a topic of significant and longstanding interest in organometallic and transition metal chemistry.^{13,14,29,54,77,534–537} As these reactions are formally forbidden, the requirement for a spin state change between reactants and products is frequently invoked to rationalize slow or non-reactivity.^{11,538,539} Nonetheless, an increasing number of reaction mechanisms with steps involving spin state changes are consistently being uncovered,^{87,88,540} highlighting the difficult-to-predict relationship between spin state changes and chemical reactivity, particularly where transition metal complexes are involved.

The probability of moving between two potential energy surfaces of different spin multiplicity is mediated by spin-orbit coupling (SOC), a property which tends to increase with increasing atomic number. For complexes of the heavier second and third row transition metal elements, SOC is often large, resulting in facile spin crossover. However, for complexes of first row transition metal elements, SOC is often low enough that non-adiabatic behavior contributes significantly to slowing reaction rates. For example, a recent study of the reaction of the triplet $^3\text{Fe}(\text{CO})_4$ with CO to yield the singlet product $^1\text{Fe}(\text{CO})_5$ found that the probability of surface hopping is only ca. 0.05.^{77,79}

With regard to organic molecules, which typically have substantially lower SOC than transition metal complexes, the probability of spin state changes can be increased by a nearby heavy atom present in a different molecule (e.g. another solute or solvent molecule); this is termed an *external heavy atom effect*. External heavy atom effects were first proposed by Kasha in the 1950's³⁶ and have since been implicated in an expansive number of other studies in both chemical and biological contexts. For example, external heavy atom effects enhance the probability of spin forbidden transitions in molecular oxygen,⁵⁴¹ fullerenes,^{64,542} and organic light-emitting diodes (OLEDs),⁵⁴³ in addition to a wide range of organic molecules.^{65,544–546} External heavy atom effects on spectral transitions have also been investigated for metal ions and complexes, albeit to a lesser extent.^{547–549}

However, external heavy atom effects on reaction rates in transition metal complexes remain almost entirely unexplored. Such is the focus of the present investigation. External heavy atom effects in transition metal complexes may be important in a wide variety of contexts in which spin state changes occur, particularly those involving reactions of first-row transition metal complexes, as these involve the lightest elements among transition metal complexes and thus will tend to have relatively low SOC properties. Examples of relevant reactions include those to produce transition metal dimers, trimers, and clusters (particularly heterometallic complexes), the catalytic activation of stannanes, or more generally any reaction forming a bond between a

transition metal element and another element of high atomic number (e.g. tin, lead, a lanthanide or actinide, etc.), or any reaction occurring in a solvent containing a heavy atom.

A limited number of experimental investigations into external heavy atom effects on chemical reaction rates in transition metal complexes have been carried out to date. Tyler and coworkers investigated the presence of a spin barrier to the geminate recombination 17-electron radicals in complexes of Fe, Mo, and Ti.²⁰⁴ Recombination efficiencies were found to be similar in the presence or absence of an external heavy atom perturber, from which it was concluded that no spin barrier was present; another possible interpretation exists, which is that an external heavy atom effect may not have been significantly observed. A combined experimental/computational study by our group also investigated the activation of stannanes (Sn-H bonds) by a series triplet, first-row transition metal reaction intermediates. In that study, we carried out calculations of SOC for the transition metal complexes and found no evidence for an external heavy atom effect; changes in SOC were found to be similar for the approach of either an Si-H or Sn-H ($Z_{\text{Si}} = 14$, $Z_{\text{Sn}} = 50$) moiety to a series of three first-row transition metal complexes.²⁷⁰

Here we set out to explore the role of external heavy atom effects in transition metal complexes with a computational study on the prototypical 16-electron reaction intermediate $\text{Fe}(\text{CO})_4$. The chemistry of iron pentacarbonyl and its photoproducts has been studied extensively, motivated both by its synthetic utility as a reagent for organometallic iron compounds, and because its rich chemistry relates broadly to many fundamental chemical phenomena, including fluxional ligand rotation, ligand substitution reactions, and two-state reactivity.^{550,551} Its CO-loss product, $\text{Fe}(\text{CO})_4$, exists in a triplet ground state in both solution and gas phases, and spin crossover to a singlet is required for subsequent chemical reactions to occur. Solution phase spectroscopic studies indicate that the triplet species does not interact substantially with weakly coordinating solvents (e.g. alkanes), and that in more coordinating solvents (e.g. alcohols) it undergoes rapid spin crossover to a singlet state with concurrent solvent coordination, as depicted in Figure 15.1.^{18,29,30}

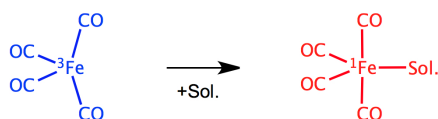


Figure 15.1. Triplet $\text{Fe}(\text{CO})_4$ undergoes solvent coordination and spin crossover to form a singlet adduct

A nonadiabatic analogue to transition state theory has been developed, which characterizes reaction rates via a minimum energy crossing point (MECP) between two potential energy surfaces, in this case of different spin multiplicity.^{76,77,79,91,552–555} The enthalpic barrier to reach the MECP is analogous to that in an adiabatic reaction, but passage over the barrier in the spin-forbidden case is also dictated by the surface hopping probability, which is closely linked to the SOC matrix element coupling the singlet and triplet states at the MECP. Previous work has found success applying such a bimolecular non-adiabatic treatment to calculating the rate constant for addition of a CO ligand to $^3\text{Fe}(\text{CO})_4$.⁷⁹ Figure 15.2 diagrams the potential energy surfaces involved in a non-adiabatic reaction involving coordination of a ligand/small molecule to triplet $^3\text{Fe}(\text{CO})_4$ to yield a singlet adduct, schematically indicating the location of the MECP at the intersection of the diabatic singlet (red) and triplet (blue) surfaces.

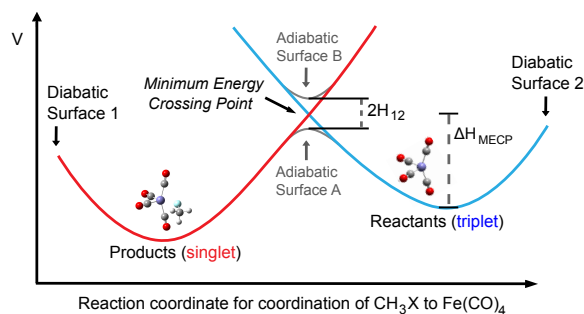


Figure 15.2. Diagram of the potential energy surfaces associated with a spin-forbidden reaction. The diabatic surfaces correspond to potential energy surfaces of a pure spin state, and their intersection defines the MECP geometry. H_{12} in the present case corresponds to the SOC matrix element coupling the two electronic surfaces. The adiabatic surfaces describe potential energy surfaces whose spin character varies smoothly from reactants to products. Adiabatic Surface A thus depicts the potential energy surface that would be followed in the limit of large SOC.

In the present study we explore the changes in SOC that occur along a bimolecular reaction coordinate for coordination of a small molecule to ${}^3\text{Fe}(\text{CO})_4$. For this purpose, we selected haloalkanes of the formula CH_3X ($\text{X} = \text{F}, \text{Cl}, \text{Br}, \text{I}$), as well as methanol ($\text{X} = \text{OH}$). The presence of a single potentially coordinating site in each of these molecules makes for a facile and straightforward comparison of the effects on SOC between the singlet and triplet states of $\text{Fe}(\text{CO})_4$ with the approach of each incoming molecule as the group X approaches the Fe center. Similar haloalkanes have also previously served as choice solvents for experimental studies on external heavy atom effects for similar reasons in terms of experimental design.^{36,547,548}

15.2 Methods

15.2.1 Density Functional Theory Calculations

To locate minimum energy crossing point (MECP) geometries for each of the $\text{Fe}(\text{CO})_4 + \text{CH}_3\text{X}$ reactions, partial geometry optimizations were carried out in singlet and triplet spin states at fixed Fe-X distances. These scans build approximate diabatic potential energy surfaces that allow us to locate a representative MECP geometry for the approach of each ligand.⁵⁴⁰ Partial geometry optimizations were carried out at constrained Fe-X separations at intervals of 0.1 Å, and a linear extrapolation between the nearest two points to the MECP on each surface was used to determine the Fe-X distance at the MECP ($\text{Fe-X}_{\text{MECP}}$). A final partial geometry optimization was then carried out at this the $\text{Fe-X}_{\text{MECP}}$ distance (in the triplet spin state) to determine the MECP structure. Because of the approximate nature of the partial optimization method to reach the MECP, the energy barrier located provides a lower bound for the MECP energy barrier (ΔH_{MECP}). As the focus of the present study is on changes in SOC with the approach of each CH_3X moiety, we were less concerned with the calculated ΔH_{MECP} values but rather with obtaining qualitatively reasonable comparisons of the $\text{Fe-X}_{\text{MECP}}$ distances for each reaction.

The DFT calculations in this study were carried out in the Gaussian09⁴³ package with the Fe-X distance as the only constrained parameter. In the case of X = OH, the Fe-O distance was used to characterize the reaction coordinate. The B3LYP hybrid functional^{37,39} was used with the 6-31+g(d,p) basis set^{129,130,373} on C, O, H, and F atoms, while the lanl2dz basis^{44,45} was used on Fe, Cl, Br, and I. Previous studies have shown the B3LYP functional to be appropriate for determining geometries of organometallic species, and that hybrid density functionals more accurately characterize the singlet-triplet energy gap for Fe(CO)₄, as compared to pure density functionals.^{79,270} Additional calculations using the 6+311g(d,p) basis²⁶¹⁻²⁶⁴ for all atoms were carried out to locate the MECP geometries with a higher level basis set to validate the use of the 6-31+g(d,p)/lanl2dz basis for determining the other calculated geometries (see Table S1 for a comparison).

15.2.2 CASSCF Calculations of Spin-Orbit Coupling Constants

SOC calculations were carried out using complete active space self consistent field (CASSCF) wavefunctions generated with the GAMES-US package⁵⁶ at the DFT optimized geometries. The full, 2-electron Pauli-Breit SOC operator was used to evaluate SOC in all calculations.^{61,62} The active space in each CASSCF calculation consisted of 10 frontier molecular orbitals occupied by 10 electrons (a (10,10) active space). The choice of active spaces for transition metal carbonyls, and specifically for iron carbonyls, has been considered previously.^{79,556} This choice of active space accounts for the double shell effect, which has been shown to be important.⁵⁹ SOC was calculated at each DFT generated triplet geometry using two sets of molecular orbitals (one for each spin state). This procedure for calculating SOC involves a corresponding orbital transformation that requires freezing the core occupied molecular orbitals from the first wave function optimized (this can be either spin state) as the SCF procedure optimizes the second wave function.⁶⁰ For consistency, the triplet spin state orbitals were always optimized first, so that the core molecular orbitals from the triplet wave function were frozen as the singlet spin state orbitals were optimized. The effect of optimizing either set of orbitals first has been considered previously and is not expected to make a significant difference.⁵⁵⁷ We also carried out our own comparisons by optimizing the singlet spin state orbitals first at several geometries, and we found negligible differences in the calculated SOC values. The lanl2dz basis^{44,45} was used for all SOC calculations. We note that there are not many basis sets available for treating atoms as heavy as iodine, and we wanted to use the same basis set on each of the coordinating groups for consistency. Since the important results of this work are largely qualitative, we feel it is safe to say that these choices do not affect the significance of our results. The results of the present SOC calculations also agree favorably with those in the literature for Fe(CO)₄ for which an all-electron double-zeta basis set was used.⁷⁹ All reported SOC values are given as the root mean square SOC (SOC_{rms}) between the three triplet substates and the nearest singlet state. Assuming rapid equilibration between triplet substates, the root mean square value is the relevant quantity for calculating the probability of crossing between electronic surfaces, and is hence the quantity relevant to the rate of spin crossover.

15.3 Results and Discussion

15.3.1 Calculation of Molecular Geometries and Spin-Orbit Coupling Matrix Elements

We began by identifying a set of representative molecular geometries of interest, including the MECPs for each reaction of interest. As noted in section II.A, MECPs were located using the partial geometry optimization method,⁵⁴⁰ which involves carrying out DFT geometry optimizations at constrained Fe-X distances (X = F, Cl, Br, I, OH) for each of CH₃X molecules approaching the iron center of Fe(CO)₄. These calculations were carried out in both the singlet and triplet spin states, allowing us to build up approximate diabatic potential energy surfaces for coordination of the CH₃X moiety to Fe(CO)₄, as diagrammed schematically in Figure 15.2. After determining the Fe-X_{MECP} distance for each reaction, a final constrained geometry optimization was performed to obtain a representative MECP geometry. The Fe-X distances and energy barriers (ΔH_{MECP}) associated with each MECP are listed in Table 15.1.

Table 15.1. MECP Fe-X distances, energy barriers and SOC_{rms} matrix elements for the coordination of CH₃X molecules to Fe(CO)₄

CH ₃ X (X=)	Fe-X _{MECP} distance (Å)	ΔH_{MECP} (kcal/mol)	MECP SOC _{rms} Matrix Element (cm ⁻¹)
F	2.35	4.85	151.2
Cl	2.91	1.22	124.4
Br	3.11	1.21	114.2
I	3.34	1.25	78.4
OH^a	2.58	0.17	183.7

(a) The Fe-O distance was used for CH₃OH

To assess the changes in SOC that occur along each reaction coordinate, the geometries obtained from constrained geometry optimizations were used to generate CASSCF wave functions for both singlet and triplet spin states, which were then used to calculate the SOC matrix elements between the singlet and triplet states. Figure 15.3 shows the SOC_{rms} matrix elements for bimolecular reactions of Fe(CO)₄ with CH₃X molecules as a function of the distance between the Fe center and the coordinating atom.

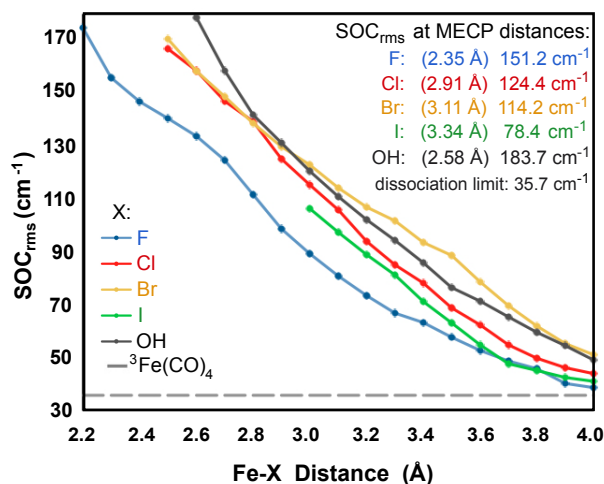


Figure 15.3. SOC_{rms} matrix elements as a function of Fe-X (X = F, Cl, Br, I, OH) distances, and at the dissociation limit (lower dashed grey line, the x-axis is not meaningful with respect to the dissociation limit value). SOC was computed at the DFT optimized geometries using CASSCF wave functions. The SOC matrix element at the MECP Fe-X distance is indicated for each reaction. Circles on the plot correspond to calculated data points, while the lines are included to aid visualization.

In all cases we found SOC to increase with the approach of the incoming CH₃X molecule. For example, the calculated SOC_{rms} matrix element for Fe(CO)₄ reacting with CH₃F increase from the dissociation limit value (i.e. for isolated Fe(CO)₄ in vacuum) of 35.7 cm⁻¹ to 151.2 cm⁻¹ at the CH₃F Fe-X_{MECP} distance of 2.35 Å. Significantly, our findings do not suggest that a heavy atom effect is at work. Similar changes in SOC were observed for the approach of each ligand to the metal center, as can be seen in Figure 15.3. From both qualitative and quantitative perspectives, only minor differences are observed, in terms of the changes in SOC, with the approach of each of the different CH₃X molecules. No clear trends or correlations are present between SOC_{rms} values and the atomic number of the incoming coordinating atom or functional group, X. In fact, when taking into account the different Fe-X_{MECP} distances, which tend to increase with the size of the incoming atom (see Table 1 or Figure 15.3), Figure 15.3 indicates the opposite of a heavy-atom trend in SOC at the MECP geometries. While each incoming group causes notable changes in SOC, it is perhaps more noteworthy that the lightest incoming groups, OH and F, are predicted to cause the greatest increase in SOC at the respective MECP geometries, and this would appear to be attributable to their close Fe-X_{MECP} distances.

In the following sections, we will explore the nature and origins of the changes in SOC with varying Fe-X distance, as well as discuss the implications of these changes for the chemistry of transition metal complexes undergoing non-adiabatic reactions.

15.3.2 Exploring the Changes in SOC Observed Along a Bimolecular Reaction Coordinate

Some existing studies on SOC in organic biradicals have provided a satisfying qualitative description of the factors responsible for CASSCF computed changes in SOC by approximating

$^3\text{Fe}(\text{CO})_4$, are 0.072 Å and 0.079 Å, respectively, and the corresponding SOC_{rms} values at the MECP geometries are 78.4 cm^{-1} and 183.7 cm^{-1} , respectively (recall that the Fe- X_{MECP} distances varied for each CH_3X group, 2.58 Å for the reaction involving CH_3I , and 3.34 Å for that involving CH_3I , refer to Table 15.1). Thus, it is again clear that it isn't simply the changes in $\text{Fe}(\text{CO})_4$ nuclear coordinates that are responsible for the changes in SOC at the MECP geometries, relative to the dissociation limit. *The presence of the incoming CH_3X molecule, and its interactions with the electronic structure of the $\text{Fe}(\text{CO})_4$ moiety, would thus appear to be key to effecting the changes in SOC.*

Second, the active space MOs, in which the unpaired triplet electron density resides, do not take on significant contributions from AOs on the coordinating atom, X. SOC depends on characteristics of the frontier orbitals of the atom or molecule in which the unpaired spin density resides. An orbital-based analysis becomes somewhat complicated in the case of a (10,10) CASSCF wave function, where configuration state functions from all possible permutations of excitations within the 10 active space orbitals contribute to the wave function. Thus to evaluate the characteristics of the active space MOs, we present a largely simplified analysis that allows a qualitative inspection of the atomic/molecular orbital contributions to the wave functions with results that offer a basic, but intuitive, level of insight into the computed SOC values. The atomic orbital contributions to each of the 10 active space orbitals in the MECP wave functions were analyzed and grouped into orbitals located on either the $\text{Fe}(\text{CO})_4$ molecule, or onto the incoming atom, X. Table 15.2 shows the (normalized) atomic orbital contributions summed for the nine atoms of the $\text{Fe}(\text{CO})_4$ moiety along with those from the coordinating atom X, averaged over the 10 active space MOs. Inspecting the values in Table 15.2, it is clear that the diradical character does not delocalize significantly onto the incoming group.

As with any simplified analysis, there are limitations and flaws to this approach that we should briefly point out. For example, the number of orbitals present on the $\text{Fe}(\text{CO})_4$ moiety or X atom are influenced by the choice of basis set, and we have not attempted to account for this in the present simplified analysis. We have also averaged over the active space orbitals, effectively making some assumption that each is equally important to the wave function, which is not the case. *Nonetheless, despite these somewhat crude simplifications, it is clear that the active space orbitals, responsible for determining SOC, do not delocalize significantly onto the incoming group, X.* This does present a physically reasonable picture, in that it seems quite reasonable the electron(s) responsible for changing the spin state of the $\text{Fe}(\text{CO})_4$ molecule should remain primarily on the $\text{Fe}(\text{CO})_4$ molecule. The frontier MOs in transition metal complexes are indeed typically spaced relatively closely in energy and have a significant amount of d-orbital character.

Third, the observed changes in SOC depend not only on the Fe-X distance, but also on the angle of approach, as shown in Figure 15.5. This simply demonstrates that the calculated SOC values depend on multiple structural coordinates, and not only on the Fe-X distance, which is not at all surprising. This angular dependence contributes to the fact that the SOC_{rms} values in Figure 15.3 do not vary in an entirely smooth manner with respect to Fe-X distance. Looking at Figure 15.5, the larger incoming groups (Cl, Br, I) show a stronger angular dependence, perhaps due to their larger valence orbitals approaching the Fe center more closely, making the active space Fe-centered MOs more sensitive to changes in their orientation. We note that the choice to not optimize the geometries at each angular orientation inspected in Figure 15.5 was made in the interest of looking at changes in a single parameter (the angle of the ligand relative to the equatorial plane), whereas the changes in Figure 15.3 are influenced by minor changes in multiple other coordinates, in addition to the Fe-X distance.

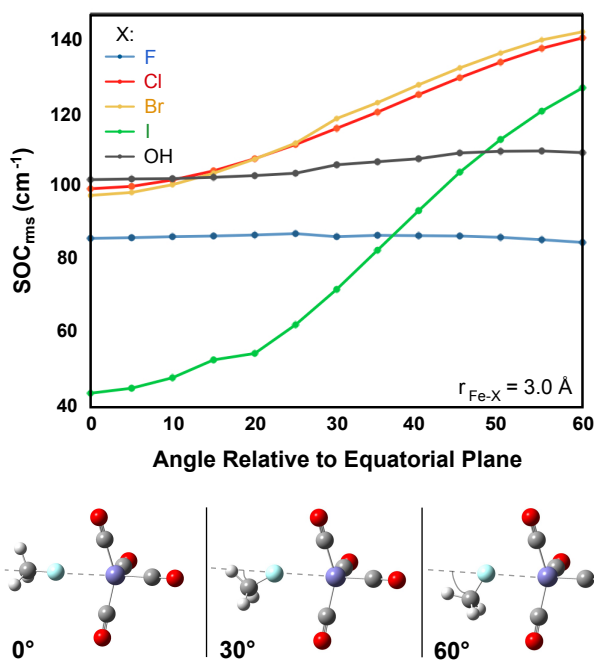


Figure 15.5. SOC_{rms} matrix elements as a function of orientation for ${}^3\text{Fe}(\text{CO})_4$ and CH_3X geometries optimized with the constraint $r_{\text{Fe-X}} = 3.0 \text{ \AA}$. Geometries of the individual molecules were not reoptimized between successive calculations, so that only their relative orientation was changed (e.g. all bond lengths and angles for the individual $\text{Fe}(\text{CO})_4$ and CH_3X moieties were held constant). These geometries are similar to those along the Fe-X reaction coordinate (Figure 16.3). The dependence of SOC on orientation illustrates the complex, multidimensional relationship between SOC and molecular geometry along the bimolecular reaction coordinate.

For $\text{Fe}(\text{CO})_4$, the approach of an incoming ligand to the vacant coordination site appears to only cause increases in SOC, relative to the dissociation limit. This is consistent with the limited number of other studies in the literature to date, in which addition of a silane, stannane,²⁷⁰ or CO ⁷⁹ were all found to increase SOC at the MECF geometry, relative to the dissociation limit. However, it remains entirely possible that addition of a ligand to the vacant coordination site(s) of other complexes could cause decreases in SOC as well. Indeed, earlier work by us²⁷⁰ indicates that addition of a silane or stannane to triplet $\text{CpV}(\text{CO})_3$ results in a decrease in SOC with approach of an incoming ligand.

15.3.3 Implications with Regard to an External Heavy Atom Effect

The extent to which a reaction behaves non-adiabatically can be considered in the context of the Landau-Zener expression describing the probability of hopping between electronic surfaces at the MECF on either a first pass through the crossing, or a return attempt.⁹¹

$$P_{SH}^{\text{Landau-Zener}}(E_H) = (1+P)(1-P) \quad (1a)$$

$$P = \exp \left[\frac{-2V_{12}}{h\Delta F} \sqrt{\frac{\mu_H}{2(E_H - E_{MECP})}} \right] \quad (1b)$$

With other factors constant, the probability for not crossing on a given attempt decreases with the exponential of the SOC matrix element squared. In the limit of small surface hopping probability, which previous work indicates is appropriate for the addition of a ligand to ${}^3\text{Fe}(\text{CO})_4$,⁷⁹ the Landau-Zener expression can be Taylor expanded to first order to show that the probability of surface hopping scales with the square of the SOC matrix element.

$$P_{SH}^{Landau-Zener}(E_H) = \frac{4V_{12}^2}{h\Delta F} \sqrt{\frac{\mu_H}{2(E_H - E_{MECP})}} \quad (1c)$$

This implies that a 3-5 fold increase in SOC at the bimolecular MEC, relative to SOC at the ground state ${}^3\text{Fe}(\text{CO})_4$ geometry (roughly the magnitude of changes observed in Figure 15.3), causes a 9-25 fold increase in the surface hopping probability. This interpretation is best regarded as a qualitative assessment, but gives an idea of the overall magnitude of the contribution of the changes in SOC to the predicted reaction rates; the increased SOC along a bimolecular reaction coordinate is predicted to accelerate the rate of the reaction by a factor of ca. 9-25 times. As we noted earlier, this effect is expected to vary depending on the complex involved, and indeed there will be reactions where SOC will decrease along a bimolecular reaction coordinate.

The more interesting result, and that which more likely extends to other complexes as well, is that *our results indicate that we should not expect an external heavy atom effect to come into play for the reaction of this first-row transition metal complex*. Similar changes in SOC were predicted with the approach of each incoming ligand, regardless of atomic number. Notably, when taking into account the differing Fe- X_{MECP} distances, we actually expect to see the opposite of a heavy atom effect, where the incoming groups of lowest atomic number (also smallest in size), are predicted to effect the greatest changes in SOC at the MEC geometry, relative to the dissociation limit.

There exist only a limited number of studies to date for comparison to the present results. SOC calculations were carried out in our earlier work on the activation of stannanes by a series of first-row transition metal complexes. As was noted earlier in this manuscript, the approach of either an Si-H ($Z_{Si} = 14$) or Sn-H ($Z_{Sn} = 50$) group to the metal center caused similar changes in SOC; in that study too, no evidence for an external heavy atom effect was found.²⁷⁰ Harvey et. al. also studies the addition of CO to $\text{Fe}(\text{CO})_4$ calculating SOC at both the ground state geometry, as well as at the MEC for the addition of CO to form $\text{Fe}(\text{CO})_4$. Their dissociation limit SOC value of 29 cm^{-1} agrees well with our calculated value of 35.7 cm^{-1} . They found that SOC at the $\text{Fe}(\text{CO})_4 + \text{CO}$ MEC increased to 66 cm^{-1} , again in qualitative agreement with the trends observed involving coordination of CH_3X molecules in the present study.⁷⁹

In light of the body of existing work on solvent external heavy atom effects, it is also worth briefly considering the implications of our present study on the possibility of external heavy atom effects on transition metal complexes by a heavy atom perturber present in the bulk solvent

(i.e. when the solvent is not explicitly one of the molecules involved in the reaction). Haloalkanes bearing chlorine, bromine, and iodine atoms have often served as choice solvents for designing experiments to test for such effects. The structure of liquids such as iodomethane, for example, are thus relevant to interpreting the implications of our present computational study on the possibility of solvent heavy atom perturbers on reaction rates of spin forbidden reactions of transition metal complexes. In neat iodomethane, the radial distribution function for nearest neighbors of the heavy element, I, places nearest intermolecular I-I interactions at ca. 3.5-4 Å, I-C interactions at ca. 3-3.5 Å, and I-H interactions at ca. 2.5-3 Å.⁵⁶² Comparison of these radial distributions to the changes in SOC shown at similar Fe-X distances in Figure 15.3 would suggest that an external heavy atom effect is not predicted to be present for a first-row transition metal complex, such as Fe(CO)₄, dissolved in iodomethane or other similar solvents.

15.4 Conclusions

In conclusion, we have found that SOC in a prototypical organometallic reaction intermediate, Fe(CO)₄, changes significantly along a bimolecular reaction coordinate, and that the changes in SOC do not appear to be significantly affected by the atomic number of the coordinating atom or functional group. Our work thus indicates that an external heavy atom effect is not expected to influence the rate of reactions of this complex. In fact, when the differing Fe-X_{MECP} distances are taken into account, the opposite of a external heavy atom type trend is predicted, with the lightest coordinating atoms (e.g. F, OH) causing the greatest increases in SOC at the MECP geometry.

We point out that while an increase in SOC was observed here with the approach of each incoming molecule along the bimolecular reaction coordinate, changes in SOC along such a reaction coordinate are difficult to predict by “chemical intuition” alone, and cases will exist in which SOC decreases with the approach of an incoming ligand.

The conclusions of this study are also relevant to reactions occurring in solvents containing heavy atoms, where external heavy atom effects have been observed in a large number of studies on organic molecules. Such effects have not previously been explored for reactions of transition metal complexes, though the results of our calculations do bear relevance to such situations. Specifically, we do not see any evidence of an external heavy atom effect by heavier elements such as Br ($Z_{\text{Br}} = 35$) or I ($Z_{\text{I}} = 53$) on this first-row transition metal complex at distances relevant to those in solution (on the order of a few angstroms). However, it is important to remember that transient collisions in liquids may place the heavy atom (e.g. I) into closer contact with the metal center for fleeting periods of time, during which more substantial perturbations on SOC may occur, and while our calculations do not directly address this possibility, we find no evidence for such an effect. It is also worth keeping in mind that the metal center of a transition metal complex is typically where the unpaired electron density will be localized, and thus the presence of ligands will tend to hinder the approach of external heavy atoms to the site (the metal center) relevant to effecting changes in spin state.

Most importantly, the results of this computational study suggest that external heavy atom effects are not expected to exert a significant influence on the rates of spin forbidden reactions of transition metal complexes. As this is among the first computational study to date to explore the role of external heavy atom effects on the rates of organometallic reactions, we hope that this will serve as a starting point for additional exploration in this area. It is important to note that

implicit in the application of computational results of the nature presented here to experimental chemistry is the assumption that nonadiabatic transition state theory can accurately characterize the rate of a nonadiabatic reaction through a single MECP geometry, and in particular that the relevant SOC value to the rate of a nonadiabatic reaction rates is solely that at the MECP geometry.

16 Summary and Outlook

As is hopefully evident from the studies described in this thesis, time-resolved spectroscopy provides a powerful tool for elucidating the dynamics of organometallic reactions. Time-resolved spectroscopic approaches can allow the observation and identification of each distinct intermediate in complex reaction mechanisms. Kinetic barriers to individual reaction steps can be directly measured, and, ideally, carefully designed experiments can be used to gain predictive insight into reactions which have not yet been studied, allowing rational design and exploration of new synthetic approaches with practically useful applications. The investigations described in this thesis represent just a tiny fraction of the contributions time-resolved spectroscopy has made to the understanding of organometallic catalysis and photochemistry over the past several decades.

Much of my motivation for studying the role spin states and spin state changes play in organometallic reactions stemmed from the fact that this area of chemistry seemed poorly understood, yet relevant to a wide range of organometallic reactions. The studies described in this thesis, combined with earlier work from the Harris group, and from other research groups, suggest that the spin state of a coordinatively unsaturated reaction intermediate can serve as a good predictive indicator of overall trends in reactivity and solution-phase dynamics. Still, there remains much work to be done to expand the scope of the species whose reactivity has been studied experimentally. A recent review article has attempted to synthesize much of the work contained in this thesis, and the reader may wish to look to this articles for a brief summaries of the overall results of much of the work described in the preceding chapters.⁵³⁶

Additionally, the state of the theoretical understanding of spin-forbidden reactions is interesting to consider. As is described in a few different areas of this thesis (see Chapter 15, for example), a nonadiabatic analogue to transition state theory has been developed to describe chemical reactions occurring on multiple potential energy surfaces. In principle, this theory should be easy for any chemist to understand on a basic level, as it is essentially identical to standard transition state theory, with the caveat that there is a non-unity probability of passing through the transition state (MECP) once it is reached. However, the extension of this theory to nonadiabatic reactions is not a topic that is commonly taught in any undergraduate or graduate chemistry course. Additionally, the literature on this topic is scarce and is not often written for a non-specialist target audience. Nonetheless, this theory is necessary for understanding the factors affecting the rates of a broad class of chemical reactions. This issue could seemingly be remedied by integrating a basic description of the theory into physical chemistry courses and textbooks. A generalized theory for treating the probability of crossing between the two potential energy surfaces (in other words, for calculating the probability of passing through the transition state analogue in a nonadiabatic reaction), was published by Landau and Zener in 1932, three years prior to the Eyring equation; hence it would not appear to be an issue of the theory needing time to develop, but instead a pedagogical issue.

The two principle quantities that influence the rate of a nonadiabatic reaction are the energy barrier to reach the MECP, and the coupling between the potential energy surfaces, which for spin-forbidden reactions is typically spin-orbit coupling (SOC). Some computational chemistry packages have begun to implement procedures for locating MECP geometries, while others have yet to do so. This should be a relatively simple routine to implement, as it only requires calculating the gradient on the relevant potential energy surfaces, and thus the quantities needed

for locating the MECP are already calculated during a typical geometry optimization. As the routines for locating MECPs become more widely implemented, it will become easy for non-specialists to regularly calculate MECP geometries for chemical reactions of interest. While approximate methods for locating MECPs are already more commonly used (e.g. the partial geometry optimization method used in several cases in this thesis), there are many chemical reactions for which partial optimization methods are not appropriate (e.g. when a single internuclear distance or bond angle does not sufficiently describe the reaction coordinate). Accurately predicting or calculating the energy barrier in a spin-forbidden reaction is also more difficult than in a reaction occurring on a single potential energy surface.

SOC remains one of the most poorly understood quantities in terms of its computation, and this is particularly true when transition metal complexes are involved. Some of the relevant considerations were addressed in Chapter 15, and here I will just point out that this remains an area in which there is much progress to be made, and where much stands to be gained from a better understanding of the properties that influence SOC. This is also a difficult topic for the average chemist to approach, and improvements in the pedagogy surrounding this topic could lower the barrier to entry for exploration and discovery.

Additionally, there have been a very limited number of studies designed to test the applicability of nonadiabatic transition state theory to experimental chemistry. As such, the scope of reactions it can be expected to accurately describe, even qualitatively speaking, has yet to be established. Of course, there are reactions where nonadiabatic transition state theory is not expected to apply. For example, the relaxation processes that immediately follow photoexcitation are one case in which case a spin-forbidden relaxation from an excited state may occur more rapidly than the rearrangement of nuclear coordinates, resulting in a Franck-Condon transition. In such cases, the spin contribution to the probability of the process will still be determined by the SOC between the relevant states via the spin selection rule. Such Franck-Condon-type transitions may also compete with those that would otherwise follow along the potential energy surface associated with changes in nuclear coordinates, and thus it is not always clear which theoretical description is appropriate.

Turning to the other topics of focus in this thesis, the work on the photochemistry of transition metal dimers and clusters elucidated the nuanced behavior of these complexes toward CO-loss and photochemically induced fragmentation. While photochemical CO-loss (or dissociation of other ligands) will likely occur to some extent in most of these complexes, the relative strengths of the metal-metal bonds, along with the other energy dissipation pathways available, will determine whether or not overall metal-metal bond cleavage products are formed. The clusters studied to date make up only a small fraction of those important to organometallic chemistry for synthetic, catalytic, and other applications. The work by our group and others using TRIR spectroscopy to study metal-carbonyl dimer and cluster photochemistry has also been the focus of a recent review article, which interested readers may wish to read.⁵¹⁸

Our exploration into metal carbonyls as CO-releasing molecules represents only one study on this topic, which has been increasing in popularity over the last ca. 10-15 years, resulting in the publication of hundreds of articles on this topic as well as numerous patents in the hopes of these complexes will find clinical applications. The primary contributions of our work in this area were to demonstrate that a molecular understanding of the chemistry that takes place during thermal and photochemical CO release can lead to meaningful mechanistic insight, and that a combined thermal and photochemical approach will often be helpful for achieving the full CO-delivery potential of these complexes.

Overall, the studies described in this thesis touch on several distinct areas of organometallic chemistry in which time-resolved infrared spectroscopy, combined with quantum chemistry calculations, were able to provide new and significant mechanistic insight. These projects, along with the body of existing work to date, demonstrate the value of time-resolved spectroscopic studies for elucidating the fundamental details governing organometallic reaction dynamics.

References

- (1) Cahoon, J. F. Ph.D. Thesis. University of California, Berkeley, 2008.
- (2) Sawyer, K. R. Ph.D. Thesis. University of California, Berkeley, 2008.
- (3) Zoerb, M. C. Ph.D. Thesis. University of California, Berkeley, 2012.
- (4) Hamm, P.; Kaindel, R.; Stenger, J. *Opt. Lett.* **2000**, *25*, 1798–1800.
- (5) Arndtsen, B. A.; Bergman, R. G.; Mobley, T. A.; Peterson, T. H. *Acc. Chem. Res.* **1995**, *28*, 154–162.
- (6) Labinger, J. A.; Bercaw, J. E. *Nature* **2002**, *417*, 507–514.
- (7) Van der Boom, M. E.; Milstein, D. *Chem. Rev.* **2003**, *103*, 1759–1792.
- (8) Jia, C.; Kitamura, T.; Fujiwara, Y. *Acc. Chem. Res.* **2001**, *34*, 633–639.
- (9) Jun, C.-H. *Chem. Soc. Rev.* **2004**, *33*, 610–618.
- (10) Siegbahn, P. E. M. *J. Am. Chem. Soc.* **1996**, *118*, 1487–1496.
- (11) Schrock, R. R.; Shih, K.-Y.; Dobbs, D. A.; Davis, W. M. *J. Am. Chem. Soc.* **1995**, *117*, 6609–6610.
- (12) Schröder, D.; Shaik, S.; Schwarz, H. *Acc. Chem. Res.* **2000**, *33*, 139–145.
- (13) Detrich, J. L.; Reinaud, O. M.; Rheingold, A. L.; Theopold, K. H. *J. Am. Chem. Soc.* **1995**, *117*, 11745–11748.
- (14) Poli, R.; Harvey, J. N. *Chem. Soc. Rev.* **2003**, *32*, 1–8.
- (15) Yang, H.; Kotz, K. T.; Asplund, M. C.; Harris, C. B. *J. Am. Chem. Soc.* **1997**, *119*, 9564–9565.
- (16) Yang, H.; Asplund, M. C.; Kotz, K. T.; Wilkens, M. J.; Frei, H.; Harris, C. B. *J. Am. Chem. Soc.* **1998**, *120*, 10154–10165.
- (17) Snee, P. T.; Yang, H.; Kotz, K. T.; Payne, C. K.; Harris, C. B. *J. Phys. Chem. A* **1999**, *103*, 10426–10432.
- (18) Snee, P. T.; Payne, C. K.; Kotz, K. T.; Yang, H.; Harris, C. B. *J. Am. Chem. Soc.* **2001**, *123*, 2255–2264.
- (19) Kotz, K. T.; Yang, H.; Snee, P. T.; Payne, C. K.; Harris, C. B. *J. Organomet. Chem.* **2000**, *596*, 183–192.
- (20) Neumann, W. P. *Synthesis* **1987**, *1987*, 665–683.
- (21) Trost, B. M.; Semmelhack, M. F.; Fleming, I. *Comprehensive Organic Synthesis: Addition to and substitutions at C-C(pi) Bonds*; Pergamon Press, 1991; Vol. 4.
- (22) Hall, C.; Perutz, R. N. *Chem. Rev.* **1996**, *96*, 3125–3146.
- (23) Bengali, A. A.; Bergman, R. G.; Moore, C. B. *J. Am. Chem. Soc.* **1995**, *117*, 3879–3880.
- (24) Wasserman, E. P.; Bergman, R. G.; Moore, C. B. *J. Am. Chem. Soc.* **1988**, *110*, 6076–6084.
- (25) Snee, P. T.; Payne, C. K.; Mebane, S. D.; Kotz, K. T.; Harris, C. B. *J. Am. Chem. Soc.* **2001**, *123*, 6909–6915.
- (26) Siegbahn, P. E. M.; Svensson, M. *J. Am. Chem. Soc.* **1994**, *116*, 10124–10128.
- (27) Blomberg, M. R. A.; Siegbahn, P. E. M.; Svensson, M. *J. Am. Chem. Soc.* **1992**, *114*, 6095–6102.
- (28) Carroll, J. J.; Haug, K. L.; Weisshaar, J. C.; Blomberg, M. R. A.; Siegbahn, P. E. M.; Svensson, M. *J. Phys. Chem.* **1995**, *99*, 13955–13969.
- (29) Besora, M.; Carreón-Macedo, J.-L.; Cowan, A. J.; George, M. W.; Harvey, J. N.; Portius, P.; Ronayne, K. L.; Sun, X.-Z.; Towrie, M. *J. Am. Chem. Soc.* **2009**, *131*, 3583–3592.
- (30) Portius, P.; Yang, J.; Sun, X.-Z.; Grills, D. C.; Matousek, P.; Parker, A. W.; Towrie, M.; George, M. W. *J. Am. Chem. Soc.* **2004**, *126*, 10713–10720.

- (31) Bachler, V.; Grevels, F.-W.; Kerpen, K.; Olbrich, G.; Schaffner, K. *Organometallics* **2003**, *22*, 1696–1711.
- (32) Dougherty, T. P.; Heilweil, E. J. *J. Chem. Phys.* **1994**, *100*, 4006–4009.
- (33) George, M. W.; Haward, M. T.; Hamley, P. A.; Hughes, C.; Johnson, F. P. A.; Popov, V. K.; Poliakoff, M. *J. Am. Chem. Soc.* **1993**, *115*, 2286–2299.
- (34) George, M. W.; Poliakoff, M.; Turner, J. J. *Analyst* **1994**, *119*, 551–560.
- (35) Lomont, J. P.; Nguyen, S. C.; Schlegel, J. P.; Zoerb, M. C.; Hill, A. D.; Harris, C. B. *J. Am. Chem. Soc.* **2012**, *134*, 3120–3126.
- (36) Kasha, M. *J. Chem. Phys.* **1952**, *20*, 71–74.
- (37) Becke, A. D. *J. Chem. Phys.* **1993**, *98*, 5648–5652.
- (38) Perdew, J. P. *Phys. Rev. B* **1986**, *33*, 8822–8824.
- (39) Lee, C.; Yang, W.; Parr, R. G. *Phys. Rev. B* **1988**, *37*, 785–789.
- (40) Perdew, J. P.; Wang, Y. *Phys. Rev. B* **1992**, *45*, 13244–13249.
- (41) Perdew, J. P.; Chevary, J. A.; Vosko, S. H.; Jackson, K. A.; Pederson, M. R.; Singh, D. J.; Fiolhais, C. *Phys. Rev. B* **1992**, *46*, 6671–6687.
- (42) Perdew, J. P.; Chevary, J. A.; Vosko, S. H.; Jackson, K. A.; Pederson, M. R.; Singh, D. J.; Fiolhais, C. *Phys. Rev. B* **1993**, *48*, 4978–4978.
- (43) Gaussian 09, Revision D.01, Frisch, M. J.; Trucks, G. W.; Schlegel, H. B.; Scuseria, G. E.; Robb, M. A.; Cheeseman, J. R.; Scalmani, G.; Barone, V.; Mennucci, B.; Petersson, G. A.; Nakatsuji, H.; Caricato, M.; Li, X.; Hratchian, H. P.; Izmaylov, A. F.; Bloino, J.; Zheng, G.; Sonnenberg, J. L.; Hada, M.; Ehara, M.; Toyota, K.; Fukuda, R.; Hasegawa, J.; Ishida, M.; Nakajima, T.; Honda, Y.; Kitao, O.; Nakai, H.; Vreven, T.; Montgomery, J. A., Jr.; Peralta, J. E.; Ogliaro, F.; Bearpark, M.; Heyd, J. J.; Brothers, E.; Kudin, K. N.; Staroverov, V. N.; Kobayashi, R.; Normand, J.; Raghavachari, K.; Rendell, A.; Burant, J. C.; Iyengar, S. S.; Tomasi, J.; Cossi, M.; Rega, N.; Millam, N. J.; Klene, M.; Knox, J. E.; Cross, J. B.; Bakken, V.; Adamo, C.; Jaramillo, J.; Gomperts, R.; Stratmann, R. E.; Yazyev, O.; Austin, A. J.; Cammi, R.; Pomelli, C.; Ochterski, J. W.; Martin, R. L.; Morokuma, K.; Zakrzewski, V. G.; Voth, G. A.; Salvador, P.; Dannenberg, J. J.; Dapprich, S.; Daniels, A. D.; Farkas, O.; Foresman, J. B.; Ortiz, J. V.; Cioslowski, J.; Fox, D. J. Gaussian Inc., Wallingford CT, 2009.
- (44) Hay, P. J.; Wadt, W. R. *J. Chem. Phys.* **1985**, *82*, 299–310.
- (45) Dunning, T. H.; Hay, P. J. *Methods of Electronic Structure Theory*; Plenum: New York, 1977; Vol. 2.
- (46) Jr, T. H. D. *J. Chem. Phys.* **1989**, *90*, 1007–1023.
- (47) Woon, D. E.; Jr, T. H. D. *J. Chem. Phys.* **1993**, *98*, 1358–1371.
- (48) Balabanov, N. B.; Peterson, K. A. *J. Chem. Phys.* **2005**, *123*, 064107.
- (49) Poliakoff, M.; Turner, J. J. *J. Chem. Soc. Dalton Trans.* **1973**, 1351–1357.
- (50) Poliakoff, M.; Turner, J. J. *J. Chem. Soc. Dalton Trans.* **1974**, 2276–2285.
- (51) Barton, T. J.; Grinter, R.; Thomson, A. J.; Davies, B.; Poliakoff, M. *J. Chem. Soc. Chem. Commun.* **1977**, 841–842.
- (52) Poliakoff, M.; Weitz, E. *Acc. Chem. Res.* **1987**, *20*, 408–414.
- (53) Hofmann, P.; Padmanabhan, M. *Organometallics* **1983**, *2*, 1273–1284.
- (54) Carreón-Macedo, J.-L.; Harvey, J. N. *J. Am. Chem. Soc.* **2004**, *126*, 5789–5797.
- (55) Smith, K. M.; Poli, R.; Harvey, J. N. *New J. Chem.* **2000**, *24*, 77–80.

- (56) Schmidt, M. W.; Baldrige, K. K.; Boatz, J. A.; Elbert, S. T.; Gordon, M. S.; Jensen, J. H.; Koseki, S.; Matsunaga, N.; Nguyen, K. A.; Su, S.; Windus, T. L.; Dupuis, M.; Montgomery, J. A. *J. Comput. Chem.* **1993**, *14*, 1347–1363.
- (57) Schäfer, A.; Horn, H.; Ahlrichs, R. *J. Chem. Phys.* **1992**, *97*, 2571–2577.
- (58) Peterson, K. A. *J. Chem. Phys.* **2003**, *119*, 11099–11112.
- (59) Roos, B. O.; Andersson, K.; Fulscher, M. P.; Malmqvist, P.; Serrano-Andres, L.; Pierloot, K. *Adv Chem Phys* **1996**, 219–331.
- (60) Iii, B. H. L.; Jafri, J. A.; Phillips, D. H.; Jr, C. W. B. *J. Chem. Phys.* **1981**, *74*, 6849–6856.
- (61) Furlani, T. R.; King, H. F. *J. Chem. Phys.* **1985**, *82*, 5577–5583.
- (62) King, H. F.; Furlani, T. R. *J. Comput. Chem.* **1988**, *9*, 771–778.
- (63) Fedorov, D. G.; Gordon, M. S. *J. Chem. Phys.* **2000**, *112*, 5611–5623.
- (64) Zeng, Y.; Biczok, L.; Linschitz, H. *J. Phys. Chem.* **1992**, *96*, 5237–5239.
- (65) McGlynn, S. P.; Azumi, T.; Kasha, M. *J. Chem. Phys.* **1964**, *40*, 507–515.
- (66) McGlynn, S. P.; Sunseri, R.; Christodouleas, N. *J. Chem. Phys.* **1962**, *37*, 1818–1824.
- (67) Seybold, P. G.; White, W. *Anal. Chem.* **1975**, *47*, 1199–1200.
- (68) Turro, N. J.; Lru, K.-C.; Chow, M.-F.; Lee, P. *Photochem. Photobiol.* **1978**, *27*, 523–529.
- (69) Amirav, A.; Even, U.; Jortner, J. *Chem. Phys. Lett.* **1979**, *67*, 9–12.
- (70) Neusser, H. J.; Siglow, K. *Chem. Rev.* **2000**, *100*, 3921–3942.
- (71) Shanowski, J. E.; Glascoe, E. A.; Harris, C. B. *J. Phys. Chem. B* **2005**, *110*, 996–1005.
- (72) MacKenzie, C. A.; Mills, A. P.; Scott, J. M. *J. Am. Chem. Soc.* **1950**, *72*, 2032–2033.
- (73) Steinfeld, J. I.; Francisco, J. S.; Hase, W. L. *Chemical Kinetics and Dynamics*; Prentice-Hall: Englewood Cliffs, NJ, 1989.
- (74) Burkey, T. J.; Majewski, M.; Griller, D. *J. Am. Chem. Soc.* **1986**, *108*, 2218–2221.
- (75) Kanabus-Kaminska, J. M.; Hawari, J. A.; Griller, D.; Chatgililoglu, C. *J. Am. Chem. Soc.* **1987**, *109*, 5267–5268.
- (76) Harvey, J. N.; Aschi, M. *Phys. Chem. Chem. Phys.* **1999**, *1*, 5555–5563.
- (77) Harvey, J. N. *Phys. Chem. Chem. Phys.* **2007**, *9*, 331–343.
- (78) Cui, Q.; Morokuma, K.; Bowman, J. M.; Klippenstein, S. J. *J. Chem. Phys.* **1999**, *110*, 9469–9482.
- (79) Harvey, J. N.; Aschi, M. *Faraday Discuss.* **2003**, *124*, 129–143.
- (80) Vollhardt, K. P. C. *Acc. Chem. Res.* **1977**, *10*, 1–8.
- (81) Vollhardt, K. P. C. *Angew. Chem. Int. Ed. Engl.* **1984**, *23*, 539–556.
- (82) Rest, A. J.; Whitwell, I.; Graham, W. A. G.; Hoyano, J. K.; McMaster, A. D. *J. Chem. Soc. Dalton Trans.* **1987**, 1181–1190.
- (83) Crichton, O.; Rest, A. J.; Taylor, D. J. *J. Chem. Soc. Dalton Trans.* **1980**, 167–173.
- (84) Yang, H.; Kotz, K. T.; Asplund, M. C.; Wilkens, M. J.; Harris, C. B. *Acc. Chem. Res.* **1999**, *32*, 551–560.
- (85) Dahy, A. A.; Koga, N. *Bull. Chem. Soc. Jpn.* **2005**, *78*, 781–791.
- (86) Dahy, A. A.; Suresh, C. H.; Koga, N. *Bull. Chem. Soc. Jpn.* **2005**, *78*, 792–803.
- (87) Gandon, V.; Agenet, N.; Vollhardt, K. P. C.; Malacria, M.; Aubert, C. *J. Am. Chem. Soc.* **2006**, *128*, 8509–8520.
- (88) Agenet, N.; Gandon, V.; Vollhardt, K. P. C.; Malacria, M.; Aubert, C. *J. Am. Chem. Soc.* **2007**, *129*, 8860–8871.
- (89) Gandon, V.; Agenet, N.; Vollhardt, K. P. C.; Malacria, M.; Aubert, C. *J. Am. Chem. Soc.* **2009**, *131*, 3007–3015.
- (90) O'Connor, J. M.; Casey, C. P. *Chem. Rev.* **1987**, *87*, 307–318.

- (91) Zener, C. *Proc. R. Soc. Lond. Ser. A* **1932**, *137*, 696–702.
- (92) Goodwin, H. A. In *Spin Crossover in Transition Metal Compounds II*; Topics in Current Chemistry; Springer Berlin Heidelberg, 2004; pp. 23–47.
- (93) Garcia, Y.; Gütllich, P. In *Spin Crossover in Transition Metal Compounds II*; Topics in Current Chemistry; Springer Berlin Heidelberg, 2004; pp. 49–62.
- (94) Goodwin, H. A. *Coord. Chem. Rev.* **1976**, *18*, 293–325.
- (95) Toftlund, H. *Coord. Chem. Rev.* **1989**, *94*, 67–108.
- (96) König, E.; Ritter, G.; Kulshreshtha, S. K. *Chem. Rev.* **1985**, *85*, 219–234.
- (97) Gütllich, P.; Hauser, A.; Spiering, H. *Angew. Chem. Int. Ed. Engl.* **1994**, *33*, 2024–2054.
- (98) Gütllich, P.; Garcia, Y.; Goodwin, H. A. *Chem. Soc. Rev.* **2000**, *29*, 419–427.
- (99) Bruce, M. I. *Chem. Rev.* **1991**, *91*, 197–257.
- (100) Shanoski, J. E.; Payne, C. K.; Kling, M. F.; Glascoe, E. A.; Harris, C. B. *Organometallics* **2005**, *24*, 1852–1859.
- (101) Baird, M. C. *Chem. Rev.* **1988**, *88*, 1217–1227.
- (102) Turaki, N. N.; Huggins, J. M. *Organometallics* **1986**, *5*, 1703–1706.
- (103) Astruc, D. *Chem. Rev.* **1988**, *88*, 1189–1216.
- (104) Tyler, D. R. *Acc. Chem. Res.* **1991**, *24*, 325–331.
- (105) Wilkinson, G. *J. Am. Chem. Soc.* **1952**, *74*, 6148–6149.
- (106) Mao, F.; Philbin, C. E.; Weakley, T. J. R.; Tyler, D. R. *Organometallics* **1990**, *9*, 1510–1516.
- (107) Fei, M.; Sur, S. K.; Tyler, D. R. *Organometallics* **1991**, *10*, 419–423.
- (108) Schut, D. M.; Keana, K. J.; Tyler, D. R.; Rieger, P. H. *J. Am. Chem. Soc.* **1995**, *117*, 8939–8946.
- (109) Goldman, A. S.; Tyler, D. R. *Inorg. Chem.* **1987**, *26*, 253–258.
- (110) Rushman, P.; Brown, T. L. *J. Am. Chem. Soc.* **1987**, *109*, 3632–3639.
- (111) Lin, Z.; Hall, M. B. *J. Am. Chem. Soc.* **1992**, *114*, 6574–6575.
- (112) Geiger, W. E. *Acc. Chem. Res.* **1995**, *28*, 351–357.
- (113) Narayanan, B. A.; Kochi, J. K. *J. Organomet. Chem.* **1984**, *272*, C49–C53.
- (114) Kuchynka, D. J.; Amatore, C.; Kochi, J. K. *Inorg. Chem.* **1986**, *25*, 4087–4097.
- (115) Kowaleski, R. M.; Rheingold, A. L.; Trogler, W. C.; Basolo, F. *J. Am. Chem. Soc.* **1986**, *108*, 2460–2461.
- (116) Haines, R. J.; Nolte, C. R. *J. Organomet. Chem.* **1970**, *24*, 725–736.
- (117) Haines, R. J.; Du Preez, A. L.; Marais, I. L. *J. Organomet. Chem.* **1971**, *28*, 97–104.
- (118) Brill, T. B.; Landon, S. J. *Chem. Rev.* **1984**, *84*, 577–585.
- (119) Collins, S. N.; Brett, C. M.; Bursten, B. E. *J. Clust. Sci.* **2004**, *15*, 469–487.
- (120) Macyk, W.; Herdegen, A.; Karocki, A.; Stochel, G.; Stasicka, Z.; Sostero, S.; Traverso, O. *J. Photochem. Photobiol. Chem.* **1997**, *103*, 221–226.
- (121) Grimme, S. *J. Comput. Chem.* **2006**, *27*, 1787–1799.
- (122) Tawada, Y.; Tsuneda, T.; Yanagisawa, S.; Yanai, T.; Hirao, K. *J. Chem. Phys.* **2004**, *120*, 8425–8433.
- (123) Vydrov, O. A.; Scuseria, G. E. *J. Chem. Phys.* **2006**, *125*, 234109.
- (124) Vydrov, O. A.; Heyd, J.; Krukau, A. V.; Scuseria, G. E. *J. Chem. Phys.* **2006**, *125*, 074106.
- (125) Vydrov, O. A.; Scuseria, G. E.; Perdew, J. P. *J. Chem. Phys.* **2007**, *126*, 154109.
- (126) Zhao, Y.; Truhlar, D. G. *Theor. Chem. Acc.* **2008**, *120*, 215–241.
- (127) Chai, J.-D.; Head-Gordon, M. *J. Chem. Phys.* **2008**, *128*, 084106.

- (128) Chai, J.-D.; Head-Gordon, M. *Phys. Chem. Chem. Phys.* **2008**, *10*, 6615–6620.
- (129) Francl, M. M.; Pietro, W. J.; Hehre, W. J.; Binkley, J. S.; Gordon, M. S.; DeFrees, D. J.; Pople, J. A. *J. Chem. Phys.* **1982**, *77*, 3654–3665.
- (130) Rassolov, V. A.; Pople, J. A.; Ratner, M. A.; Windus, T. L. *J. Chem. Phys.* **1998**, *109*, 1223–1229.
- (131) Bullitt, J. G.; Cotton, F. A.; Marks, T. J. *Inorg. Chem.* **1972**, *11*, 671–676.
- (132) Fischer, R. D.; Vogler, A.; Noack, K. *J. Organomet. Chem.* **1967**, *7*, 135–149.
- (133) McArdle, P.; Manning, A. R. *J. Chem. Soc. Inorg. Phys. Theor.* **1970**, 2128–2132.
- (134) Anna, J. M.; King, J. T.; Kubarych, K. J. *Inorg. Chem.* **2011**, *50*, 9273–9283.
- (135) Bitterwolf, T. E.; Linehan, J. C.; Shade, J. E. *Organometallics* **2001**, *20*, 775–781.
- (136) Sostero, S.; Rehorek, D.; Polo, E.; Traverso, O. *Inorganica Chim. Acta* **1993**, *209*, 171–176.
- (137) Moore, B. D.; Simpson, M. B.; Poliakoff, M.; Turner, J. J. *J. Chem. Soc. Chem. Commun.* **1984**, 972–974.
- (138) Kling, M. F.; Cahoon, J. F.; Glascoe, E. A.; Shanoski, J. E.; Harris, C. B. *J. Am. Chem. Soc.* **2004**, *126*, 11414–11415.
- (139) Cahoon, J. F.; Kling, M. F.; Schmatz, S.; Harris, C. B. *J. Am. Chem. Soc.* **2005**, *127*, 12555–12565.
- (140) George, M. W.; Dougherty, T. P.; Heilweil, E. J. *J. Phys. Chem.* **1996**, *100*, 201–206.
- (141) Sim, G. A.; Woodhouse, D. I.; Knox, G. R. *J. Chem. Soc. Dalton Trans.* **1979**, 629–635.
- (142) Blaha, J. P.; Wrighton, M. S. *J. Am. Chem. Soc.* **1985**, *107*, 2694–2702.
- (143) Li, Z. H.; Gong, Y.; Fan, K.; Zhou, M. *J. Phys. Chem. A* **2008**, *112*, 13641–13649.
- (144) Norvell, J. C.; Nunes, A. C.; Schoenborn, B. P. *Science* **1975**, *190*, 568–570.
- (145) Bianconi, A.; Congiu-Castellano, A.; Durham, P. J.; Hasnain, S. S.; Phillips, S. *Nature* **1985**, *318*, 685–687.
- (146) Kuriyan, J.; Wilz, S.; Karplus, M.; Petsko, G. A. *J. Mol. Biol.* **1986**, *192*, 133–154.
- (147) Ascone, I.; Bianconi, A.; Dartyge, E.; Della Longa, S.; Fontaine, A.; Momenteau, M. *Biochim. Biophys. Acta BBA - Protein Struct. Mol. Enzymol.* **1987**, *915*, 168–171.
- (148) Quillin, M. L.; Arduini, R. M.; Olson, J. S.; Phillips Jr, G. N. *J. Mol. Biol.* **1993**, *234*, 140–155.
- (149) Ivanov, D.; Sage, J. T.; Keim, M.; Powell, J. R.; Asher, S. A.; Champion, P. M. *J. Am. Chem. Soc.* **1994**, *116*, 4139–4140.
- (150) Lim, M.; Jackson, T. A.; Anfinrud, P. A. *Science* **1995**, *269*, 962–966.
- (151) Yang, F.; Phillips Jr, G. N. *J. Mol. Biol.* **1996**, *256*, 762–774.
- (152) Crabtree, R. H.; Lavin, M. *Inorg. Chem.* **1986**, *25*, 805–812.
- (153) Doedens, R. J.; Dahl, L. F. *J. Am. Chem. Soc.* **1966**, *88*, 4847–4855.
- (154) Yawney, D. B. W.; Doedens, R. J. *Inorg. Chem.* **1972**, *11*, 838–844.
- (155) Cotton, F. A.; Frenz, B. A.; Kruczynski, L. *J. Am. Chem. Soc.* **1973**, *95*, 951–952.
- (156) Cotton, F. A.; Troup, J. M. *J. Am. Chem. Soc.* **1974**, *96*, 1233–1234.
- (157) Enemark, J. H.; Feltham, R. D. *Coord. Chem. Rev.* **1974**, *13*, 339–406.
- (158) Richter-Addo, G. B.; Legzdins, P. *Metal Nitrosyls*; Oxford University Press: New York, 1992.
- (159) Crabtree, R. H. *The Organometallic Chemistry of the Transition Metals*; John Wiley & Sons: New York, 2001.
- (160) Meyer, R.; Schut, D. M.; Keana, K. J.; Tyler, D. R. *Inorganica Chim. Acta* **1995**, *240*, 405–412.

- (161) Lomont, J. P.; Nguyen, S. C.; Harris, C. B. *J. Phys. Chem. A* **2013**, *117*, 2317–2324.
- (162) Stiegman, A. E.; Tyler, D. R. *J. Am. Chem. Soc.* **1982**, *104*, 2944–2945.
- (163) Stiegman, A. E.; Tyler, D. R. *Coord. Chem. Rev.* **1985**, *63*, 217–240.
- (164) Stiegman, A. E.; Stieglitz, M.; Tyler, D. R. *J. Am. Chem. Soc.* **1983**, *105*, 6032–6037.
- (165) Philbin, C. E.; Goldman, A. S.; Tyler, D. R. *Inorg. Chem.* **1986**, *25*, 4434–4436.
- (166) Cahoon, J. F.; Kling, M. F.; Sawyer, K. R.; Frei, H.; Harris, C. B. *J. Am. Chem. Soc.* **2006**, *128*, 3152–3153.
- (167) Cahoon, J. F.; Kling, M. F.; Sawyer, K. R.; Andersen, L. K.; Harris, C. B. *J. Mol. Struct.* **2008**, *890*, 328–338.
- (168) Hieber, W.; Beck, W.; Zeitler, G. *Angew Chem* **1961**, *73*, 364–368.
- (169) Behrens, H.; Ruyter, E.; Wakamatsi, Z. *Anorg Allgem Chem* **1967**, *349*, 241–250.
- (170) Herberbold, M.; Wehrmann, F.; Neugebauer, D.; Huttner, G. *J Organomet Chem* **1978**, *152*, 329–336.
- (171) McCullen, S. B.; Brown, T. L. *Inorg. Chem.* **1981**, *20*, 3528–3533.
- (172) Hallock, S. A.; Wojcicki, A. *J. Organomet. Chem.* **1973**, *54*, C27–C29.
- (173) Hudson, A.; Lappert, M. F.; Nicholson, B. K. *J. Organomet. Chem.* **1975**, *92*, C11–C14.
- (174) Hudson, A.; Lappert, M. F.; Macquitty, J. J.; Nicholson, B. K.; Zainal, H.; Luckhurst, G. R.; Zannoni, C.; Bratt, S. W.; Symons, M. C. R. *J. Organomet. Chem.* **1976**, *110*, C5–C8.
- (175) Stiegman, A. E.; Tyler, D. R. *Inorg. Chem.* **1984**, *23*, 527–529.
- (176) Fawcett, J. P.; Jackson, R. A.; Poë, A. *J. Chem. Soc. Chem. Commun.* **1975**, 733–734.
- (177) Fox, A.; Malito, J.; Poë, A. *J. Chem. Soc. Chem. Commun.* **1981**, 1052–1053.
- (178) Poe, A. *Trans Met Chem Neth.* **1982**, *7*, 65–69.
- (179) Herrinton, T. R.; Brown, T. L. *J. Am. Chem. Soc.* **1985**, *107*, 5700–5703.
- (180) McCullen, S. B.; Walker, H. W.; Brown, T. L. *J. Am. Chem. Soc.* **1982**, *104*, 4007–4008.
- (181) Osborne, A. G.; Stiddard, M. H. B. *J. Chem. Soc. Resumed* **1964**, 634–636.
- (182) Zeigler, M. L.; Haas, H.; Sheline, R. K. *Chem Ber* **1965**, *98*, 2454–2459.
- (183) Stiegman, A. E.; Goldman, A. S.; Philbin, C. E.; Tyler, D. R. *Inorg. Chem.* **1986**, *25*, 2976–2979.
- (184) Busetto, C.; Mattucci, A. M.; Cernia, E. M.; Bertani, R. *J. Organomet. Chem.* **1983**, *246*, 183–188.
- (185) Allen, D. M.; Cox, A.; Kemp, T. J.; Sultana, Q.; Pitts, R. B. *J. Chem. Soc. Dalton Trans.* **1976**, 1189–1193.
- (186) Steinhurst, D. A.; Baronavski, A. P.; Owrutsky, J. C. *Chem. Phys. Lett.* **2002**, *361*, 513–519.
- (187) Yang, H.; Snee, P. T.; Kotz, K. T.; Payne, C. K.; Frei, H.; Harris, C. B. *J. Am. Chem. Soc.* **1999**, *121*, 9227–9228.
- (188) Yang, H.; Snee, P. T.; Kotz, K. T.; Payne, C. K.; Harris, C. B. *J. Am. Chem. Soc.* **2001**, *123*, 4204–4210.
- (189) Meng, Q.; Huang, Y.; Ryan, W. J.; Sweigart, D. A. *Inorg. Chem.* **1992**, *31*, 4051–4052.
- (190) Huang, Y.; Carpenter, G. B.; Sweigart, D. A.; Chung, Y. K.; Lee, B. Y. *Organometallics* **1995**, *14*, 1423–1428.
- (191) Castellani, M. P.; Tyler, D. R. *Organometallics* **1989**, *8*, 2113–2120.
- (192) Szaciłowski, K.; Macyk, W.; Stochel, G.; Stasicka, Z.; Sostero, S.; Traverso, O. *Coord. Chem. Rev.* **2000**, *208*, 277–297.
- (193) Anfinrud, P. A.; Han, C.; Lian, T.; Hochstrasser, R. M. *J. Phys. Chem.* **1990**, *94*, 1180–1184.

- (194) Anfinrud, P. A.; Han, C. H.; Lian, T.; Hochstrasser, R. M. *J. Phys. Chem.* **1991**, *95*, 574–578.
- (195) Lian, T.; Kholodenko, Y.; Locke, B.; Hochstrasser, R. M. *J. Phys. Chem.* **1995**, *99*, 7272–7280.
- (196) Adams, R. D.; Cotton, F. A. *Inorganica Chim. Acta* **1973**, *7*, 153–156.
- (197) Adams, R. D.; Collins, D. M.; Cotton, F. A. *Inorg. Chem.* **1974**, *13*, 1086–1090.
- (198) Peters, J.; George, M. W.; Turner, J. J. *Organometallics* **1995**, *14*, 1503–1506.
- (199) Sun, X. Z.; Nikiforov, S. M.; Dedieu, A.; George, M. W. *Organometallics* **2001**, *20*, 1515–1520.
- (200) Bitterwolf, T. E. *Coord. Chem. Rev.* **2001**, *211*, 235–254.
- (201) Baiz, C. R.; McCanne, R.; Kubarych, K. J. *J. Am. Chem. Soc.* **2009**, *131*, 13590–13591.
- (202) Belkova, N. V.; Gutsul, E. I.; Filippov, O. A.; Levina, V. A.; Valyaev, D. A.; Epstein, L. M.; Lledos, A.; Shubina, E. S. *J. Am. Chem. Soc.* **2006**, *128*, 3486–3487.
- (203) Wittrig, R. E.; Kubiak, C. P. *J. Electroanal. Chem.* **1995**, *393*, 75–86.
- (204) Harris, J. D.; Oelkers, A. B.; Tyler, D. R. *J. Am. Chem. Soc.* **2007**, *129*, 6255–6262.
- (205) Stiegman, A. E.; Goldman, A. S.; Leslie, D. B.; Tyler, D. R. *J. Chem. Soc. Chem. Commun.* **1984**, 632–633.
- (206) Goldman, A. S.; Tyler, D. R. *Inorganica Chim. Acta* **1985**, *98*, L47–L48.
- (207) Julliard, M.; Chanon, M. *Chem. Rev.* **1983**, *83*, 425–506.
- (208) Saveant, J. M. *Acc. Chem. Res.* **1980**, *13*, 323–329.
- (209) Chanon, M.; Tobe, M. L. *Angew. Chem. Int. Ed. Engl.* **1982**, *21*, 1–23.
- (210) Lucio Anelli, P.; Biffi, C.; Montanari, F.; Quici, S. *J. Org. Chem.* **1987**, *52*, 2559–2562.
- (211) Nooy, A. E. J. de; Besemer, A. C.; Bekkum, H. van. *Synthesis* **1996**, *1996*, 1153–1176.
- (212) De Souza, M. *Mini-Rev. Org. Chem.* **2006**, *3*, 155–165.
- (213) Vogler, T.; Studer, A. *Synthesis* **2008**, *2008*, 1979–1993.
- (214) Hoover, J. M.; Stahl, S. S. *J. Am. Chem. Soc.* **2011**, *133*, 16901–16910.
- (215) Caron, S.; Dugger, R. W.; Ruggeri, S. G.; Ragan, J. A.; Ripin, D. H. B. *Chem. Rev.* **2006**, *106*, 2943–2989.
- (216) Ciriminna, R.; Pagliaro, M. *Org. Process Res. Dev.* **2010**, *14*, 245–251.
- (217) Lagunas, A.; Mairata i Payeras, A.; Jimeno, C.; Pericàs, M. A. *Org. Lett.* **2005**, *7*, 3033–3036.
- (218) Vogler, T.; Studer, A. *Org. Lett.* **2008**, *10*, 129–131.
- (219) Maity, S.; Manna, S.; Rana, S.; Naveen, T.; Mallick, A.; Maiti, D. *J. Am. Chem. Soc.* **2013**, *135*, 3355–3358.
- (220) Lagunas, A.; Payeras, A. M. i; Jimeno, C.; Pericàs, M. A. *Chem. Commun.* **2006**, 1307–1309.
- (221) Keana, J. F. W. *Chem. Rev.* **1978**, *78*, 37–64.
- (222) Volodarsky, L. B.; Reznikov, V. A.; Ovcharenko, V. I. *Synthetic Chemistry of Stable Nitroxides*; CRC Press: Boca Raton, FL, 1994.
- (223) Mak, K. W.; Yeung, S. K.; Chan, K. S. *Organometallics* **2002**, *21*, 2362–2364.
- (224) Georges, M. K.; Veregin, R. P. N.; Kazmaier, P. M.; Hamer, G. K.; Saban, M. *Macromolecules* **1994**, *27*, 7228–7229.
- (225) Connolly, T. J.; Baldoví, M. V.; Mohtat, N.; Scaiano, J. C. *Tetrahedron Lett.* **1996**, *37*, 4919–4922.
- (226) Connolly, T. J.; Scaiano, J. C. *Tetrahedron Lett.* **1997**, *38*, 1133–1136.
- (227) Patten, T. E.; Matyjaszewski, K. *Acc. Chem. Res.* **1999**, *32*, 895–903.

- (228) Knoop, C. A.; Studer, A. *J. Am. Chem. Soc.* **2003**, *125*, 16327–16333.
- (229) Nakamura, T.; Okubo, M. *Macromolecules* **2007**, *40*, 8663–8672.
- (230) Eaton, S. S.; Eaton, G. R. *Coord. Chem. Rev.* **1988**, *83*, 29–72.
- (231) Eaton, S. S.; Eaton, G. R. *Coord. Chem. Rev.* **1978**, *26*, 207–262.
- (232) Kelman, D. J.; Mason, R. P. *Arch. Biochem. Biophys.* **1993**, *306*, 439–442.
- (233) Smirnov, A. I.; Smirnova, T. I.; Morse, P. D. *Biophys J* **1995**, *68*, 2360.
- (234) Wrobel, A.; Jezierski, A.; Gomulkiewicz, J. *FreeRad.Res.* **1999**, *31*, 201.
- (235) Borisenko, G. G.; Martin, I.; Zhao, Q.; Amoscato, A. A.; Kagan, V. E. *J. Am. Chem. Soc.* **2004**, *126*, 9221–9232.
- (236) Forbes, G. C.; Kennedy, A. R.; Mulvey, R. E.; Rodger, P. J. A. *Chem. Commun.* **2001**, 1400–1401.
- (237) Huang, K.-W.; Waymouth, R. M. *J. Am. Chem. Soc.* **2002**, *124*, 8200–8201.
- (238) Jones, C.; Rose, R. P. *New J. Chem.* **2007**, *31*, 1484–1487.
- (239) Huang, K.-W.; Han, J. H.; Cole, A. P.; Musgrave, C. B.; Waymouth, R. M. *J. Am. Chem. Soc.* **2005**, *127*, 3807–3816.
- (240) Dickman, M. H.; Doedens, R. J. *Inorg. Chem.* **1982**, *21*, 682–684.
- (241) Dickman, M. H.; Doedens, R. J. *Inorg. Chem.* **1981**, *20*, 2677–2681.
- (242) Laugier, J.; Latour, J. M.; Caneschi, A.; Rey, P. *Inorg. Chem.* **1991**, *30*, 4474–4477.
- (243) Scepaniak, J. J.; Wright, A. M.; Lewis, R. A.; Wu, G.; Hayton, T. W. *J. Am. Chem. Soc.* **2012**, *134*, 19350–19353.
- (244) Jaitner, P.; Huber, W.; Gieren, A.; Betz, H. *J. Organomet. Chem.* **1986**, *311*, 379–385.
- (245) Jaitner, P.; Rieker, C.; Wurst, K. *Chem. Commun.* **1997**, 1245–1246.
- (246) Jaitner, P.; Veciana, J.; Sporer, C.; Kopacka, H.; Wurst, K.; Ruiz-Molina, D. *Organometallics* **2001**, *20*, 568–571.
- (247) Jaitner, P.; Huber, W.; Hunter, G.; Scheidsteger, O. *J. Organomet. Chem.* **1983**, *259*, C1–C5.
- (248) Jaitner, P.; Huber, W. *Inorganica Chim. Acta* **1987**, *129*, L45–L46.
- (249) Bailey, W. F.; Bobbitt, J. M.; Wiberg, K. B. *J. Org. Chem.* **2007**, *72*, 4504–4509.
- (250) Michel, C.; Belanzoni, P.; Gamez, P.; Reedijk, J.; Baerends, E. J. *Inorg. Chem.* **2009**, *48*, 11909–11920.
- (251) Belanzoni, P.; Michel, C.; Baerends, E. J. *Inorg. Chem.* **2011**, *50*, 11896–11904.
- (252) Qiu, J. C.; Pradhan, P. P.; Blanck, N. B.; Bobbitt, J. M.; Bailey, W. F. *Org. Lett.* **2012**, *14*, 350–353.
- (253) Semmelhack, M. F.; Schmid, C. R.; Cortes, D. A.; Chou, C. S. *J. Am. Chem. Soc.* **1984**, *106*, 3374–3376.
- (254) Gamez, P.; Arends, I. W. C. E.; Reedijk, J.; Sheldon, R. A. *Chem. Commun.* **2003**, 2414–2415.
- (255) Dijksman, A.; Arends, I. W. C. E.; Sheldon, R. A. *Org. Biomol. Chem.* **2003**, *1*, 3232–3237.
- (256) Sheldon, R. A.; Arends, I. W. C. E. *J. Mol. Catal. Chem.* **2006**, *251*, 200–214.
- (257) Cheng, L.; Wang, J.; Wang, M.; Wu, Z. *Inorg. Chem.* **2010**, *49*, 9392–9399.
- (258) Perdew, J. P.; Burke, K.; Ernzerhof, M. *Phys. Rev. Lett.* **1996**, *77*, 3865–3868.
- (259) Perdew, J. P.; Burke, K.; Ernzerhof, M. *Phys. Rev. Lett.* **1997**, *78*, 1396–1396.
- (260) Adamo, C.; Barone, V. *J. Chem. Phys.* **1999**, *110*, 6158–6170.
- (261) McLean, A. D.; Chandler, G. S. *J. Chem. Phys.* **1980**, *72*, 5639–5648.
- (262) Krishnan, R.; Binkley, J. S.; Seeger, R.; Pople, J. A. *J. Chem. Phys.* **1980**, *72*, 650–654.

- (263) Wachters, A. J. H. *J. Chem. Phys.* **1970**, *52*, 1033–1036.
- (264) Hay, P. J. *J. Chem. Phys.* **1977**, *66*, 4377–4384.
- (265) Izgorodina, E. I.; Brittain, D. R. B.; Hodgson, J. L.; Krenske, E. H.; Lin, C. Y.; Namazian, M.; Coote, M. L. *J. Phys. Chem. A* **2007**, *111*, 10754–10768.
- (266) Zhao, Y.; Truhlar, D. G. *J. Phys. Chem. A* **2008**, *112*, 1095–1099.
- (267) Izgorodina, E. I.; Coote, M. L.; Radom, L. *J. Phys. Chem. A* **2005**, *109*, 7558–7566.
- (268) Izgorodina, E. I.; Coote, M. L. *J. Phys. Chem. A* **2006**, *110*, 2486–2492.
- (269) Izgorodina, E. I.; Coote, M. L. *Chem. Phys.* **2006**, *324*, 96–110.
- (270) Lomont, J. P.; Nguyen, S. C.; Harris, C. B. *Organometallics* **2012**, *31*, 3947–3957.
- (271) Lomont, J. P.; Nguyen, S. C.; Zoerb, M. C.; Hill, A. D.; Schlegel, J. P.; Harris, C. B. *Organometallics* **2012**, *31*, 3582–3587.
- (272) Owrutsky, J. C.; Baronavski, A. P. *J. Chem. Phys.* **1996**, *105*, 9864–9873.
- (273) Lomont, J. P.; Nguyen, S. C.; Harris, C. B. *J. Phys. Chem. A* **2013**, *117*, 3777–3785.
- (274) Sheldon, R. A.; Arends, I. W. C. E.; ten Brink, G.-J.; Dijkman, A. *Acc. Chem. Res.* **2002**, *35*, 774–781.
- (275) Sheldon, R. A.; Arends, I. W. C. E. *Adv. Synth. Catal.* **2004**, *346*, 1051–1071.
- (276) Ansari, I. A.; Gree, R. *Org. Lett.* **2002**, *4*, 1507–1509.
- (277) Figiel, P. J.; Leskelä, M.; Repo, T. *Adv. Synth. Catal.* **2007**, *349*, 1173–1179.
- (278) Salinas Uber, J.; Vogels, Y.; van den Helder, D.; Mutikainen, I.; Turpeinen, U.; Fu, W. T.; Roubeau, O.; Gamez, P.; Reedijk, J. *Eur. J. Inorg. Chem.* **2007**, *2007*, 4197–4206.
- (279) Mannam, S.; Alamsetti, S. K.; Sekar, G. *Adv. Synth. Catal.* **2007**, *349*, 2253–2258.
- (280) Lu, N.; Lin, Y.-C. *Tetrahedron Lett.* **2007**, *48*, 8823–8828.
- (281) Jiang, N.; Ragauskas, A. J. *J. Org. Chem.* **2006**, *71*, 7087–7090.
- (282) Gamez, P.; Arends, I. W. C. E.; Sheldon, R. A.; Reedijk, J. *Adv. Synth. Catal.* **2004**, *346*, 805–811.
- (283) Striegler, S. *Tetrahedron* **2006**, *62*, 9109–9114.
- (284) Velusamy, S.; Srinivasan, A.; Punniyamurthy, T. *Tetrahedron Lett.* **2006**, *47*, 923–926.
- (285) Ragagnin, G.; Betzemeier, B.; Quici, S.; Knochel, P. *Tetrahedron* **2002**, *58*, 3985–3991.
- (286) Dotz, K. H.; Fischer, H.; Hofmann, P.; Kreissl, F. R.; Schubert, U.; Weiss, K. *Transition Metal Carbene Complexes*; Verlag Chemie: Weinheim, 1983.
- (287) Bernasconi, C. F. In *Advances in Physical Organic Chemistry*; Academic Press, 2002; Vol. Volume 37, pp. 137–237.
- (288) Dötz, K. H.; Tomuschat, P. *Chem. Soc. Rev.* **1999**, *28*, 187–198.
- (289) Hegedus, L. S. *Tetrahedron* **1997**, *53*, 4105–4128.
- (290) Hegedus, L. S. *Acc. Chem. Res.* **1995**, *28*, 299–305.
- (291) Hegedus, L. S. In *Metal Carbenes in Organic Synthesis*; Topics in Organometallic Chemistry; Springer Berlin Heidelberg, 2004; pp. 157–201.
- (292) McGuire, M. A.; Hegedus, L. S. *J. Am. Chem. Soc.* **1982**, *104*, 5538–5540.
- (293) Gallagher, M. L.; Greene, J. B.; Rooney, A. D. *Organometallics* **1997**, *16*, 5260–5268.
- (294) Doyle, K. O.; Gallagher, M. L.; Pryce, M. T.; Rooney, A. D. *J. Organomet. Chem.* **2001**, *617–618*, 269–279.
- (295) Arrieta, A.; Cossío, F. P.; Fernández, I.; Gómez-Gallego, M.; Lecea, B.; Mancheño, M. J.; Sierra, M. A. *J. Am. Chem. Soc.* **2000**, *122*, 11509–11510.
- (296) Fernández, I.; Sierra, M. A.; Gómez-Gallego, M.; Mancheño, M. J.; Cossío, F. P. *Chem. – Eur. J.* **2005**, *11*, 5988–5996.

- (297) Gut, H.-P.; Welte, N.; Link, U.; Fischer, H.; Steiner, U. E. *Organometallics* **2000**, *19*, 2354–2364.
- (298) Servaas, P. C.; Stufkens, D. J.; Oskam, A. J. *J. Organomet. Chem.* **1990**, *390*, 61–71.
- (299) Fernández, I.; Cossío, F. P.; Sierra, M. A. *Acc. Chem. Res.* **2011**, *44*, 479–490.
- (300) Colbran, S. B.; Johnson, B. F. G.; Lewis, J.; Sorrell, R. M. *J. Chem. Soc. Chem. Commun.* **1986**, 525–527.
- (301) Burke, M. R.; Funk, T.; Takats, J.; Day, V. W. *Organometallics* **1994**, *13*, 2109–2112.
- (302) Edwards, A. J.; Leadbeater, N. E.; Lewis, J.; Raithby, P. R. *J. Organomet. Chem.* **1995**, *503*, 15–20.
- (303) Hay, C. M.; Leadbeater, N. E.; Lewis, J.; Raithby, P. R.; Burgess, K. *New J. Chem.* **1998**, *22*, 787–788.
- (304) Leadbeater, N. E. *J. Organomet. Chem.* **1999**, *573*, 211–216.
- (305) Richmond, M. G. *Coord. Chem. Rev.* **2004**, *248*, 881–901.
- (306) Wu, Y. M.; Bentsen, J. G.; Brinkley, C. G.; Wrighton, M. S. *Inorg. Chem.* **1987**, *26*, 530–540.
- (307) Leadbeater, N. E. *J. Chem. Soc. Dalton Trans.* **1995**, 2923–2934.
- (308) Kakiuchi, F.; Matsumoto, M.; Tsuchiya, K.; Igi, K.; Hayamizu, T.; Chatani, N.; Murai, S. *J. Organomet. Chem.* **2003**, *686*, 134–144.
- (309) Meijer, R. H.; Ligthart, G. B. W. L.; Meuldijk, J.; Vekemans, J. A. J. M.; Hulshof, L. A.; Mills, A. M.; Kooijman, H.; Spek, A. L. *Tetrahedron* **2004**, *60*, 1065–1072.
- (310) Shriver, D. F.; Kaesz, H. D.; Adams, R. D. *The Chemistry of Metal Cluster Complexes*; Wiley-VCH: New York, 1990.
- (311) Mingos, D. M. P.; Wales, D. J. *Introduction to Cluster Chemistry*; Prentice-Hall: Englewood Cliffs, NJ, 1990.
- (312) Fackler, J. P. *Metal–Metal Bonds and Clusters in Chemistry and Catalysis*; Plenum: New York, 1992.
- (313) Gonzalez-Moraga, G. *Cluster Chemistry*; Springer-Verlag: Berlin, 1993.
- (314) Housecroft, C. E. *Metal–Metal Bonded Carbonyl Dimers and Clusters*; Oxford Science Publishers: Oxford, U.K., 1994.
- (315) Adams, R. D.; Cotton, F. A. *Catalysis by Di- and Polynuclear Metal Cluster Complexes*; Wiley-VCH: New York, 1998.
- (316) Bruce, M. I.; Shriver, D. F.; Kaesz, H. D.; Adams, R. D. *The Chemistry of Metal Cluster Complexes*; Wiley-VCH: New York, 1990.
- (317) Dyson, P. J.; McIndoe, S. J. *Transition Metal Carbonyl Cluster Chemistry*; Gordon and Breach: Amsterdam, 2000.
- (318) Glascoe, E. A.; Kling, M. F.; Shanoski, J. E.; Harris, C. B. *Organometallics* **2006**, *25*, 775–784.
- (319) Lausarot, P. M.; Vaglio, G. A.; Valle, M. *J. Organomet. Chem.* **1984**, *275*, 233–237.
- (320) Mitchener, J. C.; Wrighton, M. S. *J. Am. Chem. Soc.* **1981**, *103*, 975–977.
- (321) Bruce, M. L.; Kehoe, D. C.; Matison, J. G.; Nicholson, B. K.; Rieger, P. H.; Williams, M. L. *J. Chem. Soc. Chem. Commun.* **1982**, 442–444.
- (322) Kondo, T.; Tsuji, Y.; Watanabe, Y. *Tetrahedron Lett.* **1988**, *29*, 3833–3836.
- (323) Caulton, K. G.; Thomas, M. G.; Sosinsky, B. A.; Muetterties, E. L. *Proc. Natl. Acad. Sci.* **1976**, *73*, 4274–4276.
- (324) Knox, S. a. R.; Stone, F. G. A. *J. Chem. Soc. Inorg. Phys. Theor.* **1970**, 3147–3153.

- (325) Brookes, A.; Knox, S. a. R.; Stone, F. G. A. *J. Chem. Soc. Inorg. Phys. Theor.* **1971**, 3469–3471.
- (326) Knox, S. a. R.; Stone, F. G. A. *J. Chem. Soc. Inorg. Phys. Theor.* **1971**, 2874–2880.
- (327) Lewis, J.; Cotton, F. A.; Deeming, A. J.; Josty, P. L.; Ullah, S. S.; Domingos, A. J. P.; Johnson, B. F. G. *J. Am. Chem. Soc.* **1971**, *93*, 4624–4626.
- (328) Cullen, W. R.; Harbourne, D. A. *Inorg. Chem.* **1970**, *9*, 1839–1843.
- (329) Cullen, W. R.; Harbourne, D. A.; Liengme, B. V.; Sams, J. R. *Inorg. Chem.* **1970**, *9*, 702–710.
- (330) Roberts, P. J.; Trotter, J. J. *J. Chem. Soc. Inorg. Phys. Theor.* **1971**, 1479–1482.
- (331) Cullen, W. R.; Harbourne, D. A.; Liengme, B. V.; Sams, J. R. *J. Am. Chem. Soc.* **1968**, *90*, 3293–3295.
- (332) Wrighton, M. *Chem. Rev.* **1974**, *74*, 401–430.
- (333) Brenner, A.; Hucul, D. A. *Inorg. Chem.* **1979**, *18*, 2836–2840.
- (334) Brenner, A. *J. Chem. Soc. Chem. Commun.* **1979**, 251–251.
- (335) Kuroda, H. *Pure Appl. Chem.* **1992**, *64*.
- (336) Jackson, R. L.; Trusheim, M. R. *J. Am. Chem. Soc.* **1982**, *104*, 6590–6596.
- (337) Hugues, F.; Smith, A. K.; Taarit, Y. B.; Basset, J. M.; Commereuc, D.; Chauvin, Y. *J. Chem. Soc. Chem. Commun.* **1980**, 68–70.
- (338) Brenner, A.; Hucul, D. A. *J. Am. Chem. Soc.* **1980**, *102*, 2484–2487.
- (339) Smith, A. K.; Besson, B.; Basset, J. M.; Psaro, R.; Fusi, A.; Ugo, R. *J. Organomet. Chem.* **1980**, *192*, C31–C34.
- (340) Hsu, L. Y.; Shore, S. G.; Dornelas, L.; Choplin, A.; Basset, J. M. *J. Catal.* **1994**, *149*, 159–170.
- (341) Duivenvoorden, F. B. M.; Koningsberger, D. C.; Uh, Y. S.; Gates, B. C. *J. Am. Chem. Soc.* **1986**, *108*, 6254–6262.
- (342) Lucenti, E.; Roberto, D.; Ugo, R. *Organometallics* **2001**, *20*, 1725–1733.
- (343) Choplin, A.; Besson, B.; D'Ornelas, L.; Sanchez-Delgado, R.; Basset, J. M. *J. Am. Chem. Soc.* **1988**, *110*, 2783–2787.
- (344) Smith, A. K.; Theolier, A.; Basset, J. M.; Ugo, R.; Commereuc, D.; Chauvin, Y. *J. Am. Chem. Soc.* **1978**, *100*, 2590–2591.
- (345) Deeba, M.; Scott, J. P.; Barth, R.; Gates, B. C. *J. Catal.* **1981**, *71*, 373–380.
- (346) Knözinger, H.; Zhao, Y. *J. Catal.* **1981**, *71*, 337–347.
- (347) Deeba, M.; Streusand, B. J.; Schrader, G. L.; Gates, B. C. *J. Catal.* **1981**, *69*, 218–221.
- (348) Collier, G.; Hunt, D. J.; Jackson, S. D.; Moyes, R. B.; Pickering, I. A.; Wells, P. B.; Simpson, A. F.; Whyman, R. *J. Catal.* **1983**, *80*, 154–171.
- (349) Besson, B.; Choplin, A.; D'Ornelas, L.; Basset, J. M. *J. Chem. Soc. Chem. Commun.* **1982**, 843–845.
- (350) Hugues, F.; Dalmon, J. A.; Bussiere, P.; Smith, A. K.; Basset, J. M.; Olivier, D. *J. Phys. Chem.* **1982**, *86*, 5136–5144.
- (351) Ballivet-Tkatchenko D.; Chau N. D.; Mozzenega H.; Roux M. C.; Tkatchenko I. In *Catalytic Activation of Carbon Monoxide*; ACS Symposium Series; American Chemical Society, 1981; Vol. 152, pp. 187–201.
- (352) Psaro, R.; Ugo, R.; Zanderighi, G. M.; Besson, B.; Smith, A. K.; Basset, J. M. *J. Organomet. Chem.* **1981**, *213*, 215–247.
- (353) Deeba, M.; Gates, B. C. *J. Catal.* **1981**, *67*, 303–307.

- (354) Commereuc, D.; Chauvin, Y.; Hugues, F.; Basset, J. M.; Olivier, D. *J. Chem. Soc. Chem. Commun.* **1980**, 154–155.
- (355) Ganzerla, R.; Lenarda, M.; Pinna, F.; Graziani, M. *J. Organomet. Chem.* **1981**, 208, C43–C45.
- (356) Johnson, B. F. G. *J. Chem. Soc. Chem. Commun.* **1976**, 703–704.
- (357) Johnson, B. F. G.; Benfield, R. E. *J. Chem. Soc. Dalton Trans.* **1978**, 1554–1568.
- (358) Benfield, R. E.; Gavens, P. D.; Johnson, B. F. G.; Mays, M. J.; Aime, S.; Milone, L.; Osella, D. *J. Chem. Soc. Dalton Trans.* **1981**, 1535–1539.
- (359) Adams, H.; Bailey, N. A.; Bentley, G. W.; Mann, B. E. *J. Chem. Soc. Dalton Trans.* **1989**, 1831–1844.
- (360) Johnson, B. F. G.; Bott, A. *J. Chem. Soc. Dalton Trans.* **1990**, 2437–2444.
- (361) Braga, D.; Anson, C. E.; Bott, A.; Johnson, B. F. G.; Marseglia, E. *J. Chem. Soc. Dalton Trans.* **1990**, 3517–3524.
- (362) Mann, B. E. *Organometallics* **1992**, 11, 481–482.
- (363) Johnson, B. F. G.; Parisini, E.; Roberts, Y. V. *Organometallics* **1993**, 12, 233–235.
- (364) Braga, D.; Grepioni, F.; Farrugia, L. J.; Johnson, B. F. G. *J. Chem. Soc. Dalton Trans.* **1994**, 2911–2918.
- (365) Adams, H.; Carr, A. G.; Mann, B. E.; Melling, R. *Polyhedron* **1995**, 14, 2771–2785.
- (366) Adams, H.; Chen, X.; Mann, B. E. *J. Chem. Soc. Dalton Trans.* **1996**, 2159–2163.
- (367) Mann, B. E. *J. Chem. Soc. Dalton Trans.* **1997**, 1457–1472.
- (368) Bentsen, J. G.; Wrighton, M. S. *J. Am. Chem. Soc.* **1987**, 109, 4530–4544.
- (369) Bentsen, J. G.; Wrighton, M. S. *J. Am. Chem. Soc.* **1987**, 109, 4518–4530.
- (370) Tyler, D. R.; Altobelli, M.; Gray, H. B. *J. Am. Chem. Soc.* **1980**, 102, 3022–3024.
- (371) Poe, J. A.; Sekhar, V. C. *J. Am. Chem. Soc.* **1986**, 108, 3673–3679.
- (372) Tro, N. J.; King, J. C.; Harris, C. B. *Inorganica Chim. Acta* **1995**, 229, 469–471.
- (373) Hehre, W. J.; Ditchfield, R.; Pople, J. A. *J. Chem. Phys.* **1972**, 56, 2257–2261.
- (374) Tyler, D. R.; Levenson, R. A.; Gray, H. B. *J. Am. Chem. Soc.* **1978**, 100, 7888–7893.
- (375) Corey, E. R.; Dahl, L. F. *Inorg. Chem.* **1962**, 1, 521–526.
- (376) Dobson, G. R.; Sheline, R. K. *Inorg. Chem.* **1963**, 2, 1313–1315.
- (377) Poliakoff, M.; Turner, J. J. *J. Chem. Soc. Chem. Commun.* **1970**, 1008–1009.
- (378) Cotton, F. A.; Hunter, D. L. *Inorganica Chim. Acta* **1974**, 11, L9–L10.
- (379) Binsted, N.; Evans, J.; Greaves, G. N.; Price, R. J. *J. Chem. Soc. Chem. Commun.* **1987**, 1330–1333.
- (380) Wei, C. H.; Dahl, L. F. *J. Am. Chem. Soc.* **1969**, 91, 1351–1361.
- (381) Cotton, F. A.; Troup, J. M. *J. Am. Chem. Soc.* **1974**, 96, 4155–4159.
- (382) Farrugia, L. J.; Gillon, A. L.; Braga, D.; Grepioni, F. *Organometallics* **1999**, 18, 5022–5033.
- (383) Li, J.; Jug, K. *Inorganica Chim. Acta* **1992**, 196, 89–95.
- (384) Jang, J. H.; Lee, J. G.; Lee, H.; Xie, Y.; Schaefer, H. F. *J. Phys. Chem. A* **1998**, 102, 5298–5304.
- (385) Hunstock, E.; Mealli, C.; Calhorda, M. J.; Reinhold, J. *Inorg. Chem.* **1999**, 38, 5053–5060.
- (386) Hunstock, E.; Calhorda, M. J.; Hirva, P.; Pakkanen, T. A. *Organometallics* **2000**, 19, 4624–4628.
- (387) Nguyen, S. C.; Lomont, J. P.; Zoerb, M. C.; Hill, A. D.; Schlegel, J. P.; Harris, C. B. *Organometallics* **2012**, 31, 3980–3984.

- (388) Poliakoff, M.; Turner, J. J. *J. Chem. Soc. Inorg. Phys. Theor.* **1971**, 2403–2410.
- (389) Fletcher, S. C.; Poliakoff, M.; Turner, J. J. *Inorg. Chem.* **1986**, *25*, 3597–3604.
- (390) Kong, Q.; Lee, J. H.; Plech, A.; Wulff, M.; Ihee, H.; Koch, M. H. *J. Angew. Chem. Int. Ed.* **2008**, *47*, 5550–5553.
- (391) Kong, Q.; Lee, J. H.; Kim, K. H.; Kim, J.; Wulff, M.; Ihee, H.; Koch, M. H. *J. Am. Chem. Soc.* **2010**, *132*, 2600–2607.
- (392) Desrosiers, M. F.; Wink, D. A.; Trautman, R.; Friedman, A. E.; Ford, P. C. *J. Am. Chem. Soc.* **1986**, *108*, 1917–1927.
- (393) Church, S. P.; Grevels, F.-W.; Kiel, G.-Y.; Kiel, W. A.; Takats, J.; Schaffner, K. *Angew. Chem. Int. Ed. Engl.* **1986**, *25*, 991–992.
- (394) Haynes, A.; Poliakoff, M.; Turner, J. J.; Bender, B. R.; Norton, J. R. *J. Organomet. Chem.* **1990**, *383*, 497–519.
- (395) Moss, J. R.; Graham, W. A. G. *J. Chem. Soc. Dalton Trans.* **1977**, 95–99.
- (396) Moss, J. R.; Graham, W. a. G. *J. Chem. Soc. Chem. Commun.* **1970**, 835–835.
- (397) Quicksall, C. O.; Spiro, T. G. *Inorg. Chem.* **1968**, *7*, 2365–2369.
- (398) Chen, H.; Tang, Z.; Huang, R.; Zheng, L. *Eur. J. Mass Spectrom.* **2000**, *6*, 19.
- (399) Muetterties, E. L. *J. Organomet. Chem.* **1980**, *200*, 177–190.
- (400) Keister, J. B. *Encyclopedia of Inorganic Chemistry: Polynuclear Organometallic Cluster Complexes*; Wiley: Chichester, U.K., 2006.
- (401) Gonzalez-Moraga. *Cluster Chemistry: Introduction to the Chemistry of Transition Metal and Main Group Element Molecular Clusters*; Springer-Verlag: New York, 1993.
- (402) Mond, L.; Hirtz, H.; Cowap, M. D. *J. Chem. Soc. Trans.* **1910**, *97*, 798–810.
- (403) Evans, J.; Johnson, B. F. G.; Lewis, J.; Matheson, T. W. *J. Am. Chem. Soc.* **1975**, *97*, 1245–1247.
- (404) Cohen, M. A.; Kidd, D. R.; Brown, T. L. *J. Am. Chem. Soc.* **1975**, *97*, 4408–4409.
- (405) Aime, S.; Milone, L.; Osella, D.; Poli, A. *Inorganica Chim. Acta* **1978**, *30*, 45–49.
- (406) Aime, S.; Gobetto, R.; Osella, D.; Milonej, L.; Hawkes, G. E.; Randall, E. W. *J. Magn. Reson.* **1985**, *65*, 308–315.
- (407) Sizun, C.; Kempgens, P.; Raya, J.; Elbayed, K.; Granger, P.; Rosé, J. *J. Organomet. Chem.* **2000**, *604*, 27–33.
- (408) Aime, S.; Osella, D.; Milone, L.; Hawkes, G. E.; Randall, E. W. *J. Am. Chem. Soc.* **1981**, *103*, 5920–5922.
- (409) Lucken, E. a. C.; Noack, K.; Williams, D. F. *J. Chem. Soc. Inorg. Phys. Theor.* **1967**, 148–154.
- (410) Haas, H.; Sheline, R. K. *J. Inorg. Nucl. Chem.* **1967**, *29*, 693–698.
- (411) Eguchi, T.; Nakayama, H.; Ohki, H.; Takeda, S.; Nakamura, N.; Kernaghan, S.; Heaton, B. T. *J. Organomet. Chem.* **1992**, *428*, 207–212.
- (412) Kempgens, P.; Hirschinger, J.; Granger, P.; Rosé, J. *Solid State Nucl. Magn. Reson.* **1997**, *10*, 95–103.
- (413) Corradini, P. *J. Chem. Phys.* **1959**, *31*, 1676–1677.
- (414) Wei, C. H.; Dahl, L. F. *J. Am. Chem. Soc.* **1966**, *88*, 1821–1822.
- (415) Wei, C. H. *Inorg. Chem.* **1969**, *8*, 2384–2397.
- (416) Farrugia, L. J.; Braga, D.; Grepioni, F. *J. Organomet. Chem.* **1999**, *573*, 60–66.
- (417) Lennertz, A. M.; Laege, J.; Mirbach, M. J.; Saus, A. *J. Organomet. Chem.* **1979**, *171*, 203–207.

- (418) Alvila, L.; Pakkanen, T. A.; Pakkanen, T. T.; Krause, O. *J. Mol. Catal.* **1992**, *71*, 281–290.
- (419) Magnus, P.; Principe, L. M.; Slater, M. J. *J. Org. Chem.* **1987**, *52*, 1483–1486.
- (420) Khand, I. U.; Knox, G. R.; Pauson, P. L.; Watts, W. E. *J. Chem. Soc. [Perkin 1]* **1973**, 975–977.
- (421) Kim, J. W.; Chung, Y. K. *Synthesis* **1998**, *1998*, 142–144.
- (422) Krafft, M. E.; Boñaga, L. V. R. *Angew. Chem. Int. Ed.* **2000**, *39*, 3676–3680.
- (423) Krafft, M. E.; Boñaga, L. V. R.; Hirose, C. *J. Org. Chem.* **2001**, *66*, 3004–3020.
- (424) Boñaga, L. V. R.; Wright, J. A.; Krafft, M. E. *Chem. Commun.* **2004**, 1746–1747.
- (425) Cabot, R.; Lledó, A.; Revés, M.; Riera, A.; Verdagué, X. *Organometallics* **2007**, *26*, 1134–1142.
- (426) Mirbach, M. J.; Mirbach, M. F.; Saus, A.; Topalsavoglou, N.; Tuyet Nhu Phu. *J. Am. Chem. Soc.* **1981**, *103*, 7590–7594.
- (427) Hino, K.; Kosugi, K.; Okunishi, E.; Yokoyama, T.; Nishi, N. *Nippon Kagakkai Koen Yokoshu* **2003**, *83*, 491.
- (428) Nishi, N.; Kosugi, K.; Hino, K.; Yokoyama, T. *Eur. Phys. J. - At. Mol. Opt. Plasma Phys.* **2003**, *24*, 97–100.
- (429) Nishi, N.; Kosugi, K.; Hino, K.; Yokoyama, T.; Okunishi, E. *Chem. Phys. Lett.* **2003**, *369*, 198–203.
- (430) Sizova, O. V.; Baranovskii, V. I. *J. Struct. Chem.* **1993**, *34*, 844–853.
- (431) Sizova, O. V.; Baranovski, V. I. *Inorganica Chim. Acta* **1993**, *214*, 113–123.
- (432) Cotton, F. A. *Inorg. Chem.* **1966**, *5*, 1083–1085.
- (433) Moskovich, S.; Reuvenov, D.; Schultz, R. H. *Chem. Phys. Lett.* **2006**, *431*, 62–66.
- (434) Morse, J. M.; Parker, G. H.; Burkey, T. J. *Organometallics* **1989**, *8*, 2471–2474.
- (435) Gittermann, S.; Jiao, T.; Burkey, T. J. *Photochem. Photobiol. Sci.* **2003**, *2*, 817–820.
- (436) Cowan, A. J.; George, M. W. *Coord. Chem. Rev.* **2008**, *252*, 2504–2511.
- (437) Heck, R. F.; Breslow, D. S. *J. Am. Chem. Soc.* **1961**, *83*, 1097–1102.
- (438) Brummond, K. M.; Kent, J. L. *Tetrahedron* **2000**, *56*, 3263–3283.
- (439) Garthwaite, J.; Boulton, C. L. *Annu. Rev. Physiol.* **1995**, *57*, 683–706.
- (440) Motterlini, R.; Leo Otterbein. *Nat Rev Drug Discov* **2010**, *9*, 728–743.
- (441) Tenhunen, R.; Marver, H. S.; Schmid, R. *Proc. Natl. Acad. Sci.* **1968**, *61*, 748–755.
- (442) Brigham and Women’s Hospital, Phase II Study of Inhaled CO for the Treatment of Idiopathic Pulmonary Fibrosis. <http://www.clinical-trials.gov/ct2/show/NCT01214187> (12 Oct 2013).
- (443) INO Therapeutics, Safety and Tolerability Study of Inhaled Carbon Monoxide in Kidney Transplant Patients. <http://www.clinicaltrials.gov/ct2/show/NCT00531856> (12 Oct 2013).
- (444) National Institutes of Health Clinical Center, Carbon Monoxide to Prevent Lung Inflammation. <http://www.clinicaltrials.gov/ct2/show/NCT00094406> (12 Oct 2013).
- (445) Queen’s University Kingston Canada, Study of Inhaling Carbon Monoxide to Treat Patients With Intestinal Paralysis After Colon Surgery. <http://www.clinicaltrials.gov/ct2/show/NCT01050712> (12 Oct 2013).
- (446) Pitchumony, T. S.; Spingler, B.; Motterlini, R.; Alberto, R. *Chim. Int. J. Chem.* **2008**, *62*, 277–279.
- (447) Pitchumony, T. S.; Spingler, B.; Motterlini, R.; Alberto, R. *Org. Biomol. Chem.* **2010**, *8*, 4849–4854.

- (448) Mann, B. E. In *Medicinal Organometallic Chemistry*; Jaouen, G.; Metzler-Nolte, N., Eds.; Topics in Organometallic Chemistry; Springer Berlin Heidelberg, 2010; pp. 247–285.
- (449) Johnson, T. R.; Mann, B. E.; Clark, J. E.; Foresti, R.; Green, C. J.; Motterlini, R. *Angew. Chem. Int. Ed.* **2003**, *42*, 3722–3729.
- (450) Zobi, F. *Future Med. Chem.* **2013**, *5*, 175–188.
- (451) Motterlini, R.; Mann, B. E.; Foresti, R. *Expert Opin. Investig. Drugs* **2005**, *14*, 1305–1318.
- (452) Alberto, R.; Motterlini, R. *Dalton Trans.* **2007**, 1651–1660.
- (453) Mann, B. E. *Organometallics* **2012**, *31*, 5728–5735.
- (454) Marques, A. R.; Kromer, L.; Gallo, D. J.; Penacho, N.; Rodrigues, S. S.; Seixas, J. D.; Bernardes, G. J. L.; Reis, P. M.; Otterbein, S. L.; Ruggieri, R. A.; Gonçalves, A. S. G.; Gonçalves, A. M. L.; Matos, M. N. D.; Bento, I.; Otterbein, L. E.; Blättler, W. A.; Romão, C. C. *Organometallics* **2012**, *31*, 5810–5822.
- (455) Seixas, J. D.; Mukhopadhyay, A.; Santos-Silva, T.; Otterbein, L. E.; Gallo, D. J.; Rodrigues, S. S.; Guerreiro, B. H.; Gonçalves, A. M. L.; Penacho, N.; Marques, A. R.; Coelho, A. C.; Reis, P. M.; Romão, M. J.; Romão, C. C. *Dalton Trans.* **2013**, *42*, 5985–5998.
- (456) Johnson, T. R.; Mann, B. E.; Teasdale, I. P.; Adams, H.; Foresti, R.; Green, C. J.; Motterlini, R. *Dalton Trans.* **2007**, 1500–1508.
- (457) Santos-Silva, T.; Mukhopadhyay, A.; Seixas, J. D.; Bernardes, G. J. L.; Romão, C. C.; Romão, M. J. *J. Am. Chem. Soc.* **2011**, *133*, 1192–1195.
- (458) Motterlini, R.; Clark, J. E.; Foresti, R.; Sarathchandra, P.; Mann, B. E.; Green, C. J. *Circ. Res.* **2002**, *90*, e17–e24.
- (459) Arregui, B.; López, B.; Salom, M. G.; Valero, F.; Navarro, C.; Fenoy, F. J. *Kidney Int.* **2004**, *65*, 564–574.
- (460) Schaefer, H. F. *Methods of Electronic Structure Theory*; Plenum Press, 1977.
- (461) Merlino, S.; Montagnoli, G. *Acta Crystallogr. Sect. B* **1968**, *24*, 424–429.
- (462) Benedetti, E.; Braca, G.; Sbrana, G.; Salvetti, F.; Grassi, B. *J. Organomet. Chem.* **1972**, *37*, 361–373.
- (463) Bruce, M. I.; Stone, F. G. A. *J. Chem. Soc. Inorg. Phys. Theor.* **1967**, 1238–1241.
- (464) Pathak, B.; Majumdar, D.; Leszczynski, J. *Int. J. Quantum Chem.* **2009**, *109*, 2263–2272.
- (465) Sobota, M.; Schernich, S.; Schulz, H.; Hieringer, W.; Paape, N.; Wasserscheid, P.; Görling, A.; Laurin, M.; Libuda, J. *Phys. Chem. Chem. Phys.* **2012**, *14*, 10603–10612.
- (466) Alessio, E.; Milani, B.; Bolle, M.; Mestroni, G.; Faleschini, P.; Todone, F.; Geremia, S.; Calligaris, M. *Inorg. Chem.* **1995**, *34*, 4722–4734.
- (467) Alessio, E.; Mestroni, G.; Nardin, G.; Attia, W. M.; Calligaris, M.; Sava, G.; Zorzet, S. *Inorg. Chem.* **1988**, *27*, 4099–4106.
- (468) Jaouen, G.; Vessieres, A.; Butler, I. S. *Acc. Chem. Res.* **1993**, *26*, 361–369.
- (469) Niesel, J.; Pinto, A.; N'Dongo, H. W. P.; Merz, K.; Ott, I.; Gust, R.; Schatzschneider, U. *Chem. Commun.* **2008**, 1798–1800.
- (470) Note 10 mM conc. .
- (471) Motterlini, R.; Mann, B.; Johnson, T.; Clark, J.; Foresti, R.; Green, C. *Curr. Pharm. Des.* **2003**, *9*, 2525–2539.
- (472) Davies, J. B.; Hallam, H. E. *J. Chem. Soc. Faraday Trans. 2 Mol. Chem. Phys.* **1972**, *68*, 509–512.
- (473) Dubost, H.; Abouaf-Marguin, L. *Chem. Phys. Lett.* **1972**, *17*, 269–273.

- (474) Jiang, G. J.; Person, W. B.; Brown, K. G. *J. Chem. Phys.* **1975**, *62*, 1201–1211.
- (475) Anderson, D. T.; Winn, J. S. *J. Phys. Chem. A* **2000**, *104*, 3472–3480.
- (476) Ziegler, T.; Tschinke, V.; Ursenbach, C. *J. Am. Chem. Soc.* **1987**, *109*, 4825–4837.
- (477) Ehlers, A. W.; Frenking, G. *Organometallics* **1995**, *14*, 423–426.
- (478) Siegbahn, P. E. M. *Theor. Chim. Acta* **1993**, *86*, 219–228.
- (479) Kealy, T. J.; Pauson, P. L. *Nature* **1951**, *168*, 1039–1040.
- (480) Miller, S. A.; Tebboth, J. A.; Tremaine, J. F. *J. Chem. Soc. Resumed* **1952**, 632–635.
- (481) Wilkinson, G.; Rosenblum, M.; Whiting, M. C.; Woodward, R. B. *J. Am. Chem. Soc.* **1952**, *74*, 2125–2126.
- (482) Payne, C. K.; Snee, P. T.; Yang, H.; Kotz, K. T.; Schafer, L. L.; Tilley, T. D.; Harris, C. B. *J. Am. Chem. Soc.* **2001**, *123*, 7425–7426.
- (483) Schuster-Woldan, H. G.; Basolo, F. *J. Am. Chem. Soc.* **1966**, *88*, 1657–1663.
- (484) Cotton, F. A. *Discuss. Faraday Soc.* **1969**, *47*, 79–83.
- (485) Dahl, L. F.; Wei, C. H. *Inorg. Chem.* **1963**, *2*, 713–721.
- (486) Bennett, M. J.; Churchill, M. R.; Gerloch, M.; Mason, R. *Nature* **1964**, *201*, 1318–1320.
- (487) Smith, A. E. *Inorg. Chem.* **1972**, *11*, 165–170.
- (488) Byers, L. R.; Dahl, L. F. *Inorg. Chem.* **1980**, *19*, 277–284.
- (489) Fitzpatrick, P. J.; Le Page, Y.; Sedman, J.; Butler, I. S. *Inorg. Chem.* **1981**, *20*, 2852–2861.
- (490) Cotton, F. A.; Rusholme, G. A. *J. Am. Chem. Soc.* **1972**, *94*, 402–406.
- (491) Cotton, F. A.; Calderon, J. L.; Takats, J. *J. Am. Chem. Soc.* **1971**, *93*, 3587–3591.
- (492) Rogers, R. D.; Bynum, R. V.; Atwood, J. L. *J. Am. Chem. Soc.* **1978**, *100*, 5238–5239.
- (493) Goel, A. B.; Goel, S.; VanDerVeer, D.; Clark, H. C. *Inorganica Chim. Acta* **1981**, *53*, L117–L118.
- (494) Casey, C. P.; O'Connor, J. M.; Jones, W. D.; Haller, K. J. *Organometallics* **1983**, *2*, 535–538.
- (495) Schonberg, P. R.; Paine, R. T.; Campana, C. F.; Duesler, E. N. *Organometallics* **1982**, *1*, 799–807.
- (496) Bennett, M. J.; Cotton, F. A.; Davison, A.; Faller, J. W.; Lippard, S. J.; Morehouse, S. M. *J. Am. Chem. Soc.* **1966**, *88*, 4371–4376.
- (497) Hart, S. L.; Duncalf, D. J.; Hastings, J. J.; McCamley, A.; Taylor, P. C. *J. Chem. Soc. Dalton Trans.* **1996**, 2843–2849.
- (498) Faller, J. W.; Murray, H. H.; Saunders, M. *J. Am. Chem. Soc.* **1980**, *102*, 2306–2309.
- (499) Habib, A.; Tanke, R. S.; Holt, E. M.; Crabtree, R. H. *Organometallics* **1989**, *8*, 1225–1231.
- (500) Imamura, Y.; Kubo, K.; Mizuta, T.; Miyoshi, K. *Organometallics* **2006**, *25*, 2301–2307.
- (501) Cotton, F. A.; Calderon, J. L.; DeBoer, B. G.; Takats, J. *J. Am. Chem. Soc.* **1971**, *93*, 3592–3597.
- (502) Tsutsui, M.; Hancock, M.; Ariyoshi, J.; Levy, M. N. *J. Am. Chem. Soc.* **1969**, *91*, 5233–5236.
- (503) Tsutsui, M.; Hudman, C. E. *Chem Lett* **1972**, 777.
- (504) King, R. B. *Inorg. Chem.* **1968**, *7*, 90–94.
- (505) Piper, T. S.; Wilkinson, G. *J. Inorg. Nucl. Chem.* **1956**, *2*, 38–45.
- (506) Fettes, D. J.; Narayanaswamy, R.; Rest, A. J. *J. Chem. Soc. Dalton Trans.* **1981**, 2311–2316.
- (507) Mahmoud, K. A.; Rest, A. J.; Alt, H. G. *J. Chem. Soc. Dalton Trans.* **1985**, 1365–1374.

- (508) Reimer, K. J.; Shaver, A. *Inorg. Chem.* **1975**, *14*, 2707–2716.
- (509) Church, S. P.; Hermann, H.; Grevels, F.-W.; Schaffner, K. *J. Chem. Soc. Chem. Commun.* **1984**, 785–786.
- (510) Looking at the spectra in the previous study by our group, the 2046 cm⁻¹ band in question; shows dynamic redshifting with increasing delay time, which is the; opposite of what one would expect for a photoproduct band undergoing vibrational cooling. This anomaly further supports the; notion that this band is an instrumental artifact and is not the result of a nascent photoproduct. .
- (511) Harpham, M. R.; Stickrath, A., B.; Zhang, X.; Huang, J.; Mara, M. W.; Chen, L. X.; Liu, D.-J. *J. Phys. Chem. A* **2013**, *117*, 9807–9813.
- (512) The reason that a lower proportion of monocarbonyl-loss product should be formed remains unclear and at this time can only be attributed to details of the electronic structure of the parent complex. .
- (513) Casey, C. P.; Jones, W. D. *J. Am. Chem. Soc.* **1980**, *102*, 6154–6156.
- (514) Dang, L. X. *J. Chem. Phys.* **1999**, *110*, 10113–10122.
- (515) Swennenhuis, B. H. G.; Poland, R.; Fan, W. Y.; Darensbourg, D. J.; Bengali, A. A. *Inorg. Chem.* **2010**, *49*, 7597–7604.
- (516) Winter, M. J. In *Advances in Organometallic Chemistry*; F.G.A. Stone and Robert West, Ed.; Academic Press, 1989; Vol. Volume 29, pp. 101–162.
- (517) Meyer, T. J.; Caspar, J. V. *Chem. Rev.* **1985**, *85*, 187–218.
- (518) Lomont, J. P.; Harris, C. B. *Inorganica Chim. Acta* DOI: 10.1016/j.ica.2014.07.064.
- (519) Kobayashi, T.; Ohtani, H.; Noda, H.; Teratani, S.; Yamazaki, H.; Yasufuku, K. *Organometallics* **1986**, *5*, 110–113.
- (520) Hughey, J. L.; Bock, C. R.; Meyer, T. J. *J. Am. Chem. Soc.* **1975**, *97*, 4440–4441.
- (521) Virrels, I. G.; George, M. W.; Johnson, F. P. A.; Turner, J. J.; Westwell, J. R. *Organometallics* **1995**, *14*, 5203–5208.
- (522) Dixon, A. J.; George, M. W.; Hughes, C.; Poliakoff, M.; Turner, J. J. *J. Am. Chem. Soc.* **1992**, *114*, 1719–1729.
- (523) Brookes, C. M.; Lomont, J. P.; Nguyen, S. C.; Calladine, J. A.; Sun, X.-Z.; Harris, C. B.; George, M. W. *Polyhedron* **2014**, *72*, 130–134.
- (524) Hooker, R. H.; Mahmoud, K. A.; Rest, A. J. *J. Chem. Soc. Chem. Commun.* **1983**, 1022–1024.
- (525) Potenza, J.; Giordano, P.; Mastropaolo, D.; Efraty, A. *Inorg. Chem.* **1974**, *13*, 2540–2544.
- (526) Curtis, M. D.; Butler, W. M. *J. Organomet. Chem.* **1978**, *155*, 131–145.
- (527) Jemmis, E. D.; Pinhas, A. R.; Hoffmann, R. *J. Am. Chem. Soc.* **1980**, *102*, 2576–2585.
- (528) Robbins, J. L.; Wrighton, M. S. *Inorg. Chem.* **1981**, *20*, 1133–1139.
- (529) Hooker, R. H.; Rest, A. J. *J. Chem. Soc. Dalton Trans.* **1990**, 1221–1229.
- (530) Virrels, I. G.; Nolan, T. F.; George, M. W.; Turner, J. J. *Organometallics* **1997**, *16*, 5879–5883.
- (531) Zhang, X.; Li, Q.; Xie, Y.; King, R. B.; Iii, H. F. S. *Dalton Trans.* **2008**, 4805–4810.
- (532) Huang, J.-S.; Dahl, L. F. *J. Organomet. Chem.* **1983**, *243*, 57–68.
- (533) Lewis, L. N.; Caulton, K. G. *Inorg. Chem.* **1980**, *19*, 1840–1846.
- (534) Collman, J. P.; Hegedus, L. S. *Principles and Applications of Organotransition Metal Chemistry*; University Science Books: Mill Valley CA, 1980.

- (535) Janowicz, A. H.; Bryndza, H. E.; Bergman, R. G. *J. Am. Chem. Soc.* **1981**, *103*, 1516–1518.
- (536) Lomont, J. P.; Nguyen, S. C.; Harris, C. B. *Acc. Chem. Res.* **2014**, *47*, 1634–1642.
- (537) Harvey, J. N. *Wiley Interdiscip. Rev. Comput. Mol. Sci.* **2014**, *4*, 1–14.
- (538) Seder, T. A.; Ouderkirk, A. J.; Weitz, E. *J. Chem. Phys.* **1986**, *85*, 1977–1986.
- (539) Ryther, R. J.; Weitz, E. *J. Phys. Chem.* **1991**, *95*, 9841–9852.
- (540) Harvey, J. N.; Poli, R.; Smith, K. M. *Coord. Chem. Rev.* **2003**, *238–239*, 347–361.
- (541) Long, C.; Kearns, D. R. *J. Chem. Phys.* **1973**, *59*, 5729–5736.
- (542) Rae, M.; Perez-Balderas, F.; Baleizão, C.; Fedorov, A.; Cavaleiro, J. A. S.; Tomé, A. C.; Berberan-Santos, M. N. *J. Phys. Chem. B* **2006**, *110*, 12809–12814.
- (543) Reineke, S.; Baldo, M. A. *Sci. Rep.* **2014**, *4*.
- (544) Kearns, D. R.; Case, W. A. *J. Am. Chem. Soc.* **1966**, *88*, 5087–5097.
- (545) Marchetti, A. P.; Kearns, D. R. *J. Am. Chem. Soc.* **1967**, *89*, 768–777.
- (546) Giachino, G. G.; Kearns, D. R. *J. Chem. Phys.* **1970**, *52*, 2964–2974.
- (547) Scott, D. R.; Becker, R. S. *J. Chem. Phys.* **1961**, *35*, 516–531.
- (548) Armstrong, A. T.; Smith, F.; Elder, E.; McGlynn, S. P. *J. Chem. Phys.* **1967**, *46*, 4321–4328.
- (549) Pellow, R.; Vala, M. *J. Chem. Phys.* **1989**, *90*, 5612–5621.
- (550) Leadbeater, N. *Coord. Chem. Rev.* **1999**, *188*, 35–70.
- (551) Poliakoff, M.; Turner, J. J. *Angew. Chem. Int. Ed.* **2001**, *40*, 2809–2812.
- (552) Delos, J. B. *J. Chem. Phys.* **1973**, *59*, 2365–2369.
- (553) Tully, J. C. *J. Chem. Phys.* **1974**, *61*, 61–68.
- (554) Zahr, G. E.; Preston, R. K.; Miller, W. H. *J. Chem. Phys.* **1975**, *62*, 1127–1135.
- (555) Lorquet, J. C.; Leyh-Nihant, B. *J. Phys. Chem.* **1988**, *92*, 4778–4783.
- (556) Persson, B. J.; Roos, B. O.; Pierloot, K. *J. Chem. Phys.* **1994**, *101*, 6810–6821.
- (557) Harvey, J. N.; Aschi, M.; Schwarz, H.; Koch, W. *Theor. Chem. Acc.* **1998**, *99*, 95–99.
- (558) Salem, L.; Rowland, C. *Angew. Chem. Int. Ed. Engl.* **1972**, *11*, 92–111.
- (559) Michl, J. *J. Am. Chem. Soc.* **1996**, *118*, 3568–3579.
- (560) Michl, J.; Havlas, Z. *Pure Appl. Chem.* **1997**, *69*.
- (561) Havlas, Z.; Michl, J. *J. Am. Chem. Soc.* **2002**, *124*, 5606–5607.
- (562) Pothoczki, S.; Pusztai, L.; Kohara, S. *J. Phys. Condens. Matter* **2007**, *19*, 335204.